



University of Calgary

PRISM: University of Calgary's Digital Repository

Graduate Studies

The Vault: Electronic Theses and Dissertations

2017

Multi-Constellation GNSS for Absolute and Relative Navigation in Highly Elliptical Orbits

Kahr, Erin Jennifer

Kahr, E. J. (2017). Multi-Constellation GNSS for Absolute and Relative Navigation in Highly Elliptical Orbits (Unpublished doctoral thesis). University of Calgary, Calgary, AB.

doi:10.11575/PRISM/27024

<http://hdl.handle.net/11023/4021>

doctoral thesis

University of Calgary graduate students retain copyright ownership and moral rights for their thesis. You may use this material in any way that is permitted by the Copyright Act or through licensing that has been assigned to the document. For uses that are not allowable under copyright legislation or licensing, you are required to seek permission.

Downloaded from PRISM: <https://prism.ucalgary.ca>

UNIVERSITY OF CALGARY

Multi-Constellation GNSS for Absolute and Relative Navigation in Highly Elliptical Orbits

by

Erin Kahr

A THESIS

SUBMITTED TO THE FACULTY OF GRADUATE STUDIES
IN PARTIAL FULFILMENT OF THE REQUIREMENTS FOR THE
DEGREE OF DOCTOR OF PHILOSOPHY

GRADUATE PROGRAM IN GEOMATICS ENGINEERING

CALGARY, ALBERTA

August, 2017

© Erin Kahr 2017

Abstract

The goal of this research project was to determine to what order of magnitude relative positions of formation flying spacecraft in highly elliptical orbits (HEO) can be measured using Global Navigation Satellite Systems. The orbit of the European Space Agency's upcoming PROBA-3 mission, with a roughly 600 km perigee and 60500 km apogee, was chosen as the test case throughout the research project. The key result was that, provided there were sufficient measurements, relative positioning could be accomplished throughout the HEO orbit to the sub-metre level in the absence of maneuvers, and to the sub-10 m level when a tight formation flying phase bracketed by maneuvers was simulated during the apogee arc. In the case of maneuvers or of too few measurements, the additional uncertainty prevents sufficiently rigorous blunder detection from being carried out, and the filter becomes extremely susceptible to outliers.

In addition to answering the original research question, it was concluded that the regional navigation systems offer a significant advantage for above the constellation users, because the slower relative motion translates into longer arcs of uninterrupted measurement data. Using live signals collected from a low Earth orbiting CubeSat, Satellite Based Augmentation System (SBAS) tracking over the Earth's limb was demonstrated, and it was proven for the first time that SBAS ranging is a viable source of positioning information for users in highly elliptical or other above the constellation Earth orbits. Finally, it was determined in the preliminary visibility studies that the entire positioning problem is extremely sensitive to the receiver's ability to acquire and track weak GNSS signals. Hardware-in-the-loop simulation and receiver design work on a software research receiver confirmed that the power in the GNSS side lobes hovers slightly below the acquisition and tracking threshold of a standard receiver, but that these signals can be acquired and tracked making use existing weak signal algorithms, dramatically improving both absolute and relative positioning accuracies.

Preface

The research project presented in this thesis was the result of co-supervision in the Position, Location and Navigation Group at the University of Calgary and the GNSS Technology and Navigation Group at the Deutsches Zentrum für Luft- und Raumfahrt, DLR. The unique access to two outstanding research institutes along with their research tools and expertise has made it possible to take on a project with extremely broad scope, and at the same time to tackle geomatics engineering, aerospace engineering and signal processing aspects of the project in depth, and understand the relationships between them.

Over the course of the studies several papers were published in order to share the results with the scientific community, the contents of which form the majority of the text in chapters three, four and five. InderScience retains the copyright for the portion of Chapter 3 published in Kahr 2013, while Wiley retains the copyright for the majority of Chapter 4. The research in these papers was carried out almost exclusively by the first author, under the guidance of Dr. Montenbruck at DLR and Dr. O'Keefe at University of Calgary. The full citations of the included papers are:

Kahr, E., Montenbruck, O., and O'Keefe, K, (2016) 'An Analysis of SBAS Signal Reception in Space,' *Navigation, Journal of the Institute of Navigation*, Vol. 63, No. 3, pp. 321-333.

Kahr, E., Montenbruck, O., O'Keefe, K. (2015) 'A Comparative Study of SBAS Systems for Navigation in Geostationary Orbit,' *Proceedings of ION GNSS+ 2015*, Tampa, FL, pp. 3875-3886.

Kahr, E., O'Keefe, K. and Montenbruck, O. (2014) 'Hardware-in-the-Loop Simulation of GNSS Signal Tracking in Highly Elliptical Orbits using the GSNRx™ Software Receiver,' *Proceedings of ION GNSS+ 2014*, Tampa, FL, pp. 1448-1458.

Kahr, E. (2013) 'Prospects of Multi-GNSS Tracking for Formation Flying in Highly Elliptical Earth Orbits', *International Journal of Space Science and Engineering*, Vol. 1, No.4 pp. 432-447. [10.1504/IJSPACESE.2013.059267](https://doi.org/10.1504/IJSPACESE.2013.059267)

Kahr, E. (2013) 'Prospects of Multi-GNSS Tracking for Formation Flying in Highly Elliptical Earth Orbits', *5th International Conference on Satellite Formation Flying Missions and Technologies*, Munich, Germany.

Acknowledgements

First and foremost, I would like to acknowledge all of those whose technical help and expertise have guided me through this research. At the top of this list are my supervisors, Dr. Oliver Montenbruck and Dr. Kyle O’Keefe. Kyle has been a friend and mentor since the beginning of my research career, when as a confused undergraduate student I found my way through his open office door in 2005 and the opportunity to work on the CanX-2 CubeSat was born. I met Oliver at the ION GNSS conference in 2010, when as an equally confused master’s student I presented some good acquisition results for CanX-2, accompanied by some very desperate attempts at orbit determination. I was rescued from my ignorance and have been collaborating with Oliver and his team at the German Aerospace Center, DLR, ever since.

Not far behind are the many faculty members and other experts at University of Calgary and at DLR. Mark, Gérard, Susan, Ali B., James, Cillian, Zhe, Aiden, Bernhard, Sergey, Adam, Rakesh, Vimal and anyone else who helped me with a lab setup or who sat still long enough to listen through an in-depth description of a GSNRx™ problem and shed some insight into solving it. I am extremely grateful for your help. I am likewise grateful for the excellent quality of the advanced courses on GNSS, estimation and related topics which form the basis of this work, and to the instructors who invested the time to develop and teach them. I find myself frequently trying to persuade people who think my thesis topic is terrifying that I’m really just applying these same basic skills to a slightly different application.

To my many friends at DLR, Andreas, Gabriella, André, Jean-Sebastien, Markus, Christian, Benjamin, Peter, and all the other short term visitors and students, not to mention countless others in the flight dynamics group, words can’t express how much I have learned from you about aerospace, both directly and indirectly through the years of team meetings, conversations, and by absorbing the general research culture at DLR. Your warmth and friendship during my many visits is very much appreciated.

I would also like to formally recognize the scholarship support I have been lucky enough to earn throughout this project. I have been almost entirely self-funded during six intense years of research, by the Natural Sciences and Engineering Research Council of Canada, Alberta

Innovates Technology Futures, Engineers Canada Manulife Financial, Zonta International, APEGA, the Institute of Navigation, the University of Calgary and the Department of Geomatics Engineering. Thank you in particular to Margaret Clarke, whose first donation to University of Calgary 52 years ago evolved into the small but mighty Robert B. Paugh Memorial Scholarship. Winning this scholarship opened a door for me into the University of Calgary's 50th anniversary celebrations, where I caught a fascinating glimpse into the world of Alberta's elite.

In the larger Calgary geomatics community, I would like to thank Tecterra for allowing an ambitious PhD Candidate to make use of their fantastic GNSS simulator, and NovAtel for their original in-kind donation of the GPS receiver flying on board CanX-2, and their support in upgrading the receiver to unlock its SBAS functionality so many years after the launch. I literally could not have produced this research project without these tools. Even more deserving of thanks are the many students at University of Toronto who operated CanX-2 during the years of GPS data collection campaigns, and dedicated their time to running my experiments. They provided my first and some of my deepest insights into spacecraft operations.

Finally, I would like to thank all my university friends and research group mates not already mentioned. PLAN team members, Munich friends, Moose crew, and most especially the original Trailer H crew: Axel, Aleks, Ali, Kaleel, Mike, Andres, Tori, Jeremy, Laura, Sam, Coral, Bernard, Mahsa, Elmira, Eric, Sergey, Billy, Rasika, Lukas, Jagmal, Dorota and Janja, among others, you know who you are! In particular, Jacky, Eunju, Mo and Ivan, who have been my grad studies friends from my masters through to the very end. You put the fun into graduate studies.

Last but not least I would like to thank my family, who have been putting up with my eccentric student schedule and nomadic lifestyle for years. I would never even have attempted this without your love and backing. Thank you!

Dedication

To Mum, Dad, Paula and Andreas,

Thank you for all the support.

Table of Contents

Abstract	ii
Preface.....	iii
Acknowledgements.....	iv
Dedication.....	vi
Table of Contents.....	vii
List of Tables	xi
List of Figures and Illustrations	xii
List of Symbols	xix
List of Abbreviations	xxii
CHAPTER ONE: INTRODUCTION.....	1
CHAPTER TWO: BACKGROUND AND HISTORY OF ABOVE THE CONSTITUTION GNSS	5
2.1 GNSS Basics.....	5
2.1.1 Trilateration	5
2.1.2 GNSS Signals, Receivers and Measurements	7
2.1.3 Position Estimation.....	12
2.1.4 Positioning Errors and Geometry	15
2.1.5 GNSS Constellations	18
2.2 Orbit Basics.....	20
2.2.1 Orbital Motion	20
2.2.2 Types of Orbits	21
2.2.3 Orbit Determination.....	23
2.3 GNSS Positioning in Orbit	24
2.4 A Brief History of Above the Constellation GNSS Positioning.....	26
2.4.1 Early Missions	27
2.4.2 Simulations and Multi-Constellation GNSS	27
2.4.3 Receivers and Recent Single Satellite Missions.....	29
2.4.3.1 SGR GEO/GIOVE-A.....	29
2.4.3.2 Topstar 3000/Topstar 3000 G2/PROBA-2	30
2.4.3.3 SBIRS GEO1	31
2.4.3.4 Antenna Characterization Experiment	31
2.4.3.5 Chang'E-5T	32
2.4.3.6 GOES-R/Viceroy-4.....	33
2.4.3.7 Mosaic GNSS/ LION Navigator/ Small GEO	34
2.4.3.8 HisGR.....	34
2.4.4 Formation Flying	35
2.4.4.1 Magnetospheric Multiscale Mission.....	35
2.4.4.2 PROBA-3.....	40
2.5 Outline of Missing Research.....	41
CHAPTER THREE: VISIBILITY SIMULATIONS	45
3.1 Introduction.....	45
3.2 Simulation and Assumptions	45

3.2.1 Simulation Software	46
3.2.2 User Spacecraft.....	46
3.2.3 Orbits and Coordinate Systems	48
3.2.4 GNSS Constellations and Signals	49
3.2.5 GNSS Receiver Parameters	52
3.3 Simulation Verification.....	55
3.4 GNSS Antenna Orientation Study	56
3.4.1 Part 1: Unconstrained Antenna Placement	57
3.4.2 Part 2: Sun-Pointing Constraint.....	61
3.4.3 Part 3: Optimal Transition from Nadir to Zenith.....	66
3.4.4 Conclusions	69
3.5 Multi-Constellation GNSS.....	69
3.5.1 Simulation assumptions.....	70
3.5.2 Results	71
3.5.2.1 Multiple MEO Constellations	71
3.5.2.2 Impact of New Signal Structures	77
3.5.2.3 Regional Systems.....	78
3.5.3 Conclusions	81
CHAPTER FOUR: AN ANALYSIS OF SBAS RECEPTION IN SPACE	83
4.1 The CanX-2 Mission and SBAS Experiment	86
4.2 SBAS Signal Power	88
4.3 Ranging Data Accuracy	97
4.4 Conclusions.....	106
CHAPTER FIVE: RECEIVER DESIGN	108
5.1 Above the Constellation Receivers	108
5.2 The GSNRx™ Software Receiver	111
5.2.1 Modifications to GSNRx™	112
5.2.2 Adding Full Timing Information.....	112
5.2.3 Adding an Orbit Propagator	113
5.2.4 Visibility Algorithm	114
5.2.5 Channel allocation	115
5.2.6 Loss of Navigation Solution.....	116
5.2.7 Tropospheric model.....	116
5.2.8 ITAR Restrictions.....	117
5.3 Simulating the HEO Environment	117
5.3.1 Simulation Epoch	117
5.3.2 GPS Constellation	117
5.3.3 HEO Spacecraft Orbit.....	118
5.3.4 HEO Spacecraft Attitude Profile	119
5.3.5 Link Budget	119
5.3.6 Ionospheric Error.....	122
5.3.7 Resulting Signal Dynamics	124
5.4 Data Collection	125
5.5 Early Receiver Results.....	127
5.5.1 Acquisition and Tracking	127

5.5.2 Raw Measurements	129
5.5.3 Navigation Solution.....	133
5.5.4 Filtered Solution	135
5.6 Conclusions.....	137
CHAPTER SIX: MULTI-CONSTELLATION AND WEAK SIGNAL TRACKING ...	139
6.1 Simulation	139
6.1.1 Hardware Setup	140
6.1.2 Simulation Setup	141
6.1.2.1 User Spacecraft Simulation	142
6.1.2.2 GNSS Constellations	145
6.1.2.3 GNSS Errors	152
6.2 Receiver Algorithms	155
6.2.1 Signals	156
6.2.2 Acquisition	158
6.2.2.1 GPS L1 C/A	160
6.2.2.2 BeiDou and Galileo	161
6.2.2.3 Dwell Time	162
6.2.2.4 Threshold Setting.....	163
6.2.3 Tracking.....	165
6.2.3.1 Pre-existing Tracking Strategies	166
6.2.3.2 HEO Tracking Strategy	167
6.2.3.3 Vector Tracking	169
6.2.4 Bit Synchronization	170
6.2.4.1 GPS L1 C/A	170
6.2.4.2 Galileo E1b	171
6.2.4.3 BeiDou B1D1	171
6.2.4.4 BeiDou B1D2	172
6.2.5 Lock Indicators and C/N ₀ Calculations	173
6.2.6 Run Time	173
6.3 Results.....	173
6.3.1 Results for the standard tracking strategy	173
6.3.1.1 Measurement Quality.....	178
6.3.2 Results for the HEO tracking strategy	182
6.3.2.1 Measurement Quality	187
6.4 Conclusions.....	194
CHAPTER SEVEN: DESIGN AND PERFORMANCE OF THE RELATIVE POSITIONING FILTER.....	196
7.1 Filter Design	198
7.2 State Propagation	202
7.2.1 Trajectory Model	202
7.2.2 Drag and Solar Radiation Pressure Coefficient Model	206
7.2.3 Empirical Acceleration Model	206
7.2.4 Clock State Model	207
7.2.5 Ambiguity Model	208
7.2.6 Filter State Transition Matrix	209

7.3 Measurement Updates.....	210
7.3.1 Measurement Errors and Weighting	212
7.3.2 Impact of Asynchronous Measurements	215
7.3.3 Outlier Detection	217
7.4 Results.....	218
7.4.1 Multi-Constellation HEO Tracking Strategy.....	218
7.4.2 Multi-Constellation Data with Imperfect Thrust Modelling	229
7.4.3 Multi-Constellation Standard Tracking Strategy.....	231
7.4.4 High Sensitivity GPS.....	233
7.4.5 Maneuver Free Zero Baseline Test.....	240
7.5 Conclusions.....	242
CHAPTER EIGHT: CONCLUSIONS	245
REFERENCES	250
APPENDIX A: SUMMARIZED GNSS SIGNALS AND SIGNAL POWERS	278
APPENDIX B: COPYRIGHT PERMISSIONS	281

List of Tables

Table 3-1: HEO Orbital Parameters.....	47
Table 3-2: Antenna Pointing Profile	60
Table 3-3: Tracking Arc Duration at Perigee	67
Table 3-4: Optimal versus inertial tracking arc lengths.....	68
Table 5-1: Orbital Elements.....	118
Table 5-2: HEO Numerical Integration Parameters.....	119
Table 6-1: Occulter spacecraft Keplerian elements at the first perigee passage.....	143
Table 6-2: Occulter and Coronagraph spacecraft parameters.....	143
Table 6-3: Simulated Broadcast Ephemeris Standard Deviations	155
Table 6-4: Acquisition Parameters.....	163
Table 6-5: Standard Tracking Strategy	166
Table 6-6: Weak Signal Tracking Strategy.....	167
Table 7-1: Force modelling for the truth trajectory and relative positioning filter.....	204
Table 7-2: Tracking jitter vs C/N ₀ in dB-Hz.....	214

List of Figures and Illustrations

Figure 2-1: GNSS Trilateration	6
Figure 2-2: Components of a GNSS Signal (Not to Scale)	8
Figure 2-3: The result of multiplying two matching signals (left) and two signals with different ranging codes (right)	10
Figure 2-4: Sample Acquisition Grid, with a detected signal at 163.5 chips and -2.75 kHz.....	11
Figure 2-5: Basic Design of a Tracking Loop	12
Figure 2-6: Keplerian Orbital Elements, from Kahr 2011	21
Figure 2-7 Scale diagram of GPS, LEO, GEO and HEO orbits and the GPS transmit gain pattern	25
Figure 3-1: Relative geometry of the PROBA-3 orbital plane, GPS orbital planes, and the Earth, as viewed from a point above the North Pole	48
Figure 3-2: Assumed transmission gain patterns for the GNSS systems.....	51
Figure 3-3: Simulated signal power for a static receiver in Calgary, Canada	54
Figure 3-4: Receiving Antenna Gain Pattern.....	54
Figure 3-5: VisSim Output for the Nominal Test Case	55
Figure 3-6: Zenith and Nadir Pointing Output from the Simulation Tool.....	56
Figure 3-7: Preferred antenna orientation in the orbital plane (pitch angle).....	59
Figure 3-8: Preferred antenna orientation in the horizon plane (yaw angle)	59
Figure 3-9: Preferred antenna orientation in the plane perpendicular to motion (roll angle)	59
Figure 3-10: HEO satellite altitude corresponding to Figure 3-7 - Figure 3-9	59
Figure 3-11: Best antenna pointing profile based on number of visible GPS satellites	61
Figure 3-12: Optimal antenna pointing with the sun at apogee, August 20 th , 2011	62
Figure 3-13: Optimal antenna pointing with the sun at anti-orbit normal, November 17 th , 2011.....	63
Figure 3-14: Optimal antenna pointing with the sun at perigee, February 16 th , 2012	63
Figure 3-15: Optimal antenna pointing with the sun at orbit normal, May 13 th , 2012	64

Figure 3-16: Optimal antenna pointing with sun pointing constraint, April 1 st 2012.....	65
Figure 3-17: Optimal GPS (left) versus inertial (right) antenna pointing directions.....	68
Figure 3-18: Optimal (left) versus inertial (right) number of tracked satellites	69
Figure 3-19: Benefit of positioning with multiple MEO GNSS constellations	72
Figure 3-20: Impact of orbital plane alignment on GPS visibility with an inertial attitude profile.....	74
Figure 3-21: Impact of orbital plane alignment on Galileo visibility with an inertial attitude profile.....	75
Figure 3-22: Impact of orbital plane alignment on GPS visibility with a sun constraint on the attitude profile	76
Figure 3-23: Impact of orbital plane alignment on GPS visibility from a Molniya orbit.....	77
Figure 3-24: Impact of a 20 dB-Hz vs. 28 dB-Hz tracking threshold on visibility	78
Figure 3-25: Comparison of the GPS, WAAS and GAGAN visibility regions.....	79
Figure 3-26: Combined SBAS and QZSS visibility	80
Figure 3-27: Visibility of the BeiDou regional system from HEO. Left: apogee opposite China, right: apogee over China	81
Figure 3-28: Combined visibility for GPS, Galileo, GLONASS, QZSS, BeiDou, WAAS, EGNOS, GAGAN, SDCM and MSAS on the PROBA-3 orbit.....	82
Figure 4-1: Distribution of SBAS satellites globally	84
Figure 4-2: Theoretical visibility of GPS, SBAS, and both from GEO satellite at 60 degrees west, assuming a downward pointing hemispheric gain antenna, an acquisition threshold of 37 dB-Hz, a tracking threshold of 30 dB-Hz, and the WAAS prototype transmit gain pattern from Iriarte et al (2009) for all SBAS	85
Figure 4-3: GAGAN PRN 127 (red) and CanX-2 tracking arcs colored by C/N ₀	89
Figure 4-4: Corrected Signal Strength on GAGAN PRN 128, reflecting the transmit antenna gain pattern.....	91
Figure 4-5: Comparison of the signal strength among SBAS satellites. WAAS is in red circles, EGNOS in blue asterisks, GAGAN in cyan triangles and MSAS in green squares.....	93
Figure 4-6: Transmit gain patterns found in literature, for GAGAN, QZSS and a prototype patch antenna design suggested for the WAAS system.....	95

Figure 4-7: WAAS prn 138 signal power colored by hemisphere. The northern hemisphere appears to benefit from 1-2 dB more gain than the southern hemisphere.	96
Figure 4-8: The PRN 127 residual/inter-system bias with and without applying fast corrections.....	99
Figure 4-9: Locations of MGEX stations and receivers used in this study	101
Figure 4-10: MSAS ranging residuals compared to a GPS single point solution.....	102
Figure 4-11: GAGAN ranging residuals compared to a GPS single point solution.....	103
Figure 4-12: WAAS ranging residuals compared to a GPS single point solution.....	104
Figure 4-13: Geographic dependence of WAAS PRN 138 ranging errors compared to a GPS single point solution. The SBAS satellite position is marked by an asterisk.....	105
Figure 5-1: Generalized GNSS visibility law for HEO	114
Figure 5-2: Assumed GPS transmit gain pattern	120
Figure 5-3: Assumed gain pattern for the user receiving antenna	120
Figure 5-4: Simulated signal power translated into to dB-Hz	121
Figure 5-5: Vertical total electron content profile for the HEO simulation.....	122
Figure 5-6: Sample ionospheric range delay on PRN 14.....	123
Figure 5-7: Simulated Doppler on all visible PRNs	124
Figure 5-8: Simulated Doppler rate on all visible PRNs	124
Figure 5-9: Laboratory setup	126
Figure 5-10: Simulated vs tracked signals	128
Figure 5-11: Carrier to noise density ratio at acquisition and loss of lock	129
Figure 5-12: Single difference pseudorange, phase and Doppler measurement quality.....	130
Figure 5-13: Theoretical 1σ tracking jitter vs actual pseudorange measurement noise	132
Figure 5-14: Theoretical 1σ tracking jitter vs actual carrier phase measurement noise	133
Figure 5-15: GSNRx TM 's internal navigation solution accuracy during a perigee passage	134
Figure 5-16: Global dilution of precision during the first perigee passage	135

Figure 5-17: Filtered Position Solution.....	136
Figure 6-1: Hardware Setup.....	141
Figure 6-2: Separation between the Occulter and Coronagraph spacecraft as a function of time	144
Figure 6-3: GNSS antenna boresight pointing direction.....	145
Figure 6-4: GPS Block IIA assumed transmit gain pattern based on a 2D pattern	147
Figure 6-5: Block IIR transmit gain pattern from Lockheed Martin	147
Figure 6-6: Newer Block IIR and Block IIR-M transmit gain pattern from Lockheed Martin ..	148
Figure 6-7: Block IIF assumed transmit gain pattern based on a 2D pattern	148
Figure 6-8: Galileo IOV transmit gain pattern.....	149
Figure 6-9: BeiDou B1 MEO assumed transmit gain pattern based on a 2D pattern	150
Figure 6-10: BeiDou B1 IGSO/GEO assumed transmit gain pattern based on a 2D pattern	150
Figure 6-11: WAAS assumed transmit gain pattern based on a 2D pattern	151
Figure 6-12: QZSS assumed transmit gain pattern based on a 2D pattern for the antenna center and WAAS side lobes	151
Figure 6-13: GAGAN L1 assumed transmit gain pattern based on a 2D pattern	151
Figure 6-14: a) Positive elevation ionospheric delay (left) b) Negative elevation ionospheric delay when the receiver is outside the ionosphere based on the point of closest approach (centre), and c) Negative elevation ionospheric delay when the receiver is in the ionosphere calculated as figure b – figure a (right)	154
Figure 6-15: GNSS Signal Structures	158
Figure 6-16: BeiDou PRN 5 data bits	172
Figure 6-17: GPS C/N ₀ at acquisition and loss of lock using standard tracking	175
Figure 6-18: Galileo C/N ₀ at acquisition and loss of lock using standard tracking	175
Figure 6-19: B1D1 C/N ₀ at acquisition and loss of lock using standard tracking	176
Figure 6-20: B1D2 C/N ₀ at acquisition and loss of lock using standard tracking	176
Figure 6-21: Number of tracked satellites on the OSC using the standard tracking strategy	177

Figure 6-22: Differential measurement errors on a pair of B1D1 signals	178
Figure 6-23: Differential measurement errors on a pair of E1b signals	179
Figure 6-24: Pseudorange residuals at a C/N ₀ of 35 dB-Hz (above) and of 45 dB-Hz (below) from the standard tracking receiver	181
Figure 6-25: Number of tracked satellites on the OSC using the HEO tracking strategy	182
Figure 6-26: GPS C/N ₀ at acquisition and loss of lock using HEO tracking.....	183
Figure 6-27: Galileo C/N ₀ at acquisition and loss of lock using HEO tracking	184
Figure 6-28: B1D1 C/N ₀ at acquisition and loss of lock using HEO tracking	184
Figure 6-29: B1D2 C/N ₀ at acquisition and loss of lock using HEO tracking	185
Figure 6-30: Pseudorange residuals at a C/N ₀ of 35 dB-Hz (above) and of 45 dB-Hz (below) from the HEO tracking receiver.....	188
Figure 6-31: Pseudorange error on PRNs E22-E25 showing an ionosphere bias.....	189
Figure 6-32: Doppler error on PRNs E22 - E25 showing an ionosphere bias.....	190
Figure 6-33: Differenced ionospheric error simulated on PRNs E22 - E25	190
Figure 6-34: Doppler latency effects with 20 ms (left) vs 10 ms (right) coherent integration time	191
Figure 6-35: Steady state pseudorange tracking error under high dynamics.....	192
Figure 6-36: Dynamics on the G21 G25 PRN pair.....	192
Figure 6-37: Commonly Tracked GNSS Satellites on the Occulter (OSC) and Coronagraph (CSC) spacecraft	193
Figure 7-1: Flow chart of a single filter step with the asynchronous filter concept	199
Figure 7-2: Clock drift output from the GNSRx™ kinematic navigation solution	201
Figure 7-3: Estimated absolute empirical accelerations using perfect measurements and a 40 x 40 gravity field model.....	205
Figure 7-4: Agreement of the pseudorange (left) and differential carrier phase (right) normalized innovations from the clock state filter with the standard normal distribution .	208
Figure 7-5: Code tracking jitter as a function of C/N ₀	213
Figure 7-6: Phase tracking jitter as a function of C/N ₀	213

Figure 7-7: Absolute position accuracy on the OSC (upper) and CSC (lower) as compared to the simulated trajectory	219
Figure 7-8: Relative position accuracy on the CSC-OSC as compared to the simulated trajectory	220
Figure 7-9: Absolute orbital filter accuracy at and following perigee	221
Figure 7-10: Relative orbital filter accuracy at and following perigee	222
Figure 7-11: Absolute position 1 sigma standard deviation (cyan) versus actual error (blue) on the OSC	224
Figure 7-12: Relative position 1 sigma standard deviation (cyan) versus actual error (blue)	225
Figure 7-13: Pseudorange (above) and GRAPHIC (below) residuals from the OSC.....	226
Figure 7-14: Between receiver single difference phase residuals.....	226
Figure 7-15: OSC estimated receiver clock offset.....	227
Figure 7-16: CSC estimated receiver clock offset	227
Figure 7-17: OSC estimated absolute empirical accelerations	228
Figure 7-18: Estimated relative empirical accelerations.....	229
Figure 7-19: Relative positioning results with a 5% error on all control thrusts	230
Figure 7-20: Relative positioning 1 sigma standard deviation (cyan) versus actual error (blue) results with a 5% error on all control thrusts	231
Figure 7-21: Absolute positioning error on the OSC using the standard tracking version of GSNRx TM	232
Figure 7-22: Relative positioning error using the standard tracking version of GSNRx TM	233
Figure 7-23: Received C/N0 for MMS1 on day 136 of 2015 showing sidelobe tracking (Winternitz et al 2017, used with permission)	234
Figure 7-24: Simulated signal strength for GPS in the multi-constellation simulation.....	235
Figure 7-25: Simulated signal strength for GPS in the GPS only simulation.....	235
Figure 7-26: Assumed transmit gain pattern for Block IIA (left) and Block IIF (right)	236
Figure 7-27: Number of tracked satellites on the OSC (left) and CSC (right)	237
Figure 7-28: Commonly tracked satellites for the GPS only data take.....	237

Figure 7-29: Absolute positioning accuracy using the high power GPS only data set on the OSC.....	238
Figure 7-30: Absolute positioning accuracy using the high power GPS only data set on the CSC	239
Figure 7-31: Relative positioning accuracy using the high power GPS only data set	240
Figure 7-32: Absolute positioning error for a high sensitivity GPS zero baseline test.....	241
Figure 7-33: Relative positioning error for a high sensitivity GPS zero baseline test.....	242

List of Symbols

\mathbf{A}	Least squares design matrix
a	Orbit semi-major axis
$\mathbf{a}_R, \mathbf{a}_T, \mathbf{a}_N$	Empirical accelerations in radial, tangential, normal directions
C	Signal power
$C(t)$	Ranging Code
C_D	Drag coefficient
C_l	Variance-Covariance matrix of the observations
C_{SRP}	Solar radiation pressure coefficient
C_x	Variance-Covariance matrix of the estimated states
c	Speed of light
cdt	Receiver clock bias
\dot{cdt}	Receiver clock drift
cdt_{ISB}	Inter-system clock bias
d_{iono}	Ionospheric error
$d\rho_{orbit}$	Orbit error
dt	Time interval
d_{tropo}	Tropospheric error
dt_{rx}	Receiver clock error
dt_{sat}	Satellite clock error
\mathbf{dx}	Least squares adjustment to the unknown states
Δ	Between receiver single difference
Δt	Time difference
e	Orbit eccentricity
E	Elevation angle to a GNSS satellite
f	Frequency
F_c	Center frequency
f_d	Doppler Frequency
ϕ	Phase in cycles
ϕ_0	Phase offset
$\Phi_{k-1,k}$	Kalman filter state transition matrix from epoch k-1 to k
Φ	Phase measurement in distance units
H	Kalman filter design matrix
G_{Tx}	Transmit antenna gain
G_{Rx}	Receiving antenna gain
GR	GRAPHIC measurement

i	Orbit inclination
I	In-phase correlator output
J	Jacobian matrix
K	Kalman gain matrix
K_B	Boltzmann's constant
l	Least squares observations
L_{atm}	Atmospheric loss
L_{path}	Free space path loss
λ	Wavelength
m	Multipath
N	Phase ambiguity
N(t)	Navigation Message
n	Noise
ν	Orbit true anomaly
ω	Orbit argument of perigee
$\dot{\omega}$	First time derivative of the argument of perigee
Ω	Orbit right ascension of ascending node
$\dot{\Omega}$	First time derivative of the right ascension of the ascending node
P	Pseudorange
P	Power
P^-	Kalman filter state covariance after a predict step/before a measurement update
P^+	Kalman filter state covariance after a measurement update
PFA	Probability of false alarm
Q	Kalman filter process noise matrix
Q	Quadrature correlator output
$Q_{\hat{x}}$	Least squares cofactor matrix
q	Individual element in the least squares cofactor matrix
R	Kalman filter measurement covariance matrix
R	Rotation matrix
r	Position vector
r^A, r^B	Position vectors, spacecraft A and B
ρ	Geometric range
S	Signal
S	Process noise standard deviation
σ	Standard deviation
σ^2	Variance
$\hat{\sigma}_0^2$	A-posteriori variance factor

t	Time
T_{sys}	System noise temperature
T_{sky}	Sky/antenna noise temperature
T_0	Receiver reference temperature
τ	Code delay
τ	Time constant
Th	Acquisition threshold
v	Velocity vector
v^A, v^B	Velocity vectors, spacecraft A and B
W	Least squares weight matrix, typically identity or C_l^{-1}
w	Least squares misclosures vector
\hat{x}	Least squares estimated state
x_0	Least squares point of expansion/initial estimate
x^-	Kalman filter state vector after a predict step/before a measurement update
x^+	Kalman filter state vector after a measurement update
$x_{GNSS}, y_{GNSS}, z_{GNSS}$	GNSS satellite coordinates
x_{rx}, y_{rx}, z_{rx}	Receiver coordinates
z	Kalman filter measurements

List of Abbreviations

ACE	Antenna Characterization Experiment
ADCS	Attitude Determination Control System
AO-40	AMSat Oscar - 40
BDS	BeiDou Navigation Satellite System
BDUT	BeiDou UTC time offset
BPSK	Binary Phase Shift Keying
C/A	Coarse acquisition
C/N ₀	Carrier to Noise Density Ratio
CanX-2	Canadian Advanced Nanospace Experiment 2
CDMA	Code Division Multiple Access
CIT	Coherent Integration Time
CNES	Centre national d'études spatiales
CODE	Center for Orbit Determination in Europe
COTS	Commercial-off-the-shelf
CSC	Coronagraph Space Craft
DIOGENE	Détermination immédiate d'orbite par GPS et navigateur embarqué
DLL	Delay Lock Loop
DLR	Deutsches Zentrum für Luft- und Raumfahrt
DOP	Dilution of Precision
ECEF	Earth Centered Earth Fixed
ECI	Earth Centered Inertial
EDOP	East Dilution of Precision
EGNOS	European Geostationary Navigation Overlay Service
EIRP	Equivalent Isotropically Radiated Power
ESA	European Space Agency
FDMA	Frequency Division Multiple Access
FFT	Fast Fourier Transform
FLI	Frequency Lock Indicator
FLL	Frequency Lock Loop
GAGAN	GPS Aided GEO Augmented Navigation
GAUT	Galileo UTC time offset
GDOP	Global Dilution of Precision
GEO	Geostationary Earth Orbit
GEONS	GPS Enhanced Onboard Navigation System
GIOVE-A	Galileo In-Orbit Validation Element
GLONASS	Globalnaya Navigationnaya Sputnikovaya Sistema
GNOS	GNSS Occultation Sounder
GNSS	Global Navigation Satellite System

GOCE	Gravity Field and Steady-State Ocean Explorer
GOES-R	Geostationary Operational Environmental Satellite - R Series
GPS	Global Positioning System
GPUT	GPS UTC time offset
GRACE	Gravity Recovery and Climate Experiment
GRAPHIC	Group and Phase Ionosphere Correction
GSFC	Goddard Space Flight Center
GSNRx™	GNSS Software Navigation Receiver
GTO	Geostationary Transfer Orbit
HDOP	Horizontal Dilution of Precision
HEO	Highly Elliptical Orbit
ICD	Interface Control Document
ICRF	International Celestial Reference Frame
IF	Intermediate Frequency
IGSO	Inclined Geosynchronous Orbit
IMU	Inertial Measurement Unit
ION	Institute of Navigation
IRAS	Inter-satellite Ranging and Alarm System
IRNSS	Indian Regional Navigation Satellite System
ITAR	International Traffic in Arms Regulations
ITRF	International Terrestrial Reference Frame
JPL	Jet Propulsion Laboratory
LEO	Low Earth Orbit
LNA	Low Noise Amplifier
MBOC	Multiplexed Binary Offset Carrier
MEO	Medium Earth Orbit
MGEX	Multi-GNSS Experiment
MGPSR	Mariposa GPS Receiver
MMS	Magnetospheric Multi-Scale Mission
MSAS	Multi-functional Transport Satellite-based Augmentation System
NASA	National Aeronautics and Space Administration
NCO	Numerically Controlled Oscillator
NDOP	North Dilution of Precision
NORAD	North American Aerospace Defense Command
OCXO	Oven-Controlled Crystal Oscillator
OSC	Occulter Space Craft
PDOP	Position Dilution of Precision
PFA	Probability of False Alarm
PiVoT	Position Velocity Time
PLAN	Position Location and Navigation

PLI	Phase Lock Indicator
PRISMA	Prototype Research Instruments and Space Mission technology Advancement
PRN	Pseudo Random Noise
PROBA	Project for Onboard Autonomy
QPSK	Quadrature Phase Shift Keying
QZSS	Quasi-Zenith Satellite System
QZUT	QZSS UTC time offset
RAIM	Receiver Autonomous Integrity Monitoring
RHCP	Right Hand Circularly Polarized
RIC	Radial, In-Track, Cross-Track
SAC-C	Satélite de Aplicaciones Científicas-C
SBAS	Satellite Based Augmentation Systems
SBIRS	Space Based Infrared System
SBIRS1	Space-Based Infrared System Satellite - 1
SDCM	System for Differential Corrections and Monitoring
SFFMT	Satellite Formation Flying Missions and Technologies
SGR	Space GNSS Receiver
SSV	Space Service Volume
STENTOR	Satellite de Télécommunications pour Expérimenter les Nouvelles Technologies en Orbite
SV	Space Vehicle
TDOP	Timing Dilution of Precision
TEAMSAT/YES	Technology, science and Education experiments Added to MaqSat/Young Engineers Satellite
TEC	Total Electron Content
TEME	True Equator Mean Equinox
TLE	Two Line Ephemeris
UERE	User Equivalent Range Error
UTC	Universal Time Coordinated
VDOP	Vertical Dilution of Precision
VTEC	Vertical Total Electron Content
VTEC	Vertical Total Electron Content
WAAS	Wide Area Augmentation System

Chapter One: Introduction

The goal of this research is to determine whether Global Navigation Satellite Systems (GNSS), and more specifically carrier phase based relative positioning, is a viable tool for relative positioning in highly elliptical orbits (HEO), and if so to determine the order of magnitude of the relative positioning accuracy. In particular, the research goal is inspired by the mission requirements of two concrete missions: the Magnetosphere Multi-Scale Mission (MMS) (Gramling 2009), by the American National Aeronautics and Space Administration (NASA), and Project for Onboard Autonomy 3 Mission (PROBA-3) (Landgraf and Mestreau-Garreau 2012) by the European Space Agency (ESA).

Both of these missions consist of more than one spacecraft flying in formation with one another, and in both cases the ensemble of spacecraft form a more powerful scientific instrument than would be possible in a single spacecraft orbiting alone. In the case of MMS, launched on March 13, 2015 (Long et al 2015), four identical satellites fly in a tetrahedron formation through the Earth's magnetosphere to study magnetic reconnection, and the distances between satellites can be changed to observe the phenomenon over a larger or smaller area. PROBA-3 is a two satellite technology demonstration mission for a distributed space telescope concept, expected to launch in 2019 (ESA 2016). The scientific payload consists of a solar coronagraph, with one satellite carrying an instrument used to image the solar corona, while the second satellite is an occulter disk which will be precisely aligned with the sun to create an eclipse. Both missions will fly in highly elliptical orbits. They will swing past the Earth at a high velocity at perigee, and will make scientific observations during the more stable apogee arc. Their requirements for relative positioning come from the need to monitor and maintain the formations of the spacecraft. It is critical for the safety of the satellites themselves that they do not collide with one another, and essential for the success of the scientific missions that the formations be monitored and maintained during the collection of data. Real time relative positioning information is required to plan and execute formation keeping maneuvers for both of these goals.

The specific research goal of studying GNSS based relative positioning required a significant amount of background information, much of which was not yet available in open literature when the project began. It also required the development of many new software tools capable of

handling the unique above the constellation data sets. Consequently, the research contributions presented in this thesis largely widen and deepen the body of knowledge about multi-constellation GNSS positioning above the GNSS constellations. Specific aspects of relative navigation are addressed in the final chapters.

The remainder of the thesis is organized as follows: Chapter two provides the history of positioning of above the GNSS constellation. The late 1990's and early 2000's saw a handful of early missions carry preliminary space capable receivers into orbits above the GPS constellation. Only small samples of GPS data were collected, but it inspired a decade in which a great deal of research and development was conducted. The project presented in this thesis began near the end of this period of intense research, and just as a new generation of above the constellation missions was preparing for launch in the mid 2010's. A great deal of new information about above the constellation GNSS positioning has been published in recent years, as the first of these modern missions were launched and begin gathering real data. The new research has allowed for a refinement of the simulation parameters in later chapters of this thesis. In addition to a review of the relevant literature, chapter two presents an introduction to GNSS positioning and the modern GNSS constellations, as well as a brief overview of positioning in orbit as compared to positioning on the Earth.

Chapter three presents an in-depth study of the positioning environment in space. It presents a study done internally for the German Aerospace Agency (Deutsches Zentrum für Luft- und Raumfahrt, DLR) to determine the optimal attitude profile for a HEO spacecraft in terms of GPS antenna accommodation and GPS visibility. It also introduces the visibility simulation software that was built to answer this and similar questions. The second half of the chapter presents further results based on the simulation tool, extending the study to an analysis of all the available GNSS and a discussion of how the visibility of the GNSS constellations impacts relative positioning. These results were presented at the Satellite Formation Flying Missions and Technologies (SFFMT) conference in 2013, and the paper was chosen for peer reviewed publication in a special conference issue of the International Journal of Space Science and Engineering.

Chapter four presents a detailed study on whether the satellite based augmentation systems (SBAS) could be used along with the standard GNSS systems as a source of measurements. It is a departure from the remainder of the thesis, in that the study targets users in geostationary in addition to highly elliptical orbits, and in that it is the only chapter presenting results based on real orbital data, collected using the GPS+SBAS receiver onboard the CanX-2 CubeSat. The idea to use SBAS as a source of positioning measurements stemmed from the visibility simulation results of Chapter three, which clearly demonstrated their advantages, and the fact that no other study of this type had ever been conducted. The research in chapter four was first presented at the ION GNSS+ 2015 conference, and has been published in *Navigation*, the Journal of the Institute of Navigation. It contains some of the most novel research and results in this thesis.

Chapters five and six present the setup, challenges, and results of hardware-in-the-loop simulations using a software GNSS receiver. Chapter five presents a preliminary, GPS-only, hardware simulation, and focuses on the modification of generic receiver algorithms to handle operations in orbit and the geometry of above the constellation positioning. The research in Chapter five was first presented at the ION GNSS+ 2014 conference. Chapter six presents the continuation of the receiver design work, and details both the setup of a multi constellation GNSS hardware simulation, and a deeper look into the signal processing algorithms implemented in the software receiver in order to reliably acquire and track three constellations under orbital dynamics and weak signal conditions. It is the backbone of the research project, and will be presented at the ION GNSS+ 2017 conference.

Finally, chapter seven presents the relative positioning research and results. The focus of this chapter is the design of a relative positioning filter capable of handling the sparsity of measurements in the simulated HEO environment, and capable of handling asynchronous measurements occurring when the receivers see too few measurements for a position fix. Achieved relative positioning accuracies based on hardware in the loop simulation are presented, along with an analysis of the suitability of GNSS positioning for relative positioning in highly elliptical orbits.

The thesis is concluded in Chapter eight, which brings together the results from each of the chapters to make recommendations on the use of multi-constellation GNSS for relative positioning in highly elliptical orbits, and for positioning above the GNSS constellations in general.

Chapter Two: Background and History of Above the Constellation GNSS

This chapter begins with an introduction to GNSS positioning in section 2.1, explaining both the basic concept of GNSS positioning and its most significant sources of error, as well as the basics of how a GNSS receiver works, and an overview of the GNSS constellations. In section 2.2.1 a basic explanation of orbital motion will be presented, and in section 2.3 an explanation of how GNSS positioning differs for a receiver in orbit as compared to a receiver on the Earth's surface. In section 2.4 the history of above the constellation GNSS research and development will be presented, along with an outline of past, current and planned missions based on a review of the last 20 years of literature on this topic. Finally, the chapter concludes in section 2.5 with a discussion of the gaps in the existing body of knowledge which this thesis seeks to fill.

2.1 GNSS Basics

Unless otherwise referenced, the information in the following sections typically came from course notes (Petovello 2014) and can be found in the standard reference texts such as Misra and Enge (2006), Kaplan and Hegarty (2006) or Parkinson and Spilker (1996).

2.1.1 Trilateration

The basic concept of GNSS is trilateration. Ranges are measured from known points (in this case GNSS satellites) to an unknown point (the receiver) and used to calculate the receiver's position. Figure 2-1 below shows the general principle of trilateration. The circle around each GNSS satellite is a line of constant range. The GNSS receiver position is the point on the Earth's surface where all three of the ranges intersect, depicted in the figure as a triangle.

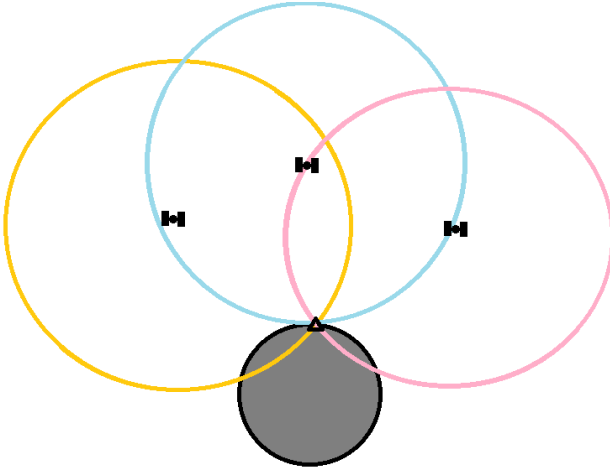


Figure 2-1: GNSS Trilateration

The ranges, ρ , in units of distance are obtained by measuring the time it takes the signal to travel from the GNSS satellite to the receiver, Δt , and multiplying it by the speed of light, c , as shown in Eq. 2-1.

$$\rho = c\Delta t$$

Eq. 2-1

Because the travel time is measured as the difference between the signal transmission time measured in the GNSS system's time, and the receive time measured on the receiver's clock, there is an additional bias due to the difference in these two clocks. As a result, rather than pure range measurements, GNSS receivers measure pseudoranges. A pseudorange is the sum of the actual geometric range between the satellite and receiver, and of the receiver clock's offset from GNSS system time expressed in units of distance, cdt_{rx} . The pseudorange equation is given in Eq. 2-2 below. In the equation, pseudorange is P , the GNSS satellite coordinates are x_{GNSS} , y_{GNSS} and z_{GNSS} , the receiver's unknown coordinates are x_{rx} , y_{rx} , and z_{rx} , the receiver's unknown clock offset in seconds is dt_{rx} , and c is the speed of light.

$$P = \sqrt{(x_{GNSS} - x_{rx})^2 + (y_{GNSS} - y_{rx})^2 + (z_{GNSS} - z_{rx})^2} + cdt_{rx}$$

Eq. 2-2

In order to calculate the receiver's position and clock offset (x_{rx} , y_{rx} , z_{rx} , dt_{rx}) a minimum of four pseudorange measurements are therefore required, forming a system of four equations in four unknowns. More typically, far more than four measurements are available, and parametric least squares or a Kalman filter is used to optimally combine the measurements from all the tracked satellites into a more accurate solution.

In the case of multi-constellation GNSS, an additional unknown, the inter-system timing bias, must be estimated for each additional GNSS system. This is required to account for the different GNSS system times as well as the hardware biases in the receiver's handling of the different incoming signals. Although there are plans to transmit information about the inter-system timing offsets from the GNSS satellites themselves to facilitate multi-constellation use, the user hardware dependent bias will still need to be either calibrated or estimated for each system. Consequently, for multi-constellation GNSS positioning an additional measurement is required for each additional system tracked.

2.1.2 GNSS Signals, Receivers and Measurements

As already mentioned, GNSS signals are transmitted by GNSS satellites, and tracked by GNSS receivers. A GNSS signal consists of typically two components modulated onto a carrier wave. These two components are the navigation message and the ranging code. The navigation message has a relatively low data rate, and relays to the user information about the GNSS system time and positions of the GNSS satellites which are required for the trilateration calculation described in the previous section. The ranging code is a repeating series of chips, which is used to identify the satellite being tracked, to measure the travel time of the signal to the receiver for forming pseudorange measurements, and to spread the energy over a wider range of frequencies which makes it resistant to interference from outside sources or other satellites from the same system. The chipping rate is orders of magnitude higher than the navigation bit rate, such that the full ranging code generally repeats at least once and typically several times within a single data bit of the navigation message. Both the navigation message and ranging code are modulated onto a sinusoidal carrier wave which has a much higher frequency again, and which brings the central frequency of the whole GNSS signal to the desired L-band frequency for transmission. Figure 2-2 shows a (not-to-scale) diagram of these three signal components.

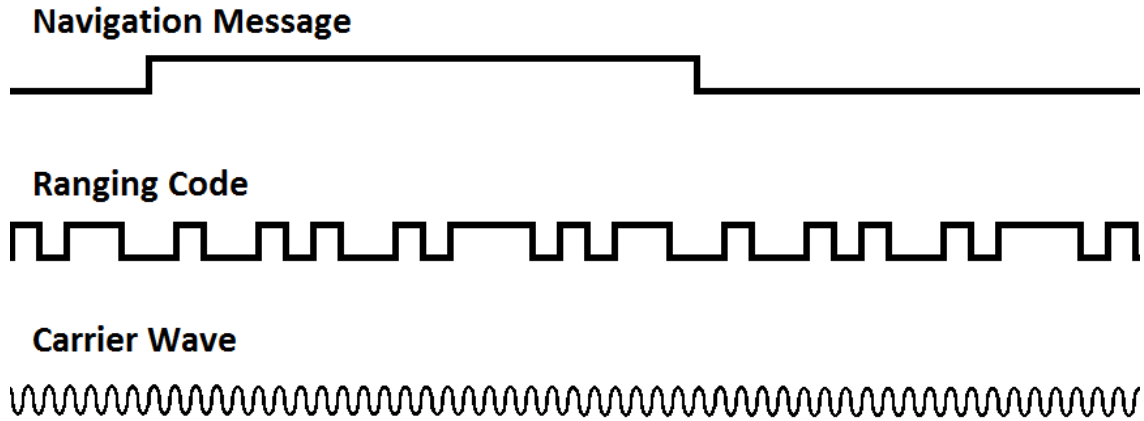


Figure 2-2: Components of a GNSS Signal (Not to Scale)

Some modern signals are slightly different. Pilot channels retain the carrier wave and ranging code, but do not have a navigation message, which removes the only unpredictable component of the signal and has advantages for weak signal tracking. Other signals have an additional secondary code, which has a lower chipping rate than the ranging code, and can be used for either time synchronization on pilot signals or to assist in the detection of the data bit boundaries.

The equation for the GPS legacy L1 signal is given as Eq. 2-3 below, where the signal is S , the signal power is P , the ranging code as a function of time is $C(t)$, the navigation message as a function of time is $N(t)$, and the carrier wave is defined by the cosine term. Within the cosine term the parameter of note is the carrier frequency, f :

$$S = \sqrt{2P}C(t)N(t)\cos(2\pi ft)$$

Eq. 2-3

Upon arriving at a receiver, the signal of Eq. 2-3 may be re-written as in Eq. 2-4, where three additional parameters have appeared: the time delay between the transmitted and incoming signal, τ , the carrier Doppler frequency, $f_d(t)$, and the initial carrier phase offset, ϕ_0 .

$$S = \sqrt{2P}C(t - \tau)N(t - \tau)\cos(2\pi(f + f_d(t))t + \phi_0)$$

Eq. 2-4

In order to acquire and track a GNSS signal, the receiver must estimate these three parameters. The delay in the incoming signal leads to a pseudorange measurement, the rate of change of the carrier frequency leads to a Doppler measurement, and the phase of the carrier wave measurement, if handled properly, provides a more precise measurement of the range or change in range and regardless is necessary to decode the navigation message.

Upon entering the receiver, the incoming signal first passes through the front end, where the carrier frequency is down converted to an intermediate frequency and the signal undergoes amplification, automatic gain control, and analog to digital conversion. Next, the signals are detected and the code delay and Doppler are estimated coarsely in an acquisition phase, in which the receiver searches every possible combination of ranging code, code delay, and Doppler to find each signal. Each signal is then handed off to a set of tracking loops, which refine the estimated code delay and Doppler, estimate the phase, and continuously update these three tracking parameters as they change over time due to satellite motion, receiver motion, and receiver clock drift.

The parameters are estimated by multiplying the incoming signal from the satellite with replica signals generated in the receiver. In signal theory this process is called demodulation. After the signals are multiplied at discrete epochs they are integrated over a time interval, typically 1 ms or longer for GNSS. The combination of multiplying and integrating is called correlation. When a replica signal is generated with the right combination of phase, Doppler and code delay, it matches the incoming signal, and the correlation of the two signals reaches its maximum value and forms a peak. If the integration time is sufficiently long and the signal parameters are sufficiently well matched, the peak is visible above the noise floor. A graphical example of this is shown in Figure 2-3, with the figure on the left showing a local maximum when the time delay (on the x axis) is zero, corresponding to a perfectly matched set of signals, and only a background noise level otherwise. The figure on the right shows only noise, because in this case signals from two different satellites, with different ranging codes, were correlated with each other and so there is no match at any time delay.

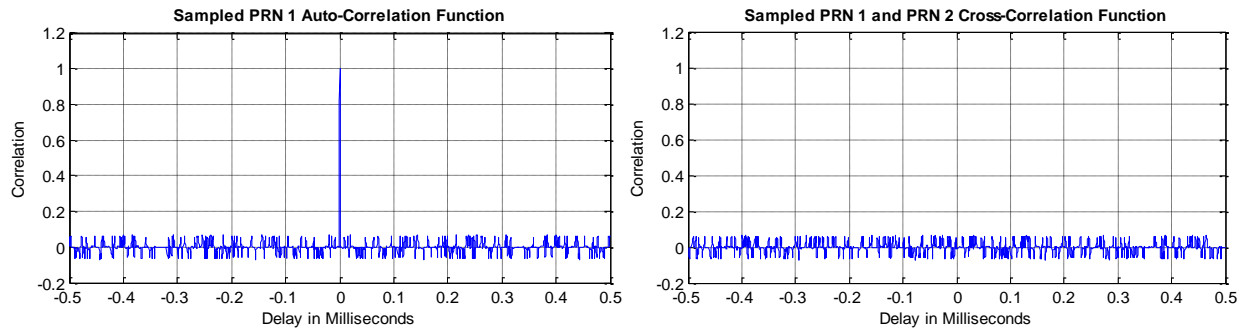


Figure 2-3: The result of multiplying two matching signals (left) and two signals with different ranging codes (right)

A second example is displayed in Figure 2-4, which shows the results of cold start signal acquisition for a GPS L1 C/A signal from PRN 1. A replica PRN 1 signal is generated at every possible combination of range delay from 0 to 1023 chips, and Doppler from -10 kHz to 10 kHz, and correlated with the incoming signal. There is only one peak visible in the grid, where the replica code delay and Doppler match with the actual code delay and Doppler of the incoming signal, in this case at 163.5 chips and -2.75 kHz. When the replica signal is generated using an incorrect code delay or Doppler, which is the case at every other point in the plot, the correlation of the replica and incoming signal does not form a peak, and no signal should be detected or tracked. A very weak incoming signal may also go undetected, because the peak is too low compared to the background noise formed by all of the incorrect combinations.

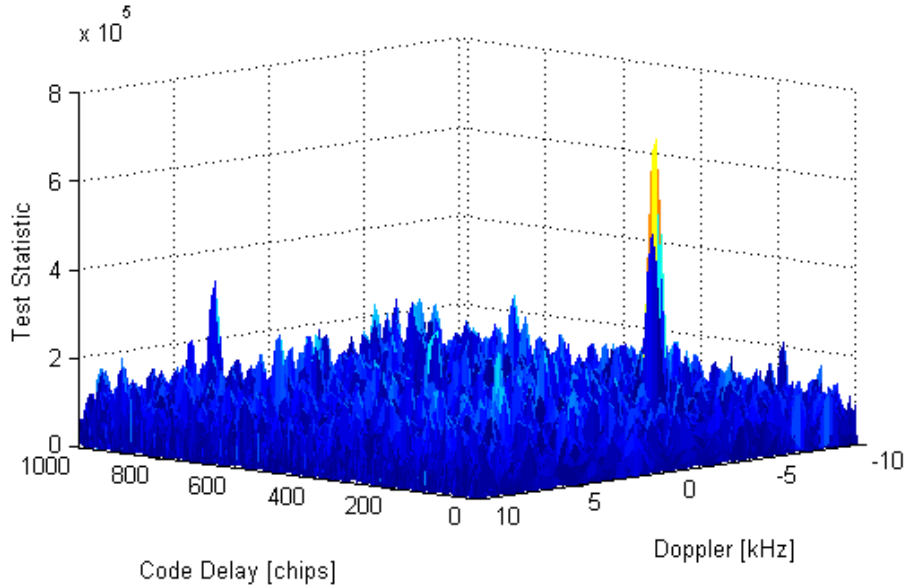


Figure 2-4: Sample Acquisition Grid, with a detected signal at 163.5 chips and -2.75 kHz

After acquisition tests the full range of possible permutations and combinations to find a signal, tracking takes over. The receiver generates only a few replica ranging codes (using the Numerically Controlled Oscillator or NCO), one on the signal itself, one slightly ahead in time, and one slightly delayed in time. These prompt, early and late replica signals are correlated with the incoming signal, and the correlator outputs are compared. For a correlator spacing of half a chip, in the ideal case the prompt correlator would return a peak value of 1, while the early and late correlators would each return a value of 0.5 halfway up the correlation peak. Depending on the relative heights of the peaks, it is therefore possible to monitor how the signal parameters are changing over time (using a discriminator), and predict the signal parameters for the next epoch in the future (using a filter). Further, both a replica code using a sine component, and a replica code using a cosine component are correlated with the incoming signal, and the relative magnitude of the correlator outputs is used to measure the incoming signal's phase. The Doppler is measured as the change in phase over time by taking data from two consecutive tracking epochs. Figure 2-5 below shows the basic concept of a tracking loop.

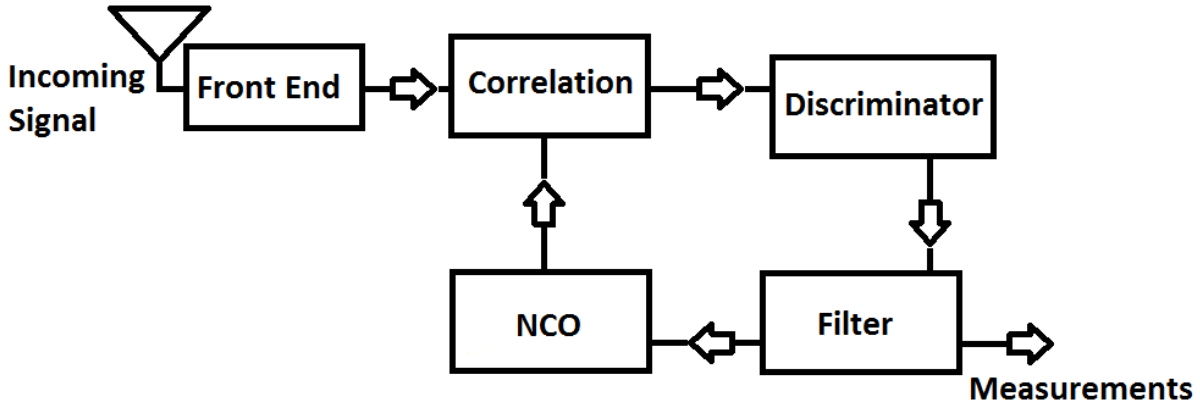


Figure 2-5: Basic Design of a Tracking Loop

2.1.3 Position Estimation

In order to estimate position, least squares or a Kalman filter are typically used. Least squares optimally combines the measurements by minimizing the sum of the squared errors. Because the GNSS observation equation is non-linear, parametric, iterative least squares is used. The iterative least squares equations are given as Eq. 2-5 and Eq. 2-6 below, and a description of the variables follows.

$$dx = (A^T W A)^{-1} A^T W w$$

Eq. 2-5

$$\hat{x} = x_0 + dx$$

Eq. 2-6

The parametric least squares process begins with a point of expansion or initial estimate of the unknowns, x_0 . At each iteration, a correction, designated dx , is calculated using Eq. 2-5, and applied using Eq. 2-6 to get the estimated values for the unknowns, \hat{x} . When dx approaches zero, the iteration is stopped and \hat{x} is the final value of the unknowns.

In Eq. 2-5, A is the linearized design matrix, containing the partial derivatives of the observation equation (Eq. 2-2) with respect to the unknowns as shown in Eq. 2-7 below, with m rows and n

columns, where n is the number of states and m is the number of measurements. W is an optional weight matrix with the dimensions $m \times m$, and is typically taken as the inverse of the variance-covariance matrix of the measurements, C_l , as shown in Eq. 2-8. The misclosure vector, w , has length m and is the difference between the actual observation and the modelled observation, as shown in Eq. 2-9.

$$A = \begin{bmatrix} \frac{\partial P_1}{\partial x_{rx}} & \frac{\partial P_1}{\partial y_{rx}} & \frac{\partial P_1}{\partial z_{rx}} & \frac{\partial P_1}{\partial cdt_{rx}} \\ \vdots & \vdots & \vdots & \vdots \\ \frac{\partial P_m}{\partial x_{rx}} & \frac{\partial P_m}{\partial y_{rx}} & \frac{\partial P_m}{\partial z_{rx}} & \frac{\partial P_m}{\partial cdt_{rx}} \end{bmatrix} = \begin{bmatrix} x_{rx} - x_{GNSS}^1 & y_{rx} - y_{GNSS}^1 & z_{rx} - z_{GNSS}^1 & 1 \\ \rho_1 & \rho_1 & \rho_1 & \vdots \\ \vdots & \vdots & \vdots & \vdots \\ x_{rx} - x_{GNSS}^m & y_{rx} - y_{GNSS}^m & z_{rx} - z_{GNSS}^m & 1 \\ \rho_m & \rho_m & \rho_m & 1 \end{bmatrix}$$

Eq. 2-7

$$W = C_l^{-1} = \begin{bmatrix} \sigma_{P1}^2 & \cdots & \sigma_{p1pm} \\ \vdots & \ddots & \vdots \\ \sigma_{pmp1} & \cdots & \sigma_{Pm}^2 \end{bmatrix}^{-1}$$

Eq. 2-8

$$w = l - \sqrt{(x_{GNSS} - x_{rx})^2 + (y_{GNSS} - y_{rx})^2 + (z_{GNSS} - z_{rx})^2} - cdt_{rx}$$

Eq. 2-9

Finally, the covariance matrix of the states, $C_{\hat{x}}$, is calculated as show in Eq. 2-10. The a-posteriori variance factor $\hat{\sigma}_0^2$ is calculated based on C_l , the residuals, and the degrees of freedom, and should be approximately 1 if the input measurement variances in C_l are realistic and agree with the measurement residuals. If the a-priori variance factor and a-posteriori variance factor are statistically the same, as determined through statistical testing using the global test, the a-priori variance factor is typically used instead (not shown here).

$$C_{\hat{x}} = \hat{\sigma}_0^2 (A^T W A)^{-1}$$

Eq. 2-10

Least squares is generally used to solve for each epoch independently, except in cases where the receiver is known to be either stationary or in a trajectory that can be otherwise parameterized into constant unknown values, such as an orbit.

Kalman filtering, on the other hand, is a commonly used estimation technique which optimally combines new information from the measurements with a-priori information about the states from the previous epochs. It consists of a predict step, in which the state and its covariance information are predicted forward in time based on a model of the system's dynamics, and an update step, when new measurements are integrated into the solution. At each update step a Kalman gain matrix is used to weight the a-priori information versus the measurement information, such that the information with the highest confidence steers the estimate of the unknowns. Many references on the Kalman filter exist, for example Welch and Bishop (2006).

The prediction step consists of two equations, one to update the states based on the dynamics model (Eq. 2-11) and one to update the covariance matrix of the states (Eq. 2-12).

$$x_k^- = \Phi_{k-1,k} x_{k-1}^+$$

Eq. 2-11

$$P_k^- = \Phi_{k-1,k} P_{k-1}^+ \Phi_{k-1,k}^T + Q_k$$

Eq. 2-12

where x_k^- and P_k^- are the predicted states and covariance of the states at the current epoch k , x_{k-1}^+ and P_{k-1}^+ are the states at the end of the previous epoch of estimation $k-1$, $\Phi_{k-1,k}$ is the state transition matrix from the previous epoch to the current epoch, and Q_k is the process noise matrix. The process noise quantifies the additional uncertainty added to the system as a result of the prediction imperfectly describing the actual change in the states from epochs $k-1$ to k .

The update step consists of three equations, to calculate the Kalman gain (Eq. 2-13), to apply observations to the estimated states (Eq. 2-14), and to update the covariance matrix of the states based on the new measurement information (Eq. 2-15).

$$K_k = P_k^- H^T (H P_k^- H^T + R)^{-1} \quad \text{Eq. 2-13}$$

$$x_k^+ = x_k^- + K_k (z_k - h(x_k^-)) \quad \text{Eq. 2-14}$$

$$P_k^+ = (I - K_k H) P_k^- \quad \text{Eq. 2-15}$$

where x_k^- and P_k^- are the output of the above described prediction step, x_k^+ and P_k^+ are the output state and state covariance matrix after the update step, K_k is the Kalman gain matrix, H is the least squares design matrix A , R is the same as the least squares covariance matrix C_I , and $(z_k - h(x_k^-))$ are the innovations and are calculated using the same equation as for the least squares misclosure vector, where z is the vector of measurements and $h(x)$ is the functional model.

2.1.4 Positioning Errors and Geometry

The error in a GNSS position is the product of two factors: The error on an individual measurement, referred to as the User Equivalent Range Error (UERE), and the positioning geometry, which is expressed as a Dilution of Precision (DOP). In Eq. 2-16 below, σ can be either the standard deviation along one dimension of the (relative) position, or it can be a more global measure of the (relative) position error in 2D, or 3D depending on whether a DOP for a single component, a horizontal DOP, a three dimensional positioning DOP (PDOP), or relative positioning DOPs are used. If the global DOP, GDOP is used, including the impact of the uncertainty in time, σ is the four dimensional uncertainty. Note that Eq. 2-16 assumes the UERE is the same on all measurements.

$$\sigma = \text{UERE} * \text{DOP} \quad \text{Eq. 2-16}$$

The User Equivalent Range Error is the error on the GNSS range measurements used as input to estimate the position. It contains the contributions of all the error sources present in GNSS positioning. The most significant error sources are listed below:

- *Noise, n* – Noise is a stochastic error source, coming from the background system noise temperature of the environment through which the signal is transmitted, as well as from tracking jitter in the receiver.
- *Multipath, m* – Multipath is an error source occurring when a signal does not travel from the satellite to the receiver via a straight line path, but rather gets reflected off of one or several surfaces before being received. The response of the receiver to the combined line of sight and reflected signals is the multipath error.
- *Receiver Clock Error, cdt_{rx}* – Receiver Clock Error is an error stemming from the fact that the receiver time is not synchronized to the GNSS system time, which leads to a receiver clock related bias on the measurements. Receiver Clock Error is generally estimated as a fourth unknown in GNSS positioning.
- *GNSS Satellite Clock Error, cdt_{sat}* – Satellite Clock Error is the difference in the time being kept by the atomic clock onboard the GNSS satellite, as compared to the GNSS system time scale, which is maintained by the ground control segment based on an ensemble of clocks.
- *GNSS Satellite Orbit Error, $d\rho_{orbit}$* – Orbit Error is the geometric difference in position between the actual position of the GNSS satellite's transmit antenna at the time a signal is sent, and the position calculated using its broadcast ephemeris message. Only the component of the orbit error along the line of sight between the satellite and the receiver impacts positioning.
- *Ionospheric Delay, d_{iono}* – Ionospheric path delay, or in the case of carrier phase measurements path advance, is a result of both the refraction and delay of the GNSS signals as they pass through the ionosphere. The ionospheric error is a function of both the total electron content along the path taken by the signal, and of the frequency of the signal, because the ionosphere is a dispersive medium for signals in the L-band. The ionosphere reaches its peak density at approximately 300 km above the surface of the Earth, and extends from approximately 50 km to over 1000 km above the Earth.

- *Tropospheric Delay*, d_{tropo} – Tropospheric error is caused by the refraction of signals through the Earth's troposphere. For GNSS applications, the troposphere is defined as the non-dispersive part of the atmosphere extending up to approximately 40 km above the Earth's surface. The tropospheric path delay is a function of the temperature, pressure and water vapour content of the troposphere.

Consequently, assuming the individual errors are zero mean, Gaussian and uncorrelated the UERE can be calculated from the other error sources as:

$$UERE = \sqrt{n^2 + m^2 + cdt^2 + cdT^2 + d\rho_{orbit}^2 + d_{iono}^2 + d_{tropo}^2}$$

Eq. 2-17

The dilution of precision, DOP, can be computed from the least squares design matrix, A . First, the cofactor matrix must be computed as:

$$Q_{\hat{x}} = (A^T A)^{-1}, Q_{\hat{x}} = \begin{bmatrix} q_{xx} & q_{xy} & q_{xz} & q_{xt} \\ q_{yx} & q_{yy} & q_{yz} & q_{yt} \\ q_{zx} & q_{zy} & q_{zz} & q_{zt} \\ q_{tx} & q_{ty} & q_{tz} & q_{tt} \end{bmatrix}$$

Eq. 2-18

After which the DOPs can be obtained from its diagonal elements as

$$GDOP = \sqrt{q_{xx} + q_{yy} + q_{zz} + q_{tt}}, PDOP = \sqrt{q_{xx} + q_{yy} + q_{zz}}, TDOP = \sqrt{q_{tt}}$$

Eq. 2-19

Note easting, northing, horizontal and vertical DOPs can be similarly obtained if the cofactor matrix is rotated from the Earth centered Earth fixed frame to a local (east, north, up) or similar frame.

2.1.5 GNSS Constellations

There are currently four global GNSS systems planned or in existence (GPS, GLONASS, Galileo and BeiDou 3), three regional systems (QZSS, IRNSS, and BeiDou 2) and five satellite based augmentation systems (WAAS, EGNOS, GAGAN, SDCM and MSAS). This section briefly introduces each of them.

GPS is the fully operational American GNSS, consisting of a minimum of 24 active satellites in six orbital planes, with an orbital radius of approximately 26561 km. The GPS satellites historically transmit a civilian signal on the L1 frequency, and a precise military signal on the L2 frequency, but the system is being modernized to transmit a modernized L1 civilian signal in addition to the legacy signal (IS-GPS-800D), and civilian signals on L2 and L5, both of which have modernized signal structures (IS-GPS-200H, IS-GPS-705D). Of particular relevance for this work, GPS is also the first constellation to officially recognize the space user community, in particular users above the constellation, by adding a defined space service volume (SSV) to the interface control document, which guarantees a level of service for users up to geosynchronous orbit (Bauer et al 2006, IS-GPS-200E). While the SSV only officially goes into effect beginning with the GPS III satellites, a recent NASA mission found that the current level of GPS availability above the constellation dramatically exceeds the specified levels, and there is a currently a strong push to redefine the specifications and protect the existing level of service (Bauer 2015ab, Parker et al 2016).

GLONASS is the fully operational Russian GNSS, consisting of 24 active satellites in three orbital planes with an orbital radius of 25478 km and currently transmitting legacy civilian signals on L1 and L2. GLONASS uses frequency division multiple access (FDMA) to distinguish between satellites, which adds an element of complexity as each satellite transmits at slightly different frequencies, but modernization plans include transmitting code division multiple access (CDMA) signals on L1, L2, L3 and L5. (Russian Institute of Space Device Engineering 2008, Stupak 2010, Revnivykh 2011) A new ICD, clearly defining the modernization plans, is expected to be released in English in the very near future. A draft in Russian was already released in December 2016.

Galileo is the European GNSS currently under development. As of June 2017 eighteen satellites have been launched, thirteen of which are fully operational, two partially operational due to an orbit injection failure, two still being commissioned, and one which failed (European GNSS Service Centre 2017). The full system is designed to contain 27 satellites plus 3 active spares in 3 orbital planes with an orbital radius of 29601 km, and will transmit E1, E5a and b, and E6 signals. (European Union 2010)

BeiDou Navigation Satellite System (BDS) is the Chinese GNSS currently under development. It is being completed in phases. The first consisted of experimental satellites, the second (BeiDou 2) is a regional system consisting of a combination of satellites, four in geostationary orbit (GEO), five in inclined geosynchronous orbit (IGSO), and four in medium Earth orbit (MEO), which was declared fully operational at the end of 2012. At the time this research began, only the B1 signal was defined in the test ICD, and even then only the ranging code was defined, not the navigation message required to use the system. Independently, both B2 and B3 signals at the same frequencies as Galileo E5b and E6 had been observed and tracked (China Satellite Navigation Office 2011, Hauschild et al 2012, Montenbruck et al 2013). A full ICD published in late 2012 revealed the navigation data message structures, and an updated version published in late 2013 revealed the B2 signal structure for the regional system (China Satellite Navigation Office 2012, 2013). An updated version was released in November 2016 (China Satellite Navigation Office 2016). The third phase (BeiDou 3), consisting of a global system of 27 MEO satellites as well as 5 GEO and 3 IGSO satellites, is expected to be operational by 2020. The new global system will have different signals than the existing system, although it appears that backward compatibility on B1 will be maintained (Li et al 2015, Xiao et al 2016).

The Quazi-Zenith Satellite System (QZSS) is Japan's regional augmentation system which is currently under development. According to the current ICD it will consist of three geosynchronous satellites (one is currently operating) in elliptical orbits such that they are at apogee over Japan, as well as one geostationary satellite, to supplement other GNSS systems in urban canyons (IS-QZSS-PNT-001). The QZSS system will transmit on the same L1, L2 and L5 frequencies as GPS for maximum compatibility, and will also transmit two augmentation system signals, LEX and L1-SAIF, on a different frequency and different PRN respectively.

The satellite based augmentation systems (SBAS) typically consist of payloads on geostationary communications satellites re-transmitting information to aid GPS/GNSS positioning for users. A primary purpose of SBAS is to provide the aviation community with better positioning integrity. There exist a number of systems, including the US WAAS (FAA/DoT 2008), European EGNOS (European Commission 2013), Japanese MSAS, Indian GAGAN, and Russian SDCM (Russian Space Systems 2012) which consist of 1-3 satellites each. These systems transmit L1 signals compatible with GPS, and an L5 signal is also planned or transmitted on several of the systems.

IRNSS is the Indian Regional Navigation Satellite System, also known as NavIC or the Navigation Indian Constellation. It consists of a minimum of seven satellites, 3 GEO and 4 IGSO, which were launched from 2013 to 2016 (ISRO 2016). The satellites transmit an L-band signal aligned with GPS L5, as well as an S-band signal (ISRO 2014). Because the first satellite was launched in 2013 and the interface control document was first published in June 2014, both after the research presented here was already well underway, the IRNSS system was not considered in any part of this study and is only included here for completeness.

2.2 Orbit Basics

2.2.1 Orbital Motion

The orbital motion of the planets of our solar system has been studied for millennia; however the basis of our modern description of orbits came from Johann Kepler and Isaac Newton. Kepler empirically determined three laws;

- Orbits can be described as conic sections with the central body at one focus
- The radius vector of an orbiting body sweeps out equal areas in equal times
- The square of the period is proportional to the cube of the semi-major axis for satellites orbiting the same central body.

He also defined a set of six parameters to describe orbital motion. The four angular parameters are inclination, true anomaly, argument of perigee, and right ascension of the ascending node, as depicted in Figure 2-6. The perigee is the point of closest approach of the satellite to the central body, the apogee is the point of farthest approach (not labelled in the figure) and the ascending node is the point where the orbital plane crosses the equator plane with the satellite travelling

from the southern hemisphere to the northern hemisphere. The remaining two elements, semi-major axis, a , and eccentricity, e , describe the size and shape of the ellipse.

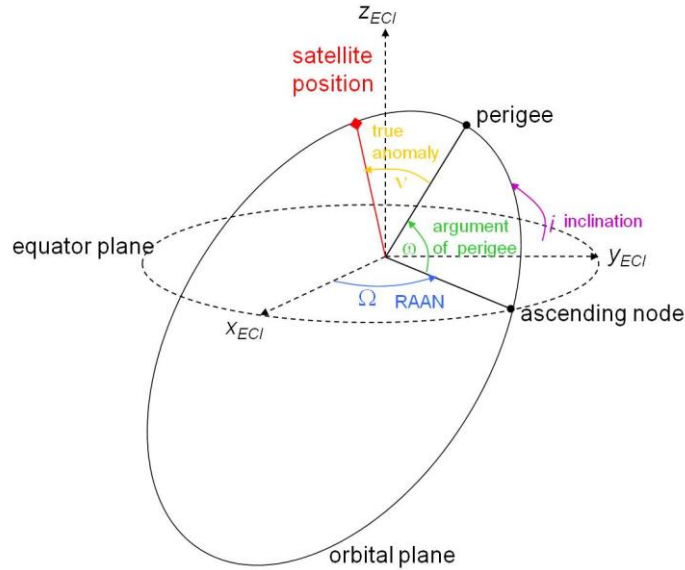


Figure 2-6: Keplerian Orbital Elements, from Kahr 2011

Kepler's laws of satellite motion were later derived mathematically using Newton's three laws of dynamics, under the assumption of a perfect two-body system, in which the central body can be reduced to a point mass and the only force is due to the central body's gravitational potential. As an alternative to the six Keplerian elements, this type of orbit can also be fully defined by the satellite's 3D position and 3D velocity vectors at a single epoch.

A more realistic model of orbital motion includes perturbing forces, such as gravitational effects due to an uneven distribution of the central body's mass (perturbations, tides) or to other celestial bodies (sun, moon, planets), and surface forces such as drag and solar radiation pressure, among others.

2.2.2 Types of Orbits

Three categories of satellite orbits are of particular significance for this work. First, medium Earth orbits (MEO) are used for the majority of GNSS satellites. These orbits are nearly circular and have a semi-major axis of approximately 26000 km, corresponding to an orbital period on

the order of 12 hours. In the case of GPS, the orbital periods are exactly 12 siderial hours, which lead to a repeating geometry for users on the Earth's surface, with a 3 minute and 56 second shift from day to day. GLONASS, Galileo, and the global part of BeiDou System are also comprised of MEO satellites, at slightly different altitudes.

The second significant category is geosynchronous orbits, which have a period of exactly 24 siderial hours, and a corresponding semi-major axis of approximately 42000 km. Geosynchronous satellites are set into prograde orbits, which mean they rotate with the Earth, and remain at approximately the same longitude over the Earth's surface. Inclined geosynchronous orbits (IGSO) oscillate between the northern and southern hemisphere, while geostationary orbits (GEO) have zero inclination, and therefore remain over the same point above the Earth's equator. The regional GNSS systems such as BeiDou, IRNSS, and QZSS, as well as the satellite based augmentation systems all use geosynchronous orbits. The SBAS satellites are all geostationary, or nearly geostationary, while the regional systems require a combination of GEO and IGSO satellites to provide users with a sufficiently diverse positioning geometry. Aside from their use as positioning satellites, the majority of communications satellites globally are in geostationary orbit, which has led to significant crowding at the required orbital altitude and tight constraints on missions to remain in their required orbital slots. Consequently, users in geostationary orbit also stand to benefit from above the constellation GNSS research.

The third category of orbits, and the focus of the majority of this work, are highly elliptical orbits. These orbits have eccentricities on the order of 0.8, where the possible value of eccentricity ranges from 0 for a perfectly circular orbit to 1 for a parabola/escape trajectory. Following from Kepler's law of equal areas, at perigee HEO satellites swing past the Earth at a great velocity, where they experience stronger forces due to gravitational perturbations and potentially also atmospheric drag. At apogee HEO satellites travel more slowly and also in a more stable orbit, where perturbing forces such as solar radiation pressure and gravitational effects of other celestial bodies dominate, but are overall less significant than the perturbing forces at perigee.

2.2.3 Orbit Determination

Orbit determination is the process of estimating the trajectory a satellite follows, and can be done based either entirely on measurements epoch by epoch, called kinematic orbit determination, or based entirely on the physics describing an orbit, called dynamic orbit determination. A combination of the two methods, referred to as reduced-dynamic orbit determination, is most typically used. Reduced dynamic orbit determination constrains the solution to a realistic trajectory based on orbital dynamics, but allows for some flexibility, through the addition of empirical acceleration states, so that the solution can follow the measurements when the dynamics model does not perfectly describe the motion. This could for example be due to unmodelled higher order gravity field terms, changing atmospheric conditions, or un-modelled changes in the drag and solar radiation pressure resulting from changes in the satellite's attitude among others.

Orbit determination can be done in post processing or in real time. For post-processed orbit determination least squares is typically used, similar to the process outlined in section 2.1.3. In this case the states are typically the initial orbit conditions (position and velocity) as well as empirical accelerations over fixed time periods, satellite specific parameters such as drag and solar radiation coefficients, measurement system parameters such as a GNSS receiver clock offset, and potentially maneuver magnitudes and directions, among others. In this case a long arc of input data is typically used, covering at least one full orbit but more often one or several days of observations (Montenbruck et al 2005, Lutz et al 2016). Alternatively, for real time orbit determination, generally carried out onboard a satellite, a Kalman filter is typically used (D'Amico 2010, Wang et al 2015, NASA GSFC 2006, Roth 2010). In this case measurements are processed as they come in, and the states are typically the current orbital position and velocity, as well as parameters such as drag and solar radiation pressure coefficients, and measurement system parameters. Empirical accelerations may or may not be explicitly estimated, because the process noise already allows some flexibility into the orbit determination process.

2.3 GNSS Positioning in Orbit

GNSS positioning in low Earth orbit does not drastically differ from positioning on the Earth's surface, aside from a larger range of Doppler due to spacecraft velocity (+/- 42 kHz rather than +/- 5 kHz for a receiver on the ground) and the possibility of an antenna pointing in some direction other than zenith, which may lead to a reduced field of view and number of tracked GNSS satellites. The combination of these two factors can make acquisition extremely challenging, but are not insurmountable.

In addition to challenges faced in low Earth orbit, the positioning environment above the constellation is significantly degraded in terms of signal strength and geometry. This is depicted in Figure 2-7, which shows a scale diagram of a GPS orbit, a low Earth orbit, a geostationary orbit, and three highly elliptical orbits corresponding to the PROBA-3 mission (Llorente et al 2013) and two phases of the Magnetosphere Multiscale Mission (Bamford et al 2009), all reduced to the same plane for comparison. Also included in the figure is the outline of the GPS signal availability region, based on a C/N₀ value of 33 dB-Hz and the GPS block II/IIA pattern published by Czopek and Schollenberger (1993).

It can be seen from the figure that the GNSS satellites transmit the majority of their power towards the Earth, and users above the constellations must make do with the main lobe signal spilling over the Earth's limb, or the weaker side lobe signals. In both cases, additional free space path loss makes the signals weaker than they would be for a user on the Earth or in low Earth orbit. The strongest signals, grazing the Earth's surface, are degraded by atmospheric effects and subject to significant path delay. Furthermore, it is unlikely that a standard receiver would be able to track sufficient signals for a position fix due to the limited visibility, and what signals are acquired and tracked all come from the same part of the sky, leading to very high dilution of precision values which limit the achievable single point positioning accuracy even when a position can be calculated.

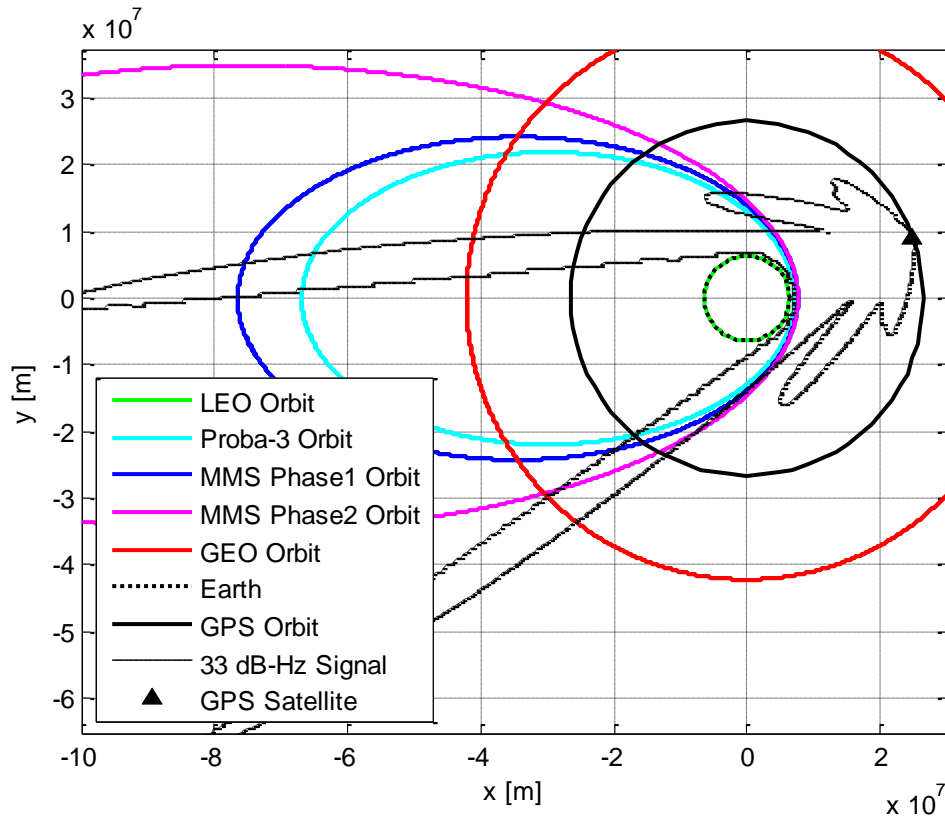


Figure 2-7 Scale diagram of GPS, LEO, GEO and HEO orbits and the GPS transmit gain pattern

In the case of a receiver in geostationary orbit the dynamics are not dramatically different than they are on the Earth, but without specialized weak signal capabilities or a high gain antenna pointed consistently downward towards GNSS satellites visible over the Earth's limb, the receiver may never actually get a position fix to aid its acquisition or to initialize an on-board orbit determination filter. In the case of highly elliptical orbits, the conditions change dramatically from perigee to apogee. During the brief passage through perigee, a receiver would benefit from positioning geometry similar to that on the Earth's surface, but is subject to an extremely large velocity (for a PROBA-3 type orbit on the order 11 km/s) which corresponds to an even wider range of Doppler shifts than experienced in low Earth orbit (+/- 48 KHz), as well as very high Doppler rates of change, up to 70 Hz/s. At apogee, the conditions are similar to those in GEO, with only a minimal number of weak signals available, but solutions such as high gain receiving antennas are less practical because of the varying conditions over the entire orbit.

Between perigee and apogee additional challenges may occur, in particular near-far effects. This occurs if the receiver passes near enough to a GPS satellite on the same side of the Earth for it to jam out the weaker signals spilling over the Earth's limb, and cause the receiver to loose lock.

2.4 A Brief History of Above the Constellation GNSS Positioning

The first use of GNSS on a spacecraft was in the early 1980's, on the LandSat 4 satellite which was launched on July 16, 1982 (Birmingham et al 1983). LandSat-4 carried a two channel GPS receiver and alternated measurements on the requisite four satellites, combining them with a Kalman filter, and underwent long periods where no position solution was possible as the full constellation of GPS satellites had yet to be launched. In spite of the early challenges, it was already apparent that an instrument allowing for both precise positioning and timing on-board a spacecraft, with no requirement for ground support, was invaluable. Since then, the use of GNSS receivers on low Earth orbiting spacecraft has become routine.

The first interest in above the constellation GPS positioning appeared in literature approximately 15 years later, in the late 1990's. The late 1990's and early 2000's saw a handful of pioneering missions carrying GPS receivers above the constellation, which proved that GPS signals could be received but that service was limited. There followed an intense decade of research and development to enable reliable use of above the constellation GPS, and as additional systems have come online, GNSS. Over the same time frame GPS was adopted for relative navigation of formation flying satellites in low Earth orbits. Over the past few years there has been an explosion of new results, as the missions and technologies developed over the past decade reach maturity and are launched.

The early above the constellation missions are presented in section 2.4.1, the simulation work for above the constellation positioning and multi-constellation GNSS is presented in section 2.4.2, the single satellite above the constellation missions and receivers in section 2.4.3, and the formation flying missions in section 2.4.4.

2.4.1 Early Missions

Tracking of both the main and side lobes of the GPS signals from spacecraft above the GPS constellation was demonstrated in 1997 by the student Falcon Gold experiment, which captured snapshots of the available signals and transmitted them to the ground (Powell et al 1999), and by the TEAMSAT/YES (Bandecchi and Ockels 1998, Smith 1998) and EQUATOR-S missions which both demonstrated closed loop tracking (Balbach and Eissfeller 1999). All of these missions were proof of concept studies that only lasted for a few days or weeks, collecting minimal data. The amateur radio satellite, AO-40, was launched into HEO in 2000, carrying a GPS receiver with one of its goals being to map the side lobes of the GPS signals (Moreau et al 2002, Davis et al 2002). According to a paper published in 2000, an unidentified military satellite in geostationary orbit had also been regularly using GPS for positioning for years prior to the publication (Kronman 2000). Further, the geostationary STENTOR satellite planned to carry a GPS receiver into orbit with the DIOGENE (Détermination immédiate d'orbite par GPS et navigateur embarqué) orbital filter integrated (Mehlen and Laurichesse 1999, Gerner et al 2000). The STENTOR launch in 2002 unfortunately failed, ending the early era of above the constellation GPS experiments.

2.4.2 Simulations and Multi-Constellation GNSS

Numerous feasibility studies have been carried out assessing the positioning capabilities of GPS for different mission concepts. Enderle (1999) assessed GPS for spacecraft attitude control in a geostationary transfer orbit, which could have positive repercussions for accurately positioning geostationary satellites into their final orbital slots, but finds that the attainable attitude accuracy is too limited by the poor visibility.

The Computer Sciences Corporation (2002) further investigated the ability to recover accurate positioning of a geostationary satellite after a manoeuvre using GPS under different conditions, and determined the results were best when both GPS coverage was available immediately after the manoeuvre and the manoeuvre was included in the filter's dynamics modeling.

Ruiz and Frey (2005) studied the impact of using a single vs. dual frequency receiver (in both cases tracking GNSS satellites down to 200 nautical miles above the Earth's surface, with

ionospheric delay modeled) in geosynchronous orbit, and of tracking side lobes vs. only the main beam. They found that when a visibility threshold of -185 dBW was assumed (approximately 25 dB-Hz) at least one GNSS satellite was always visible, and using either dual frequency or tracking side lobes allows for a filtered position error of well under 100 m, compared to 200 m with single frequency main lobe only positioning.

Carpenter et al (2004) analyzed GPS positioning during navigation to the moon as well as scenarios involving two Earth/Moon libration points, but did not use a realistic model of the increase in measurement noise with decreasing carrier to noise density ratio (C/N_0). Fedora and Tyler (2007) carried out a realistic hardware in the loop simulation of navigation to and from the moon using an integrated military off the shelf receiver with integrated INS.

Asaki et al (2008) found that the ASTRO-G mission's requirement of 10 cm absolute orbit determination accuracy could be met using a combination of dual frequency GPS measurements at altitudes up to 3500 km and SLR measurements up to the 25 000 km apogee. Further to the GPS navigation study, combined GPS/GLONASS was also considered for the ASTRO-G mission (Priv. Comm. O. Montenbruck).

Bradley et al (2010) and Axelrad et al (2011) suggested a method for simultaneously positioning and acquiring weak signals called collective detection, in which the sum of the weak signals is detected rather than individual signal detections, and demonstrated its potential for positioning geostationary satellites.

Due likely to the drop in the number of satellites in the late 1990's and mid 2000's, tracking of the GLONASS satellites outside the constellation has rarely been considered. In the period of research in the mid 2000's only a minimal number of satellites, such as GOCE and SAC-C, even carried GPS/GLONASS capable receivers in LEO (Casotto et al 2002, Rebhan et al 2000). A single GLONASS study was carried out in 2002, by Yanovsky et al assessing the feasibility of combined GPS/GLONASS for a Russian scientific HEO mission called "Resonance", which has a precise timing requirement of 1 microsecond. It was found that with both systems there were points throughout the orbit where four GNSS satellites were simultaneously visible to update the

clock solution. Few details are given, but the “Resonance” study appears to assume GLONASS has identical characteristics to GPS in terms of transmit gain patterns.

Galileo has yet to reach full operational capability, but a significant number of research groups have carried out studies to demonstrate its potential benefit. Among them are Dion et al (2007) of SUPAERO, who had a software simulated space environment for LEO and GEO and were creating a software receiver for testing new algorithms with both Galileo and GPS, with the flexibility to change as more solid Galileo design decisions were made. Lorga et al (2010ab) of the European Space Agency and affiliated institutions have likewise done software visibility simulations of GEO and HEO to assess feasibility of combined GPS and Galileo, and further found that incorporating knowledge of the orbital dynamics into the tracking loop provided significant advantages in terms of weak signal tracking and positioning accuracy. Qiao et al (2009ab) of China and Australia have done less detailed visibility simulations but included results for all four GNSS constellations, separately and combined. A more recent study by Rathinam and Dempster (2016) looks at the visibility of global and regional constellations, except IRNSS, over a global grid of points based on the preliminary space service volume definitions for the various constellations.

2.4.3 Receivers and Recent Single Satellite Missions

Beyond the simulation studies, more concrete developments were made in the form of missions and hardware GPS receivers. While most of the developments have been carried out in parallel, they are presented here in roughly chronological order by launch or anticipated launch.

2.4.3.1 SGR GEO/GIOVE-A

In the decade between the early and recent above the constellation missions the only mission launched into an orbit above the GPS constellation carrying a GPS receiver was the GIOVE-A MEO satellite in December 2005, equipped with an SGR-GEO receiver from Surrey Satellite Technology Ltd. The receiver is a 12 channel single frequency L1 C/A receiver based on COTS components with a stable oven-controlled crystal oscillator (OCXO) reference oscillator, weak signal tracking capability and an 8 dBi high gain antenna. Aside from a brief campaign in 2006 (Ebinuma and Unwin 2007) the receiver remained powered off until the main L-band payload

was retired in 2012 (Unwin et al 2013). The receiver tracked both main and side lobes, and was updated to use 10 ms coherent integration to track rather than 1 ms. It has an acquisition threshold of 42 dB-Hz based on 1 ms integration, and a tracking threshold of either 37 dB-Hz with 1 ms integration or 30 dB-Hz with 10 ms integration. The GPS transmit pattern side lobes were tracked and mapped but without regard to azimuthal dependence, which led to somewhat inconsistent results given the extent of the azimuthal variation documented in later publications. Two important results were that the receiver was able to achieve a position fix 75% of the time, and the documentation of “atmospheric chimneys” or suddenly increasing atmospheric effects on individual satellites as the line of sight approached the Earth, which seriously degraded the (often minimally constrained) position solution by several kilometres, and defied attempts at orbit determination.

Beyond the one SGR-GEO receiver, Surrey does not appear to have pursued the development of above the constellation receivers. Their SGR-Axio receiver designed for low Earth orbit is however one of a very limited number of multi-constellation space receiver to support three constellations: GPS, GLONASS and Galileo (Surrey Satellite Technology Ltd. 2014). Also among the triple constellation LEO receivers is JPL’s TriG receiver (MOOG 2016).

2.4.3.2 Topstar 3000/Topstar 3000 G2/PROBA-2

The French national space agency (CNES) and partner companies have continued development on Topstar 3000, the space GPS receiver which was integrated into the failed STENTOR satellite. The original receiver was designed for weak signal tracking, with the ability to feed information from an integrated IMU or the navigation filter into the NCO to aid tracking of very weak signals, which was the basis of their “code only” mode (Issler et al 1998). The new version, Topstar 3000 G2, has the additional ability to track L2CL signals and has since been flown on the low Earth orbiting satellite PROBA-2 (Serre et al 2006), launched in 2009. While it does not produce carrier phase measurements suitable for relative navigation with integer ambiguity resolution, it does incorporates the weak tracking abilities of the earlier receiver, tracking code and phase down to 27 dB-Hz and code only down to 20-22 dB-Hz on L1. L2C can also be acquired at 31 dB-Hz and tracked down to 29 dB-Hz, in keeping with the envisaged use of the

receiver for GEO and HEO missions (Montenbruck et al 2010). The Topstar receiver has unfortunately not, to date, had an opportunity to fly above the constellation.

2.4.3.3 SBIRS GEO1

The Space Based Infrared System (SBIRS) GEO 1 mission, launched on March 7, 2011, is the second known mission to carry a GPS receiver into geostationary orbit (Barker and Frey 2012), after the mission documented by Kronman (2000). It is a military satellite with the primary goal of missile warning and missile defense, carrying an unspecified model of dual frequency GPS receiver, apparently capable of both L1 and L2 P(Y) tracking, and a directional high gain antenna with 9 dBi of gain. The narrow antenna beam, and the fact that the center of the beam was pointed at the Earth and subject to greater thermal noise, made side lobe tracking impossible for this mission. The main lobe tracking and dual frequency measurements were, however, of sufficient quality to characterize the ionospheric errors as well as the difference in equipment group delay on L1 and L2, because the signals were tracked at larger angles off the boresight of the GPS transmit antennas than is typically possible. It was found that the group delay changes much faster on L1 than on L2, which ultimately causes an effect which looks like an ionospheric advance rather than delay on the dual frequency measurements. This effect has both a spacecraft and azimuthal dependence, and requires calibration.

2.4.3.4 Antenna Characterization Experiment

Two bodies of work which have dramatically improved the realism of simulation studies have been released in the past few years. The first is the release of the GPS Block IIR and IIRM gain patterns by Lockheed Martin in 2013 (Marquis 2013, Marquis and Reigh 2015) and the second is the Antenna Characterization Experiment (ACE) study by NASA, ongoing since 2014 (Martzen et al 2015). ACE makes use of a transponder on a geostationary satellite to re-transmit the GNSS signals received to the ground, where they are processed by both an upgraded version of the same state of the art receiver flying on MMS (see section 2.4.4.1), and by the Mariposa GPS Receiver (MGPSR). The MGPSR uses combinations of 1 ms integrations of up to 30 seconds, along with data bit aiding, to track all signals in view down to 0 dB-Hz. It operates on buffered data with a delay. As a result of the ACE experiment the transmit gain patterns of all the blocks

of GPS satellites currently flying have been mapped to 90 degrees off bore sight, and an assessment of the measurement quality achieved from the side lobes is expected future work.

2.4.3.5 Chang'E-5T

On October 23, 2014 China launched the Chang'E-5T lunar probe for a 196 hour test flight as part of the Chinese Lunar Exploration program. (Fan et al 2015) The spacecraft consisted of two components, a return vehicle, and a service module which has ultimately been placed into lunar orbit. Both carried 24 channel GPS/GLONASS L1 C/A weak signal capable receivers, the details of which are presented by Wang et al (2015). The return module receiver was activated twice, at altitudes from 5000 to 60000 km above the Earth as the vehicle was launched and as it returned. A third data set was collected with the service module's receiver on November 18th during the Earth-lunar transfer orbit, which tracked only two GPS satellites, but up to an altitude of 140000 km, according to Liu et al (2017). The hardware consisted of two antennas on opposite sides of the spacecraft, with 10 dB peak gain and 2 dB gain in a 40 degree field of view for omnidirectional signal reception. The receivers have an oscillator stability of 10^{-6} , which was synchronized to GPS time roughly every 10 minutes to maintain 0.5 ms alignment. The receivers have a reported acquisition threshold of 29 dB-Hz (which equates to -175 dBW) and tracking threshold of 26 dB-Hz.

Side lobes were tracked regularly, on both constellations, and on average more than 8 GPS satellites were tracked and more than 4 GLONASS satellites. At least four GPS satellites were tracked 98% of the time. Chang'E-5T is the first mission to track GLONASS outside of the constellations at all, and found that while there were fewer measurements than from GPS and they were of lower quality, if they were appropriately weighted they could be used to significantly improve the orbit determination. GLONASS was particularly helpful for bridging periods of less than four GPS satellites when it was used along with a-priori knowledge of the GPS-GLONASS system offset.

According to Liu et al (2015), Chang'E-5T had a close flyby of GLONASS satellite R06, passing within 2000 km, and the satellite was tracked from below to above. The signal power data from the close encounter and tracking of the other GLONASS satellites was analysed to

extract a gain pattern, and the result is presented in Liu et al (2017). This is an extremely valuable result, as it is the only concrete information about GLONASS transmit patterns published to date. Their results show that the GLONASS pattern has side lobes with significant azimuthal variation, and that the overall pattern most closely resembles that of the GPS block IIR-M satellites.

2.4.3.6 GOES-R/Viceroy-4

The Geostationary Operational Environmental Satellite – R Series (GOES-R) was launched on November 19, 2016 (GOES-R Series Program Office 2017). It is carrying a General Dynamics Viceroy-4 GPS receiver, which has been designed for the GOES-R mission specifically. The receiver has weak signal tracking capabilities and it is expected to meet the navigation accuracy requirement of 75 m, 3 sigma, in the along-track and cross-track axis, and 100 m, 3 sigma, in the radial axis (Chapel et al 2015). The receiver is able to track the side lobes, and lab testing has shown that it typically tracks 8 satellites and can obtain a position fix within 8 minutes 95% of the time, but does not specify if this is a cold or warm start. A unique feature of this mission is the requirement for the payload instruments to continue normal operations during station keeping and momentum unload maneuvers, which in part is what drove the decision to adopt GPS positioning.

Unique to the GOES-R body of work is a study by Voboril et al (2016) assessing the sensitivity of the GPS navigation to solar flares. It finds that a geostationary satellite can expect events lasting from 0.5 to 3 hours on average seven times per year, based on 25 years of historical data. During these events the noise floor is expected to increase, based on Spirent simulations to the point that the Viceroy-4 receiver under test lost lock on all tracked GPS satellites. It was also found that for GOES-R the onboard orbit filter could easily bridge the gap, making the system insensitive to solar flares.

Other missions carrying General Dynamics receivers above the constellation, some already launched and some expected in the coming years, are documented by Bauer (2015a). Many of them are classified and as such not documented in open literature.

2.4.3.7 Mosaic GNSS/ LION Navigator/ Small GEO

Two different receivers have been developed by Astrium/Airbus Defense and Space: MosaicGNSS and LION Navigator. At the time this research project began the most realistic and detailed investigations into multi-constellation GNSS outside the service volume, including both receiver weak tracking and acquisition behaviour and spacecraft orbits and operations, were conducted within the scope of these projects (Filippi et al 2010, Kuehl et al 2011, Barrios-Montalvo 2010).

The MosaicGNSS receiver is an 8 channel GPS L1 C/A receiver, with significant space flight heritage in low Earth orbit. According to the receiver's data sheet, it has an acquisition threshold of 30 dB-Hz and a tracking threshold of 26 dB-Hz (Airbus 2014). It has been chosen to fly on the SmallGEO series of satellites (Zentrgraf et al 2010). The first of these, Hispasat –AG1, was launched into geostationary orbit on January 28, 2017 (European Space Agency 2017).

The goal of the LION Navigator receiver design was to build a single receiver suitable for all missions (LEO, GTO and GEO) rather than having to tailor the receiver to a particular mission, as is the case with the Mosaic GNSS receiver (Hartrampf et al 2015). The LION Navigator receiver supports 36 single frequency channels, and is capable of tracking GPS L1 C/A, L2C and L5, as well as Galileo E1 and E5a, as long a sufficient channels are available. It offers single point solutions as well as a built in Kalman filter, and can take in satellite attitude information to assist in visibility predictions and accelerations from maneuvers to aid the Kalman filter. The achieved tracking threshold is 20 dB-Hz. In a realistic hardware in the loop GEO scenario a 3D RMS positioning accuracy of ~ 20m was achieved. According to the earlier work there are plans to extend the receiver to GLONASS and BeiDou (Kuehl et al 2011). As of yet the LION Navigator has not flown in space.

2.4.3.8 HiSGR

The Chinese Academy of Space Electronic Information Technology (ASEIT) reports the development of a space receiver suitable for all orbits from LEO to trans-lunar (Wang et al 2017). The receiver has several different software packages that can be used, depending on the end use. It ultimately supports, in various modes of operation, weak acquisition down to 15 dB-

Hz and weak signal tracking using an adaptive tracking loop, a high fidelity orbit model for use with an on-board orbit filter to produce filtered position solutions in real time, a built in MEMS IMU and an integrated positioning mode making use of an ultra-tightly coupled GPS/INS Kalman Filter which provides Doppler aiding to the weak signal tracking, GPS reflectometry, radio occultation, and changes to the software by tele-command. It is currently a GPS L1/L2 receiver with the integration of BeiDou B1I and B3I in the near future.

2.4.4 Formation Flying

Alongside the developments in above the constellation navigation, the space community has also adopted GNSS as a tool for relative navigation of formation flying satellites over the past decade. Some examples of missions currently flying in low Earth orbit are the gravity field mission GRACE, which makes use of the precisely known distance between the spacecraft to measure the gravity field gradient (Tapley et al 2004), the imaging mission TerraSAR-X/ TanDEM-X which uses the different perspectives from two spacecraft to obtain 3D Earth elevation models (Krieger et al 2007), the A-train collaboration, which consists of independent scientific missions sharing an orbit with a few minutes of along-track separation to take temporally and spatially correlated measurements from a variety of scientific instruments (Kidder et al 2007), or the technology demonstration mission PRISMA, which is capable of autonomous formation control and collision avoidance (Persson et al 2005, D'Amico 2010).

There are also two above the constellation formation flying missions, the Magnetospheric Multiscale Mission (MMS) and the Project for Onboard Autonomy 3 (PROBA-3).

2.4.4.1 Magnetospheric Multiscale Mission

By far the most significant body of work in terms of receiver design and relative positioning for formation flying in HEO has been carried out in preparation for the Magnetospheric Multiscale Mission (MMS) (Curtis 1999). The mission, launched on March 13, 2015, consists of four satellites flying in a tetrahedron formation and spinning at 3 rpm, with the goal of studying magnetic reconnection. The mission will have two phases in order to study both the day and night side of the Earth's magnetosphere, the first a HEO orbit with its apogee at 12 Earth radii on

the day side of the Earth, and the second a HEO with its apogee at 25 Earth radii on the night side/in the magnetotail (Bamford et al 2009, Long et al 2015).

A number of bodies of work into above the constellation positioning have been ongoing in parallel for roughly the past decade. Goddard Space Flight Centre (GSFC) used simulations to investigate different estimation algorithms for relative positioning in HEO using GPS and cross-link measurements (Gramling et al 2000, Kelbel et al 2001, Long et al 2002). Extensive theoretical work on receiver design and integer ambiguity resolution has been done by Psiaki and Mohiuddin (2001, 2002, 2005, 2007, 2008). Building on the early work by GSFC and Psiaki, the PiVoT and Navigator space GPS receivers have been developed and extensively tested, and much of the testing has been specific to the MMS formation flying in HEO requirements. All MMS work makes use of GPS only, in keeping with the US policy that operations may not depend on other GNSS, although they may be included to assist operations or scientific goals (van Graas 2009).

2.4.4.1.1 Theoretical Work

Theoretical orbit determination work leading to the design of the MMS relative navigation concept was carried out by GSFC in the early 2000's. Gramling et al (2000) tested an assortment of absolute and relative positioning estimators using GPS pseudorange measurements and radio cross-link measurements for formation flying in a 500 km x 7000 km elliptical orbit. The work was extended in Kelbel et al (2001) to include more realistic simulations of clock biases, and to include the orbit for the first phase of the MMS mission. They determined that a receiver with a lower acquisition threshold than previously used would be necessary to meet the MMS positioning requirement of 100 km absolute positioning and 1% of the distance between the spacecraft for relative positioning. They also determined that clock drift and biases were a significant factor. The work was further extended in Long et al (2002) to more rigorously simulate the error sources, particularly clock biases and the use of an ultra-stable oscillator.

Theoretical receiver design work was also carried out. Psiaki (2001) describes acquisition algorithms capable of acquiring at extremely low carrier to noise density levels for potential use in Geostationary orbit, and in (2002) extends the work to present a filter for weak tracking. The

novel receiver designs are demonstrated to work in post-processing but are far too computationally expensive for real time. In 2005, Psiaki and Mohiuddin present a method of carrier phase ambiguity resolution for relative positioning outside the GPS service volume. It makes use of purely kinematic positioning, and therefore depends on tracking at least five GPS satellites simultaneously. To meet this requirement, dual frequency measurements are required to track GPS satellites setting near the Earth's surface and estimate ionospheric electron content degrading their signals, and weak signal tracking is required to track GPS side lobes. To meet these requirements, it is therefore assumed that it is possible to track down to 18 dB-Hz on L1 and 15 dB-Hz on L2C for receivers in geostationary orbits, and 12 dB-Hz on L1 and 9 dB-Hz on L2C for receivers in HEO with an apogee at 17 Earth radii. A very rigorous software simulation is set up, which is described in detail in Psiaki and Mohiuddin (2007), and it is demonstrated that although no present day receiver is capable of tracking at these low C/N₀ values, under the simulated noise and geometry conditions carrier phase integer ambiguity resolution is in fact possible in GEO and HEO. The work is extended in Mohiuddin and Psiaki (2008) to include orbital dynamics in the position filtering.

2.4.4.1.2 Receiver Design

Extensive work was also carried out in the area of developing a suitable GPS receiver for use above the GPS service volume. Initially the PiVoT (Position Velocity Time) receiver was developed for use above the GPS service volume (Long et al 2000, Dvorak-Wennersten et al 2001, Moreau et al 2000, Moreau 2001, Garrison et al 2001). It is a 24 channel GPS L1 receiver. The modifications compared to a standard receiver were substantial, consisting of improved satellite selection for all geometries, improved acquisition for weak side lobes, modified tracking loops, consideration of a pseudorange ambiguity that resulted from the Mitel GPS builder-2 receiver when tracking higher than 20 Earth radii, research into the use of a high quality clock, and integration of the GEONS (GPS Enhanced Onboard Navigation System) filter. It underwent testing in hardware in the loop simulations both before modifications to the tracking loops were made (Moreau et al 2001) and after (Moreau et al 2005). In order to avoid potential intellectual property conflicts, the PiVoT receiver was eventually superseded by the Navigator receiver.

The Navigator receiver, developed largely by the same group, builds on PiVoT technology but for licensing concerns does not use any of the same software. It is fundamentally based on the weak acquisition research of Psiaki (2001), who introduced the “half-bits” acquisition strategy for GPS L1 C/A signals, allowing for longer integration insensitive to data bit transitions. Psiaki’s work went through substantial adaptations and upgrades to work within the constraints of space hardened electronics in real time (Winternitz et al 2004). For maximum flexibility, Navigator has been designed to work in real time with no external aiding, and is capable of acquiring even weak signals in cold start in two minutes. Testing of scenarios above the main GPS constellation using the formation flying test bed at Goddard Space Flight Centre is described by Bamford et al (2005, 2006) and a full description of the receiver hardware, software, and performance under testing in various orbit scenarios is given by Winternitz et al (2009). Winternitz also describes plans for future development for a “Navigator Duo” receiver, which should have the capability for 15 dB acquisition and tracking based on a vector tracking loop design described in (Psiaki 2002), and depending on the availability/design of a front end may also at some point incorporate GPS L2C and L5, Galileo, INS integration and antenna beam forming. The GPS III paper by Ramakrishnan et al (2013) primarily presents a GPS antenna modelled in software to determine what the side lobes look like for above the constellation tracking, but also mentions extending the Navigator Receiver to Galileo E1.

2.4.4.1.3 Mission Design

Kelbel et al (2003) tested several navigation concepts for the first phase of the Magnetospheric Multiscale Mission, including ground station tracking (range or two-way Doppler measurements), GPS code measurements, cross link range measurements between formation members, and combinations of the above. For the first phase MMS has a post processed absolute positioning accuracy requirement of 100 kilometres and relative positioning accuracy requirement of 1 %, which equates to 100 m at apogee when the spacecraft will be 10 km apart. It was determined that of the scenarios capable of meeting the positioning requirements, a combination of GPS L1 C/A and cross link measurements was most favorable in terms of balancing accuracy and operational simplicity.

The Intersatellite Ranging and Alarm System (IRAS) instrument, which incorporates the Navigator GPS receiver, GEONS navigation filter, and cross link transceivers was chosen for MMS. It uses onboard filters for real time positioning and accurate timing, with measurements downloaded to the ground for conjunction assessment and manoeuvre planning. It underwent testing in the Goddard Space Flight Centre's Formation Flying Test Bed, which led to the discovery that GPS L1 C/A alone was sufficient to meet the accuracy requirements, and the elimination of the cross link ranging. The absence of the cross link transceivers means that the satellites have no capability to transmit data among themselves or do real time relative navigation. Instead, relative positioning is done in post processing on the ground (Bamford et al 2009). Further, prior to launch, hardware testing of one fully functional flight model Navigator receiver under the most accurate possible simulation scenarios was carried out and predicted between 0-3 visible satellites at the phase 1 apogee, with more than 12 tracked at perigee, and 0-2 satellites at the phase 2 apogee (Lulich et al 2012).



2.4.4.1.4 Since Launch

MMS mission was launched on March 13, 2015, with each of the four spacecraft carrying a Navigator receiver, as well as four antennas. The satellites are spin-stabilized, spinning at a rate of 3 rpm, and the antennas are situated on four sides of the spacecraft perpendicular to the spin axis. GPS tracking is handed off from one antenna to the next every five seconds (Long et al 2015). Due to the constant change in ambiguity, only pseudorange data are processed, both onboard using the GEONS filter and post-processed on the ground (Farahmand et al 2015). The most immediate and significant result from the navigation system was that on average 8 satellites were tracked throughout the orbit, and a reported onboard filtered positioning accuracy of 12 m at apogee was achieved, vastly exceeding the pre-launch performance predictions (Witnernitz et al 2016). A ground tracking campaign was initially carried out to assess the onboard GPS navigation performance, but it was almost immediately apparent that the onboard results were reliable, significantly simplifying the operations (Farahmand et al 2015). One very important outcome of the MMS mission is that the pseudoranges are unbiased, indicating that even side lobes of the GPS antennas produce reliable, positioning quality signals, a fact which was previously unproven.

The MMS receivers, in addition to the Psiaki half-bits acquisition method, use 20 ms coherent integration in their tracking loops to maintain lock on the weak signals (Witnernitz et al 2009). Each receiver has a dedicated Ultra Stable Oscillator, in order to meet positioning and timing requirements even when GPS satellites cannot be tracked (Winternitz et al 2016). To overcome the spacecrafts' spin rates they have two correlators dedicated to each PRN, one tracking normally and the next already attempting acquisition on the incoming signal from the next antenna to rotate into view (Winternitz et al 2017). The receiving antennas were designed in-house (Winternitz et al 2017), and have a peak gain of 4 dB which rolls off to 3 dB at 60 degrees off-boresight (Bamford et al 2009), offering a 120 degree field of view (Long et al 2015).

Apart from the MMS mission, the Navigator receiver design has been licensed to two companies, and has also been flown in various forms on the AFRL ANGELS geostationary space situational awareness mission launched in July 2014 (Inside GNSS News 2014b), and on the Orion capsule test flight in December 2014 to establish how well its re-acquisition would perform after the radio blackout associated with the capsule's re-entry, among others (Winternitz et al 2017, Bauer 2015ab). A modified version is also part of the data collection system for ACE, previously described in section 2.4.3.4.

2.4.4.2 PROBA-3

PROBA-3 is planned to launch in 2019 (European Space Agency 2016) with the goal of demonstrating autonomous and precise close formation flying in HEO. A giant 150 m solar coronagraph consisting of two spacecraft, one carrying an occulter disk and the other the coronagraph instrument, has been chosen as the mission's scientific payload to provide realistic constraints, as the mission is a proof of concept mission for future large telescope mission concepts (The PROBA-3 Phase A Team 2007, Mestreau-Garreau et al 2011, Fernandez Ibarz et al 2011). Aside from the coronagraph, the mission will be used to demonstrate formation acquisition from various initial conditions, resize manoeuvres and formation rotations, precision (mm level) formation flying, collision avoidance and rendezvous in HEO. It will also be flexible enough to be reconfigured for other experiments once the main objectives are accomplished.

The satellites will manoeuvre twice per orbit, to set up the formation for scientific data collection after the perigee passage and to disassemble the formation and put the satellites at a safe distance for the following perigee passage. The PROBA-3 orbit will be highly elliptical with a perigee of 600 km and an orbital period of approximately 20 hours (Llorente et al 2013, Landgraf and Mestreau-Garreau 2013).

Relative positioning for PROBA-3 will be carried out through a series of instruments which will hand off control to one another. GPS will be used at and near perigee for formation acquisition, and two optical instruments, coarse and fine, will be used for the precise formation flying for six hours at apogee (Mestreau-Garreau et al 2011). Although the mission design documented in open literature claims that a single frequency L1 only GPS receiver will be flown, and this receiver has also been used to carry out the preliminary studies (Perea et al 2010, DLR/GSOC 2012), in the final design the satellites will actually carry a PODRIX receiver from RUAG Space (Bauer 2015ab). According to its data sheet, the PODRIX receiver is a dual frequency L1/L5 GPS/Galileo receiver, with either 18 dual frequency channels or 24 single frequency channels, but no specialized weak signal capabilities (Ruag Space 2016). The details of the unit to fly on PROBA-3 have not been published, but the latest information from RUAG is that it will be a single antenna, dual frequency GPS/Galileo receiver (Montenbruck 2017).

Because of its requirements for tightly controlled autonomous formation flying, and its use of GNSS to support the relative positioning, the PROBA-3 mission has been chosen as the basis for the majority of the research presented in this thesis. This research distinguishes itself from the actual PROBA-3 mission because it considers GNSS relative positioning throughout the entire orbit, with no consideration of optical sensors, while the actual mission will only use GNSS positioning through the perigee passage, and will use the optical sensors exclusively to control the fine alignment of the satellites during scientific data takes at apogee.

2.5 Outline of Missing Research

In summary, a number of methods for improving positioning in HEO have been suggested and simulated. Among them are weak signal tracking, using multiple GNSS constellations, using dual frequency data for tracking closer to the Earth's limb and to aid carrier phase ambiguity

resolution, using highly stable oscillators, and integrating orbital dynamics. Several missions have also been launched into orbits above the constellations in recent years: GIOVE-A, SBIRS-1, ACE, Chang'E 5T, GOES-R, Hispasat-AG1 and finally MMS, with several more launches planned in the next few years. In spite of this, there are still many open questions, which this thesis seeks to answer.

First, while a great number of simulation studies have been carried out for the visibility of multi-constellation GNSS, most of them are focused on a specific mission, and few of them have considered a wider overview of factors such as the alignment of the orbital planes in more general terms. Also, because every mission has constraints on the spacecraft attitude guided by critical factors such as solar panel orientation, thermal considerations, and payload orientation, no general study has been conducted to determine the ideal case for GNSS antenna accommodation and pointing direction. While it is fairly obvious that a GNSS antenna should point to zenith when the user satellite is in LEO, or point to nadir when the user satellite is above the GNSS constellations, the ideal case during a HEO satellite's transition between the two is less clear. Finally, while the main global constellations (GPS, GLONASS, Galileo and BeiDou 3) have been considered in a number of visibility studies, the regional systems have only occasionally been considered, and the satellite based augmentation systems have never even been mentioned. The visibility studies of Chapter 3 strive to fill these gaps.

Over the course of setting up the simulations of Chapter 3, it became immediately apparent that while some standard assumptions could be made about the MEO GNSS systems, little to no information was available about the satellite based augmentation systems. No reliable information was available on their transmit antenna gain patterns, and even the quality and reliability of their ranging services was rarely discussed, and never in the context of a space user. In fact only one spacecraft, ENEIDE (Zin et al 2007) seems to have carried an SBAS capable receiver into space at all. At the same time, it was clear that these systems should not be ignored for two reasons. First, they stand to provide a substantial improvement in geometry for a HEO satellite approaching or leaving perigee, when the GNSS satellites in MEO are only visible near the Earth's limb but geostationary satellites are potentially still visible overhead. Second, because these satellites also transmit in L-band their signals present the possibility for the same

“near-far” jamming problem as any other GNSS satellite, possibly made worse by an increased transmit power focused into a narrower beam to compensate for their higher orbits. Unfortunately, the lack of concrete information appears to have led to their exclusion from the body of above the constellation GNSS research. The study presented in Chapter 4, presenting real flight results from CanX-2, fills in many of these knowledge gaps.

To date, the only constellations tracked above the constellation are GPS, and in the case of the ChangE’5T1 spacecraft, GPS + GLONASS. The use of multi-constellation GNSS is limited on the one hand by policy, because only GPS promises service to space users, but on the other hand by the current state of the art in space receiver technology, coupled with the fact that with the exception of GPS and GLONASS, all the other navigation systems are still young, in many cases still incomplete, and often the definitive ICD’s were only recently released. While studies have certainly been conducted for ground and indoor positioning weak signal tracking of the new signal structures, relatively little research has been done considering the problem from the perspective of a space user. The groups with the most advanced receivers are in many cases companies building commercial products rather than academics, with the detailed receiver design work being proprietary. Although significant work is planned to create multi-constellation receivers capable of tracking all the constellations, at present only dual constellations space receivers appear to actually exist, and the GPS/GLONASS/Galileo triple constellation LEO receivers developed by Surrey Satellite Technology Ltd and JPL. The dual frequency space receivers are mainly GPS/Galileo receivers developed in various European institutions and profiting from the common L1 and L5 frequencies. The exceptions are the GPS/GLONASS receiver flown on the ChangE-5T lunar probe test and a GPS/BDS receiver onboard the Fengyun-3C LEO satellite (Wang et al 2014). Both because no suitable products were available at the time this research began, and because a black box receiver wouldn’t allow for the exploration of different signals, constellations, or acquisition or tracking strategies, a significant effort was made in the present work to bring the GSNRx™ software receiver up to the level of a space receiver, presented in Chapter 5 followed by research to find a suitable set of weak signal acquisition and tracking parameters for three constellations and four signals, presented in Chapter 6. This body of work was driven by the need to collect sufficient data under realistic receiver operating conditions to conduct a relative positioning study, but it resulted in a receiver

 that would, were it implemented in hardware rather than software, have capabilities competitive with and even exceeding the current cutting edge in multi-constellation, above the constellation space receivers.

Finally, previous work carried out in above the constellation ambiguity resolution is limited almost exclusively to the study presented in Mohiuddin and Psiaki (2008), which is based on highly realistic rigorous simulations, with the exception of required receiver performance levels which demand acquisition, tracking and navigation data at extremely low signal levels (12 to 18 dB-Hz) which are not practically realizable by any existing receiver. Essentially, the previous work has proven that the dynamics and poor geometry of a higher orbit do not prevent successful ambiguity resolution, provided a sufficient number of satellites are reliably tracked. The only mission in a position to actually test carrier phase based relative positioning with real data would be the Magnetospheric MultiScale Mission; however, with the spacecraft spinning at a rate of 3 revolutions per minute and the GPS tracking handed off between four antennas, the carrier phase ambiguities change roughly every five seconds, making the phase data exceedingly difficult to work with. Furthermore, the mission's relative positioning requirements are easily met by differencing the individual pseudorange-based, filtered position solutions of the spacecraft, making such a complicated relative navigation system unnecessary. The work presented in Chapter 7 extends the state of the art by presenting the first study of carrier phase based relative positioning under realistic receiver operating conditions, as well as the first multi-constellation relative positioning results for highly elliptical orbits.

Chapter Three: Visibility Simulations

3.1 Introduction

When this research project began, in spite of the ongoing interest the only receiver actually flying in space above the GPS constellation was onboard the GIOVE-A satellite, a precursor to the Galileo constellation. The receiver could only undergo very limited operations when the main L-band transmitting payload was not in use. Consequently, in spite of the limited data from the early missions and a handful of visibility simulation studies, there was very little understanding of many of the variables which would impact HEO relative positioning accuracy using GNSS. In general, the more broad simulations studies were lacking realism, while the studies focused on particular missions tested only a narrow set of mission specific parameters.

This chapter seeks to fill some of the knowledge gaps. It first presents the development of a flexible visibility simulation environment, along with the choice of parameters to populate the simulation, in section 3.2, and the testing and calibration of the simulation environment in section 3.3. The majority of the chapter presents the results from two visibility studies. The first seeks to answer questions about the ideal attitude for a HEO satellite's GPS antenna (section 3.4), and the second explores in greater detail the use and advantages of multi-constellation GNSS for relative positioning in HEO (section 3.5).

3.2 Simulation and Assumptions

In order to better understand the above the constellation signal environment and to assess the value of all the GNSS constellations, a simulation tool was created to calculate the geometry and link budgets of the GNSS satellites relative to a receiver on the ground or to a receiver on a user defined satellite. A goal of the visibility simulation was to have the software remain as flexible as possible, in order to easily change any element of the simulation. In the process of building the simulation a vast number of assumptions had to be made and justified in order to obtain results: assumptions about user receiver hardware, about the mission carrying it, and about the GNSS receivers.

3.2.1 Simulation Software

Creating a simulation which was flexible enough to handle any of the various GNSS system designs, including future information expected to be released in the forthcoming ICD's for BeiDou or the modernized GLONASS signals was not trivial. Although the basic operating principle of all the GNSS is the same, some fairly fundamental concepts, for example identifying satellites by PRN number or the format of the orbit information, not to mention the available signals, can be dramatically different from system to system.

In order to handle the vast variety of information, a series of objects was created in Matlab, most notably satellites, antennas, signals, and receivers, which could be combined in any configuration. At each simulation epoch all satellites are propagated forward, their attitudes are calculated, and for each receiving antenna and receiver pair, lists of visible or tracked incoming signals are compiled based on realistic link budget calculations. The simulation environment therefore makes it possible to test different attitude profiles, different receiver design assumptions, or complex user satellite systems with multiple receiving antennas on different faces of the satellite. Any number of GNSS satellites can be included or excluded, and each GNSS satellite can be tailored to accurately model block dependent signals, signal power levels, and even unique transmit gain patterns for different frequency bands.

This makes it possible to easily scale the simulation by adding or removing GNSS satellites (for example to compare GPS only results to GPS and Galileo), signals (for example to compare L1 vs. L2 with realistic relative signal strengths) or antennas (for example adding several receiving antennas to a single HEO satellite to compare different antenna orientations). The detailed parameters chosen to populate the simulation are explained in the following sections, along with the link budget calculations.

3.2.2 User Spacecraft

Given the end goal of studying relative positioning for formation flying satellites in highly elliptical orbits, the European Space Agency's PROBA-3 mission has been used throughout this thesis as the test case. Basing the simulations on a real mission adds realism to the study and generates more interest than a purely hypothetical case.

Table 3-1 summarizes the assumed orbital elements, which are based off of Llorente et al. (2013) and the same as those used for the study by Ardaens et al. (2012). For the time of ephemeris, which is not specified in any of the references, a date near in time to the simulation is always chosen. The evolution of the orbit over time, which occurs at a rate of $\dot{\omega} = 10.3$ degrees/year for the argument of perigee and $\dot{\Omega} = -32.5$ degrees/year for the right ascension of the ascending node due to the Earth's oblateness, has been neglected given the simulation period of 1-2 days. In the visibility simulation, simple Keplerian motion is assumed for the user spacecraft.

Table 3-1: HEO Orbital Parameters

Element	Value	Units
a	37039887	metres
e	0.80620521	
i	59	degrees
ω	187	degrees
Ω	142	degrees
ν	0	degrees

Figure 3-1 depicts the relative geometry of the assumed PROBA-3 orbit, Earth, and GPS constellation in Earth centred inertial coordinates from a vantage point above the North Pole. In this case the GPS constellation was defined by two line ephemerides (TLEs) from April 26th, 2012. From the figure it can be seen that the PROBA-3 orbit falls between two GPS orbital planes.

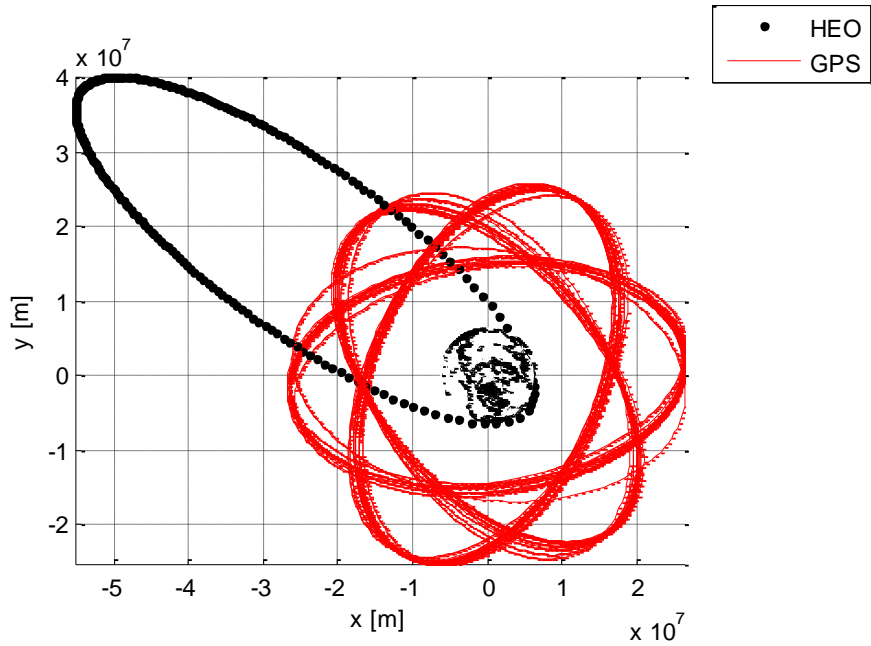


Figure 3-1: Relative geometry of the PROBA-3 orbital plane, GPS orbital planes, and the Earth, as viewed from a point above the North Pole

3.2.3 Orbits and Coordinate Systems

Orbit information for the various GNSS satellites is not consistently available in any one format, in particular because one goal of the visibility simulation was the inclusion of the SBAS satellites. Additionally, in the early stages of this research project very few satellites from the newer GNSS systems had actually been launched, and even preliminary services were not yet available. As a starting point, two line element sets (TLEs) were therefore used as the basis for the orbits of the GNSS satellites. While they are not extremely accurate (on the same order of magnitude as an almanac), TLEs are readily available for all GNSS satellites on the Celestrak website (Kelso 2000) in a single consistent format. Two line elements for five “constellations” of GNSS satellites are available for inclusion in the simulator: GPS, GLONASS, Galileo, BeiDou and SBAS. For the practical reason that QZSS is included in the SBAS two line element file available from the Celestrak website, it has for the time being been included as an SBAS system in spite of the fundamental technology differences. Indian IRNSS was excluded due to the absence of an ICD and the earlier stage of development of this system at the time the visibility simulation was created.

To supplement the real TLE data, a tool was written to read in a file of TLEs for a partial constellation, for example Galileo, and using it as the starting point to generate TLEs for a full Walker constellation (Walker 1984).

The working coordinate system of the visibility simulation is the two line elements' TEME (True Equator Mean Equinox) system, which is an inertial coordinate system. There are, however, two approximations, first that the position of the sun used for determining the HEO satellite attitude is calculated using the equation for the approximate solar position in the J2000 inertial frame, and second that the orbit of the HEO satellite is defined by a set of Kepler elements. Neither of these approximations makes an impact on the relatively coarse visibility simulation results.

3.2.4 GNSS Constellations and Signals

As previously mentioned, six sources of satellite navigation signals were considered in this study: GPS, GLONASS, Galileo, BeiDou, QZSS and SBAS. In addition to the orbit information contained in the two line elements, the simulated GNSS satellites have been populated with constellation specific antennas and signals. The level of realism in the assumptions differs dramatically from constellation to constellation, and to begin with only the GPS, Galileo and GLONASS satellites could be populated. This was due to the difficulty in finding up-to-date and complete information for BeiDou and for the various SBAS systems. In particular, the unique design of each SBAS/QZSS satellite, and the higher altitudes of both SBAS and some BeiDou satellites, made it impossible to assume they had similar transmit antenna patterns to the other GNSS.

The GNSS satellites were defined using information primarily from the GPS ICD (ICD-GPS-200C IRNs 12345, IS-GPS-200E, IS-GPS-705B, IS-GPS-800B), the Galileo ICD (OD-SIS-ICD Issue 1.1), and the GLONASS ICD and modernization information (Russian Institute of Space Device Engineering 2008, Stupak 2010, Revnivykh 2011), the BeiDou test ICD and relevant literature at the time the simulation was set up (BeiDou-SIS-ICD-Test, Hauschild et al 2012) , and the QZSS ICD at the time the simulation was set up (IS-QZSS V1.4). The GNSS constellations were defined such that the differences between blocks and signals could be taken into account, using the information summarized in Appendix A.

While the software is, for the most part, capable of populating the distinct blocks realistically, no algorithm or look up table was ultimately implemented capable of determining which block a particular GNSS satellite belongs to. Given the different methods of identifying unique GNSS satellites for the different constellations and the possibility that at some point it will be desirable to use almanacs or broadcast ephemerides to define the GNSS constellations rather than TLEs, this task is non-trivial. Instead, each constellation has been given a default set of signals and antennas. All GPS satellites use the GPS III signals/strengths, all Galileo and GIOVE satellites use the Galileo signals/strengths, and all GLONASS satellites use the block M (open FDMA) signals/strengths.

The design of the GNSS satellites, in terms of transmitting antenna gain pattern and equivalent isotropically radiated power (EIRP), makes a very significant difference in the signal strength at a given point in space, and therefore in the number of trackable GNSS satellites. The assumed gain patterns are depicted in Figure 3-2.

The GPS pattern is an average of the four orientations of the Czopek pattern (Czopek and Schollenberger, 1993), which was found to agree well with all other alternatives found in literature (Ebinuma and Unwin, 2007; Ericson et al., 2010; Fisher and Ghassemi, 1999; Moreau et al., 2002). The GAGAN pattern was presented by Jyoti et al. (2005), the centre of the QZSS pattern by Noda et al. (2010) and a WAAS prototype by Iriarte et al. (2009). The Galileo patterns for both 1.575 GHz (L1/E1) and 1.237 GHz (low band, E5 and E6) were obtained from (Montesano et al 2005).

For lack of better information, the GLONASS and BeiDou MEO patterns were assumed to be the same as GPS with the side lobes removed. Based on the resemblances in the partial patterns in the GPS and GLONASS ICDs, this approach should give reasonable if pessimistic results because it ignores the possibility that side lobes might exist. An extensive search yielded no publicly available GLONASS specific pattern; however, discussion with the GLONASS representatives at ION GNSS 2012 revealed that the GLONASS ICD signal levels apply up to 2000 km above ground level.

The WAAS prototype is used for all SBAS systems not otherwise specified, and the QZSS profile was assumed for the BeiDou IGSO/GEO satellites. Although there is known to be strong azimuth dependence in the GNSS patterns, insufficient information was available to adequately model it, and instead all gain patterns were assumed to be rotationally symmetric. Block dependence in the gain was also ignored in all cases except to differentiate MEO and geosynchronous satellites for BeiDou. All GNSS satellites were set up such that the transmit antennas were pointing to nadir.

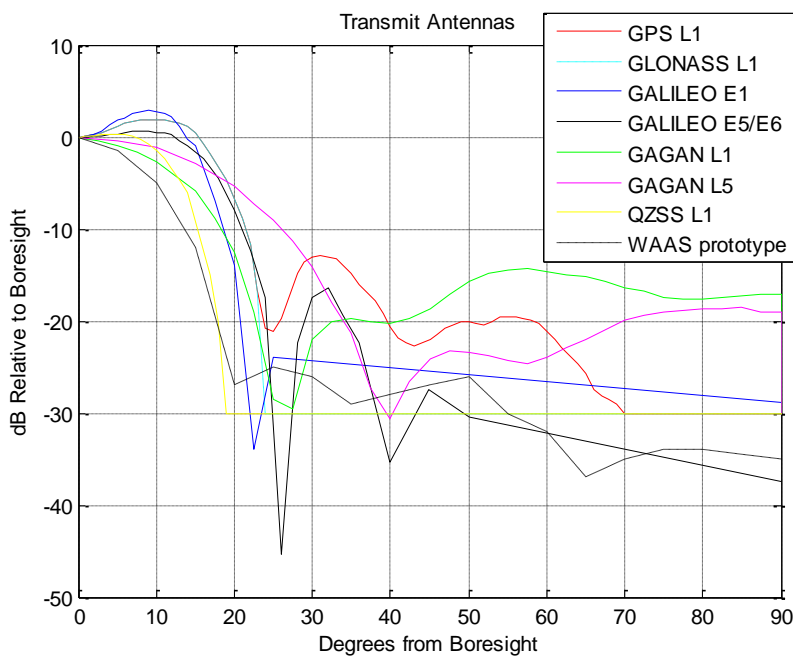


Figure 3-2: Assumed transmission gain patterns for the GNSS systems

The EIRP values were back-calculated from the minimum received signal powers for a user on the Earth and a GNSS satellite at 5 degree elevation (specified in the systems' ICD's and summarized in Appendix A), the transmission gain patterns of Figure 3-2, an assumed atmospheric loss of 2 dB on the Earth, and a free space path loss calculated based on the nominal orbital altitudes of the GNSS constellations, following the example for GPS in Kaplan and Hegarty (2006).

The signal power at an arbitrary point in the HEO orbit can then be calculated as in Eq. 3-1.

$$C(dBW) = EIRP(dBW) + G_{Tx}(dB) + L_{atm}(dB) + L_{path}(dB)$$

Eq. 3-1

where C is the signal power, EIRP is as discussed above, G_{Tx} is the transmit antenna gain in the direction of the point as defined in Figure 3-2, L_{atm} is the atmospheric loss assumed to be zero, and L_{path} is the free space path loss. To compensate the assumption that atmospheric loss is zero in HEO, a 500 km mask of the Earth was added to exclude signals passing through the peak ionosphere and the dense atmosphere near the Earth's surface. Atmospheric bending has consequently also been neglected in the visibility simulations.

L_{path} is both range and frequency dependent, and is calculated in dB as shown in Eq. 3-2, where λ is the signal's wavelength and ρ is the geometric length of the path (Moreau 2001). The result is a negative value.

$$L_{path} = 20 \log_{10} \left(\frac{\lambda}{4\pi\rho} \right)$$

Eq. 3-2

3.2.5 GNSS Receiver Parameters

The choice of GNSS receiver has an impact on all aspects of the study. The behaviour of a particular receiver is determined by the front end and the acquisition and tracking loop algorithms, which are built on many minor design decisions and which may be unique to particular signals. These determine not only which signals and systems may be tracked, but also whether the receiver is able to acquire and track a signal with a given received power. There are therefore an uncountable number of implicit assumptions built into any simulation of this type.

For the purposes of this study, the receiver behaviour has been modelled by two numbers, the acquisition threshold and the tracking threshold. All signals at or above the acquisition threshold are assumed to be instantaneously acquired, and it is assumed that lock is maintained until the

signal drops below the tracking threshold. No consideration has been given to the time required for acquisition because it is expected to be on the order of a few minutes, insignificant given the orbital period of a HEO satellite and the corresponding simulation time step of 5 minutes.

The equation used to translate signal power at the receiving antenna to the carrier to noise density ratio, C/N_0 , is Eq. 3-3 below.

$$C/N_0(\text{dBHz}) = C(\text{dBW}) + G_{Rx}(\text{dB}) - (K_B(\text{dBW / KHz}) + T_{sys}(\text{dBK}))$$

Eq. 3-3

C is the signal strength at the receiving antenna as defined in the previous section, G_{Rx} is the receiving antenna gain in the direction of the GNSS satellite as defined in Figure 3-4, K_B is Boltzmann's constant, and T_{sys} is the system noise temperature.

The T_{sys} value is the sum of the sky/antenna temperature, T_{sky} , and the receiver noise temperature. The receiver noise temperature derives from a reference temperature T_0 as well as the noise figures, NF , losses, L , and gains, G , of the receiver front end. The equation for T_{sys} is Eq. 3-4 below (van Dierendonck, 1996).

$$T_{sys} = T_{sky} + T_0 [L_1 - 1 + L_1[NF_1 - 1 + G_1^{-1}[L_2 - 1...]]]$$

Eq. 3-4

A “typical” value for T_{sys} of 207.1 K, or equivalently 23.2 dB-K, based on calculations in Lachapelle (2009) has been used. This results in reasonable peak C/N_0 values, on the order of 53 dB-Hz for a 3 dB RHCP hemispheric antenna on the Earth’s surface, as shown in Figure 3-3. In Lachapelle (2009) the reference temperature is assumed to be 290 K, as in van Dierendonck (1996). However, according to the HEO specific link budget computations in Moreau (2001), which use slightly different equations, it appears that T_{sky} is neglected altogether and the reference temperature T_0 ranges from 180 K to 290 K depending on the antenna pointing direction. The difference in the two equations is on the order of 2 dB Hz, which is well within

the level of uncertainty of the GNSS transmit gain patterns, but again highlights the extent to which the results should be taken in context.

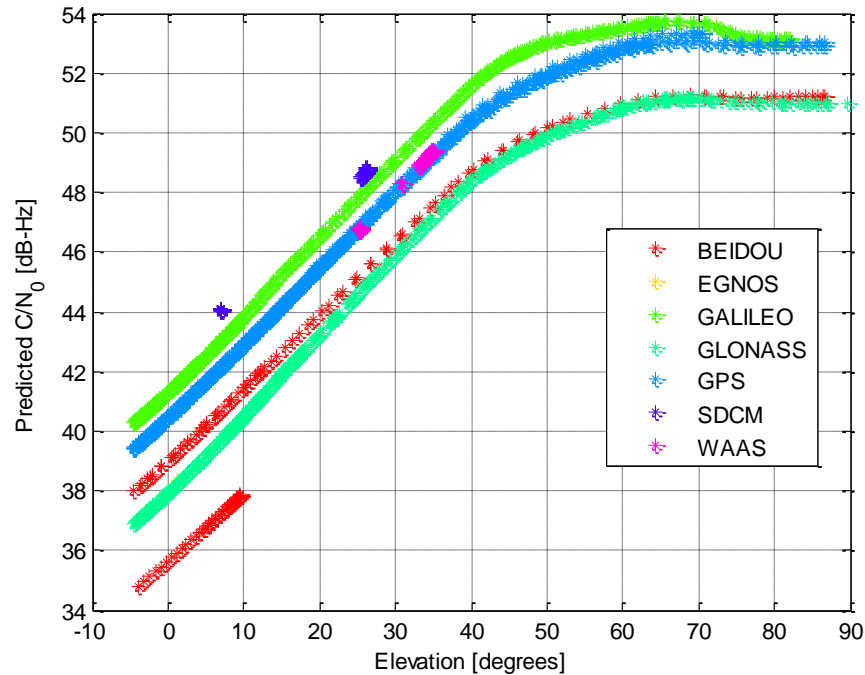


Figure 3-3: Simulated signal power for a static receiver in Calgary, Canada

Finally, the receiving antenna was assumed to be hemispheric, with the gain pattern of Figure 3-4, a hard cut off 85 degrees from bore sight, and a 3 dB peak gain.

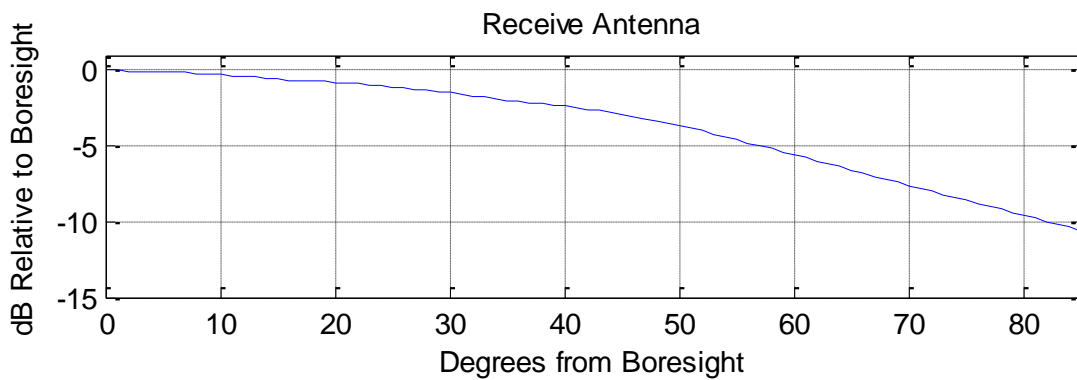


Figure 3-4: Receiving Antenna Gain Pattern

3.3 Simulation Verification

The initial test of the software was to compare it to the visibility simulation tool (VisSim) written by DLR's Space Flight Technology group at the German Space Operations Centre for a study on the suitability of GPS for the PROBA-3 mission (DLR/GSOC 2012). One significant difference exists, which is that the GPS Yuma almanacs have been used in VisSim, while TLEs have been used in the simulation tool described here. TLEs and almanacs from the same day as the simulation were used to minimize propagation differences. All other differences, such as the link budget computation, step size, atmospheric mask, use of GPS L1 only etc. were synchronized for the best possible comparison.

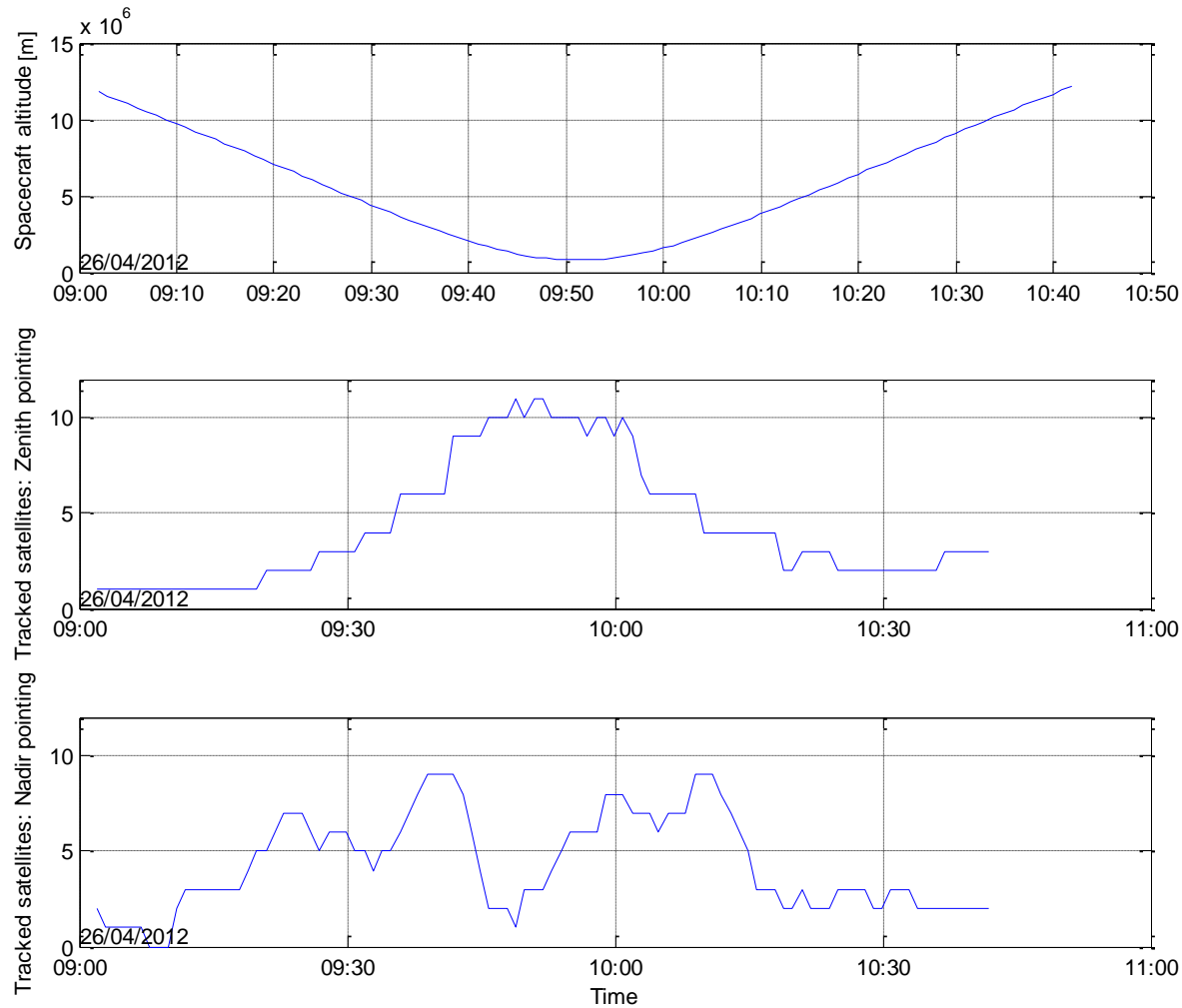


Figure 3-5: VisSim Output for the Nominal Test Case

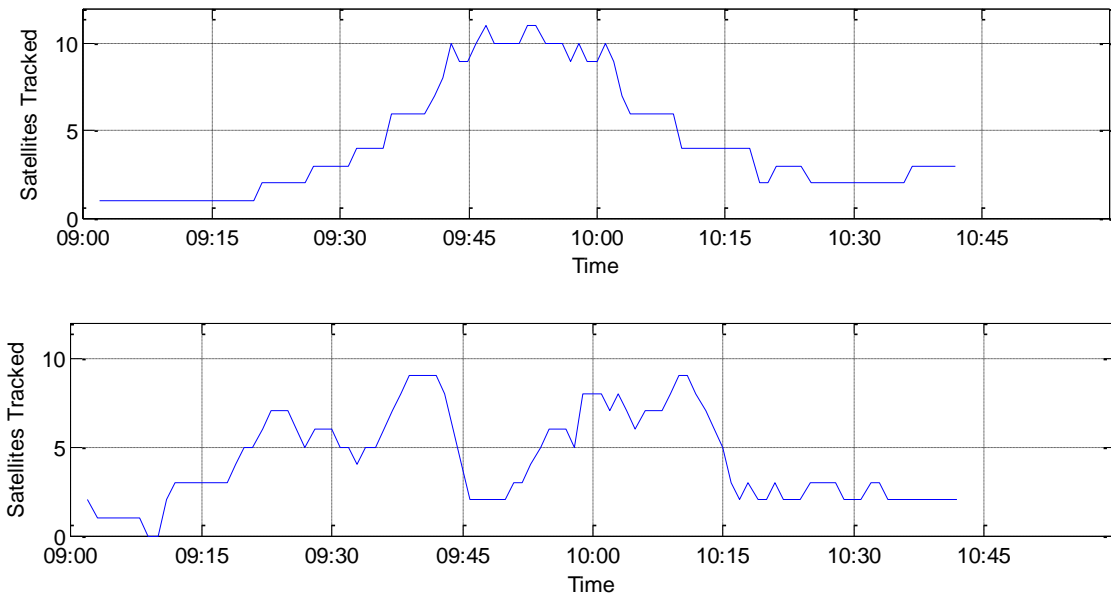


Figure 3-6: Zenith and Nadir Pointing Output from the Simulation Tool

The results differ by at most one satellite for individual epochs, which can be explained by the different sources of GNSS position information. Otherwise the two independent implementations agree closely and demonstrate that no major inconsistencies exist between the simulation tools. Note that these results are not truly zenith and nadir pointing, but as close as possible given the constraint on the PROBA-3 mission that one satellite axis is sun-pointing.

3.4 GNSS Antenna Orientation Study

Because every mission has constraints on the spacecraft attitude resulting from critical factors such as solar panel orientation, thermal considerations, and payload orientation, no general study has been conducted to determine the ideal case for GNSS antenna accommodation and pointing direction on a satellite in highly elliptical orbit. While it is fairly obvious that a GNSS antenna should point upward when the user satellite is in relatively close proximity to the Earth's surface in LEO, or that it should point downward to see the maximum number of GNSS signals when the receiver is above the GNSS satellites, the ideal case during a HEO satellite's transition between the two is less clear. The goal of this study is to systematically determine the optimal antenna pointing direction for a PROBA-3 type mission throughout the orbit.

The antenna pointing study has been carried out in three parts. The first part determines the optimal pointing direction given no constraints on the user spacecraft attitude, and the second part repeats the study with the constraint that one face of the satellite is sun pointing. The third part of the study implements a more detailed check of the results by calculating the mean duration over which GNSS satellites can be tracked.

3.4.1 Part 1: Unconstrained Antenna Placement

The antenna study was conducted by simulating a user spacecraft in the PROBA-3 type orbit described in section 3.2.2. Only GPS was considered, and the constellation was defined using the published NORAD two line element sets for August 17th, 2011. The receiver was further given an acquisition and tracking threshold of 35 dB Hz, with all GNSS satellites at lower C/N₀ being excluded.

The spacecraft was then given an array of receiving antennas with different pointing directions, and at each antenna, at each epoch of the simulation, the visible GNSS constellation was calculated. Finally, at each epoch the optimal antenna was selected based on three criteria:

- Highest number of satellites tracked
- If multiple antennas tracked the same number of GNSS satellites, and more than four GNSS satellites were tracked, the lowest PDOP
- If either less than four GNSS satellites were tracked or multiple antennas had the same PDOP, the highest average C/N₀

For this first part of the study, a radial, in-track, cross-track (RIC) attitude profile was assumed for the PROBA-3 spacecraft. This profile consisted of the first axis aligned with the radial direction, the second axis perpendicular to the radial vector and aligned roughly in-track, and the third axis aligned with orbit normal. The PROBA-3 satellite was populated with 36 receiving antennas pointing 10 degrees apart in a wheel configuration, to test one degree of freedom at a time. Three simulations were run, to test for the ideal pitch angle, yaw angle, and roll angle of the antenna.

Figure 3-7 to Figure 3-9 show the results of the analysis in the RIC frame. In each plot the three different marker styles indicate three consecutive perigee passages. The level of agreement between the three sets of markers indicates the consistency of the results under different GPS constellations.

The angles along the y axis in each figure indicate the pointing directions of the antennas. In Figure 3-7 a rotation in pitch was tested, with the angle measured from the in-track direction (0 degrees), positive towards zenith (90 degrees). In Figure 3-8 a rotation in yaw was tested, with angles measured from in-track (0 degrees), positive towards orbit normal (90 degrees). In Figure 3-9 a rotation in roll was tested, with the angle measured from orbit normal (0 degrees), positive toward zenith (90 degrees). For comparison, a corresponding time series showing the altitude of the PROBA-3 satellite relative to the GPS satellites and the main lobe of the GPS transmit antennas is shown in Figure 3-10.

There is a very clear pattern in the optimal antenna orientation in Figure 3-7 and Figure 3-9, with good agreement between the three perigee passages. A nadir pointing antenna is preferred above an orbital radius of approximately 1.5×10^7 m or time to perigee of 0.5 hours, below which the antenna should ideally be rotated at a uniform rate until it is zenith pointing exactly at perigee and returns to nadir pointing as the HEO satellite again crosses above 1.5×10^7 m. This trend is visible by the cross patterns in Figure 3-7 and Figure 3-9 extending 0.5 hours on either side of the perigee passage.

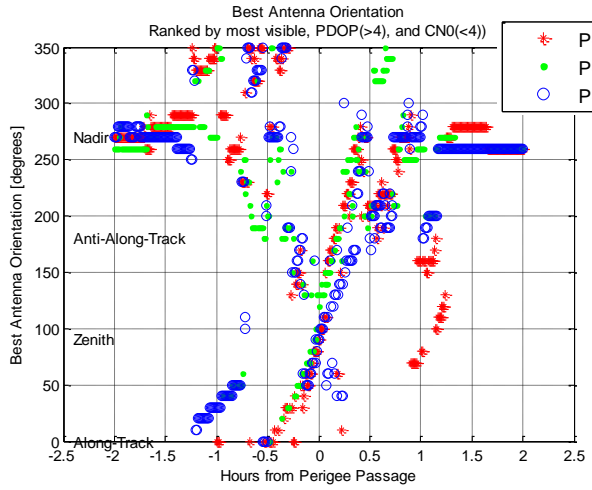


Figure 3-7: Preferred antenna orientation in the orbital plane (pitch angle)

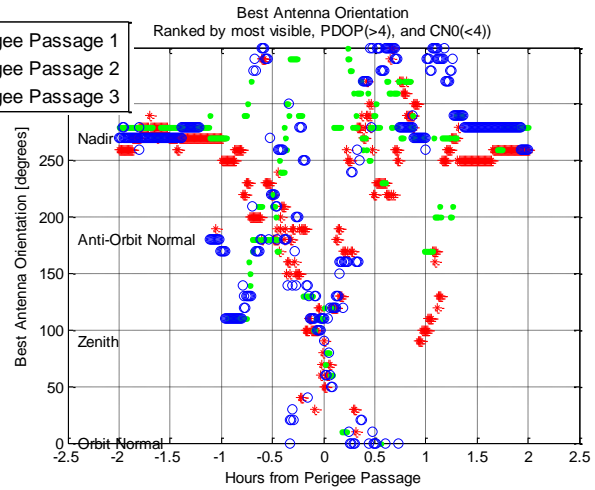


Figure 3-9: Preferred antenna orientation in the plane perpendicular to motion (roll angle)

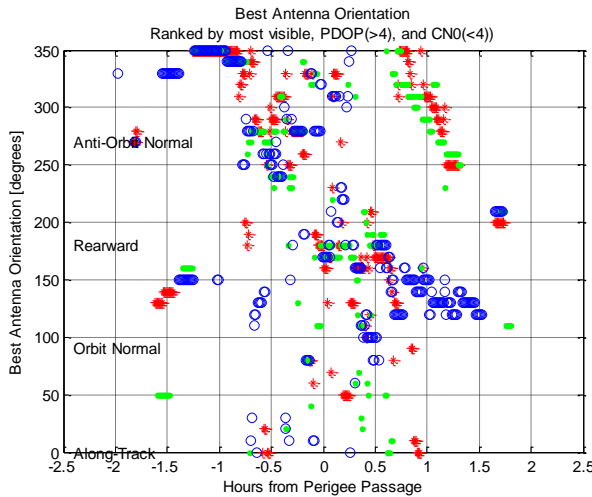


Figure 3-8: Preferred antenna orientation in the horizon plane (yaw angle)

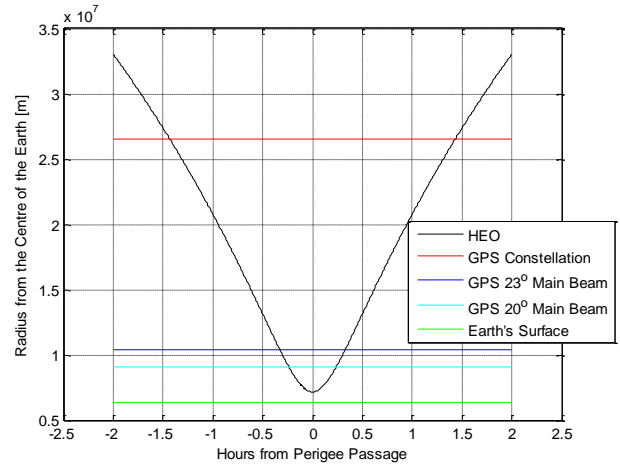


Figure 3-10: HEO satellite altitude corresponding to Figure 3-7 - Figure 3-9

Intuitively, for a satellite in LEO the antenna should always be zenith pointing, so it is a surprising result that the antenna on a HEO satellite should only point to zenith for a single epoch. In order to better understand the results, the same test was applied while changing the perigee height. Based on the perigee height results (not shown) the ideal pointing profile was simplified to the three rules in Table 3-2. The boundary values are $R_1 = 1.5 \times 10^7$ m and $R_2 = 8.5 \times 10^6$ m, and have been determined empirically.

Table 3-2: Antenna Pointing Profile

Satellite Radius	Ideal Boresight Elevation Angle
radius > R ₁	-90°
R ₂ < radius < R ₁	180°/(R ₁ – R ₂) * ((R ₁ + R ₂)/2-radius)
radius < R ₂	90°

Note that in the transition region between nadir and zenith pointing this table only specifies an ideal elevation to which the antenna should point, but no yaw angle. From Figure 3-8 it can be seen that without zenith or nadir pointing as options, the optimal direction is well scattered across the full range of possible yaw angles. It can be concluded that in terms of number of tracked satellites, geometry and power there is no clear best pointing direction in the HEO satellite's horizon plane.

These results do not take into account the length of the tracking arcs on individual GPS satellites, which are certainly impacted by a rotation of the antenna pointing direction in yaw. Tracking arc length is an important consideration because longer uninterrupted tracking arcs are desirable for carrier phase positioning in order to maintain a constant phase ambiguity. It is investigated in more detail in section 3.4.3.

The antenna pointing profile as determined in this part of the study is depicted in Figure 3-11, where the region in blue is the ambiguous transition from zenith to nadir.

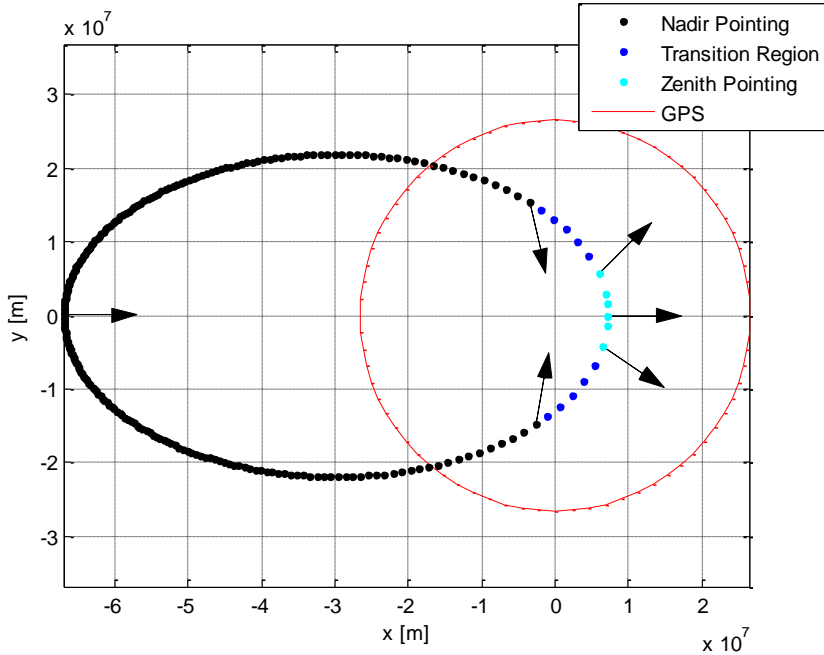


Figure 3-11: Best antenna pointing profile based on number of visible GPS satellites

3.4.2 Part 2: Sun-Pointing Constraint

For the second part of the study a sun-pointing profile was used. This profile consisted of one axis always pointing sunward, one axis aligned as close to zenith/nadir as possible while respecting the sun-pointing constraint, and one axis completing the orthogonal coordinate frame. In this case the HEO satellite was defined as having 38 receiving antennas, in order to simultaneously compute the visible constellation from a sun-pointing antenna, an anti-sun pointing antenna and antennas spaced every 10 degrees in the plane perpendicular to the satellite-sun vector.

Tests using TLEs from August 17th, 2011, November 17th, 2011, February 17th, 2012, April 1st, 2012 and May 17th, 2012 were conducted for the sun-pointing case to understand the dependence of the results on the seasonal change in the sun's position relative to the orbit.

The test was carried out for August 20th, 2011 (sun at apogee, Figure 3-12), November 17th, 2011 (sun anti-orbit-normal, Figure 3-13), February 16th, 2012 (sun at perigee,

Figure 3-14), and May 13th, 2012 (sun orbit-normal, Figure 3-15), to highlight seasonal dependencies caused by the changing position of the sun relative to the orbital plane. Points between these critical dates (October 1st, January 1st, April 1st and July 1st) were also tested, and the results for April 1st, 2012, which are representative of all four cases, have been included in Figure 3-16. Note in the figures the sun's distance from the Earth is not to scale, and merely indicates the direction of the vector to the sun.

In the following figures 0 degrees is normal to the sun-Earth-satellite plane, and 90 degrees is as close as possible to zenith given the sun-pointing constraint. For convenience the anti-sun-pointing and sun-pointing antennas have been plotted on the same axes, and are -10 degrees and -20 degrees respectively, as labeled in the figures.

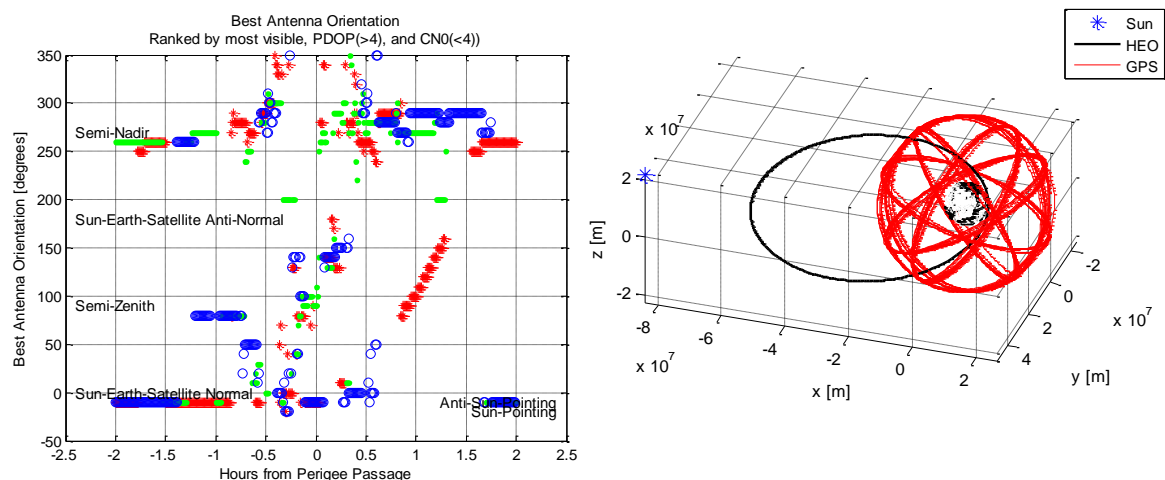


Figure 3-12: Optimal antenna pointing with the sun at apogee, August 20th, 2011

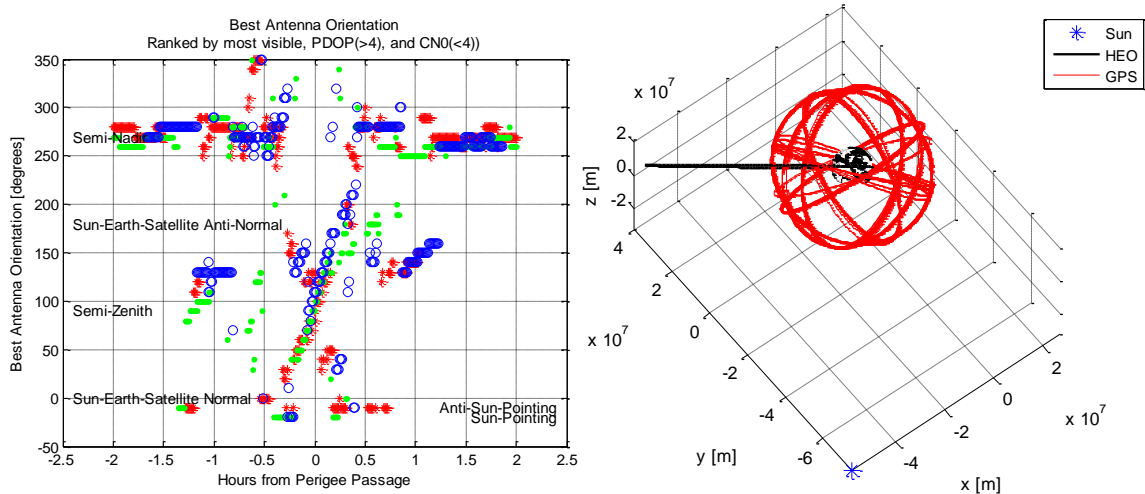


Figure 3-13: Optimal antenna pointing with the sun at anti-orbit normal, November 17th, 2011

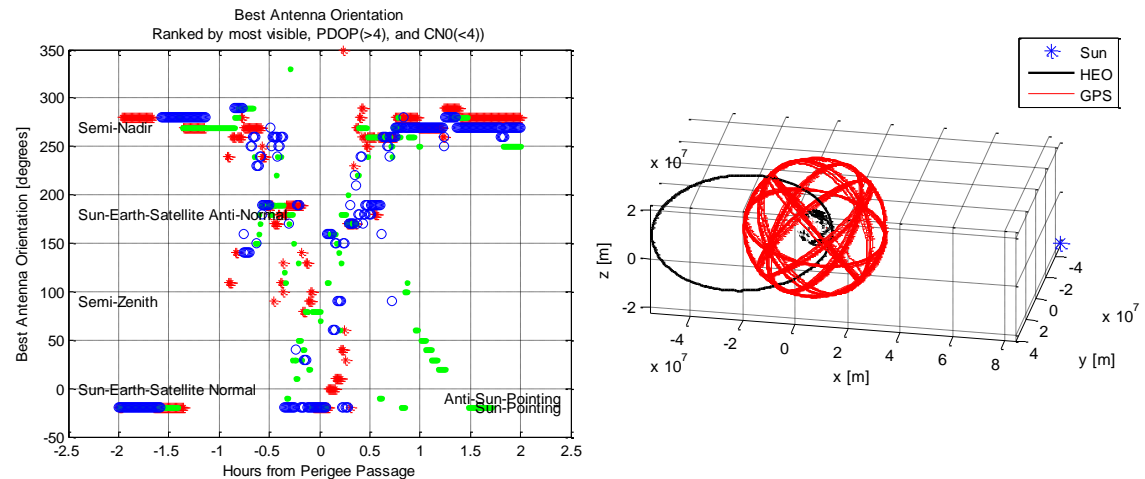


Figure 3-14: Optimal antenna pointing with the sun at perigee, February 16th, 2012

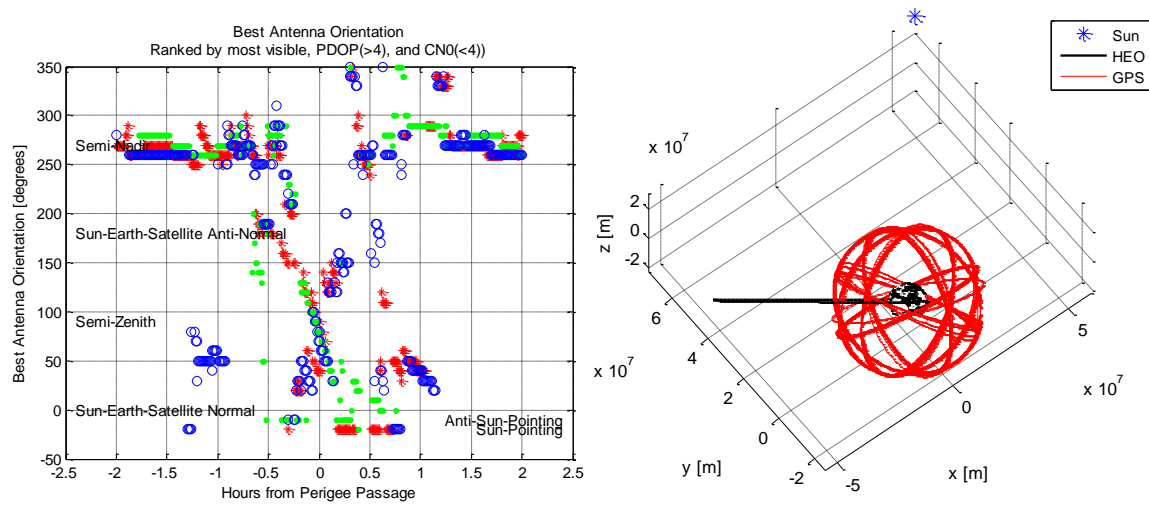


Figure 3-15: Optimal antenna pointing with the sun at orbit normal, May 13th, 2012

From the seasonally dependent plots it can be interpreted that the optimal profile of part 1 still holds. For the cases where the sun is at perigee (Figure 3-14) or apogee (Figure 3-12) this is particularly apparent, as the sun-pointing or anti-sun-pointing antennas are almost perfectly aligned with the zenith/nadir directions. When the sun is normal to the orbital plane the results closely resemble those of Figure 3-7, with an antenna rotation in the orbital plane being preferred.

At times of the year between these critical dates the best results are also obtained when the antenna is able to follow some profile resembling the unconstrained results, as depicted in Figure 3-16.

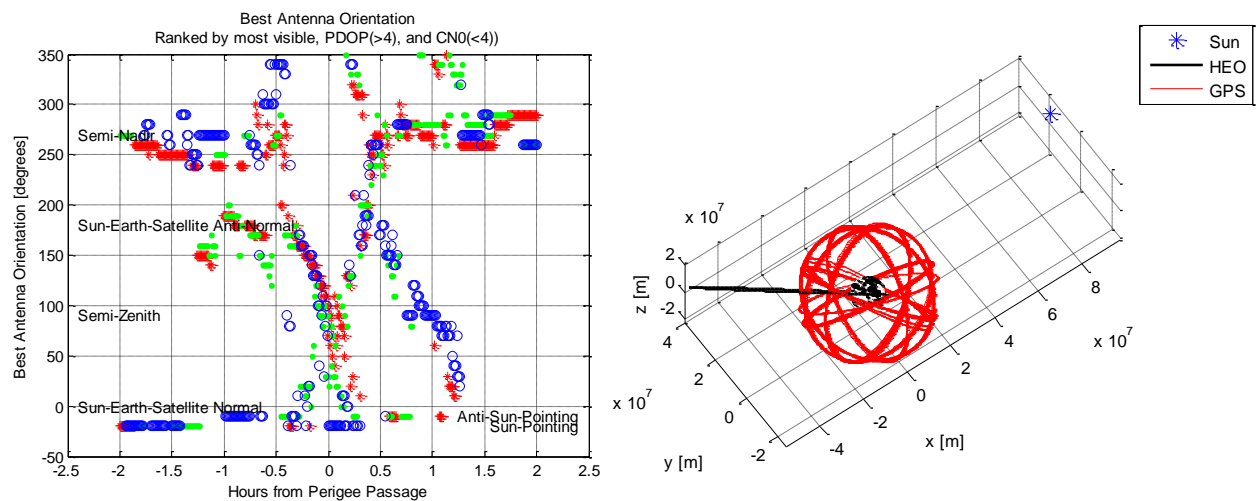


Figure 3-16: Optimal antenna pointing with sun pointing constraint, April 1st 2012

For a spacecraft with a sun-pointing constraint placing the antenna on a face of the spacecraft that is free to rotate about the satellite-sun vector allows for the best results, because there is more flexibility to actively change the antenna orientation to follow the GNSS constellation. This result would not hold for a sun-synchronous orbit with the line of apsides aligned with the satellite-sun vector.

3.4.3 Part 3: Optimal Transition from Nadir to Zenith

This part of the study investigates in further detail the ideal yaw angle for the GPS antenna while it transitions between zenith and nadir. The metric used to evaluate the options was the mean tracking arc duration for all satellites tracked through the perigee passage by a particular antenna. The statistics are calculated for GPS satellites tracked beginning two hours before perigee and extending two hours after perigee. A receiver tracking threshold of 25 dB-Hz and an acquisition threshold of 35 dB-Hz were assumed. All satellites in view at carrier to noise density ratios equal to or greater than 35 dB-Hz are assumed to be instantly acquired, and loss of lock is assumed as soon as the C/N₀ drops below 25 dB-Hz.

The GPS antenna pointing direction for this part of the study has been defined by two angles, an elevation angle and a yaw angle. The elevation angle was set using the empirical rule from the first part of the study, in Table 3-2. Two possible yaw angle profiles were tested. First a constant yaw angle of 0 °, +/-45 °, +/-90 °, +/-135 ° or 180 ° measured from the in-track axis were tested, such that for a cross track transition the antenna transitioned to and from zenith on the same side of the HEO satellite. Next, complementary sets of yaw angles were tested, for example 0° as the HEO satellite approaches perigee and 180° as it departs, for a continuous rotation in the same direction.

Results of the tracking arc duration are given in Table 3-3, where both the total number of tracked GPS satellites, mean tracking duration and mean duration that GPS satellite were acquirable (visible above 35 dB-Hz) are shown. The table contains the mean result of 14 unique perigee passages under different GPS constellations, simulated from August 20th to 31st, 2011.

It can be seen from the table that rotations to and from zenith with the same yaw angle had similar results for all yaw angles, with tracking arc durations on the order of 43 minutes and acquisition arcs of 23 minutes. From this it can be concluded that a cross-track rotation offers no notable benefit. There was, however, a clear advantage when complementary yaw angles in the orbital plane, (0 degrees approaching perigee and 180 degrees departing perigee) were used, with a mean tracking arc of 52 minutes and mean acquisition window of 28 minutes. Less unique GPS

satellites are tracked, which is in keeping with the earlier result that all yaw angles have a roughly equal number of visible satellites at each epoch. The optimal combination is highlighted in yellow.

Table 3-3: Tracking Arc Duration at Perigee

yaw angle [degrees]		number tracked	mean tracking arc duration [minutes]	mean acquirable duration [minutes]
approach	depart			
0	0	36	42	24
45	45	37	42	23
90	90	38	42	23
135	135	37	42	23
180	180	35	45	24
-135	-135	35	45	24
-90	-90	38	42	23
-45	-45	38	41	23
0	180	31	52	28
45	-135	31	50	27
90	-90	37	43	22
135	-45	41	37	20
180	0	41	37	21
-135	45	41	38	21
-90	90	38	41	23
-45	135	34	47	26

Due to the similarity of the optimal profile with an inertial pointing antenna, a comparison was made. The antenna pointing direction in the inertial case was along the line of apsides towards the perigee, such that it would be nadir pointing at apogee and zenith pointing at perigee. Figure 3-17 illustrates the difference between the inertial pointing profile and optimal GPS profiles

during a perigee passage, Table 3-4 compares the tracking arc and acquisition duration of the two profiles, and Figure 3-18 shows the number of tracked satellites for the two profiles for a full orbit, beginning and ending at perigee.

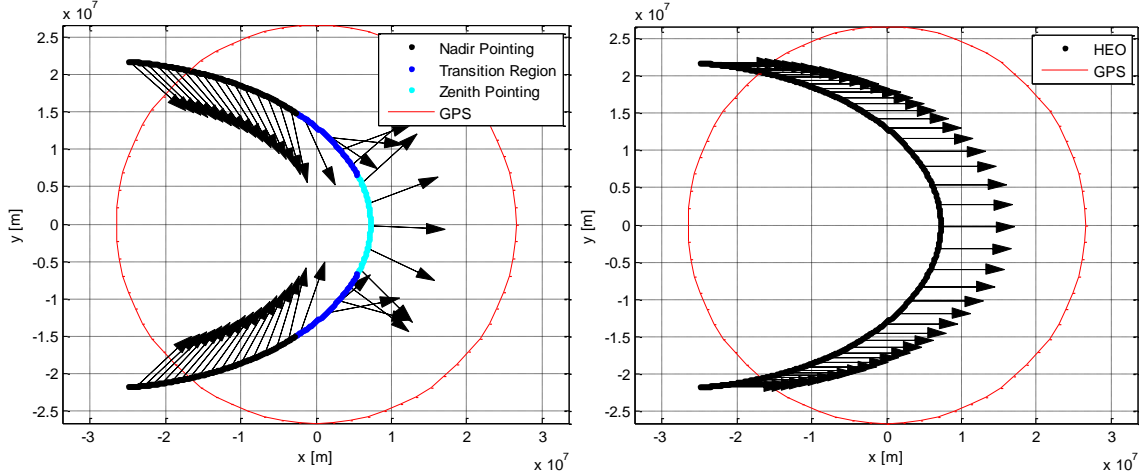


Figure 3-17: Optimal GPS (left) versus inertial (right) antenna pointing directions

Table 3-4: Optimal versus inertial tracking arc lengths

Pointing Profile	number tracked	mean tracking arc duration [minutes]	mean acquirable duration [minutes]
Optimal GPS	31	52	28
Inertial towards Perigee	20	64	42

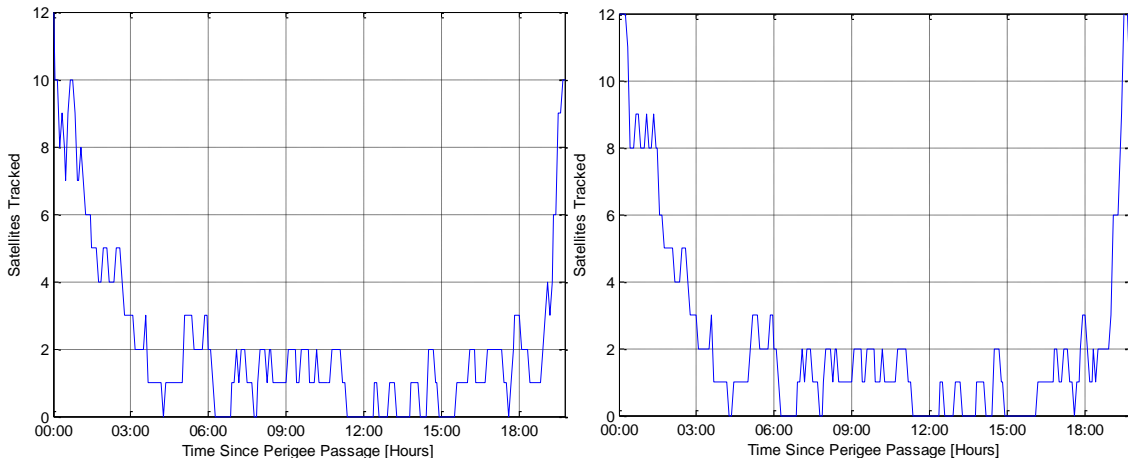


Figure 3-18: Optimal (left) versus inertial (right) number of tracked satellites

The tracking arc lengths for the inertial case indicate a significant advantage, with an average tracking duration of 64 minutes rather than 52 under the same GPS constellations. The comparison of the number of tracked satellites over a single perigee passage shows significant differences in the periods from 00:00-5:00 hours and 16:00-19:45 hours, but neither case is obviously better than the other, with the optimal GPS case performing better from 4:00 to 5:00 and 15:00 to 17:00, and the inertial case performing better during the perigee passage.

3.4.4 Conclusions

The ideal GPS antenna pointing direction for a PROBA-3 type HEO, neglecting the sun constraint, is inertial pointing with the antenna bore sight aligned with the line of apsides and pointing towards perigee. This attitude profile allows for the longest tracking arcs on individual GPS satellites through the perigee passage, and maintains the GPS constellation within the antenna's field of view at high altitudes.

The best antenna attitude for the sun pointing case is the attitude most closely aligned with the optimal inertial pointing direction. For the majority of the year, this is an antenna located on a side of the spacecraft perpendicular to the sun-pointing face, because it has the freedom to rotate 360 degrees and align as closely as possible with the line of apsides. For the critical times of the year when the sun is aligned with the orbit's perigee or apogee, an antenna on the sun-pointing face or anti-sun pointing face, respectively, is best.

3.5 Multi-Constellation GNSS

Beyond the attitude profile study, several other open areas of research remained to be answered by the visibility simulation. For example, it was clear that a standard, commercial GNSS receiver would not be suitable for use in HEO, but was it better to design a specialized receiver for multi-constellation GNSS, or one that would focus on weak signal tracking? How significant was the influence of lowering a receiver's acquisition threshold, versus its tracking threshold? Similarly,

if future missions discovered that the GNSS signals beyond the Earth’s limb were in fact weaker than previously thought, or stronger, how would that impact the entire problem? Which constellations, and more specifically which of the new signal structures, were more or less advantageous for the high dynamics and weak signals of HEO? And how did the number of visible satellites differ for a constellation in three orbital planes, such as GLONASS or Galileo, as opposed to the GPS constellation’s six orbital planes? What, if any, benefit would the new geostationary navigation satellites from the regional systems offer? This section seeks to answer these questions, and interprets the results in the context of both a formation flying mission and of a single receiver in space.

3.5.1 Simulation assumptions

The multi-constellation GNSS studies use the same PROBA-3 Orbit as introduced in section 3.2.2, but unlike the attitude study consider the results in the context of both absolute and relative positioning.

In carrying out the research two attitude profiles were assumed. The first is the “ideal” inertial profile from the previous study. The second attitude profile is a sun-pointing profile, in keeping with the PROBA-3 mission requirements. It makes the assumption that the GNSS antenna is on a face orthogonal to the sun pointing vector, and is therefore able to freely rotate about the sun vector such that the antenna bore sight is as closely aligned with the ideal profile as possible.

The sun pointing profile introduces a time of year dependence into the results, with two optimal dates in mid-May and mid-November when the sun vector is normal to the orbital plane and the sun-pointing profile reduces to the ideal profile, and two critical dates in mid-February and mid-August when the sun is aligned with perigee and apogee respectively, and the antenna is forced to point perpendicular to the ideal case.

When interpreting the results in the context of a formation flying missions, the overarching assumption is that the formation flying spacecraft share nearly identical attitude profiles, and therefore all visible GNSS satellites are commonly visible to all receivers in the formation.

The positions of the GNSS satellites have all been computed from two line element sets (TLEs) for January 14 and 15, 2013, and the simulations were carried out for same dates for a realistic alignment of the GNSS satellites. Only GNSS satellites that were launched and operational in January 2013 have therefore been simulated. The exception is the Galileo constellation, in which case the TLEs of the existing four satellites were used as the starting point and modified to obtain TLEs for a full 27 satellite Walker constellation.

Unless otherwise stated, the results presented in this study were generated assuming a common acquisition threshold for all signals and constellations of $C/N_0 = 33$ dB Hz and a tracking threshold of $C/N_0 = 25$ dB Hz.

As a final note, it should be mentioned that in spite of the efforts made to model them, transmission gain patterns and EIRP remain significant sources of uncertainty in any study of this type. As was proven by the Chang'E-5T and MMS mission performance years after this simulation was set up, some of the assumption made here are extremely conservative, at least for GPS and GLONASS, and with a high sensitivity receiver far more GNSS satellites are visible than predicted. While the exact results in terms of numbers of visible satellites should therefore not be taken out of context, the conclusions drawn from the comparisons of different simulator runs are still considered entirely valid, and they are important because they are the basis for many of the design decisions in the coming chapters of this thesis.

3.5.2 Results

Although a considerable number of cases have been tested in the simulation, a small subset of the results are presented which highlight the potential benefits of multiple MEO constellations, new signal structures, and regional systems.

3.5.2.1 Multiple MEO Constellations

For kinematic positioning, the number of unknowns using a single GNSS system is four, regardless of whether it is single point or relative kinematic positioning. Three of these unknowns are the 3D (relative) position components, and the fourth is the (relative) time offset.

The time offset is of particular importance for relative positioning, because it allows the measurements from multiple receivers to be synchronized. At orbital velocity even a slight timing difference can lead to a large error in relative position. For example, 1 millisecond in the PROBA-3 orbit translates to an along track error of 1 metre at apogee or 11 metres at perigee. It is therefore a minimum requirement of kinematic positioning to simultaneously track four common GNSS satellites. More GNSS satellites well distributed in the sky provide more accurate positioning.

The left hand plot in Figure 3-19 depicts an example of the GPS only visibility from a highly elliptical PROBA-3 type orbit over one period, beginning and ending at perigee. The minimum kinematic positioning conditions are only met during the perigee passage at the beginning and end of the plot. However, knowledge of the orbital dynamics can also be used to supplement the GNSS measurements, so that even a single common GNSS satellite can be used to provide information about the relative clock offset. The timing accuracy in this case is only as good as the knowledge of the orbital position, where, given the GNSS signals are travelling at the speed of light, each 30 cm of position error along the signals line of sight equates to 1 ns of timing error. Additional measurements provide an update to the relative position estimate.

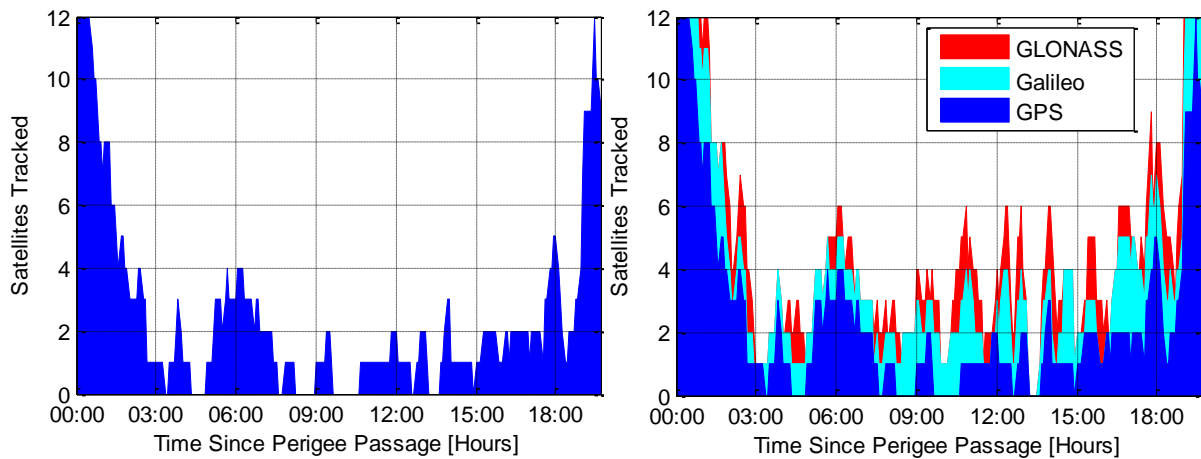


Figure 3-19: Benefit of positioning with multiple MEO GNSS constellations

The right hand plot in Figure 3-19 depicts the advantage of using three GNSS systems simultaneously. In this case an additional unknown is added for each new GNSS system, to account for inter-system timing biases caused by both signal-dependent receiver hardware delays

and the different realizations of UTC that each system is referenced to. In spite of the additional unknowns, there is a clear advantage in terms of the number of tracked satellites using multiple GNSS systems. Take for example the spike in visibility 11 hours past perigee, when two GLONASS and three Galileo satellites are visible in addition to the one GPS satellite, briefly providing the necessary six measurements for resolution of the relative time, two inter-system biases, and three relative positioning coordinates. These visibility results are highly dependent on the input assumptions about the alignment of the orbital planes, about the antenna pointing profile, and about the formation flying orbit, as shown by the following results.

Tests using different right ascension of the ascending node values for the formation flying orbit revealed a strong dependence on the alignment of the apogee with the GNSS orbital planes, which evolves over time. The best results in terms of number of tracked satellites are obtained when a GNSS orbital plane is grazing the Earth from the perspective of the above the constellation user. The impact of orbital plane alignment is therefore more pronounced for Galileo and GLONASS with three orbital planes, as opposed to GPS with six. These results are illustrated in Figure 3-20 and Figure 3-21, which for each 5 degree increment in orbital plane alignment summarize the portion of the orbit where >4, 3, 2, 1 or no measurements were visible for GPS and Galileo respectively.

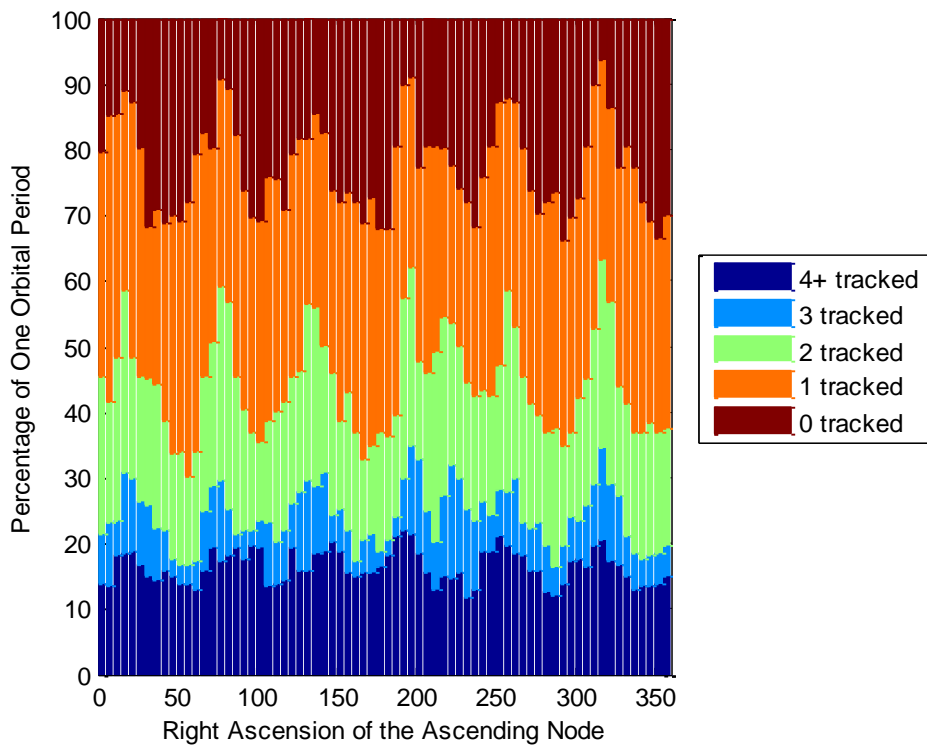


Figure 3-20: Impact of orbital plane alignment on GPS visibility with an inertial attitude profile

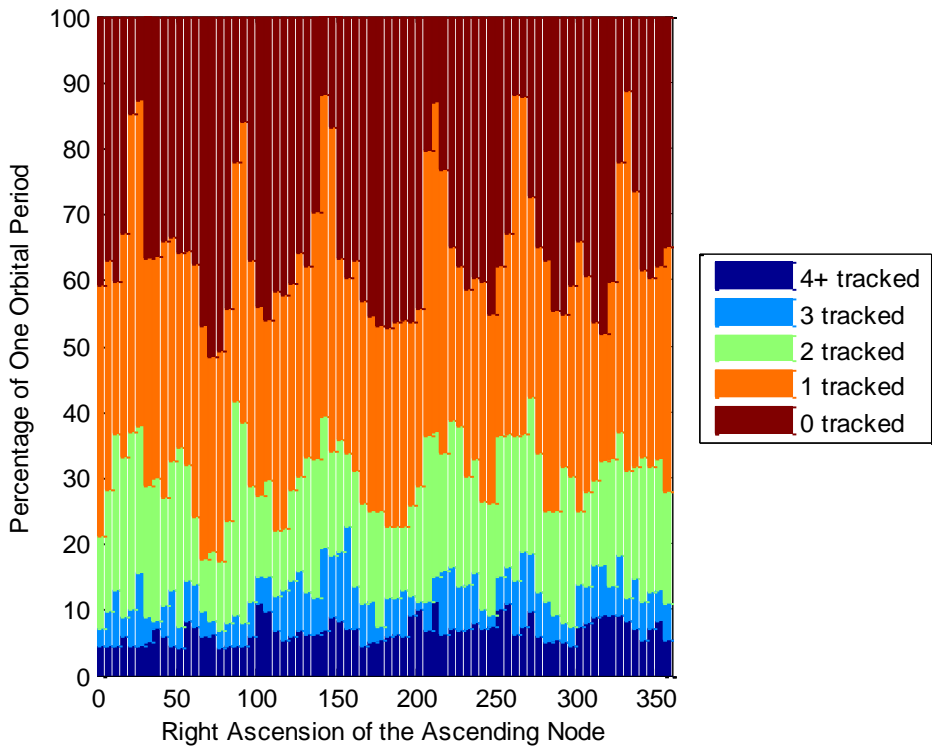


Figure 3-21: Impact of orbital plane alignment on Galileo visibility with an inertial attitude profile

Tests with the sun-pointing profile around critical dates revealed that no satellites from any GNSS system are visible for several hours at apogee. The impact of the sun pointing constraint is illustrated in Figure 3-22, which similar to the previous figures was generated by changing the orientation of the PROBA-3 type orbit in 5 degree increments under the GPS constellation and sun position of January 15, 2013. The critical alignments occur at right ascensions of 150 degrees and 330 degrees, when only the 30% of the orbit near perigee has any GNSS coverage. These GPS only results are representative for all the GNSS constellations, although in the case of GLONASS where no side lobes were simulated only the 10% of the orbit near perigee has GNSS coverage.

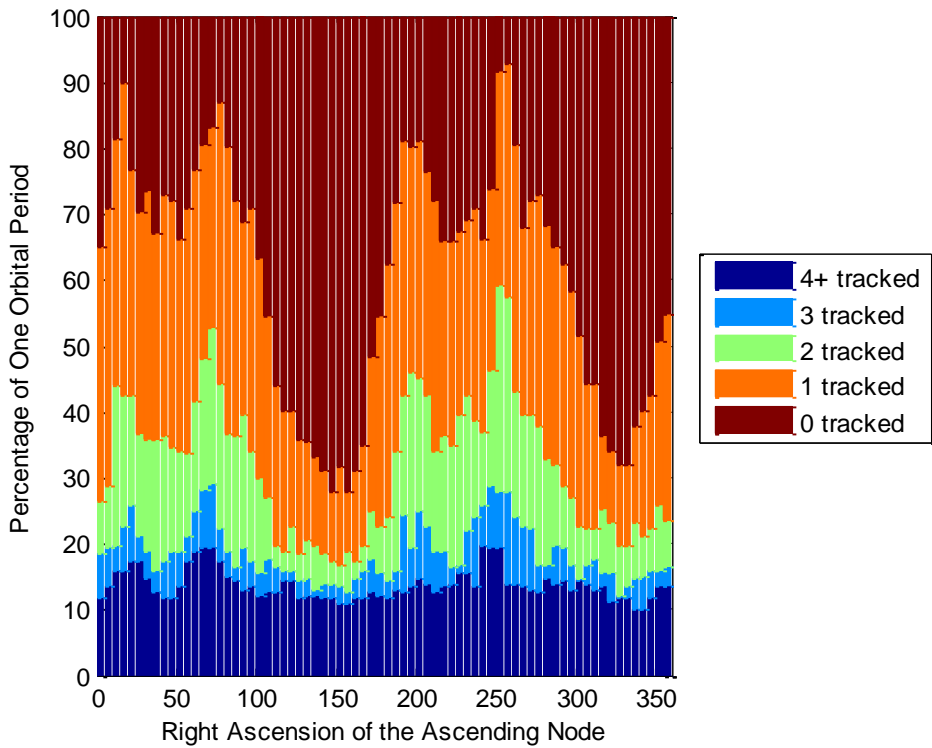


Figure 3-22: Impact of orbital plane alignment on GPS visibility with a sun constraint on the attitude profile

Finally a similar test conducted by replacing the PROBA-3 orbit with a Molniya user orbit, illustrated in Figure 3-23, demonstrated improved MEO visibility. This is because more GNSS orbital planes are grazing the Earth from the Molniya satellite point of view and because the Molniya orbit is lower, both of which mean GNSS signals are strong enough to track. The results were generated using a TLE for Molniya 3-53, which has a 12 hour orbital period and an inclination of 64 degrees, and an eccentricity of 0.75, with the apogee passage occurring over the Northern Hemisphere.

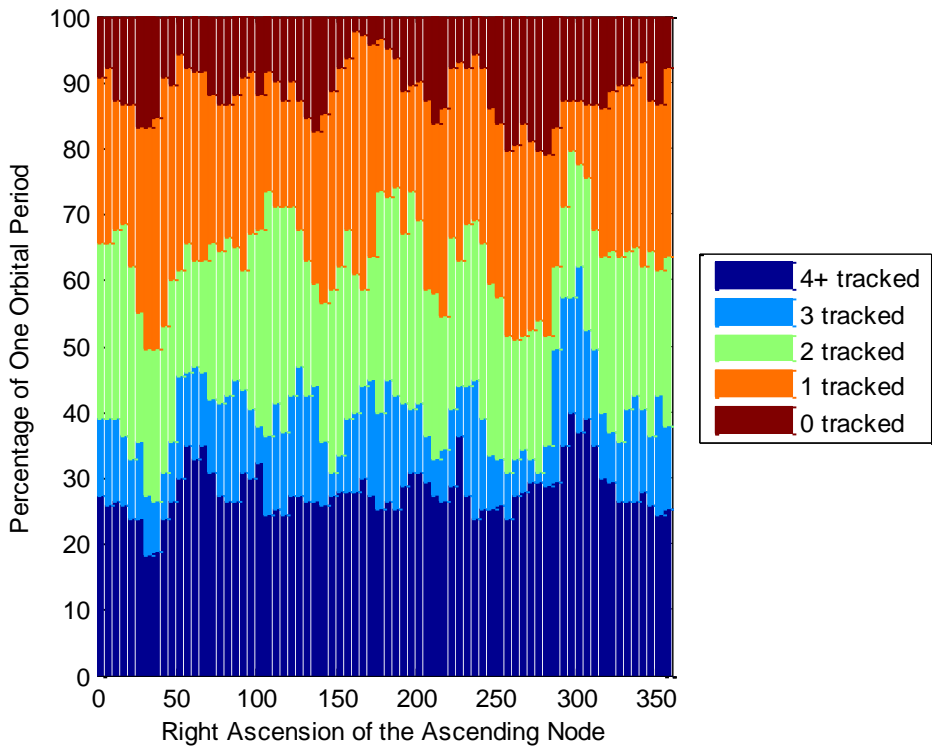


Figure 3-23: Impact of orbital plane alignment on GPS visibility from a Molniya orbit

3.5.2.2 Impact of New Signal Structures

The additional GNSS systems and modernized GNSS signals also offer advantages for weak tracking. In particular, many of the new signals have data and pilot components, which on one hand make for a higher combined signal strength, and on the other hand allow for improved weak tracking on the pilot signal because there are no unknown data bit transitions to interrupt tracking. Figure 3-24 shows the visibility of the Galileo E1 data/pilot signal based on tracking thresholds of 28 dB-Hz for normal tracking vs. 20 dB-Hz for a tracking algorithm taking advantage of the data/pilot signal structure. The tracking thresholds are based on Julien (2005).

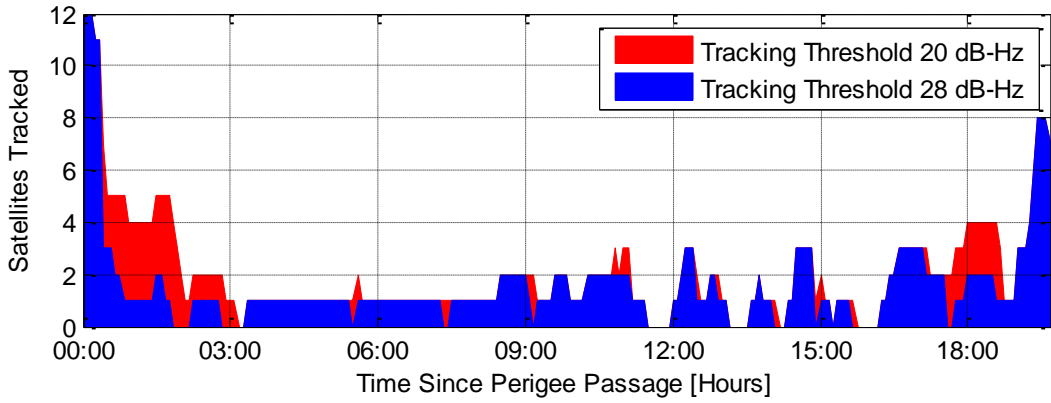


Figure 3-24: Impact of a 20 dB-Hz vs. 28 dB-Hz tracking threshold on visibility

The decreased tracking threshold has clear advantages, in particular for maintaining lock on side lobes of the GNSS signals when leaving or approaching perigee. At higher altitudes, the tracking arcs are extended by 5-10 minutes, bridging gaps and providing some overlap in tracked satellites for example in the period from 4 to 8 hours past perigee.

Other simulation parameters can be modified to achieve similar results. Lowering the acquisition threshold extends the tracking arcs as well, by allowing signal to be acquired earlier. Changing the assumed transmit pattern for the GNSS satellites can likewise increase or decrease the chances of acquiring side lobes and maintaining lock, as can raising or lowering the assumed EIRP or the receiver noise temperature. The sensitivity of the results to the input assumptions highlights the limited reliability of any study of this type, but also clearly demonstrates that investing in weak tracking is worthwhile as a means of mitigating the impact of unknown GNSS visibility.

3.5.2.3 Regional Systems

Neither QZSS nor the SBAS systems appear to have been considered for HEO positioning in previous studies, and until recently the BeiDou system suffered from a severe lack of publicly available information which made any sort of visibility assessment difficult. There are however several reasons these satellites are worth investigating.

First, they stand to provide a substantial improvement in geometry for a HEO satellite approaching or leaving perigee, when the GNSS satellites in MEO are only visible near the Earth's limb but the SBAS/QZSS/BeiDou GEO/IGSO satellites are potentially still visible overhead. Second, they are characterized by a potentially higher transmit power focused into a narrower beam to compensate for their higher orbits. While the higher transmit power could be an advantage for tracking over the Earth's limb assuming a wide enough beam, it may also add to the "near-far" jamming problem. These factors are illustrated in Figure 3-25, which compares the visibility regions for the GPS, WAAS and GAGAN antenna patterns. The SDCM antennas additionally may be pointed 7 degrees northward for better coverage of the Russian territory, which also increases the amount of spill-over beyond the Earth (Karutin 2014). Finally, the QZSS and SBAS satellites enjoy excellent compatibility with GPS in terms of the signal structures, which are identical for QZSS and nearly identical with a higher data rate for SBAS.

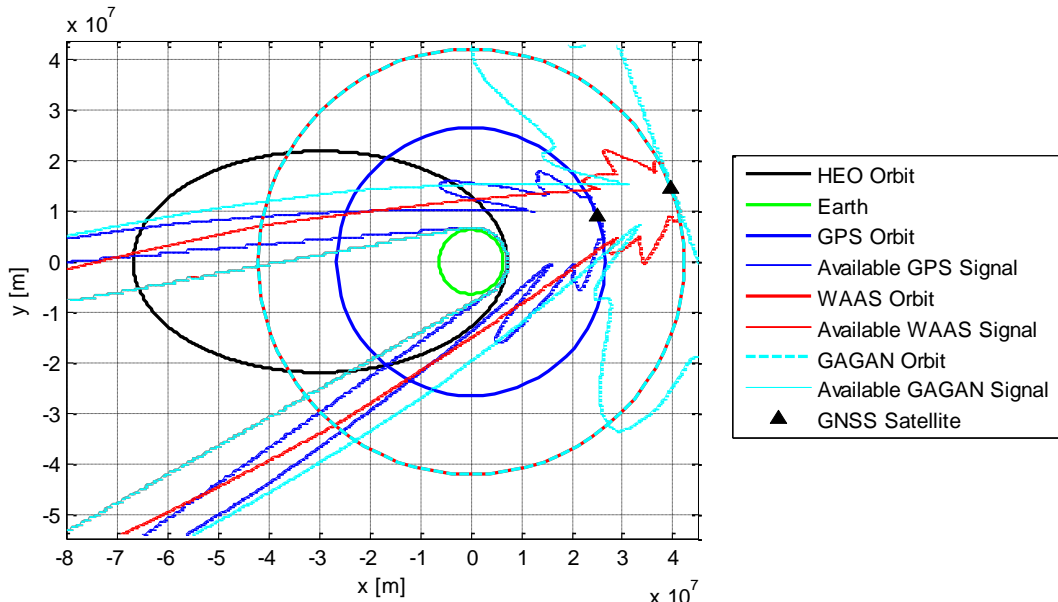


Figure 3-25: Comparison of the GPS, WAAS and GAGAN visibility regions

The potential disadvantages are that the intersystem biases are not well documented and may be substantial for a user so far outside the intended SBAS coverage regions. SBAS use a "bent pipe" approach rather than onboard atomic clocks, in which the signals are constantly monitored from the ground and adjusted to maintain accurate timing compared to GPS for a ground user in a specified coverage area (FAA/DoT 2008). Also, neither EGNOS nor SDCM is currently

transmitting sufficiently accurate orbit data for navigation, and in general the SBAS orbits and clocks may be substantially less accurate than GPS. Finally, input parameters used in the link budget calculations for these systems are particularly poorly known, so the results are only a rough first approximation of what might be possible.

Nevertheless, as depicted in Figure 3-26 the results show promise. Nearly constant single satellite coverage of the PROBA-3 orbit is achieved despite only one QZSS and 12 SBAS satellites being simulated, as compared to a 27 MEO satellite constellation. Occasional tracking of multiple satellites occurs, and the tracking arcs are longer than for the MEO satellites with less frequent loss of lock and acquisition. Because the SBAS satellites are typically in geostationary orbits along the equator, the coverage is particularly good for the PROBA-3 orbit but would be quite limited for a polar orbit. Note the other GNSS are excluded here to more clearly highlight the SBAS contribution, not because an SBAS only system is being suggested.

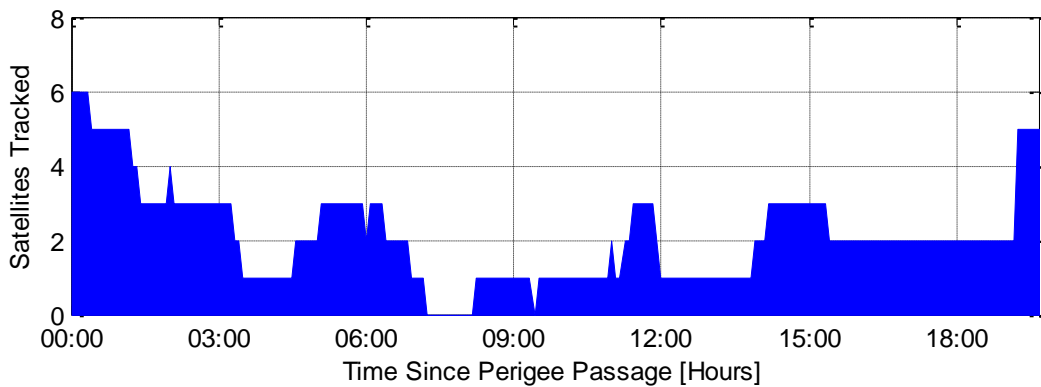


Figure 3-26: Combined SBAS and QZSS visibility

Even more interesting results are obtained for the regional BeiDou system, shown in Figure 3-27. Predictably, the visibility results vary dramatically depending on the alignment of the HEO and GNSS constellations. When the HEO apogee is opposite China (left) the visibility very nicely complements the MEO systems, with the best conditions occurring at or near apogee. On the contrary, when the apogee is over China (right) BeiDou contributes very little, with only brief tracking of the MEO satellites at apogee. While the time of day dependence reduces the usefulness of BeiDou for a 20 hour orbit, a properly aligned HEO mission with a 24 hour orbital period or a mission in geosynchronous orbit could experience a substantial benefit.

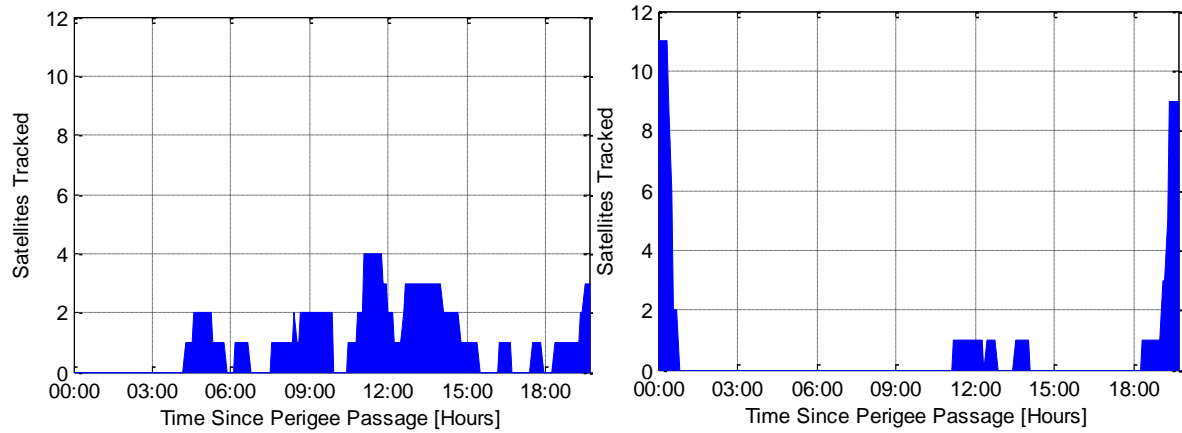


Figure 3-27: Visibility of the BeiDou regional system from HEO. Left: apogee opposite China, right: apogee over China

3.5.3 Conclusions

The combined visibility of the GNSS and SBAS systems is shown in a stacked bar plot in Figure 3-28, which highlights that there is beyond doubt benefit to be gained from using multiple GNSS constellations for relative positioning outside the GNSS service volumes. However, the GNSS signals present outside of the GNSS constellations are at the threshold of detectability for a typical receiver, with the result that small changes in input conditions can have a fairly drastic impact on simulation results.

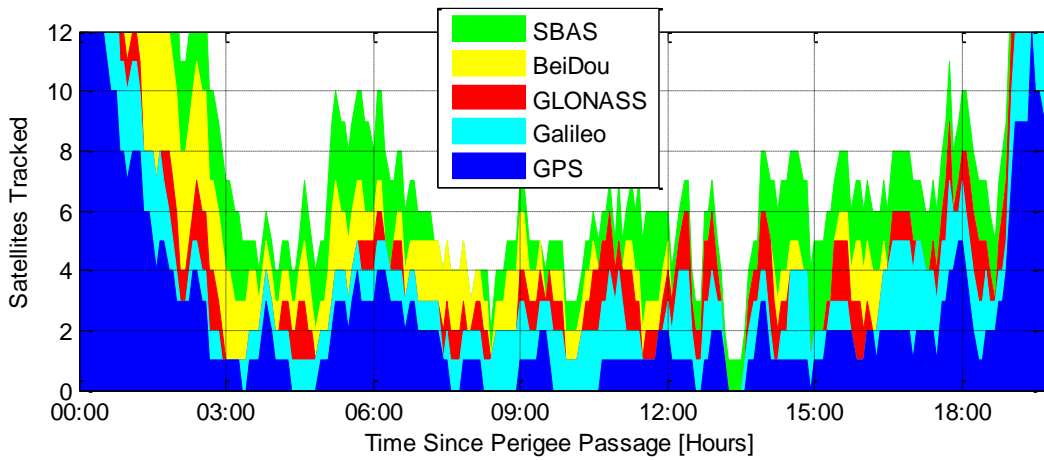


Figure 3-28: Combined visibility for GPS, Galileo, GLONASS, QZSS, BeiDou, WAAS, EGNOS, GAGAN, SDCM and MSAS on the PROBA-3 orbit

It can be concluded that the availability of signals from any of the GNSS systems is highly dependent on mission parameters such as the alignment of the GNSS systems with the HEO orbital plane, the receiver antenna orientation, and the HEO orbital period with respect to the GNSS orbital periods. Other factors such as acquisition speed, the minimum required signal power for acquisition and the minimum required signal power for tracking are equally influential, and are dependent on the receiver design. Further, the visibility is strongly affected by factors such as the alignment of the GNSS systems with respect to each other, which evolves over time and will depend on the epoch of a future HEO formation flying mission, or the transmission gain patterns of the GNSS satellites, which for most systems still have not been published on a sufficient level of detail for truly accurate results in 2017. For this reason, having the flexibility to track signals from all the constellations will best protect mission designers from the specific weaknesses of individual systems.

Because a small change in the mission design can potentially result in a drastic change in the availability of GNSS measurements, and because the unknown environmental factors have such a strong influence but cannot at present be accurately modelled, adapting the receiver design for weak signal tracking, and optimal performance at HEO dynamics is also worth the investment.

Chapter Four: An Analysis of SBAS Reception in Space

In addition to their use in highly elliptical orbits, there is a renewed interest in putting GNSS receivers on geostationary satellites. A driving reason is the crowding in the geostationary orbit, which is leading to tighter positioning requirements for station keeping (ESA Space Debris Office 2017, Johnson-Freese 2007). Additionally, an important reason for the revived interest in GNSS based HEO navigation is electric propulsion orbit transfer from LEO to GEO (Zin et al 2015). Autonomous GNSS navigation can help to reduce the costly ground infrastructure and operations during this time consuming mission phase.

In the previous chapter it was clearly demonstrated that regional systems stand to be valuable for above the constellation users, in particular for a user receiver in geostationary orbit which may have geostationary navigation satellites permanently in view over the Earth's limb. The SBAS satellites are a particularly attractive option as additional sources of ranging measurements, because their signals and navigation messages are designed for compatibility with GPS. The SBAS part of the visibility study in Chapter 3 was, however, severely limited in its accuracy by the absence of concrete information with which to populate the simulation. This chapter is therefore a departure from the main body of the research work, and presents an in depth analysis of the viability of using SBAS ranging for above the constellation applications.

There are currently five SBAS operating or under development: American WAAS, European EGNOS, Indian GAGAN, Russian SDCM and Japanese MSAS. The Japanese Quazi-Zenith Satellite System (QZSS) also transmits SBAS signals. Each system consists of two or three geostationary satellites, which broadcast clock, orbit and atmospheric corrections as well as integrity data to GPS users on the GPS L1 and, in the future L5, frequencies. Previous studies have assessed the use of SBAS transmitted corrections for space users in low Earth orbit, (Kim and Lee 2015, Kim and Kim 2015), but aside from a few studies assessing the measurement quality (Wanninger 2008, Rho and Langley 2008, Schempp et al 2008) and a preliminary study of the SBAS orbit determination capability (Pogorelc et al 1997) the ranging function of the SBAS satellites has largely been ignored.

Unlike GNSS, the SBAS satellites do not carry atomic clocks but are actively monitored and controlled by a network of ground stations, with their broadcast messages being generated on the ground and retransmitted to users from the satellites in a bent-pipe transponder design. The data rate is 250 bits/second, with two symbols per bit (Fortin et al 2014), which is ultimately ten times faster than GPS L1 C/A navigation data. With the exception of EGNOS (EGN-SDD SoL, V1.0) the SBAS also support ranging, which means that their measurements can be integrated into GPS positions solutions as additional GPS-like measurements. Each system provides corrections and integrity data valid in a limited country or region, but the end result is a fairly even global availability of SBAS ranging signals which are not service area specific. The locations of the SBAS satellites, based on NORAD two line elements from May 2015, are shown in Figure 4-1.

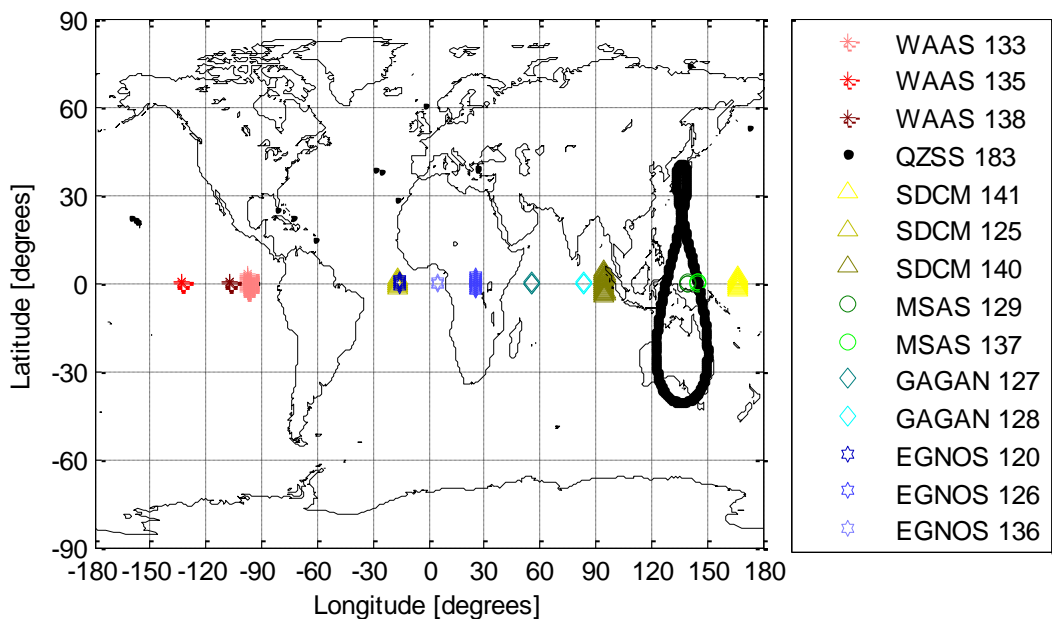


Figure 4-1: Distribution of SBAS satellites globally

Depending on its longitude, a geostationary satellite attempting to use GNSS for positioning could gain a significant benefit from tracking inter-visible SBAS satellites over the Earth's limb, because they are in the same orbital plane and would therefore be permanently in view. The benefit is demonstrated in Figure 4-2, which shows the number of visible GPS and SBAS satellites from a GEO satellite in a longitude slot of 60 degrees west, where both MSAS satellites are visible.

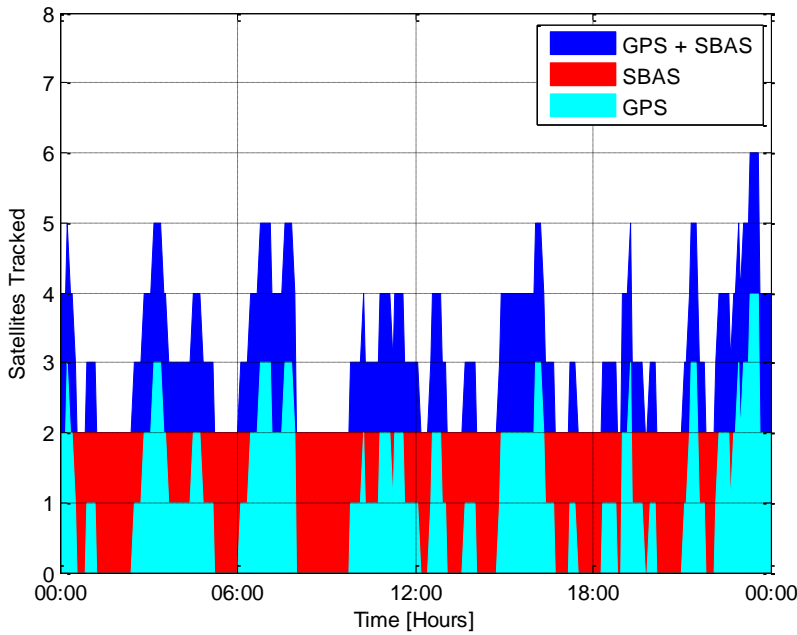


Figure 4-2: Theoretical visibility of GPS, SBAS, and both from GEO satellite at 60 degrees west, assuming a downward pointing hemispheric gain antenna, an acquisition threshold of 37 dB-Hz, a tracking threshold of 30 dB-Hz, and the WAAS prototype transmit gain pattern from Iriarte et al (2009) for all SBAS

However, for the SBAS satellites to be considered as a viable source of above the constellation positioning information, several important questions come up:

- Does their bent-pipe transponder design prevent a useable level of signal accuracy outside of their specified service areas?
- What do the transmit antenna gain patterns look like? Do they transmit directionally towards their service areas, or are they designed to maintain a constant power density over the Earth's surface by compensating for the Earth's curvature similar to the GPS antenna designs?
- Does any signal power spill over the Earth's limb? Is the spill-over concentrated over the northern hemisphere? Does it offer sufficient power for acquisition and tracking?
- Does the higher rate navigation data make acquisition or tracking from space more challenging?

The GPS payload onboard the CanX-2 CubeSat offered a unique opportunity to study the SBAS systems from low Earth orbit. Because SBAS satellites are geostationary, it is impossible to get a

uniform global comparison between the systems, particularly in terms of signal power, using GNSS monitoring stations on the Earth's surface. No two antenna and receiver combinations have exactly the same link budget, because of subtle differences in the antenna, LNA, cables, front end design and internal processing algorithms. A direct comparison of data collected with different user hardware is therefore unlikely to produce meaningful results. Additionally, studying SBAS signal power from fixed receivers on the Earth's surface has the disadvantage of fixed viewing geometry, with the SBAS satellite remaining at the same elevation in the receiver's field of view. Mapping the gain patterns from the Earth would therefore require a significant level of international cooperation, and even data coverage over the Earth's surface would be unlikely.

In contrast, CanX-2's low earth orbit allowed for a single unchanging receiver and antenna pair to circle the Earth, tracking arcs of SBAS data that are well distributed spatially, in order to consistently map the signal strengths of the SBAS navigation signals. It also allowed for an initial assessment of the ranging accuracy from a space borne receiver.

The remainder of this chapter has been divided into three main sections. Section 4.1 presents a brief overview of the CanX-2 mission, the hardware it carries, and the SBAS tracking experiment. Section 4.2 presents the transmit gain pattern study, and section 4.3 presents the achieved SBAS ranging accuracy on the Earth and in space. Finally, the conclusions about the suitability of SBAS as a source of positioning information above the GNSS constellations are presented in section 4.4.

4.1 The CanX-2 Mission and SBAS Experiment

CanX-2 is a three unit CubeSat measuring 35 x 10 x 10 cm. It was designed and built at the University of Toronto's Space Flight Laboratory, and launched into a near polar, 630 km orbit on April 28, 2008. Its orbit is sun-synchronous with a 9:30 AM descending node, and a 98° inclination (Sarda et al 2009).

CanX-2 carries a commercial, geodetic grade NovAtel OEM4-G2L dual frequency L1/L2 GPS receiver as a scientific payload. The antenna is a dual frequency AeroAntenna AT2775-103 patch antenna, with a roughly hemispheric gain pattern. While the GPS receiver and antenna were originally intended for a radio-occultation experiment, the design of the commercial receiver allowed for SBAS tracking functionality to be unlocked years after its launch. In September 2013, the receiver was therefore upgraded to an SBAS capable receiver, and the focus of the GPS experiment changed.

Two channels, previously dedicated to tracking L1 and L2 signals from a GPS satellite, were converted to SBAS L1 channels by applying a new software license code. At the time that the receiver's original firmware was released in 2004 only the American WAAS was formally supported, but thanks to a forward thinking design PRNs 120-139 are all defined in the receiver, making it possible to track WAAS, EGNOS, GAGAN, and MSAS satellites which all share an identical L1 signal and data structure. Unfortunately no SDCM data was collected prior to the end of the GPS payload operations in fall 2015.

While the receiver's performance on CanX-2 was already well documented prior to the SBAS capability being turned on, one important point to reiterate is that the GPS payload suffers from a lower than expected signal power level which was only diagnosed after launch (Kahr et al 2011). The result is that the reported carrier to noise density ratios are roughly 10 dB lower than would normally be expected for a geodetic grade receiver in the same setting, and the measurements experience a corresponding increase in noise, both of which impact the results of the current study.

Another aspect of the mission design which impacts the current study is the CubeSat's attitude determination and control system (ADCS). The satellite benefits from a system based on sun-sensors, magnetometers and a dynamics wheel. The long axis of the satellite is aligned with orbit normal, and the pitch angle about this axis can be actively controlled such that the GPS antenna, which is mounted on a face perpendicular to the rotation axis, can be pointed in any desired direction in the orbital plane. During GPS data collections the antenna was typically pointed

either to zenith or rearward, depending on the experiment goals. While the attitude control was previously accurate to 5 degrees (Sarda et al 2009), analysis shows that it degraded over CanX-2's first seven years in orbit. While the nominal attitude was still achieved some of the time, logged attitude data suggest that sudden rotations and drifts on the order of tens of degrees were occurring during this data collection campaign.

The GPS payload was operated on a rotating experiment schedule, and was limited to arcs of approximately 85 minutes in duration due to power, data volume and attitude control system constraints of the CubeSat. The result was that approximately every third month was dedicated to GPS experiments, with a few data sets collected each week during GPS data campaigns.

A total of 61 data takes demonstrating successful SBAS tracking were collected for this study. The majority were collected with a zenith pointing GPS antenna for more reliable tracking, while ten were collected with a rear pointing antenna in an attempt to better assess the signals tracked over the Earth's limb.

All of the fully operational WAAS, EGNOS, MSAS and GAGAN satellites were successfully tracked, as well as one of the newer EGNOS satellites, PRN 136. Several attempts were also made to track the Russian SDCM system's PRN 125 satellite (SDCM also consists of PRNs 140 and 141 which are outside of the NovAtel receiver's defined range), but SDCM was not yet fully operational (supported by Stupak 2015) and was not transmitting on the days in question. The Japanese QZSS system also transmits SBAS signals on PRNs not defined in CanX-2's receiver. Both SDCM and QZSS have therefore been excluded from the remainder of the study.

4.2 SBAS Signal Power

The first goal of the CanX-2 SBAS experiment was to map the transmit gain patterns of the SBAS satellites, which is of critical interest for potential users in GEO and HEO orbits. This section of the chapter attempts to shed light on the similarities or differences in the SBAS transmit patterns based on real tracking data from CanX-2, and compares the findings to the few gain patterns found in literature.

While CanX-2's low Earth orbit is not high enough to analyze the side-lobes of SBAS transmit gain patterns, it allows for an understanding of the centers of the gain patterns which are a good indication of how different the designs of the SBAS transmit antennas are. It also provides a first indication of whether tracking over the Earth's limb is possible. A sample map showing the tracking results for GAGAN PRN 127 is shown in Figure 4-3. Each line is a CanX-2 tracking arc, coloured based on the raw measured C/N_0 value reported by the receiver. The signal powers of the other active SBAS satellites have likewise been mapped from CanX-2's low Earth orbit.

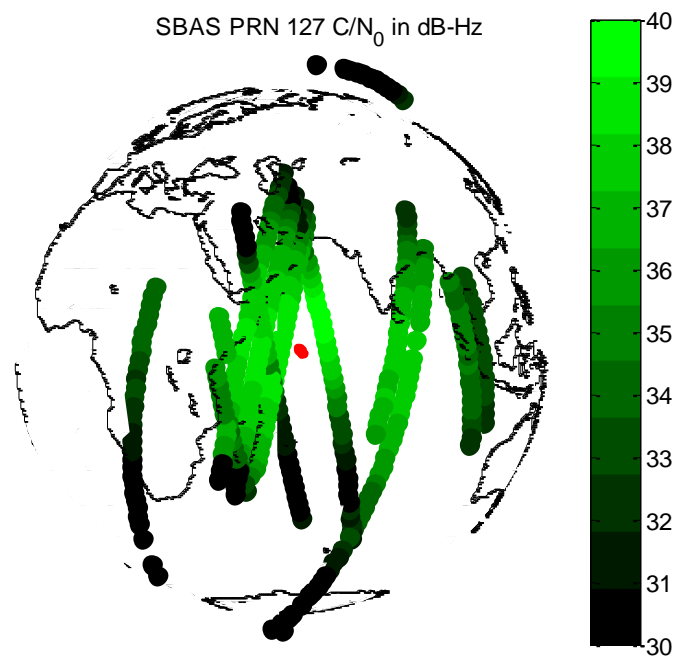


Figure 4-3: GAGAN PRN 127 (red) and CanX-2 tracking arcs colored by C/N_0

From the figure, several of the results of this study are immediately apparent. First, it is clear that the high rate SBAS data in no way prevented acquisition or tracking of the signals from a receiver in space, which is in keeping with the earlier ENEIDE mission results (Zin et al 2007). The SBAS signal strength is in fact centered at the equator, and sufficient power spills over the Earth that CanX-2 was able to track at least one satellite from each of the four studied SBAS systems over the Earth's limb both in the northern and southern hemispheres. CanX-2's orbit, GPS antenna, and attitude profile unfortunately make the collection of East/West data arcs,

which would be more relevant to GEO tracking, impossible. While tracking SBAS satellites at cross-track would theoretically be possible, the signals are unfortunately too weak to acquire with CanX-2's hardware unless the SBAS satellite is overhead.

Approximately 10 dB lower carrier-to-noise-density ratios (C/N_0) are observed from CanX-2 compared to typical values observed on the Earth's surface, which are in keeping with the equipment onboard the CubeSat, and not a difficulty in tracking SBAS. Given the 6 dB of additional free space path loss to a receiver in GEO or HEO, this is also a strong indication that the signal power would still be sufficient to track the SBAS satellites in higher orbits. Tracking would only improve if more favorable hardware (and a more favorable attitude profile) was used.

The link budget equation describing the carrier to noise density ratio (C/N_0) in dB-Hz at a GNSS receiver is shown below, where $EIRP$ is the equivalent isotropically radiated power in dB-W, G_{Tx} and G_{Rx} are the transmit and receive antenna gains in the direction of the line of sight in dB, L_{path} and L_{atm} are the free space path loss and atmospheric loss in dB respectively, K_B is Boltzmann's constant in dBW/kHz, and T_{sys} is the system noise temperature in dBr. (Van Dierendonck 1996) The first five terms describe the signal strength, while the final two terms describe the noise.

$$C/N_0 = EIRP + G_{Tx} - L_{path} - L_{atm} + G_{Rx} - K_B - T_{sys}$$

In order to better analyze systematic differences, the observed C/N_0 values were adjusted to remove Boltzmann's constant K_B , free space path loss, L_{path} , and the CanX-2 receive antenna's gain pattern, G_{Rx} . CanX-2's gain was measured in an anechoic chamber with a mock-up of the satellite before launch, and validated against the flight results in Kahr et al 2011. Atmospheric loss, L_{atm} , is assumed to be zero because CanX-2's low Earth orbit is already above a significant portion of the atmosphere. Data points collected when the CanX-2 nominal and measured attitudes differed by more than 10 degrees were rejected in order to overcome the attitude determination difficulties, resulting in only half of the roughly 3000 data points collected across all satellites, all systems being included in the gain pattern analysis.

The remaining quantity, $EIRP + G_{Tx} - T_{sys}$, was plotted for each SBAS satellite as a function of angle off-boresight, assuming rotationally symmetrical gain patterns and nadir pointing transmit antennas for the SBAS satellites. A mean value was calculated for each 1 degree bin. A sample figure for GAGAN PRN 128 is shown in Figure 4-4 below, where the points are colored based on whether they were collected in the northern or southern hemisphere in order to highlight systematic differences.

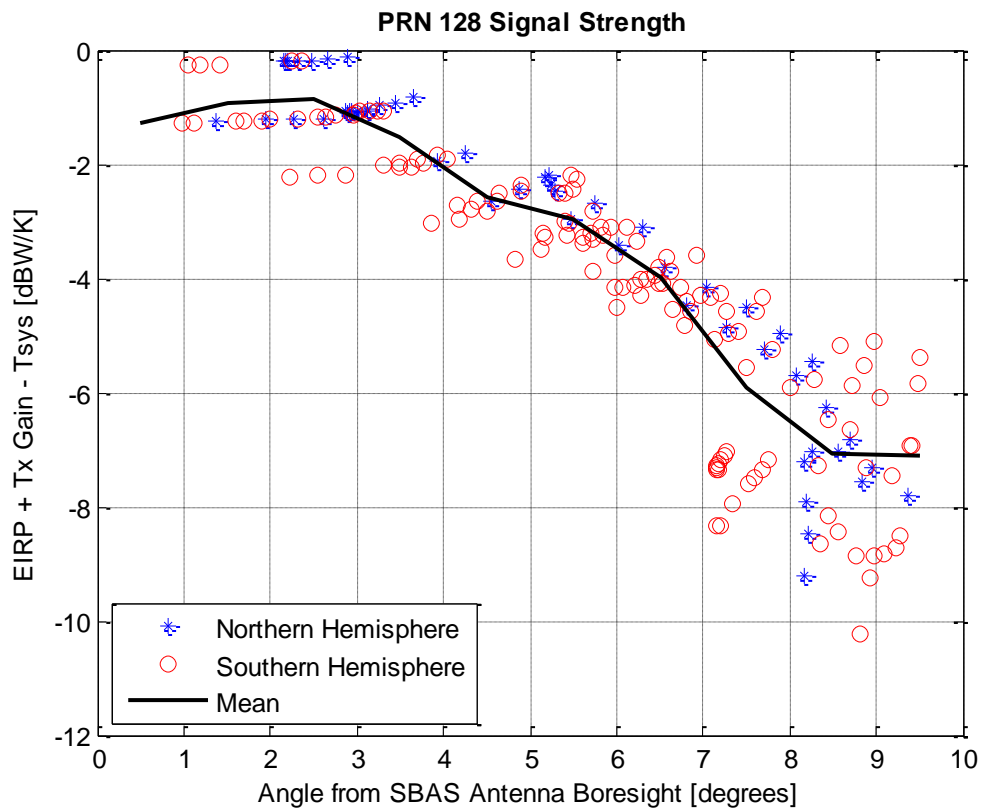


Figure 4-4: Corrected Signal Strength on GAGAN PRN 128, reflecting the transmit antenna gain pattern

The greater noise in the data after roughly 8.5 degrees off-boresight is a result of the fact that CanX-2 is beyond the edge of the Earth from the perspective of the SBAS satellite. Some SBAS signals are tracked at low positive elevations while CanX-2 is still on the same side of the Earth as the SBAS satellite, while others are tracked over the Earth's limb at negative elevations in the receiver's field of view. The receive antenna gain characteristics at negative elevations are

poorly understood, as the signals are either passing through or refracting around the body of the CubeSat.

It is not possible to separate out the remaining three quantities in the figure: system noise temperature, EIRP and transmission gain. System noise temperature is dependent on the environment and hardware onboard CanX-2. As stated in the previous chapter, a typical value for a geodetic receiver would be \sim 23 dB-K (Lachapelle 2009), but it is higher for CanX-2's setup. It is assumed that T_{sys} is a constant value common to all CanX-2 tracking, and does not significantly influence the comparison of SBAS systems with each other. EIRP is the total power transmitted by the SBAS payload on a particular satellite. The MSAS MTSAT-1R satellite, for example, has an EIRP of 31 dB-W (Kramer 2015) and the other SBAS systems are expected to transmit power on the same order of magnitude. The actual value however is not known for every system and satellite, therefore could not be calibrated out. The systematic differences in the curves of Figure 4-5 are therefore a combination of differences in the transmit gain patterns and EIRPs of the SBAS satellites.

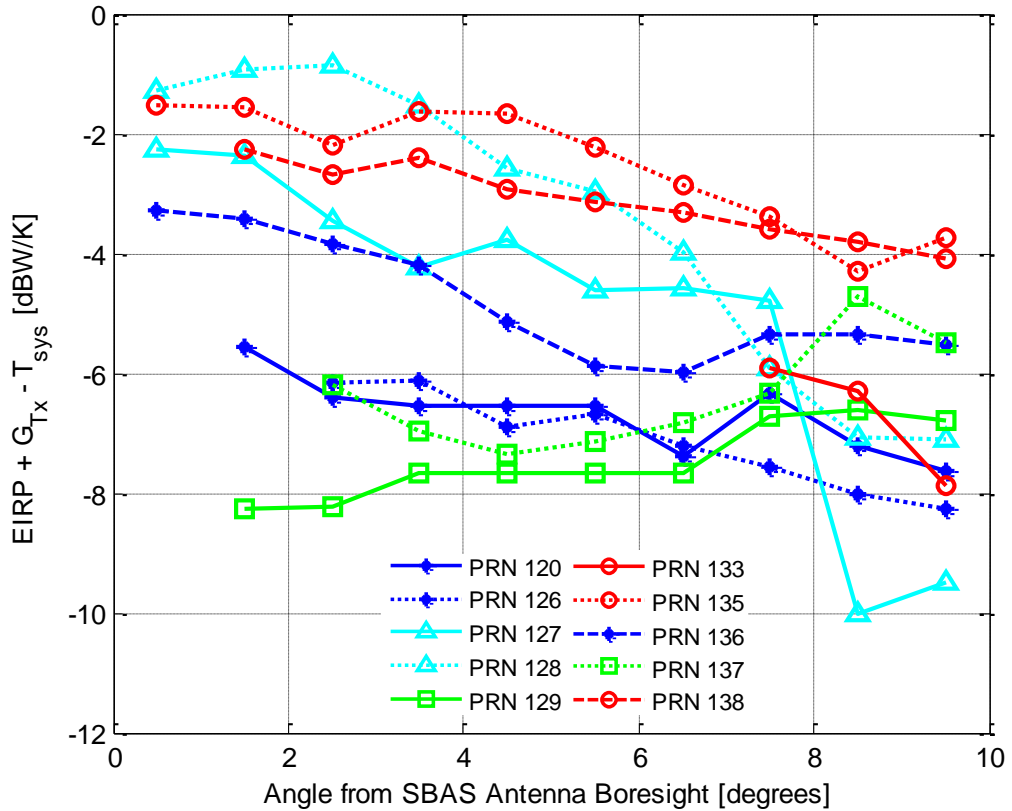


Figure 4-5: Comparison of the signal strength among SBAS satellites. WAAS is in red circles, EGNOS in blue asterisks, GAGAN in cyan triangles and MSAS in green squares.

It is possible to draw several conclusions from Figure 4-5. First, it appears that satellites from the same system share a similar antenna design, but have slight offsets in the power level on the order of 1 dB. The WAAS system has the highest overall power level, and seems to have a transmit antenna pattern with the peak power at boresight and only a moderate drop off of about 2 dB in the first 10 degrees off-boresight. The signal is still strong enough to track past the limb of the Earth. WAAS PRN 133 appears to have weaker power than PRNs 135 and 138 by 2-3 dB, but was only tracked near the edge of the Earth so that the center of the gain pattern could not be mapped. A weaker EIRP may explain why it was tracked so rarely in spite of dedicated efforts to acquire it, but it also has a greater inclination than the other WAAS satellites, and therefore its orbit is not as well described by the SBAS almanac format over the time intervals between CanX-2 data takes. The poor a-priori knowledge of the orbit would also have made acquisition

less likely. Because so little PRN 133 data were collected, it is impossible to determine whether the center of its gain pattern is similar to the other WAAS satellites.

EGNOS seems to have a similarly shaped gain pattern to WAAS, but a lower power by roughly 4 dB on the two fully operational satellites, PRN 120 and 126. The newer satellite, PRN 136, appears to have a roughly 2 dB higher power than the older EGNOS satellites. The PRN 136 results are however less reliable than the other curves, because the satellite began transmitting later than the others, resulting in a limited number of CanX-2 data arcs during which it was tracked. The limited available data are likely the cause of the dip in signal power at 6 degrees off-boresight.

The GAGAN gain pattern appears to be narrower than WAAS or EGNOS, with a steep drop off of roughly 6 dB at 10 degrees off-boresight, as compared to the center of the pattern. This is an indication that GAGAN is less suitable for space users in GEO, and is probably visible in a narrower window near the Earth's surface unless the narrow main beam is accompanied by strong side-lobes.

Finally, the MSAS system pattern shows a completely different trend than the others. While it has the weakest signal levels overall, it also appears to have an antenna design which curves around the Earth in order to mitigate free-space path loss for users anywhere on the Earth's surface, in spite of its smaller service area. This is a similar design concept to the MEO navigation satellites.

One interesting feature of the MSAS system is that for continuity of service, both satellites can transmit either or both of the assigned MSAS PRNs (Montenbruck et al 2014). For the assessment here it has been assumed that each PRN was transmitted from its own satellite, as depicted in the map in Figure 4-1. However, both signals appear to have been transmitted from the same satellite over the course of several days in the spring of 2015, and it is possible that other such periods have had a minor influence in the result of this gain pattern study.

For comparison with the observation data, three transmit gain patterns from literature have been plotted from 0 to 10 degrees off-boresight and are shown in Figure 4-6. Interestingly, the literature pattern for QZSS (Noda et al 2010) is the only gain pattern for a geosynchronous satellite which follows the Earth's curvature, and like MSAS is also a Japanese system. The observed MSAS pattern however appears to be wider than the documented QZSS gain pattern, with a peak gain at roughly 10 degrees off-boresight, as opposed to the QZSS pattern's peak at 5 degrees off-boresight. The EGNOS and WAAS patterns agree reasonably well with the literature pattern for GAGAN (Jyoti et al 2005), while the actual GAGAN gain pattern appears to be much narrower, matching the WAAS prototype patch antenna pattern (Iriarte et al 2009). In spite of a long search no further SBAS gain patterns were found in literature.

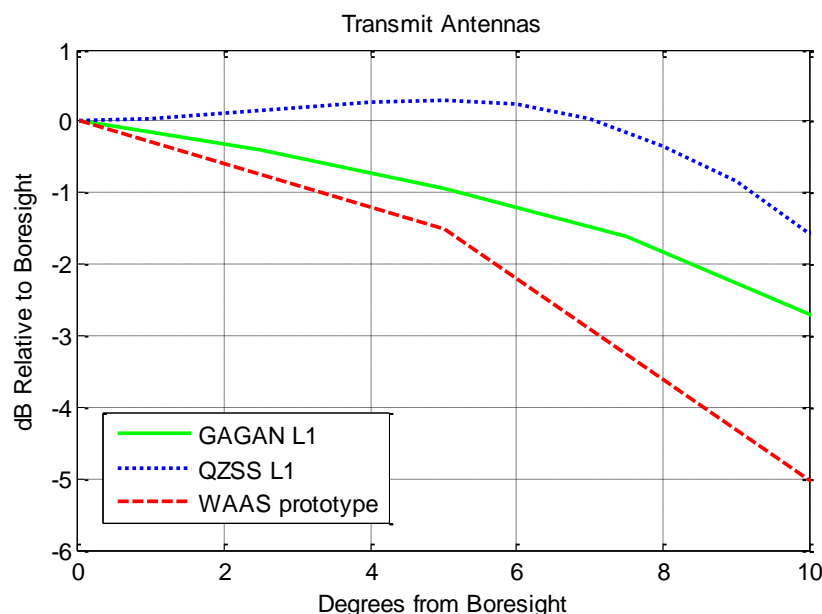


Figure 4-6: Transmit gain patterns found in literature, for GAGAN, QZSS and a prototype patch antenna design suggested for the WAAS system.

Finally, a last interesting result was discovered when the points for the WAAS system were colored based on hemisphere. It appears that the WAAS system transmits roughly 1-2 dB higher power to users in its service area in the northern hemisphere than towards the southern hemisphere. A sample plot for PRN 138 is shown in Figure 4-7, and the PRN 135 results (not

shown) reveal an equally strong trend. While this may impact space users, as a result of the higher noise level in the CanX-2 data it is not possible to see a significant difference in signal power spilling over the Earth in the northern versus southern hemispheres. The only non-WAAS satellite to exhibit a similar trend is the newer MSAS satellite, MTSAT-2, although the trend was not as pronounced as it is for the WAAS satellites. This result should however be taken in the context of the data collection quality. While the data clearly shows a strong hemispheric trend, it is not possible to completely rule out the risk that the attitude system on the satellites is subject to systematic biases over different parts of the Earth, which might produce a similar trend in the data.

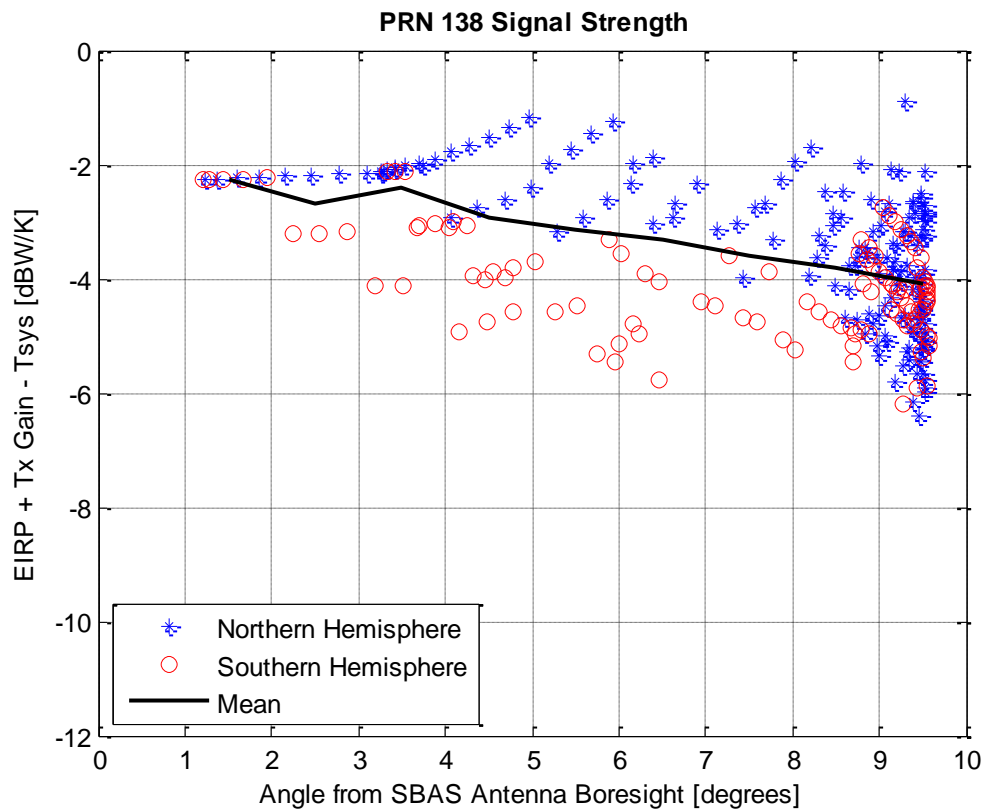


Figure 4-7: WAAS prn 138 signal power colored by hemisphere. The northern hemisphere appears to benefit from 1-2 dB more gain than the southern hemisphere.

4.3 Ranging Data Accuracy

While the CanX-2 flight results indicate that SBAS tracking off the edge of the Earth is possible, in order to make use of the ranging signals for positioning in HEO they must also be adequately accurate. Ranging accuracy is particularly important to a HEO or GEO user, because the weak geometry and minimal signal level can make the position solution particularly susceptible to bad measurements. Each SBAS system is monitored and actively controlled by a network of ground based stations in a somewhat limited geographical area; therefore, there is no guaranteed level of service for a user in space or even outside the specified coverage area. It is important to understand whether the SBAS signals outside of their service area suffer from different atmospheric effects or residual clock effects requiring special handling.

EGNOS officially does not support ranging, and does not transmit sufficiently accurate broadcast ephemeris information for positioning (EGN-SDD SoL, V1.0); therefore, this part of the study has been limited to WAAS, GAGAN and MSAS. A previous study assessing the accuracy of the WAAS L1 and L5 signals was published in 2008, which characterized signal noise and biases, and found that the ranging error on WAAS signals was predictably noisier than GPS (roughly 4 m, as compared to 1 m for GPS) (Rho and Langley 2008). Similar conclusions were drawn by Wanninger (2008) and Fortin et al (2014). The most thorough study of WAAS ranging is found in Schempp et al (2008), with a discussion of SBAS ranging errors due to receiver biases, contributions of multipath at the user's station or in the ground infrastructure of the WAAS system, the difficulty in orbit and clock parameter determination for GEO satellites, code carrier divergence, and others based on a thorough understanding of the WAAS infrastructure. Unlike the previous studies, this section of the chapter presents an assessment of SBAS absolute ranging accuracy based on positioning residuals, and also investigates the ranging accuracy beyond the SBAS service areas, which is of particular importance for space users attempting to position over the Earth's limb.

CanX-2 offers only short data arcs and suffers from significant measurement noise, therefore even a reduced dynamic orbit solution is limited to a few metres of accuracy at best (Kahr et al 2011). Due to the lack of a reliable CanX-2 position solution for comparison, ranging data from

the global network of MGEX IGS stations (Montenbruck et al 2014) have been used for the majority of the SBAS ranging accuracy study rather than the CanX-2 data. In addition to the benefits of static setups, the MGEX stations provide longer data arcs for a more thorough assessment.

In order to calculate SBAS range residuals, single point position solutions were calculated making use of GPS and SBAS measurements. At each data epoch, three position unknowns, GPS system time, and a GPS-SBAS inter-system time bias were estimated. The amount of input data was limited such that only one SBAS satellite was included in the positioning solution. As a result, the inter-system bias is minimally constrained, and is essentially the residual of the SBAS measurement as compared to the single point GPS solution. It reflects both any actual timing differences between the SBAS satellite time and GPS system time, as well as any other errors on the SBAS range measurement and model.

For a consistent handling of the systems, single frequency data were used for all GPS and SBAS measurements. Ionospheric corrections were applied from the Ionex files available from the University of Bern's Center of Orbit Determination in Europe (CODE), and both tropospheric corrections and differential code biases were also applied. For the GPS constellation, precise orbit and clock products from the IGS were used. For the SBAS systems no precise products are published, so the SBAS Message Type 9 broadcast ephemerides were used.

The SBAS broadcast ephemerides alone are not sufficiently accurate to use for ranging, because the data suffer from large residual clock errors on the order of 100 m. To get sufficiently accurate ranging information, the fast corrections must be applied to the ranging data in addition to the clock term in the broadcast ephemerides (RTCA DO-229D), while the slow corrections should not be applied.

Insufficient data were originally logged to properly correct the SBAS ranges, either from the MGEX ground network or onboard CanX-2. In order to continue the study, three Septentrio receivers, including the MGEX stations in Yellowknife, Canada, and Sydney, Australia, as well

as a receiver at DLR's Oberpfaffenhofen location in Germany, were configured to log the SBAS corrections of all SBAS satellites and systems for several weeks. Ultimately two sources of historical SBAS corrections are also publicly available, containing data for a few months after they are transmitted: the William J. Hughs FAA Technical Center website for WAAS and the CNES SERENAD server for all systems. The University of New Brunswick also has an archive of WAAS corrections from one satellite of more than 10 years, available to interested parties.

The dramatic improvement offered by the fast corrections over a week of GAGAN tracking is shown in Figure 4-8. Without the corrections, the SBAS ranging measurements are subject to clock errors of potentially a few hundred metres. These errors are present in all three SBAS systems, but appear to occur less frequently in the WAAS measurements.

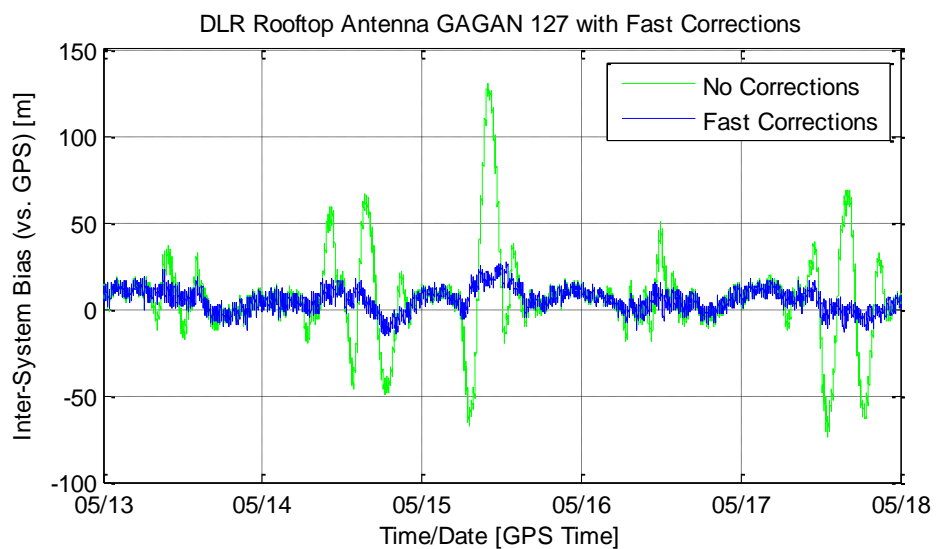


Figure 4-8: The PRN 127 residual/inter-system bias with and without applying fast corrections

The fast corrections are broadcast in messages 2-5 every six seconds, however to interpret them the PRN mask, which is transmitted in message 1 approximately every five minutes, is also required. The PRN mask is only expected to change when GNSS satellites are launched or reach

the end of service. Message 7 also complements the fast corrections, by providing information about the duration of their validity.

Note that for the best consistency between SBAS and GPS ranging measurements, ideally all of the SBAS corrections should be applied to the full constellation of tracked GPS satellites as well. Universally applying the corrections ensures any biases caused at the WAAS ground infrastructure or by a difference in system timing is universally applied across all GNSS measurements and ends up grouped into the receiver clock bias, without degrading the position solution. Although applying corrections to the GPS measurements would be logical for receivers in the SBAS service areas, the consequences of applying them outside the service areas or in space is an open question. Applying SBAS corrections to the GPS measurements was therefore not done in this study, which according to Schempp et al (2008) may account for up to 50 ns (15 m) of additional inter-system bias due to asynchronicity of the GPS system time and WAAS system time.

The stability and absolute accuracy of the SBAS ranging measurements, with fast corrections applied, for both MSAS satellites, are show in Figure 4-10, for both GAGAN satellites in Figure 4-11, and for all three WAAS satellites in Figure 4-12. In all three figures, the stations depicted with black inter-system bias curves are within the defined service areas, while the stations with the colorful curves are far outside the service areas. For reference, the locations of the MGEX stations used for the ranging data assessment are shown on the world map in Figure 4-9.

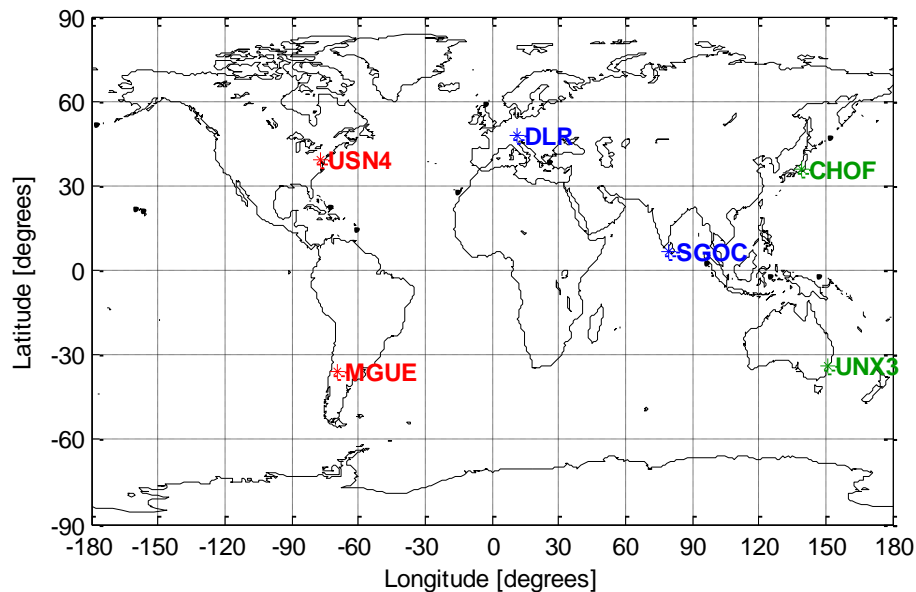


Figure 4-9: Locations of MGEX stations and receivers used in this study

From Figure 4-10, it can be seen that a residual timing bias is present in the data from the MSAS system, on the order of +/- 10 m. This timing offset compared to GPS system time is however consistent on both MSAS satellites (over this period each PRN was transmitted from its own satellite), and at both stations, in spite of a substantial geographic distance between them. It is not correlated to the quality of the GPS single point position solution. This consistency in the bias suggests that the majority of the error could be eliminated by differencing measurements. Aside from a slight bias, which may be receiver hardware dependent, the ranging quality at the Sydney station, UNX3, was comparable to the quality at the Japanese station, CHOFE, in the center of the MSAS service area.

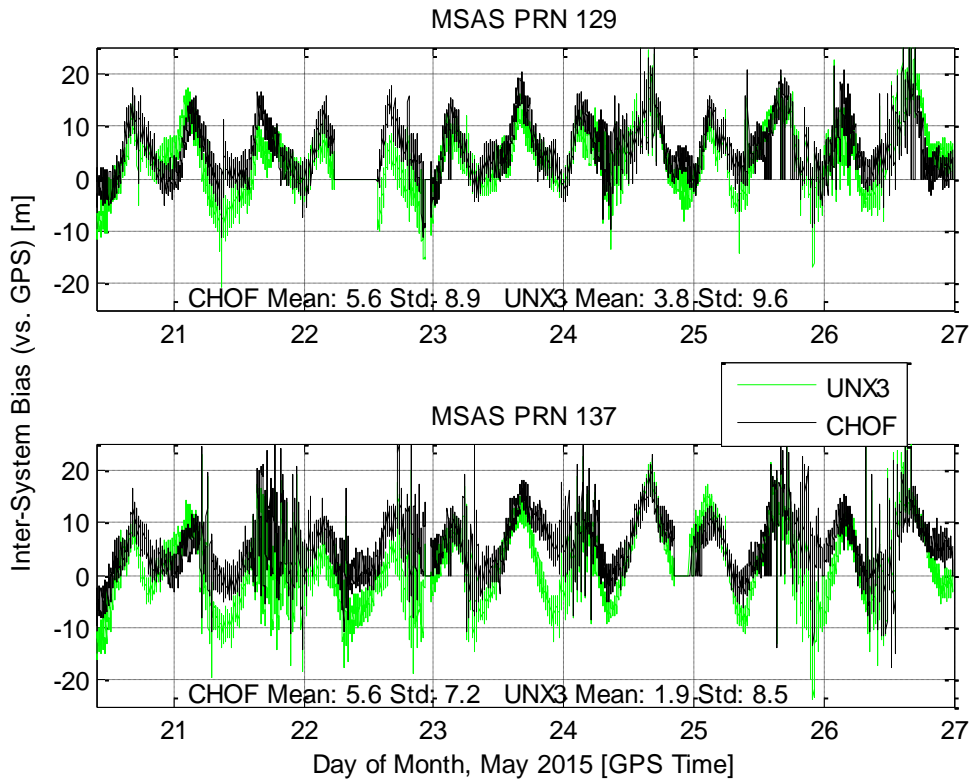


Figure 4-10: MSAS ranging residuals compared to a GPS single point solution

A far more significant difference was revealed for the GAGAN measurement quality, in Figure 4-11. A very good ranging accuracy was obtained from the SGOC station in Sri Lanka, off the southern tip of India, from mid-day May 21st until the end of the test period, with noisier measurements being obtained initially on the 20th and 21st. The combined time-varying and systematic ranging errors observed at SGOC were on the order of 5 m. On the contrary, the out-of-service-area receivers in Germany (DLR, PRN 127) and Sydney (UNX3, PRN 128) have much higher noise. Given the narrower GAGAN gain pattern and the extremely low elevations of the GAGAN satellites from DLR and Sydney, this higher noise is likely explained by low elevation atmospheric effects and lower carrier to noise densities. Both the DLR and Sydney stations observed time-varying errors as well, which appear to be quite station dependent and inconsistent. Coupled with the lower signal power near the edge of the Earth, GAGAN is less

likely to provide good quality ranging information to geostationary satellites over the Earth's limb than the other SBAS.

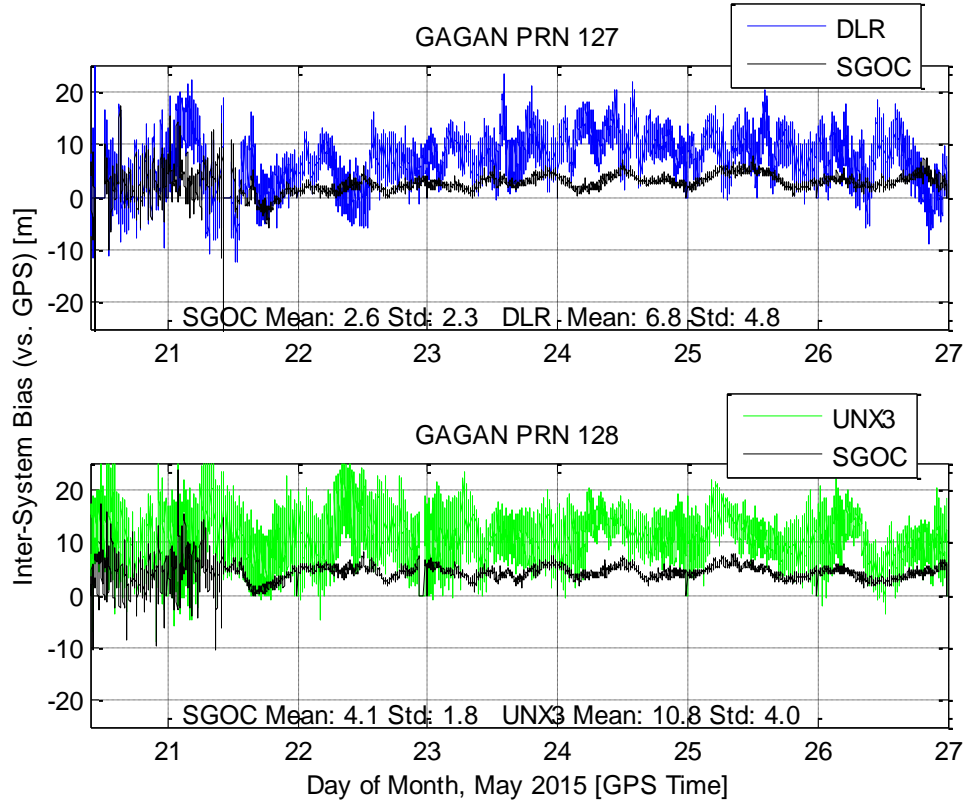


Figure 4-11: GAGAN ranging residuals compared to a GPS single point solution

The WAAS system consistently provided the best performance, with lower time-varying errors and systematic biases, shown in Figure 4-12. This result is consistent with its larger ground monitoring network and service area. The performance from the MGUE station in South America is better in terms of the mean inter-system bias but worse in terms of standard deviation than the performance at the US Naval Observatory's MGEX station in the continental US. At MGUE, PRN 135 is subject to rapidly fluctuating range errors, and PRN 138 shows daily variations larger than those at USN4 but with the same frequency. The difference in the nature of the errors between the PRNs suggests that the effects are caused by remaining un-modelled atmospheric effects. Clock errors would be common to the station if they were caused by the receiver clock, common to the PRN if they were caused by the satellite clock, or common to both if they were caused by a system time offset as is the case with GAGAN. Because the satellites

are geostationary, multipath and orbit errors would vary much more slowly with time if at all. PRN 133 had very consistent performance, but higher noise than the other WAAS satellites consistent with its lower observed signal power.

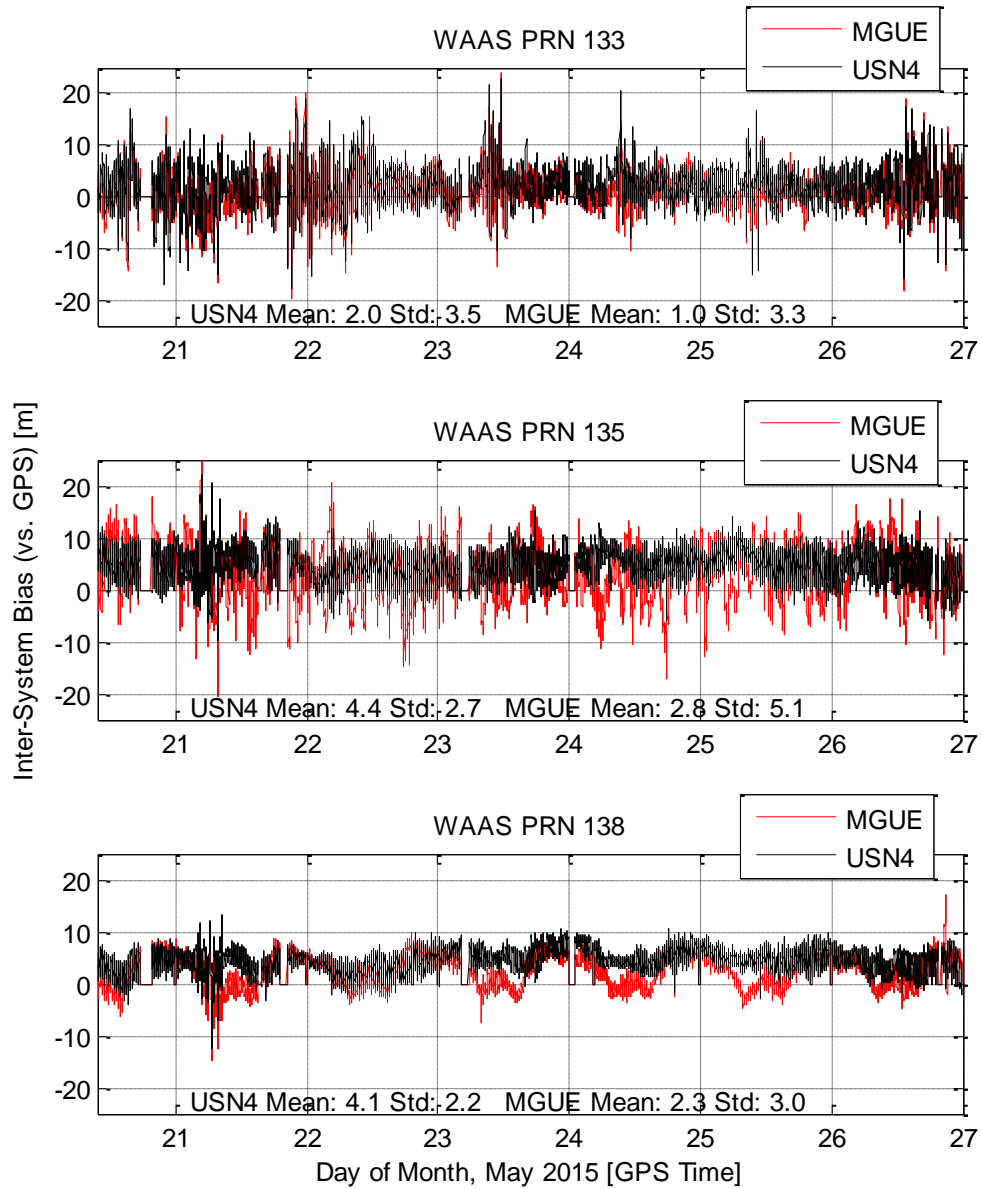


Figure 4-12: WAAS ranging residuals compared to a GPS single point solution

As a final step, a pair of CanX-2 data sets for WAAS and GAGAN, collected at the same time as the fast correction data on the ground, were processed using the same technique as the ground based data. The results for WAAS PRN 138 are shown in Figure 4-13, overlaid on a world map to get a sense of the geographic dependence of the ranging accuracy. The figure demonstrates

that a ranging accuracy of better than 10 m was generally achieved when the satellite was passing through the WAAS service area. Higher positioning residuals of up to 30 m can be observed when CanX-2 passes over the pole, particularly after CanX-2 begins to set and the WAAS satellite is tracked over the Earth's limb. This result is not at all surprising, as the WAAS satellite is being tracked at negative elevation through the body of the CanX-2 CubeSat, and the signal is passing through layers of increasing ionospheric density as the line of sight approaches the surface of the Earth.

In order to mitigate these increased atmospheric effects over the Earth's limb, dual frequency measurements could be used. The SBAS systems are being upgraded to transmit L5 as well as L1 signals, with L5 already transmitted from the WAAS and GAGAN satellites. Although it is not yet fully operational even on these systems, L5 will eventually be part of a modernized SBAS service for the aviation community (Walter et al 2013). Neither CanX-2's receiver nor antenna are L5 capable; therefore, a study of the second SBAS frequency remains as a potential area of future work for a different satellite mission.

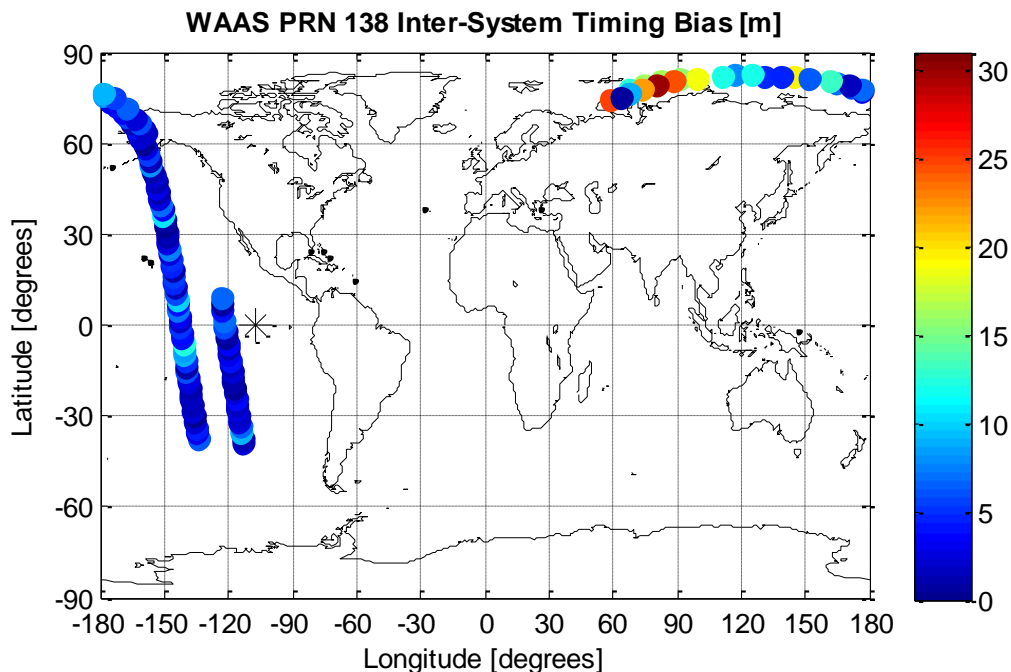


Figure 4-13: Geographic dependence of WAAS PRN 138 ranging errors compared to a GPS single point solution. The SBAS satellite position is marked by an asterisk.

4.4 Conclusions

This chapter provided a first look at its major advantages and drawbacks of using SBAS ranging to supplement the other GNSS measurements for above the constellation users. It was demonstrated that sufficient SBAS signal power spills over the edge of the Earth in both the northern and southern hemispheres to make signal acquisition and tracking possible for users in higher orbits, in spite of the higher SBAS data rate. Further, the maps of the centers of the antenna gain patterns indicate that SBAS satellites have significant differences in their transmit antenna designs and available signal power, which suggests that they have substantially different side lobes as well.

The assessment of absolute SBAS ranging accuracy found that being able to decode the SBAS messages will be essential for any space receiver taking advantage of the SBAS signals, not only for the broadcast ephemeris but also in order to apply the fast corrections to the ranging measurements and avoid significant clock errors. Absolute SBAS ranging errors as compared to GPS positioning solutions were on the order of 10-20 m for WAAS, GAGAN and MSAS when fast corrections were applied to the SBAS measurements.

Of the three systems which support ranging measurements, WAAS was found to be the most suitable for tracking in GEO and HEO, with the highest signal power, a wide main beam, and the best ranging accuracy. MSAS has a transmit gain pattern well suited to tracking over the Earth's limb, but transmitted lower power overall and had a significant and non-constant intersystem timing bias compared to GPS, varying by +/- 10 m. In order to get the best performance from the MSAS measurements both satellites should therefore be tracked, making it possible to either solve for or difference out this bias. GAGAN was less suited to GEO or HEO use, having a narrower beam width than the other systems and the largest ranging errors, potentially as a result of the system's monitoring network being over the magnetic equator. Finally, EGNOS has a similar transmit gain pattern to GPS, but weaker transmitted power, and in its current state it does not support ranging. It is therefore unsuitable for use as a source of GEO or HEO positioning information.

This study only presents a first look at SBAS ranging. An important note for future users is that in this study SBAS corrections were only applied to the SBAS ranging measurements, without applying them consistently to the GPS measurements. This inconsistent handling may account for a significant portion of the observed inter-system biases. While applying the corrections to GPS would potentially allow for much closer agreement with SBAS, a more thorough investigation would be required to understand the benefits and drawbacks of applying SBAS corrections to GPS measurements at a receiver in space, and to understand the potential problems which would arise if more than one SBAS system was simultaneously tracked over the Earth's limb. Finally, while the higher SBAS data rate did not prevent acquisition or tracking from low Earth orbit, it could present a problem for weak signal tracking applications, because it would limit coherent integration time at 2 ms rather than the 20 ms achievable with the GPS L1 C/A code.

The quantitative improvement in positioning offered by including SBAS, or any other GNSS system, would be highly mission specific. Aside from the GNSS system design considerations explored in this chapter, it depends on the weak signal tracking capabilities of the receiver, which may make tracking SBAS unnecessary, and on the orbital slot, which may or may not have line of sight visibility to any SBAS satellites. In addition to the GNSS measurements, the quality of the onboard clock, the design of the navigation filter, and the sophistication of any onboard orbital dynamics models all play a role in determining the achievable orbital accuracy. The coming chapters explore these other design considerations in detail.

Chapter Five: Receiver Design

While the larger goal of this body of research is to study relative positioning in highly elliptical orbits (HEO) using multi-constellation GNSS, previous research in this area was fundamentally limited first by the lack of availability of multi-constellation, multi-frequency receivers capable of operating in the HEO environment, and second by the lack of available information to reliably simulate all the GNSS signals and systems. The next two chapters focus on the development of a suitable multi-constellation GNSS receiver for HEO positioning research, and in parallel present the development of the detailed hardware GNSS simulations which were used to develop and test the receiver, and ultimately used as the basis for the relative positioning results.

5.1 Above the Constellation Receivers

A limited number of groups are taking on the problem of multi-constellation receiver design for above the constellation applications, guided by the requirements of specific missions, or by a desire to produce a commercially available space receiver. Leading the field of above the constellation GPS receivers is the Goddard Space Flight Centre's Navigator receiver (Winternitz et al 2016), designed over 15 years by NASA for use on the MMS mission among others, and based the earlier experience gained from the AMSAT-OSCAR 40 amateur radio satellite which was launched into HEO in 2000 (Moreau et al 2002). The Navigator receiver tracks GPS L1 C/A signals only. It implements the half-bits weak signal acquisition strategy of Psiaki (2001) modified to run in hardware rather than software, a 20 ms coherent integration time (Winternitz et al 2009), and dedicates two correlators to each PRN to assist the handoff of tracking between antennas for the spinning spacecraft (Winternitz et al 2017).

Equally significant is the receiver which flew on the Chang'E-5T lunar return vehicle in 2014 (Fan et al 2015, Liu et al 2015), which also has weak signal capabilities in addition to a high gain antenna, and demonstrated combined GPS and GLONASS tracking above the constellation for the first time. Both the Navigator on MMS and the receiver on Chang'E-5T have demonstrated tracking of on average 8 GPS signals up to altitudes above 60000 km, and Chang'E-5T also demonstrated tracking of an average of 4 GLONASS satellites.

Additional above the constellation receiver design work is being undertaken by various companies and institutes in Europe and globally, which has resulted in the development of several receivers either for specific missions or as commercial products. The European Topstar 3000 Receiver is capable of tracking GPS L1 and L2C, and has weak signal tracking capabilities (Issler et al 1998, Serre et al 2006, Montenbruck et al 2010). The MosaicGNSS receiver by Airbus is an 8 channel GPS L1 only receiver able to track to 26 dB-Hz and acquire at 30 dB-Hz. It was launched into GEO on Hispasat-AG1 on January 28, 2017 (Zentgraf et al 2010, Airbus 2014, European Space Agency 2017). The modernized LION Navigator receiver (not the same as NASA's Navigator), developed by the same team as MosaicGNSS, supports 36 single frequency channels and is capable of tracking GPS L1, L2, L5 and Galileo E1, E5a given enough channels are available. It also has weak signal tracking capabilities and claims tracking down to 20 dB-Hz was achieved in hardware testing, although it is not specified for which signal (Hartrampf et al 2015). The Italian Space Agency has funded a study by Thales Aleina Space to incorporate a GPS/Galileo receiver into their next generation onboard computer, SMU-V2, which will be used by geostationary satellites to assist with navigation during electric propulsion maneuvering (Zin et al 2015).

For the past decade a 12 channel, single frequency GPS L1 C/A receiver developed by Surrey Satellite Technology Ltd., called SGR GEO, has been flying above the GPS constellation on the GIOVE-A satellite (Ebinuma and Unwin 2007, Unwin et al 2013). Surrey has meanwhile developed a multi-constellation model called SGR-Axio for use in LEO, which is capable of GPS, GLONASS, and Galileo (Surrey Satellite Technology Ltd. 2014), but they do not appear to have pursued above the constellation receiver development or weak signal tracking. One of the only multi-constellation space receivers to consider BeiDou is the GNOS instrument, also developed for LEO, which has an ultra-stable oscillator, 14 dual frequency GPS channels, and 8 dual frequency BeiDou channels, with some dedicated to radio occultation and some to navigation. It is flying on the Fengyun-3C low Earth orbiting radio occultation satellite (Wang et al 2014).

Additionally, a few classified American missions have carried General Dynamics receivers into GEO (Bauer 2015a), along with the GOES-R weather satellite carrying a General Dynamics Viceroy 4 (Chapel et al 2015) launched on November 19, 2016 (GOES-R Series Program Office 2017). Finally, the European Space Agency's Project for Onboard Autonomy 3 mission (PROBA-3) will carry a PODRIX receiver capable of tracking GPS/Galileo L1/L5 signals, but with no specialized weak signal capabilities, into highly elliptical orbit in 2019 (Bauer 2015a, European Space Agency 2016, Ruag Space 2016).

Very few, if any, of these receivers were available when this research began, and none would allow for the flexibility and access to source code necessary to test a wide variety of signals and systems with different acquisition and tracking algorithms. The only triple constellation space receivers are the SGR-Axio and TriG, which are only intended for use in LEO, while all of the receivers are commercial products based on fixed hardware implementations and which do not allow a user to make algorithmic changes. Meanwhile, it was clear from the beginning of the project that being able to explore weak signal acquisition and tracking algorithms was of value, given that the side lobe signals of the GNSS satellites are marginally detectable. For the same reason being able to explore all the signals and systems was of value. It was also clear that commercial geodetic grade receivers, while they support a wider array of constellations, would be unlikely to handle the strange viewing geometries of a highly elliptical orbit. This chapter therefore presents the adaptation of the GNSS Software Navigation Receiver (GSNRxTM) for use as an above the constellation research tool.

The remainder of this chapter is divided into five sections. Section 5.2 contains a discussion of the GSNRxTM software receiver and the modifications which were required to adapt it for space applications, section 5.3 contains a discussion of the HEO test simulation setup, section 5.4 discusses the hardware setup required in support of the software receiver, and finally section 5.5 presents preliminary results in the form of receiver acquisition and tracking metrics in addition to single point and filtered positioning accuracy. Final receiver and filter results are presented in Chapters 6 and 7. Section 5.6 concludes the chapter.

5.2 The GSNRxTM Software Receiver

The Position Location and Navigation Group at the University of Calgary has been developing a C++ class based software receiver, GSNRxTM, over the past decade (Petovello et al 2009). GSNRxTM is predominantly a research tool, and its design has been driven by the need for a platform which can be quickly expanded to handle new signals and systems, as well as new acquisition and tracking concepts, to keep up with both the state of the art in GNSS research and with the rapid expansion of available GNSS systems and modernized signals. For years the GSNRxTM software has been constantly evolving as multiple researchers and students develop new algorithms in parallel, which has led to advanced functionality and a large library of interchangeable GSNRxTM algorithms.

The existing receiver software at the beginning of this project already offered significant advantages for HEO positioning research. Among them were the ability to acquire and track GPS L1 C/A, L2C and L5, GLONASS L1 and L2, Galileo E1 and E5, and BeiDou B1 signals. While it was not designed with space applications in mind, the software receiver was more accessible and significantly more easily modified than a commercial or hardware receiver. Additionally, significant work had already been carried out for weak signal tracking applications, for example the implementation of vector based tracking (Petovello et al 2008a), and long coherent integration times for extremely weak signal tracking (Gowdayyanadoddi et al 2015) among others. While the previous research had been targeted at indoor positioning applications, with modifications it would be equally valid for an orbital application. Finally, the receiver already produced geodetic quality measurements, and carrier phase ambiguity resolution had been previously demonstrated, which tied in with the larger goal of conducting relative positioning research. The receiver also had drawbacks, most significantly the substantial learning curve required to be able to successfully modify the software, and the fact that some of the previous research applications were limited proof of concept case studies, not attempts to create robust production level software with all features simultaneously available.

Prior to this research, none of the GSNRxTM applications had been related to space, and so the majority of this chapter is dedicated to describing the extensive changes to the receiver that were

made in order to handle the HEO positioning environment, or any orbital GNSS scenario, in preparation for the multi-constellation and weak signal research goals.

5.2.1 Modifications to GSNRxTM

The most significant modification required to turn GSNRxTM into a HEO-capable receiver was the inclusion of a simple orbit propagator to aid acquisition, and, more fundamentally, to include complete timing information. The channel allocation logic was also adjusted, and the visibility algorithm was rewritten to handle HEO geometry. Minor adjustments were also required to handle position outages at high velocity, to properly handle the tropospheric range correction at orbital altitudes, and remove the ITAR (International Traffic in Arms Regulations) restrictions. Each of these are described in more detail in the following sections.

5.2.2 Adding Full Timing Information

GSNRxTM was previously set up to operate exclusively based on second of week information, with week rollovers handled by making the assumption that no ephemeris was ever more than half a week out of date. This assumption allowed the receiver to calculate its position even before the full ephemerides were decoded. However, the full timing information, including the number of 1024 week rollovers in the case of GPS, is essential to be able to convert from the inertial frame of the orbit propagation to the Earth fixed frames of GNSS navigation.

The first and most time consuming step was therefore to update GSNRxTM to use the full timing information in a way that maintained its full functionality as a multi-constellation receiver. In order to do this, the following functionality was added or updated:

- The receiver was updated to take the number of GPS 1024 week rollovers as mandatory input from the user option file.
- The user option file was also updated to take an optional initial week field, to be used along with the initial time for a warm start.
- The GNSS system time conversion lookup table and associated functions (for multi-constellation GNSS) were updated to handle different week numbers for different systems, and to handle the long term bit overrun week rollover information.

- The navigation message decoders for GPS L1 and GLONASS were updated to properly decode the week, and pass it along to the other parts of the receiver as necessary.
- The decoding of the time of ephemeris information was likewise checked and updated as necessary to properly handle week of ephemeris for GPS, GLONASS and BeiDou.
- Live L1/E1/B1 multi-constellation data was collected during both a GLONASS and a GPS + Galileo + BeiDou week rollover to test the new functionality.

It remains to implement week decoding for the GPS CNAV messages, Galileo navigation messages, and BeiDou navigation messages. Also, the tracked Galileo satellites during the live signal tests, conducted May 17, 2014, were not yet broadcasting real ephemeris information on E1, so GSNRx™'s handling of the Galileo week rollover could not be tested, and insufficient BeiDou satellites were visible during the rollover to test a BeiDou only navigation solution.

5.2.3 Adding an Orbit Propagator

The receiver was modified to take six Kepler elements and a time of ephemeris as input from the user, in order to enable it to propagate and predict its orbital position. A Kepler orbit propagator and a conversion from ECI to ECEF coordinates were added to the receiver code. With a user input initial time, the receiver is now capable of calculating its own approximate position at any point in the future or past, within the validity of the input orbital elements. The Keplerian orbit model was chosen based on the ease of implementing it, and because the data sets are limited in duration to approximately one day in the context of the HEO hardware-in-the-loop simulations. Over this time span even the most significant perturbations could be neglected for the intended applications.

The approximate orbit position and velocity is useful for a multitude of reasons. First and foremost, it is used to aid the acquisition. The position, along with the modified visibility algorithm, is used to predict which GNSS satellites are visible, while taking into account the geometry of HEO and the GNSS transmit beam widths. The velocity is used to predict the Doppler shifts at which to start searching. In cold start the Doppler search space for a PROBA-3 type HEO is +/- 50 kHz rather than +/- 5 kHz for a receiver on the ground, which is dramatically

reduced by calculating the relative orbital dynamics of the HEO and GNSS satellites. Finally, upon acquiring the first signal, the approximate receiver clock is set based on the calculated time of flight from the orbital position of the receiver and GNSS satellite, rather than the typical assumption that a GNSS signal travels 70 ms to the ground from a MEO satellite and 120 ms from a GEO satellite.

In the future, the orbit model also opens up the possibility of using acquisition and tracking strategies tailored to the approximate signal strength and dynamics of a given GNSS satellite, which can be calculated in advance.

5.2.4 Visibility Algorithm

The visibility algorithm was re-written in order to take into account all the geometric possibilities occurring over the course of the HEO orbit. The typical visibility algorithm, in which all GNSS satellites above a certain elevation mask are visible, was retained, but a second set of criteria was added to make it more universal for a space user, as shown in Figure 5-1.

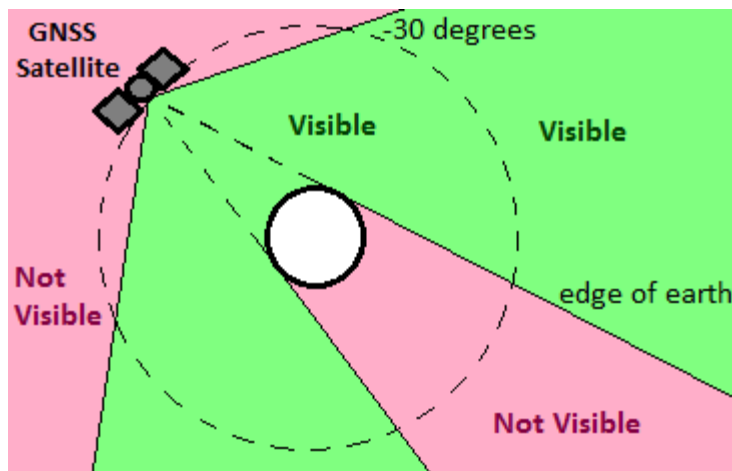


Figure 5-1: Generalized GNSS visibility law for HEO

The elevation of the receiver is calculated with respect to the local level frame of the GNSS satellite. If the receiver has an elevation above -30° , it is determined to be outside of the GNSS

transmit gain pattern, including the second side lobe, and so the GNSS satellite is not visible. If the receiver is between -30° and the edge of the Earth, the GNSS satellite is deemed visible, in order to avoid limiting assumptions about side lobe signal strengths. If the receiver is between the edge of the Earth and -90° (nadir of the GNSS satellite), a further test is needed to determine whether the GNSS satellite is above the receiver and visible, or blocked by the Earth. In this case the GNSS satellite's elevation is calculated with respect to the receiver's local level frame, as in a more typical ground application, and if the GNSS satellite is at positive elevation it is deemed to be overhead and visible.

The user spacecraft's antenna gain pattern and attitude profile have not been taken into account, to leave the receiver code as general as possible.

5.2.5 Channel allocation

Channel allocation in a software receiver is significantly different than it is in hardware receiver, particularly when the software receiver is running in post-processing mode. Because a software receiver has no physical hardware, there are a theoretically unlimited number of tracking channels, but more channels running in parallel lead to more simultaneous computations, and ultimately a slower run time. The receiver had previously been assigned a minimum and maximum number of GNSS satellites to track, with a sky search being carried out when the number of tracked satellites drops below the minimum, and the search ending when it rose to the maximum. Further, the original receiver would continue searching for any PRN that was theoretically visible, rather than reallocating the channel to search for newly risen PRNs if the acquisition repeatedly failed, for example due to a building obstructing the line of sight.

Because the number of visible satellites changes dramatically from perigee to apogee of a highly elliptical orbit, the previously fixed number of channels in GSNRxTM was exchanged for a fixed number of “search channels” which would constantly scan the full range of PRNs for additional GNSS satellites, and flexible number of tracking channels. If a signal is acquired, the channel moves on to tracking, and a new acquisition channel is created to continue the search at the next untracked PRN. The number of tracking channels therefore increases each time a satellite is

acquired, and the channels are deleted as soon as lock is lost. Using this strategy the full constellation of available satellites is tracked through the perigee arc, but a minimum of resources are used for acquisition attempts at apogee. A single search channel sweeps through the full GPS constellation roughly every 10 seconds, frequently enough not to miss the limited opportunities for main beam tracking at apogee which last roughly 8 minutes.

This avoids having the 35 channels required for triple constellation positioning at perigee all conducting a computationally expensive sky search at apogee. It also prevents the receiver from dwelling on PRNs which, although theoretically visible, are too weak to acquire. If no PRNs are theoretically visible, there will be no acquisition channel until a new PRN comes into view.

5.2.6 Loss of Navigation Solution

As with most receivers, GSNRxTM was designed to attempt the acquisition of additional GNSS signals using its last known position and velocity upon losing its navigation fix. In the case of the PROBA-3 HEO, the receiver will have to operate for as long as 19 hours between navigation fixes, during which time its position and velocity change dramatically. In order to handle this case, a switch was added causing GSNRxTM to revert to the Kepler orbit for acquisition and visibility calculation after ten consecutive failed position updates. If no Kepler orbit is defined, it reverts to the typical ground assumptions.

5.2.7 Tropospheric model

Within its navigation solution, GSNRxTM applies an altitude dependent tropospheric correction. Unfortunately, the orbital altitudes are outside of the validity region of the tropospheric model. A switch was therefore added to disable the tropospheric delay correction if a valid Kepler orbit is available. As with the re-acquisition logic, if no Kepler orbit is defined GSNRxTM reverts to the typical corrections, under the assumption that it is being used for a ground application.

5.2.8 ITAR Restrictions

As a final modification step, it was necessary to disable the ITAR (International Traffic in Arms Regulations) related height and speed limits in the receiver while testing GSNRx™ in orbital scenarios. These prevent the output of measurements or navigation data if the receiver is higher than 18000 m above ground level or travelling at velocities above 515 m/s (US State Department 2017, Inside GNSS News 2014a).

5.3 Simulating the HEO Environment

In order to test the receiver's suitability for HEO GNSS positioning under realistic operating conditions, having a representative simulation was critical. In order to test the software receiver a GPS simulation was set up using a GSS 7700 Spirent hardware simulator. This section documents the aspects of the simulation setup which were most significant for the initial receiver performance results or modified from the earlier visibility simulations.

5.3.1 Simulation Epoch

The simulation was set to begin at midnight GPS Time on November 7, 2011. It began one hour before a perigee passage of the HEO, covered a full orbit, and extended one hour after the subsequent perigee passage in order to be able to test filter re-convergence after an apogee arc. The total simulation duration was 21 hours and 45 minutes.

5.3.2 GPS Constellation

As a first step towards multi-constellation GNSS research, GPS only was simulated using readily available equipment. The GPS constellation was simulated using a YUMA almanac for November 6, 2011. Based on files from earlier simulation work, radial component orbital errors were added to the simulated GPS constellation. While both the L1 C/A and L2 C signals were simulated, only L1 C/A has been used.

5.3.3 HEO Spacecraft Orbit

The HEO orbit was modelled based on the PROBA-3 orbit as defined in Llorente et al (2013). For this simulation it was defined at the initial simulation epoch by a set of orbital elements in the J2000 inertial frame, given in Table 5-1. These parameters result in an orbital period of 19 hours and 45 minutes, a perigee 800 km above the Earth's surface, and an apogee 60524 km above the Earth's surface, roughly three times farther than the GPS constellation. The tabulated value for mean anomaly corresponds to 1 hour before the perigee passage.

Table 5-1: Orbital Elements

semi-major axis	37039887 m
eccentricity	0.80620521
inclination	59 °
argument of perigee	-173 °
right ascension of the ascending node	142 °
mean anomaly	341.732 °

While the orbital elements are entered into the simulator in the inertial frame, at the start of the simulator run Spirent's software converts them to Earth centered Earth fixed (ECEF) coordinates and numerically integrates them in the ECEF frame for the duration of the simulation. The relevant simulation settings for the HEO orbit propagation are listed in Table 5-2. The spacecraft specific parameters were obtained from Ardaens et al (2012), and are the values for the PROBA-3 Occulter spacecraft.

Table 5-2: HEO Numerical Integration Parameters

Parameter	Setting	Units
Environment Parameters		
inertial coordinate system	J2000	
gravity model	JGM3	
gravity order	70	
solar radiation pressure (SRP)	variable	
solar pressure	4.56E-06	N/m ²
Spacecraft Parameters		
aerodynamic coefficient, C_D	1.29	
drag reference surface	1.81	m ²
SRP coefficient, C_{SRP}	1.29	kg
SRP reference area	1.81	m ²
vehicle mass	196	kg

5.3.4 HEO Spacecraft Attitude Profile

The ideal case inertial attitude profile from Chapter 3, shown in Figure 3-17 was adopted for the hardware simulation.

5.3.5 Link Budget

The aspect of the simulation which most dramatically influences the results is the link budget. The simulation made use of the same azimuth-averaged GPS transmit pattern developed for the visibility simulation in Chapter 3 and used by Ardaens et al (2012), which was digitized from Czopek and Schollenberger (1993). It is shown in Figure 5-2, along with the four digitized cross sections. The pattern was assumed to be rotationally symmetric.

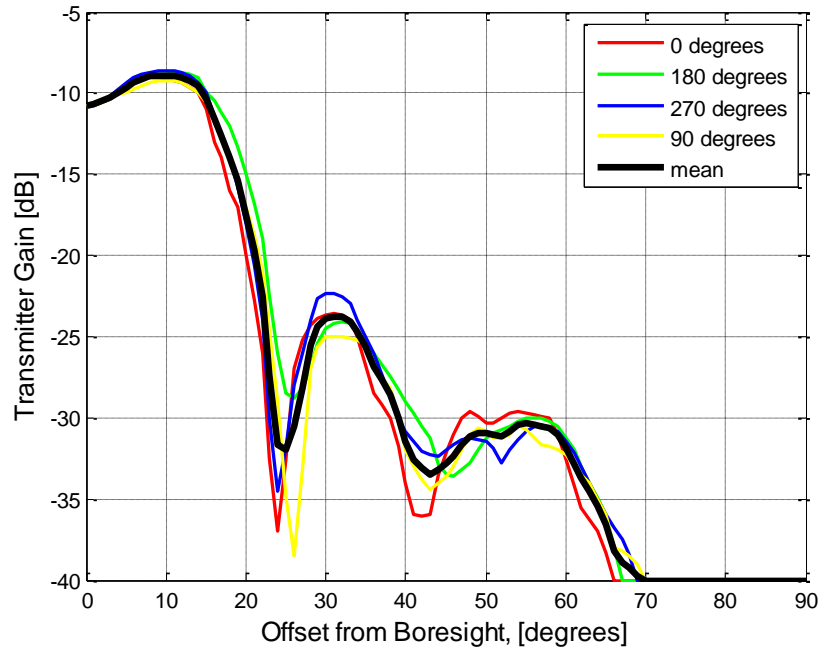


Figure 5-2: Assumed GPS transmit gain pattern

For the receiving antenna, the hardware simulation also made use of the same hemispheric receive antenna pattern as Ardaens et al (2012), shown in Figure 5-3. Additionally, to compensate for the greater noise in hardware GPS simulation as compared to live signal tests a global power offset of +8 dB was applied to all generated signals, as in Ardaens.

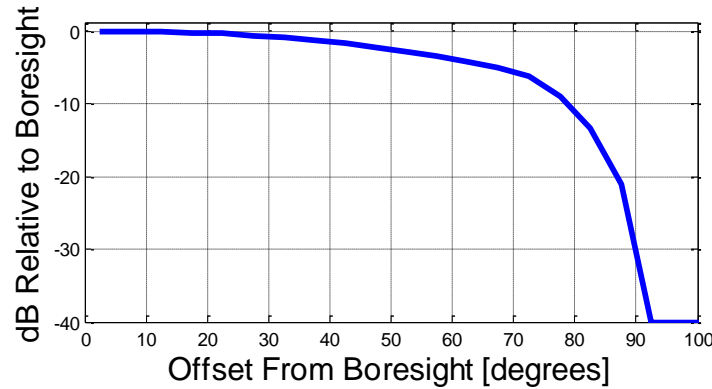


Figure 5-3: Assumed gain pattern for the user receiving antenna

The resulting power levels output from the simulator are shown in Figure 5-4. They have been translated into C/N_0 values using a receiver-specific constant, based on the theory previously introduced in Eq. 3.3 and 3.4. The simulator has 12 channels, and was set up to select which PRNs should be simulated based on signal strength. The figure therefore shows only the 12 strongest signals. The Earth obscuration mask was set to 0 degrees, so signals are simulated until the moment they set behind the Earth rather than masking out low elevation satellites.

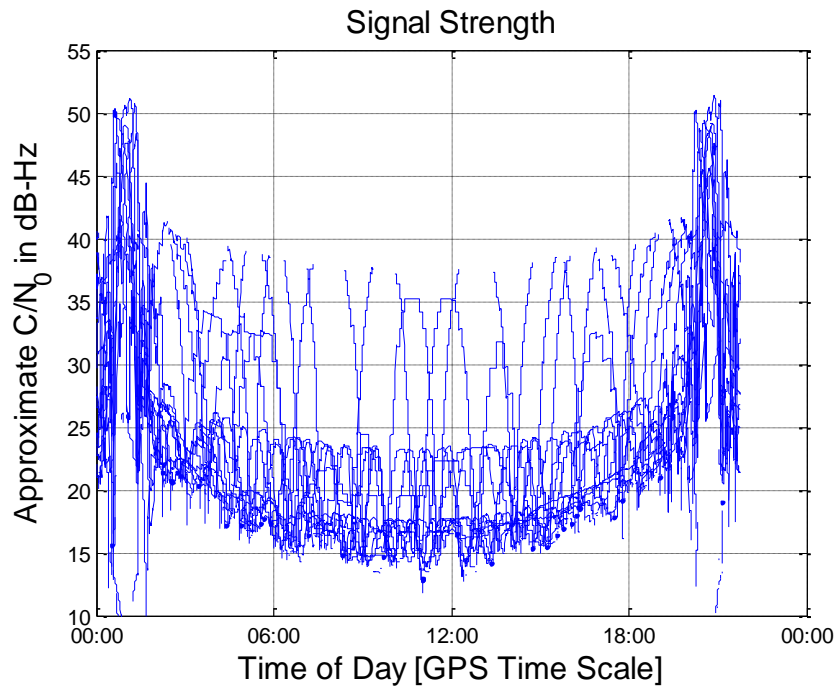


Figure 5-4: Simulated signal power translated into to dB-Hz

There are several clearly visible patterns in Figure 5-4. The perigee passages at 1:00 and 20:45 are characterized by strong signals, up to 50 dB-Hz, which agree well with the typical range of values on the Earth's surface. During the apogee arc, the maximum signal strengths occur rarely and only reach levels of 40 dB-Hz on GPS satellites setting behind the Earth or rising on the other side, when the receiver briefly crosses their main beams. The vast majority of signals at apogee are below 25 dB-Hz, and un-acquirable. It should be noted that while this figure accurately depicts what was simulated here, it was proven much later by the MMS mission that the side lobes are much stronger, nearly 30 dB-Hz as seen from their higher orbit and 7 dB gain antennas (Winternitz et al 2017, Olson et al 2012).

5.3.6 Ionospheric Error

Given that the majority of signals strong enough to track pass near the Earth's limb, ionospheric delay was also simulated to produce realistic results. In order to simulate the ionosphere in a way that was compatible with the simulator, mathematically simple, and reasonably representative, a linear ramp in vertical total electron content (VTEC) was assumed, shown in Figure 5-5. The simulator then uses this profile to model appropriate range delays on both slant and occulting signals.

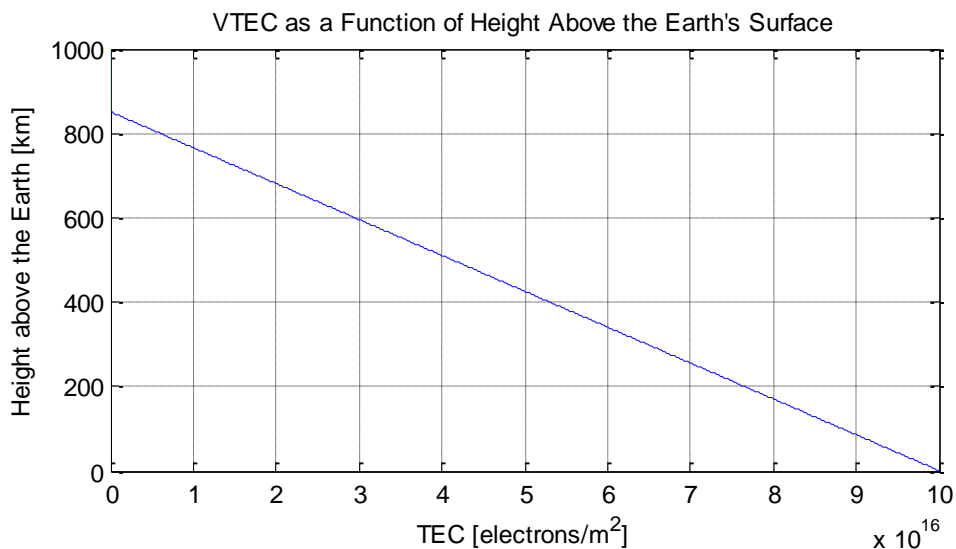


Figure 5-5: Vertical total electron content profile for the HEO simulation

The value at the Earth's surface was assumed to be 1×10^{17} e-/m², which is the Spirent default TEC value and which is representative of mild ionospheric activity. The VTEC value decreased to 0 e-/m² 850 km above the Earth's surface, in order to simulate a mild delay during the HEO satellite's 800 km perigee passage. The underlying assumption is a constant electron density up to 850 km and no electrons above.

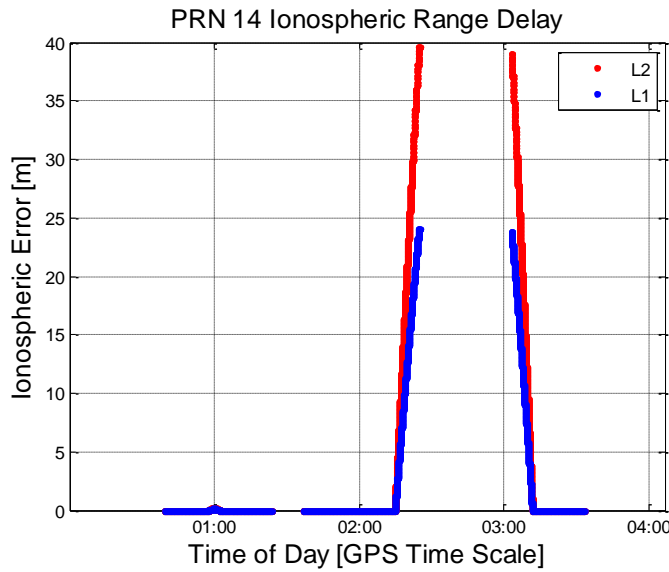


Figure 5-6: Sample ionospheric range delay on PRN 14

An example of the resulting ionospheric delay on L1 and L2, in metres, is shown in Figure 5-6. GPS satellites above the receiver at perigee (1:00 in the figure) experience only minimal delay of 40 cm or less, while setting and rising GPS satellites experience 20 m of range delay or greater on L1 (2:30 and 3:15 respectively).

This profile is not entirely realistic. In truth, the electron density reaches a peak value at approximately 300 km above the Earth's surface, and the ionospheric delay is therefore greatest when the signal's point of closest approach is at that height, tapering off both above and below. A very nice analysis of ionospheric delay as seen from the SBIRS geostationary satellite's dual frequency receiver in the context of above the constellation positioning is presented by Barker and Frey (2012). As compared to their flight results, the simulation here is accurate in the rough order of magnitude, and in the fact that only main lobe signals near the Earth's surface are significantly impacted by the ionosphere. It is pessimistic in that the simulated signals are subject to slightly more delay at tangent point altitudes above and below the 300 km peak. The simulation is optimistic in that the signals would actually be subject to a higher rate of change of ionospheric delay as they pass through the 300 km peak, which could slightly degrade both tracking due to faster code-carrier divergence, and relative positioning error cancellation.

5.3.7 Resulting Signal Dynamics

To put the remainder of the receiver design discussion into context, the simulated signal dynamics for the HEO orbital scenario are shown in Figure 5-7 and Figure 5-8.

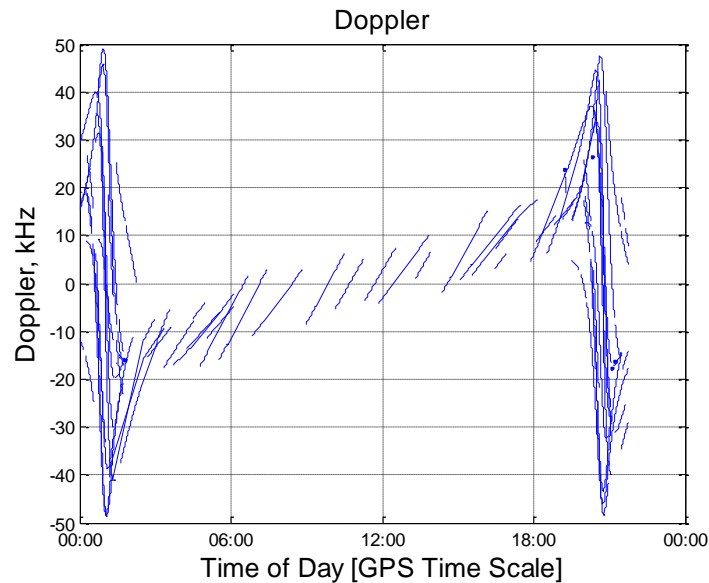


Figure 5-7: Simulated Doppler on all visible PRNs

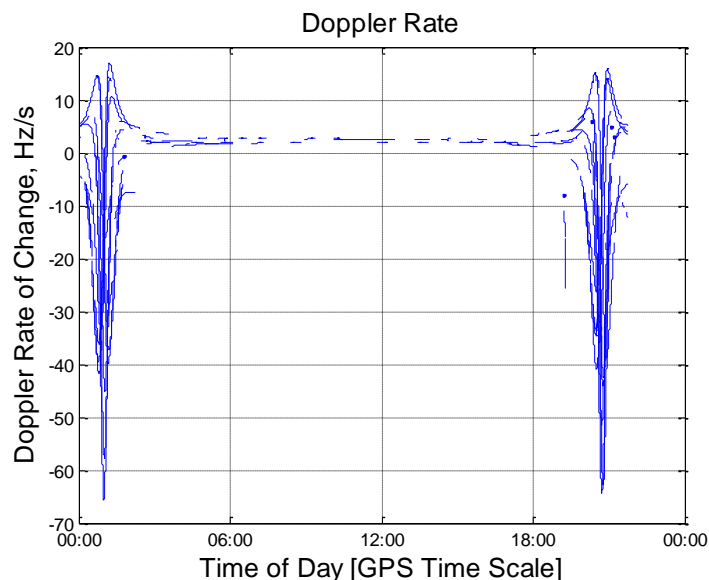


Figure 5-8: Simulated Doppler rate on all visible PRNs

It can be seen from the figures that the two perigee passages are characterized by Doppler shifts of up to +/- 50 kHz and Doppler rates as large as -65 kHz/s. On the other hand, between perigee passages the Dopplers remain bounded in a +/- 20 kHz window, with values even closer to zero at the apogee (roughly 11:00 in the figures). More importantly in terms of tracking loop design, the Doppler rates are nearly constant through the transition and apogee regions when the visible signals are weak. This is an important feature of the HEO orbit, because it means that it is rarely or never necessary to track weak signals and high dynamics simultaneously, which would present a bigger challenge.

5.4 Data Collection

There are aspects of using a software receiver that, depending on the setup, can differ dramatically from using a hardware receiver. It is possible to run GSNRxTM either in real time (Ma et al 2011) or in post processing mode. In real time mode the number of correlations that can happen in parallel are limited by the resources of the computer running the receiver software, which among other challenges makes acquisition more difficult. Every test of the receiver would also require a whole new simulator run. To avoid these disadvantages intermediate frequency (IF) data was collected once, which required the storage of the approximately 22 hours of IF samples, and the receiver was subsequently run in post processing mode. This methodology allowed repeated processing of the same set of IF data to test receiver developments and bug fixes.

While the receiver on its own is a very capable piece of technology, it isn't possible to collect GNSS data without a supporting hardware setup. Connected to the previously mentioned Spirent GSS7700 simulator was a low noise amplifier, followed by a front end driven by a high end external oscillator, and finally a RAID array for data logging. The full setup is shown in Figure 5-9.

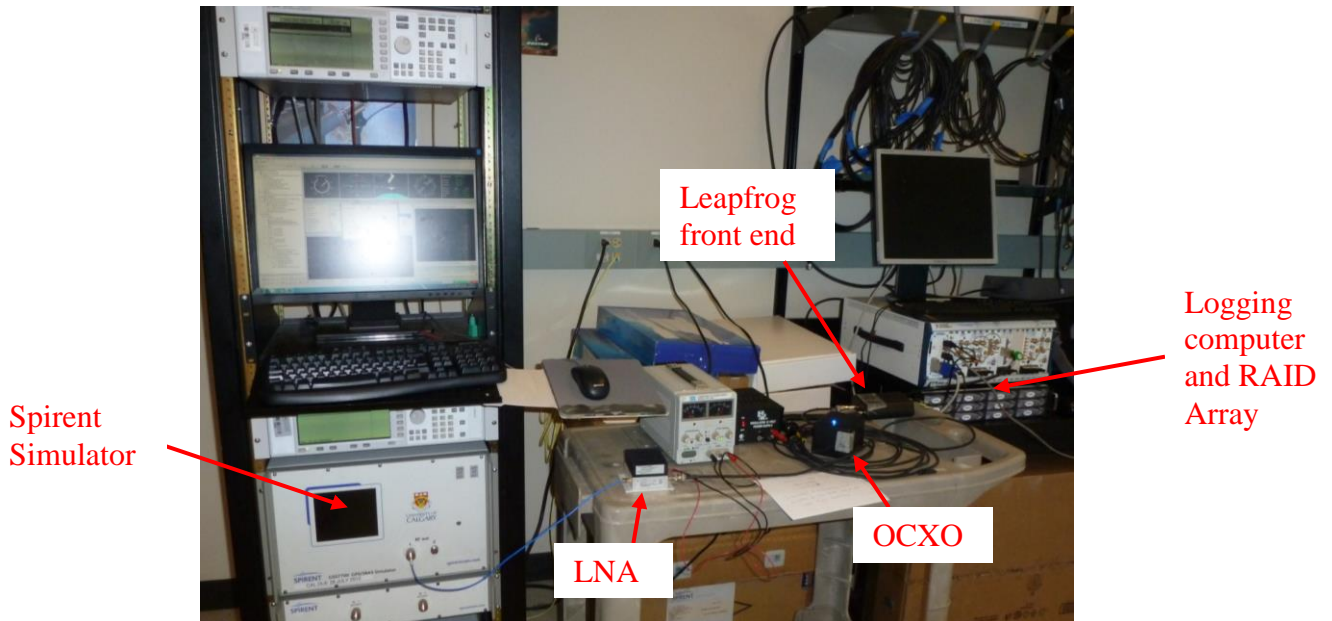


Figure 5-9: Laboratory setup

The decision to use a stable external oscillator was driven by the expected sparsity of measurements. Using a stable clock adds to the strength of the measurements, as less information is required to estimate the updated receiver clock offset at each epoch, and more information is therefore left over to provide meaningful positioning information in an orbital filter. The clock is a Morion MV 89-A03E double oven crystal oscillator (OCXO) with a short term stability of $2 \times 10^{-12}/\text{s}$ (Morion 2012). The simulator uses its own internal oscillator.

The choice of a front end was made based on data volume. The chosen front end is a two channel reconfigurable front end developed in-house in the PLAN group (Morrison 2010), called the Leapfrog. It uses 2 bit quantization and packs the data into an efficient format to reduce the file sizes. It has a reconfigurable sampling rate, from 10 to 40 MHz. For the purposes of the testing, the front end was set up to log L1 and L2 at 10 MHz with a 4 MHz one sided front end bandwidth. Only the L1 data has been considered for the present study. The resulting packed data size was approximately 400 GB, and the unpacked data size was slightly more than 1.5 TB for each channel. The packed data was logged to a raid array belonging to another piece of lab equipment, which was the only available storage with both the capacity and the speed to record the large volume of IF samples during the full simulator run.

5.5 Early Receiver Results

The resulting IF samples were processed through GSNRx™ repeatedly during the receiver modification work. The results from a final run of the data through the modified receiver are analyzed here in terms of acquisition, tracking, raw measurement and navigation performance. These early results are the starting point for the further receiver development presented in Chapter 6.

5.5.1 Acquisition and Tracking

An overview of where GSNRx™ succeeded in tracking signals, as compared to the strong signal generated by the hardware simulator, is shown in Figure 5-10. Only signals simulated above -132 dBm (approximately 37 dB-Hz) are included in the figure for a clearer comparison. It can be seen that the basic model of GSNRx™ has an acquisition threshold close to 37 dB-Hz, but that it was able in several cases to acquire weaker signals. It can also be seen that after acquisition, the signals can be tracked to significantly lower carrier to noise density ratios, as would be expected. A good example of this occurs at 11:00.

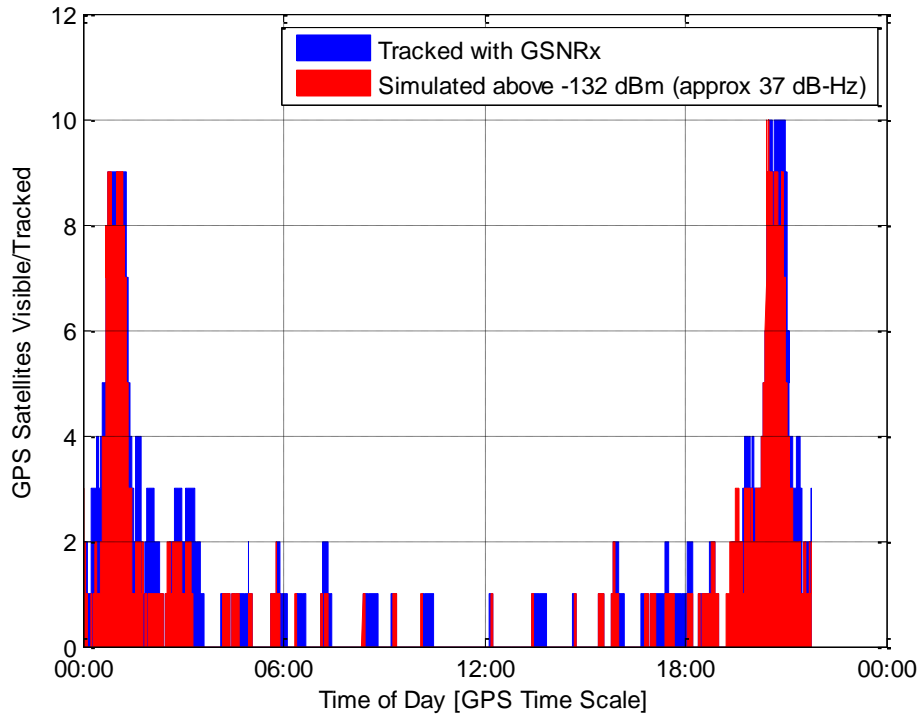


Figure 5-10: Simulated vs tracked signals

Figure 5-11 summarizes the C/N_0 values at acquisition and loss of lock over the entire 22 hour simulation. In the upper plot, the 37 dB-Hz or higher acquisition threshold is clearly visible. The loss of lock plot below shows a bi-modal distribution, which can be explained by the two possible loss of lock events for a receiver in HEO. The lower peak, centered at 28 dB-Hz, is a result of signals fading as the receiver approaches a null between lobes on the transmit gain pattern. The higher peak, centered at 39 dB-Hz, is the result of strong main lobe signals vanishing when GPS satellites set behind the Earth.

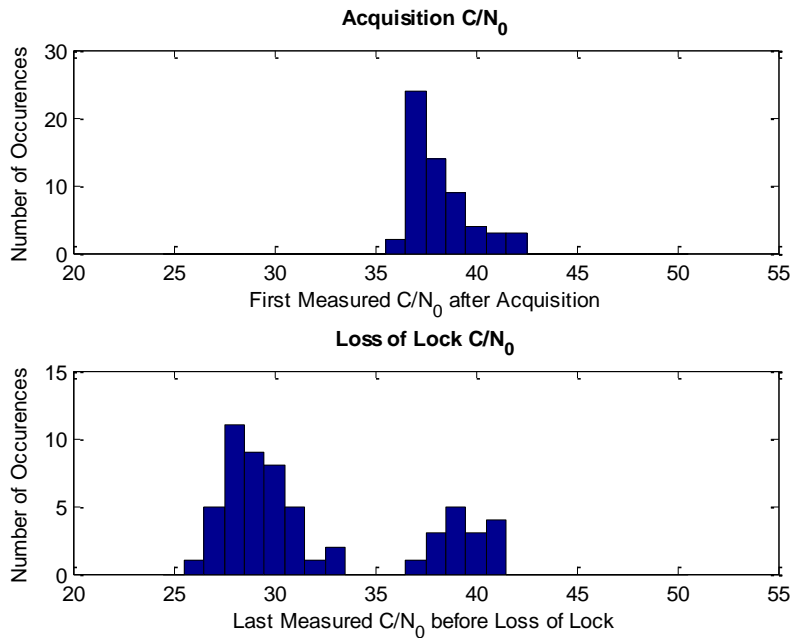


Figure 5-11: Carrier to noise density ratio at acquisition and loss of lock

5.5.2 Raw Measurements

The raw measurement quality was assessed by calculating a single difference between measurements to remove receiver clock effects, and differencing the result from the Spirent truth values to remove geometry as well as orbital and atmospheric errors, as per Holt et al (2003). Figure 5-12 contains the results of the raw measurement assessment between PRNs 9 and 25, when they were simultaneously tracked for a period of 55 minutes during the first perigee passage. The C/N₀ values, included in the fourth subplot for comparison, show a clear step pattern which results from the Spirent interpolation algorithm and agrees well with the simulator truth values.

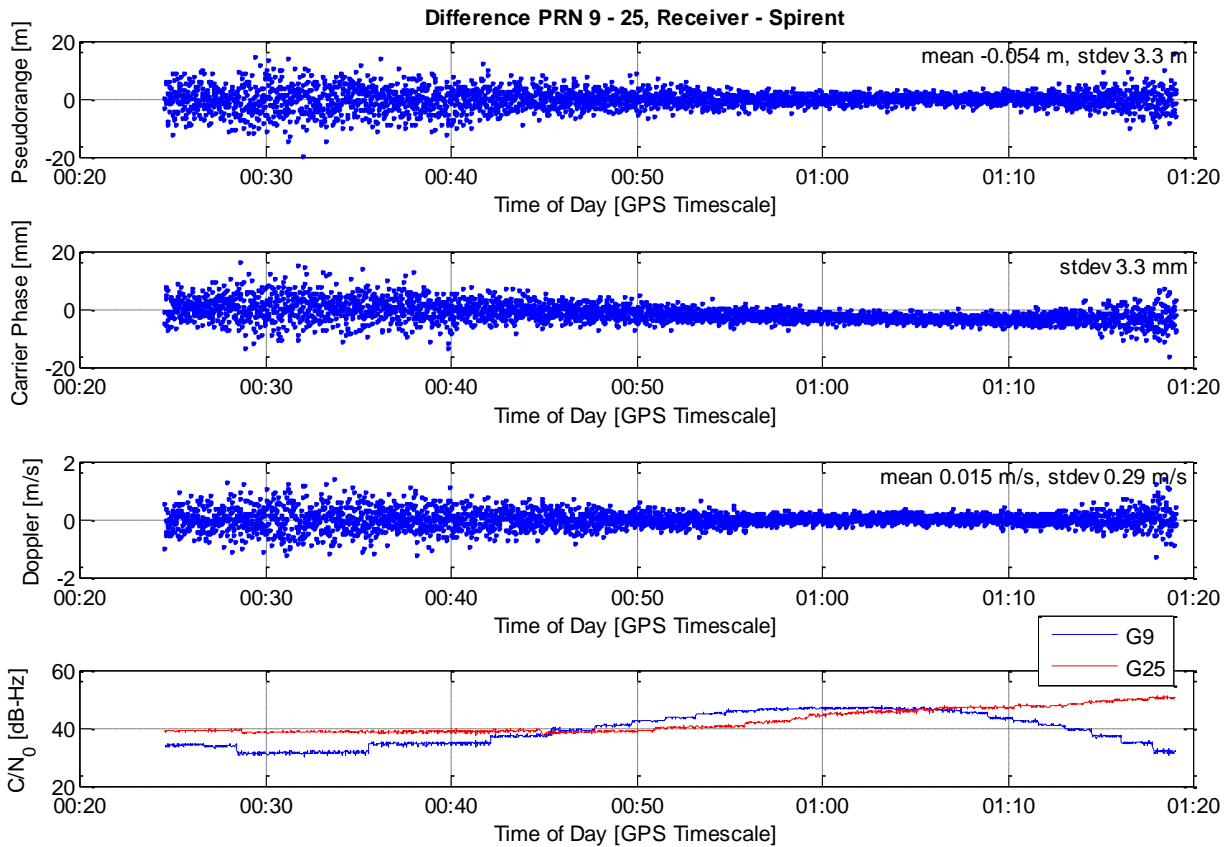


Figure 5-12: Single difference pseudorange, phase and Doppler measurement quality

A small timing offset, of 1.6 micro seconds, had to be applied to compensate for a time stamping mismatch between the Spirent truth trajectory and GSNRx™ measurements. The problem reflects a mismatch between the timing of code and phase measurements, but includes the combined contributions of receiver and simulator and is first mentioned in (Montenbruck et al 2006). Without this correction, time varying errors of a few mm appear in the phase differences. The root cause of the timing offset is unknown.

The noise levels in the pseudorange, carrier phase and Doppler plots show a clear C/N_0 dependence. The theoretical thermal noise jitter for the linear combination of PRNs 9 and 25 was calculated based on the equations for code and carrier tracking loops in Eq. 5-1 and Eq. 5-2 from Ward et al (2006), and plotted along with the actual pseudorange and phase noise in Figure 5-13

and Figure 5-14. In the equations, $\sigma_{thermalDLL}$ and $\sigma_{thermalPLL}$ are the code and phase thermal tracking noise standard deviations in metres, c is the GPS defined speed of light, T_c is the chipping period in s/chip, λ is the signal's wavelength in metres, B_{DLL} and B_{PLL} are the code and carrier loop bandwidths, here $B_{DLL} = 0.5$ Hz and $B_{PLL} = 15$ Hz, B_{fe} is the front end bandwidth, here 8 MHz, CIT is the coherent integration time, here 10 ms, C/N_0 is the carrier to noise density in dB-Hz, and D is the early to late correlator spacing, here 0.4 chips.

$$\sigma_{thermalDLL} = \frac{c}{T_c} \sqrt{\frac{B_{DLL}}{2 \cdot C/N_0} \left(\frac{1}{B_{fe} \cdot CIT} + \frac{B_{fe} \cdot CIT}{\pi - 1} \left(D - \frac{1}{B_{fe} \cdot CIT} \right)^2 \right) \cdot \left(1 + \frac{2}{CIT \cdot C/N_0 (2 - D)} \right)}$$

Eq. 5-1

$$\sigma_{thermalPLL} = \frac{\lambda}{2\pi} \sqrt{\frac{B_{PLL}}{C/N_0} \left(1 + \frac{1}{2 \cdot CIT \cdot C/N_0} \right)}$$

Eq. 5-2

The figures show reasonable agreement between the actual noise standard deviation and the theoretical values. The code measurements appear to have somewhat more noise than would theoretically be expected, while the phase noise shows closer agreement. Additionally, the carrier phase error shows no cycle slips, which is a promising result for the future relative positioning work. A constant ambiguity value was removed from the carrier phase time series.

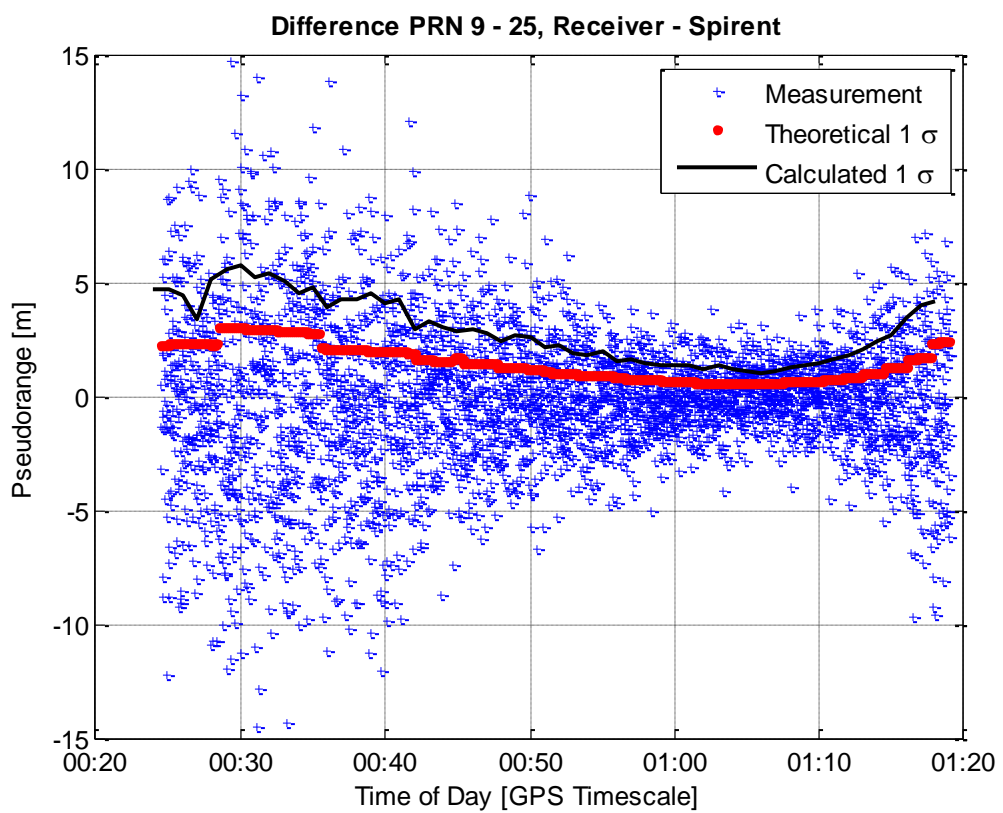


Figure 5-13: Theoretical 1σ tracking jitter vs actual pseudorange measurement noise

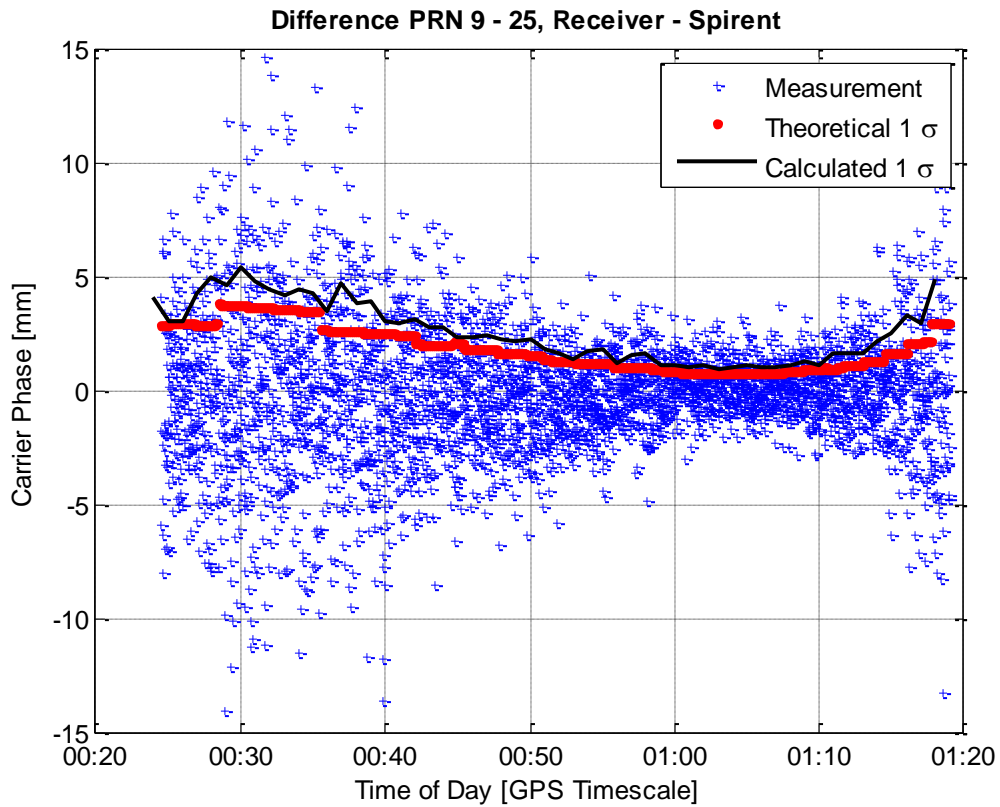


Figure 5-14: Theoretical 1σ tracking jitter vs actual carrier phase measurement noise

5.5.3 Navigation Solution

In addition to the measurements, the receiver's ability to produce an accurate navigation solution was assessed. A position solution was only possible during the perigee passages. The position solution over the first perigee arc is broken into tangential, normal and cross track components and compared to the Spirent truth trajectory in Figure 5-15. The fourth subplot shows the time series of the simulated ionospheric delay on all satellites for comparison. The receiver reaches perigee at 60 minutes.

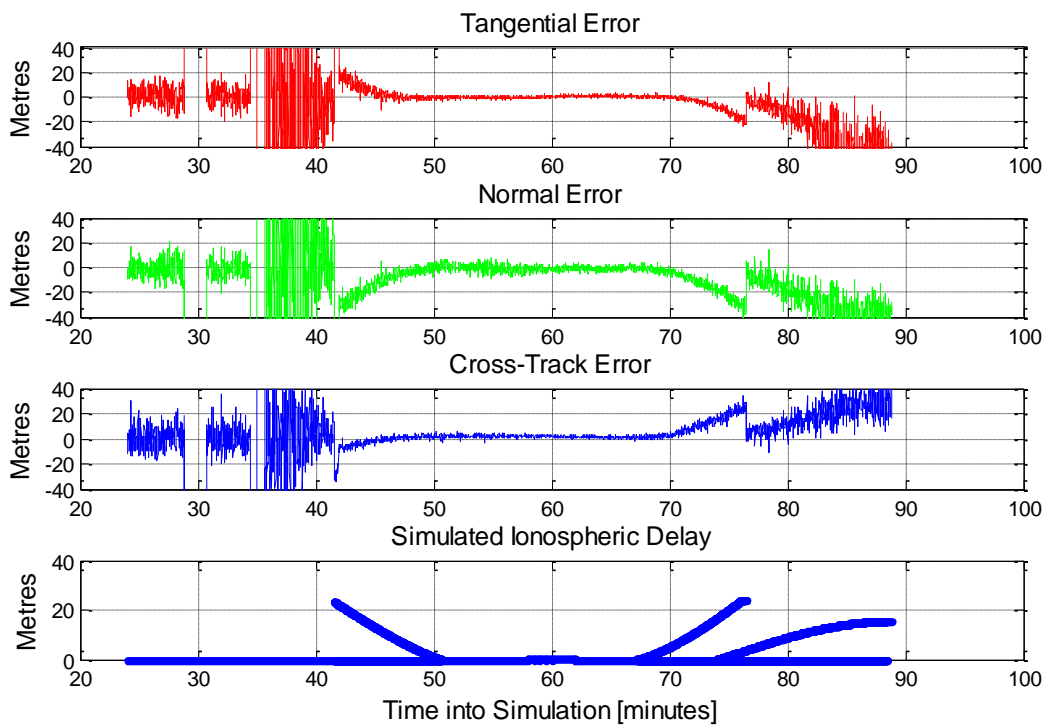


Figure 5-15: GSNRxTM's internal navigation solution accuracy during a perigee passage

The errors appear large at first glance, but it is clearly visible that there is a strong correlation between the simulated ionospheric delay and the position errors. Where no ionospheric effects are simulated, or very minimal effects at perigee, the navigation solution is zero mean. When significant ionospheric delay is simulated from roughly 40-50 minutes and 70-90 minutes, it comes entirely from GPS satellites grazing the Earth's surface, which are clustered in one part of the sky and therefore all bias the solution in the same direction. Their impact on the navigation solution is not surprising, because the version of GSNRxTM used for this work has no algorithms to mitigate or correct ionospheric errors, and no effort is currently being made to mask out signals grazing the Earth. Mitigating ionospheric effects will clearly be important for future work.

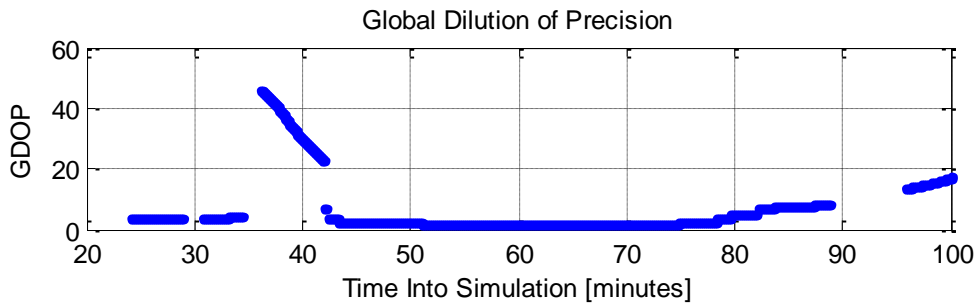


Figure 5-16: Global dilution of precision during the first perigee passage

Another source of error in the navigation solution is noise, which is particularly significant between 35 and 40 minutes. At present, the receiver's internal navigation solution has been set up to use single point least squares solutions, so no filtering is being applied to reduce the noise. In this case, the noise is being magnified by the poor geometry before the receiver has fully reached perigee, shown in Figure 5-16.

Several strategies could be implemented to dramatically improve the navigation solution, for example a more robust outlier detection to reject the biased measurements, a more conservative elevation mask to block out the signals closest to the Earth, the use of dual frequency measurements to mitigate ionospheric range delays, and the use of a filter tuned for orbital dynamics to better filter out the noise and constrain the solution.

5.5.4 Filtered Solution

A preliminary filtered solution was calculated outside of the software receiver. The filter is an extended Kalman filter, with the prediction step carried out using an orbital model and fourth order Runge-Kutta numerical integration. The filter models the Earth's gravity field to degree and order 10, solar radiation pressure, luni-solar gravity perturbations, tides, and atmospheric drag. The filter intentionally does not use the same orbit model as the simulator, to avoid unrealistically good results from a “perfect” orbit model. The spacecraft area, initial solar radiation pressure coefficient and initial drag coefficient used for the filter were also all increased by 10% compared to the true values in Table 5-2. The filter makes use of the GRAPHIC (Group

and Phase Ionospheric Correction) linear combination, which is essentially the average of pseudorange and phase measurements (Yunck 1996). The GRAPHIC measurements are ionosphere free but subject to float ambiguities which must also be estimated in the filter.

The results presented here use a preliminary filter design, based on a LEO filter (Montenbruck and Ramos-Bosch 2008), which had yet to be optimally tuned for HEO. It later evolved into the relative positioning filter of Chapter 7. Here, no outlier detection or removal had been implemented, and the filter initialization was not robust. A good initialization was particularly important for the sparse initial data set, because the filter has insufficient time to recover and fully converge from a poor initial position during the perigee arc.

In spite of the preliminary design, the filtered results are of interest in order to get a more realistic idea of the achievable GPS based position accuracy throughout the HEO orbit, rather than exclusively at perigee. The results for a full orbit, beginning 15 minutes before the first perigee passage (for good initialization) and extending to the end of the simulation, are shown in Figure 5-17.

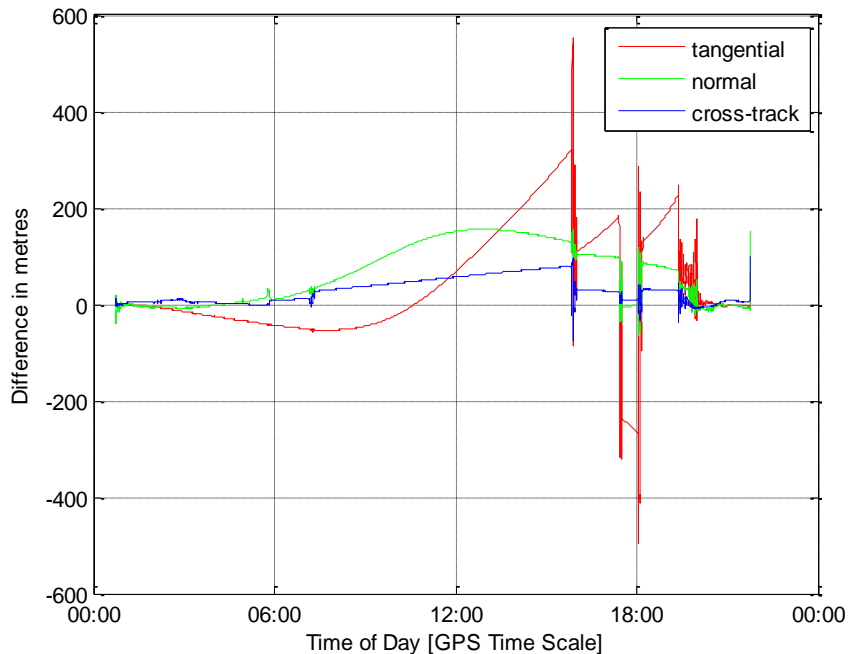


Figure 5-17: Filtered Position Solution

The filtered results are significantly better than the receiver's navigation solution, with metre level accuracy at perigee, and less susceptibility to the ionospheric errors, and availability throughout the orbit. No component having errors greater than 300 m, except briefly as it converged with the addition of new measurements, even after 8 hours of pure propagation. This result was particularly encouraging, because in spite of the preliminary version of the algorithm it agreed well with the achieved accuracies from the earlier MMS HEO study presented in Bamford et al (2009). The filter was able to re-converge for the second perigee passage, and the GPS measurement updates, which occurred each time two or more signals were tracked, are clearly visible in the filtered solution. This is in keeping with expectations as only a simple clock model, estimating clock bias but not drift, is employed in the preliminary filter.

5.6 Conclusions

The outcome of the work presented in this chapter is that the GSNRxTM software receiver was brought to a solid starting point for further HEO receiver design research. The central "bookkeeping" algorithms of the receiver were updated to work with simulated orbital data, and tested for GPS L1 C/A signals with a hardware simulator. Under testing it was proven that the standard GPS acquisition and tracking algorithms in the receiver provide sufficient measurement quality to proceed with the relative positioning research. A preliminary filtered result was also shown to achieve performance in keeping with the relevant literature at the time.

It was found that the basic HEO version of GSNRxTM could be further improved to greatly enhance its performance. With updates, the navigation solution could be adjusted to screen out low elevation PRNs, filter the solution from epoch to epoch, apply ionospheric range delay corrections to signals, or even to implement a more robust outlier detection strategy such as receiver autonomous integrity monitoring (RAIM). In keeping with the end goal of relative positioning, these considerations have not been addressed in the receiver, and are instead implemented into the relative positioning filter of Chapter 7.

The looming problem of sparse data, however, also appears in the first hardware in the loop simulation. In keeping with the conclusions of Chapter 3, the weak signal and multi-constellation capabilities of the receiver are explored next in order to provide a solution. While the weak signal acquisition and tracking algorithms were briefly tested at this point, it came as no surprise that significant redesign would be required to adapt them for the HEO use case. The version of GSNRx™ presented here was also ready to test with multi-constellation data, as the receiver was already GPS, GLONASS, Galileo and BeiDou capable.

The next steps in the receiver design work were therefore to produce a more sophisticated simulation, with multiple constellations and a pair of user receivers, and to look more closely at the weak signal acquisition and tracking toolboxes, all of which are presented in Chapter 6.

Chapter Six: Multi-Constellation and Weak Signal Tracking

Building on the single constellation work of the previous chapter, this chapter presents first the creation of a sophisticated simulation of GPS L1, Galileo E1 and BeiDou B1 signals for use with the GSNRx™ software receiver in section 6.1. In section 6.2 there follows a more detailed look at the signal structures of those signals, and the further adaptation of GSNRx™ to reliably acquire, track, and produce accurate pseudorange, Doppler and phase measurements. The focus is on how the signal design and HEO environment guided the receiver algorithm choices. Finally, the measurement availability and quality under different acquisition and tracking algorithms is assessed in section 6.3 accompanied by a discussion of how the specifics of each constellation and its signal structures impact the HEO positioning problem.

This study is unique in several aspects. It is among the first studies of this type to take into account the azimuthal variation in the transmit gain patterns of the GNSS satellites. Also, it is one of the first, if not only study to consider the BeiDou regional system, and the inherent advantages of the higher geostationary and inclined geosynchronous satellites, in anything other than a visibility simulation for above the constellation positioning. It provides a fair comparison of the performance achieved with each of the three systems, based on the strengths and limitations of the signal structures and the constellation geometry, as well as the acquisition and tracking algorithms implemented in the software receiver. Finally, it puts the results into the context of existing missions.

6.1 Simulation

As in the previous chapter, the basic test setup for this research consists of three parts: A hardware GNSS simulator which recreated the signal environment at the user's antenna, a hardware front end which sampled and down-converted the incoming signals and logged binary intermediate frequency data to files, and the software GNSS receiver used to post processes the IF data. As in the previous chapter, the simulation was set up first, the simulator and front end run were run in real time once in January 2015 to produce the data sets, and the resulting data was used as the basis for all the receiver design and testing tasks as well as the results in this and the following chapter.

Three simulations were made. The first was a 15 minute simulation of a stationary receiver positioned in mainland China, to provide a simplified test case with low dynamics and strong signals in a location where the global and regional systems were visible. The remaining two were 21 hour and 45 minute data arcs, corresponding to a single orbit for a pair of formation flying spacecraft in a PROBA-3 type highly elliptical orbit.

6.1.1 Hardware Setup

The hardware setup is shown in Figure 6-1. The simulator is a Spirent GSS8000 hardware simulator capable of simulating GPS, Galileo, GLONASS, BeiDou, SBAS and QZSS. It was decided to log binary IF data during the simulations to facilitate receiver development, which has the disadvantage of producing a massive volume of data. The study was therefore limited by the availability of hardware which could write data sufficiently fast to log IF samples, while also offering sufficiently large storage to hold a single file covering a full HEO orbit.

The same Leapfrog front end and Morion MV 89-A03E double oven crystal oscillator as previously mentioned were reused for the multi-constellation work. The simulator uses its own internal oscillator. The data was logged onto a Panasonic Toughbook laptop with an internal 1 TB solid state drive, which was able to keep up with both the high logging rate and volume of data for two simulations, each 21 hours and 45 minutes in duration. A total of approximately 800 GB of raw IF data was logged.

The selected frequencies for the two front end channels were L1 (1575.42 MHz) and B1 (1561.098 MHz), which allowed for the capture of GPS L1, Galileo E1 and BeiDou B1 data. For future use, QZSS and select SBAS satellites were also simulated, taking full advantage of the capabilities of the simulator and the shared L1 frequency, but they have not been considered for the present study. B1 was chosen for the second frequency rather than GLONASS L1 because it allowed the novelty of the GEO and IGSO satellites belonging to the BeiDou regional system to be explored, and because no transmit gain pattern information could be found for the GLONASS

satellites. IRNSS was neglected as no interface control document had been published at the time the simulation was set up, it provides no L1 signals, and it was not supported by the simulator.

Despite the advantages that dual frequency data would have offered, L5/E5a was also not a viable option for the simulation because of its wider bandwidth. It would have required 40 MHz logging (on both channels) which would ultimately have produced four times as much IF data. The resulting volume, approximately 1.6 TB for a single 22 hour simulation, exceeded the storage capacity of the largest commercially available solid state drive at the time of the data collection, and earlier testing showed that the USB port on the available raid array did not reliably supply sufficient power to the Leapfrog front end to run uninterrupted for 22 hours.

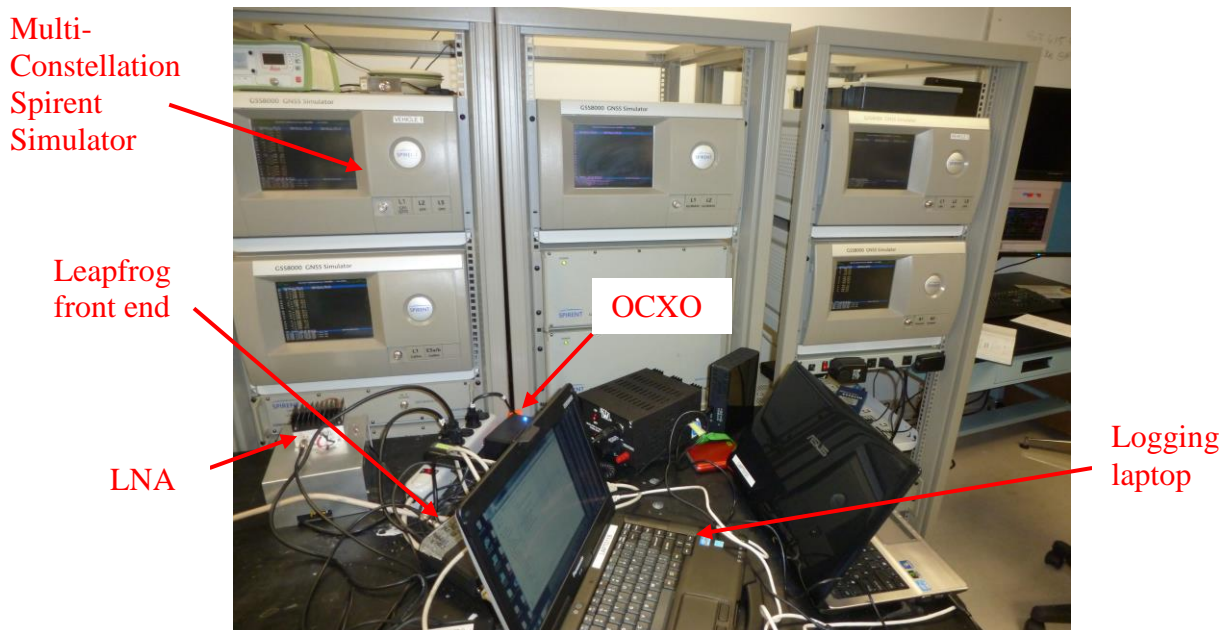


Figure 6-1: Hardware Setup

6.1.2 Simulation Setup

As in previous chapters, the simulation is based on the European Space Agency's planned PROBA-3 mission. The mission consists of two spacecraft, and is a technology demonstration mission for both autonomous formation flying in highly elliptical orbit and for the distributed space telescope concept. A solar coronagraph was chosen as the scientific payload to fit with the mission's space telescope technology demonstration goal. During scientific data takes, the

Occulter Spacecraft (OSC) will cast a circular shadow on the Coronagraph Spacecraft (CSC), which will then be able to image the solar corona under eclipse conditions. During PROBA-3 operations the formation will be dissolved for the perigee passage to avoid the risk of a collision between the satellites, and recaptured for a six hour arc at apogee, during which point the spacecraft will fly in tight formation 150 m apart and aligned with the sun (Landgraf and Mestreau-Garreau 2013, Llorente et al 2013).

The simulation was set up to begin at midnight, GPS time, of November 21, 2014, which corresponds to GPS week 1819, second of week 432000. A GPS UTC offset of 16 seconds was used, which is the actual value for 2014, and the Earth orientation parameters were otherwise set to zeros. As for the previous simulation the duration of the simulation was 21 hours and 45 minutes, with the simulation beginning one hour before a perigee passage, covering one full orbit, and ending one hour after the subsequent perigee passage, making it possible to test the receiver and navigation filter through all phases of an orbit.

6.1.2.1 User Spacecraft Simulation

The PROBA-3 spacecraft were simulated based on the parameters in Table 6-1 and Table 6-2. In contrast to the simplified orbits used for the previous simulation work, user motion files were created outside of the simulator software in order to more closely model the PROBA-3 mission operations. C++ software was written to make the desired user motion files based on the orbit propagation libraries of the GNSS Technology group at DLR. The trajectories were based on the osculating Keplerian elements for the OSC at the first perigee, which were converted to an Earth centered inertial state vector and propagated using a sophisticated orbit model, with a 70x70 gravity field model, and modelling of the solar radiation pressure, drag, ocean tides, luni-solar perturbations and general relativity. Note these are not the same elements as those used in Chapter 6. Based on a conversation with members of the PROBA-3 mission team at the SFFMT conference (Tarabini Castellani priv. com. 2013), the orbital parameters from the previous chapter have been modified to lower the perigee to 600 km from the original 800 km.

Table 6-1: Occulter spacecraft Keplerian elements at the first perigee passage

Semi-major axis	36943137 m
Eccentricity	0.811111
Inclination	59 degrees
Longitude of Ascending Node	142 degrees
Argument of Perigee	-173.0 degrees
Mean Anomaly	0 degrees

Table 6-2: Occulter and Coronagraph spacecraft parameters

PROBA-3 Occulter		PROBA-3 Coronagraph	
Mass	196 kg	Mass	414 kg
Area	1.81 m ²	Area	3.34 m ²
C _{SRP}	1.29	C _{SRP}	1.50
C _D	1.29	C _D	1.50

In keeping with the science requirements of the actual PROBA-3 mission, the maneuvering Coronagraph spacecraft has a static separation from the free flying Occulter spacecraft during science operations.

In order to generate the initial conditions for the simulation trajectory, the Occulter's state was first propagated backwards in time, prior to the simulation start, to the end of the previous apogee measurement arc. At this point the Coronagraph's position was defined as a point 150 m away from the Occulter in the anti-sun direction, and its velocity was defined as the Occulter's velocity vector plus a 0.05 m/s maneuver in the radial direction to break up the formation. Both spacecraft's orbits were then propagated forward to the start time of the simulation to get realistic initial conditions one hour prior to the first perigee passage.

From the initial conditions the positions and velocities of both spacecraft were propagated throughout the simulation, with the following maneuvers applied to the Coronagraph spacecraft:

1. A formation recapture maneuver 20 minutes past the first perigee arc
2. A drift stop maneuver 3 hours before the apogee passage
3. A period of six hours of tight formation flight extending from three hours before apogee to three hours after apogee, in keeping with the actual mission's data collection requirements. During the tight formation flight the Coronagraph's position is constrained to be at a distance of 150 m from the Occulter in the anti-sun direction, and it has the same velocity as the Occulter
4. A maneuver of 0.05 m/s in the radial direction to break up the formation at the end of the tight formation flying arc, for a safe perigee passage

In order for the GNSS simulator to produce smooth signals, acceleration and jerk are also required as input. These were calculated from the orbital positions and velocities using Hermite interpolation. The distance between the two spacecraft throughout the simulation is shown in Figure 6-2.

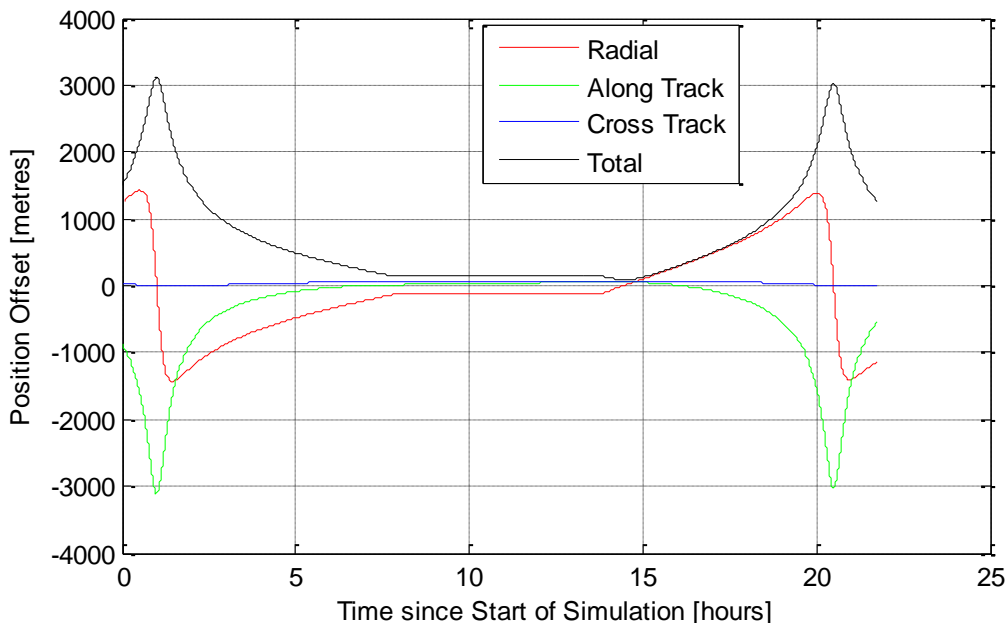


Figure 6-2: Separation between the Occulter and Coronagraph spacecraft as a function of time

The satellites were further given a realistic attitude profile. Although the original goal was to give the spacecraft the same ideal, inertially fixed attitude profile as in previous chapters, an error in the coordinate conversion from ECEF to ECI led to a fixed inertial attitude with the antenna bore sight pointing approximately 15 degrees off perigee for both spacecraft, as shown in Figure 6-3. While the resulting profile is slightly less optimal than the intended profile in terms of GNSS tracking, it is one that is realistic given the PROBA-3 constraint that one axis remain sun-pointing.

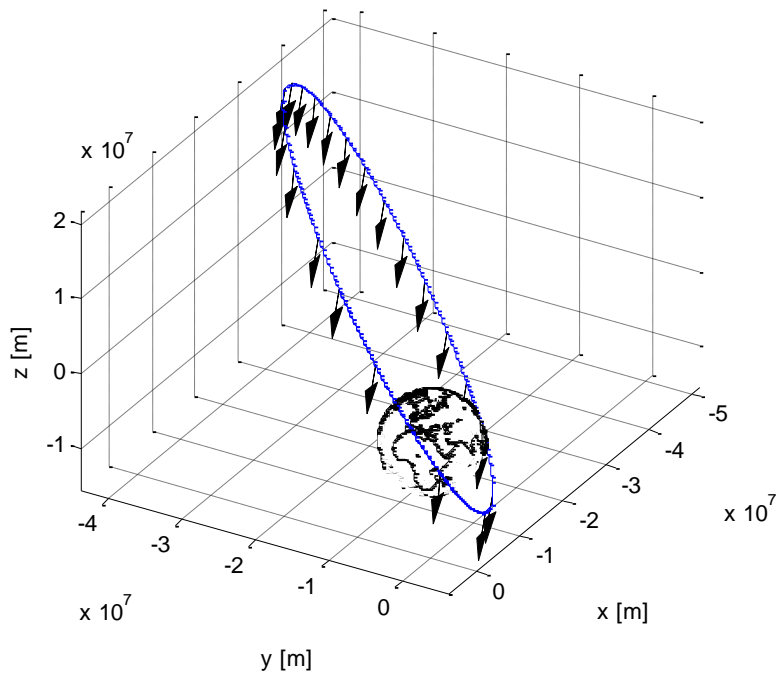


Figure 6-3: GNSS antenna boresight pointing direction

Finally, the same receiving antenna was simulated as in the previous chapter, with a rotationally symmetric hemispheric gain pattern.

6.1.2.2 GNSS Constellations

The GNSS constellations were simulated, where possible, using real data for the date under study. GPS was simulated based on a Yuma almanac for November 21, 2014. Galileo was simulated as a 27 satellite full Walker constellation (Walker 1984), calculated by starting with

the broadcast ephemerides of the satellites already launched by Nov 21, 2014 and filling in the remaining slots in the constellation. Originally, a full BeiDou constellation was similarly computed based on the broadcast ephemerides from November 21, 2014 with additional MEO's added to obtain a 24 satellite Walker constellation. The 24 satellite Walker constellation assumption is based on the GPS World Almanac website (GPS World 2016). Four satellites were then removed to fit within the 30 PRN limit defined by Spirent. Unfortunately, the ephemerides for this particular date triggered a bug in Spirent's handling of the geostationary satellites' ephemerides. The bug was reported to Spirent, but ultimately the default BeiDou constellation file shipped with the simulator had to be used. This file consists of five GEO, and five IGSO satellites forming the regional part of the system, and 20 MEO satellite approximately evenly distributed throughout the globe.

The other critical information for realistically simulating the GNSS constellations are the transmit antenna gain patterns. Unlike previous above the constellation positioning studies and previous chapters, the full azimuthal variation of the antenna gain patterns was considered here. The GPS gain patterns were modelled based on Czopek and Schollenberger (1993) in the case of Block IIA, were taken from the published transmit gain patterns from Lockheed Martin (Marquis 2013) in the case of Block IIR and IIR-M, and modelled based on Fisher and Ghassemi (1999) in the case of Block IIF.

For the Block IIA and IIF antennas designed by Boeing, when this simulation was set up only single cross sections were available, with no information regarding the azimuthal variation. The published patterns were compared to published flight results from GIOVE-A, the earlier AO-40 mission and the SV 49 study (Ebinuma and Unwin 2007, Moreau et al 2002, Ericson et al 2010). Using the published cross sections available in literature as the starting point, 3D patterns were created for use in the simulation. It was assumed that the published patterns were representative of the peak side lobe power, with a sinusoidal variation in azimuth reducing the side lobe power to a minimum of -40 dB at other azimuths. Based on the symmetry of the Lockheed Martin patterns it was assumed that the GPS antennas would have four peaks and four nulls. The resulting patterns used for this study are depicted in Figure 6-4 to Figure 6-7.

Since the simulation was run, NASA published the results of their Antenna Characterization Experiment study (Martzen et al 2015), which revealed that the Block IIA and Block IIF patterns somewhat resemble the original Lockheed Martin Block IIR pattern, with the major exception of a different orientation of the antenna on the Block IIF satellites. These results were unfortunately not yet available at the time the multi-constellation simulation was set up and run, and have consequently not been considered for the work presented in this chapter.

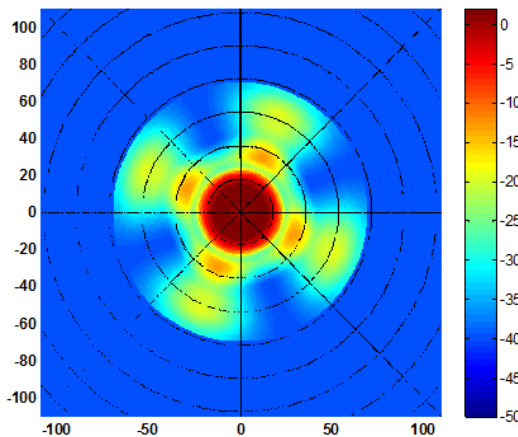


Figure 6-4: GPS Block II A assumed transmit gain pattern based on a 2D pattern

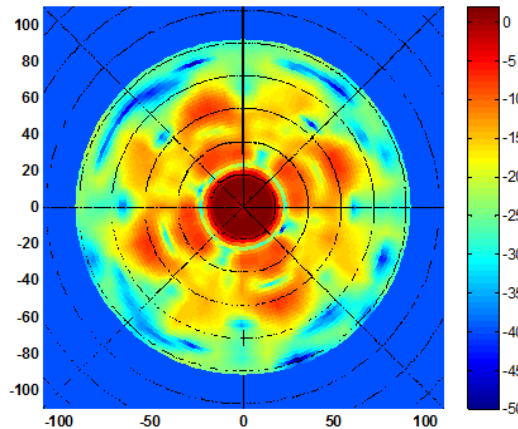


Figure 6-5: Block IIR transmit gain pattern from Lockheed Martin

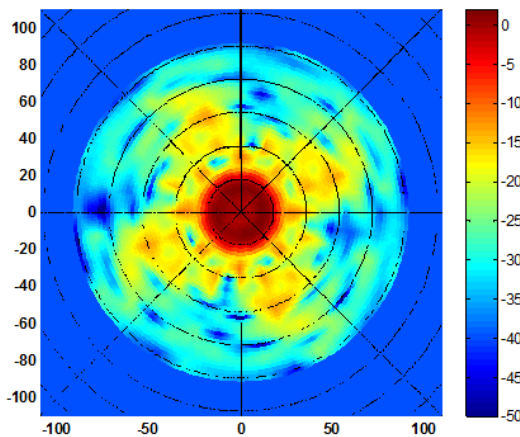


Figure 6-6: Newer Block IIR and Block IIR-M transmit gain pattern from Lockheed Martin

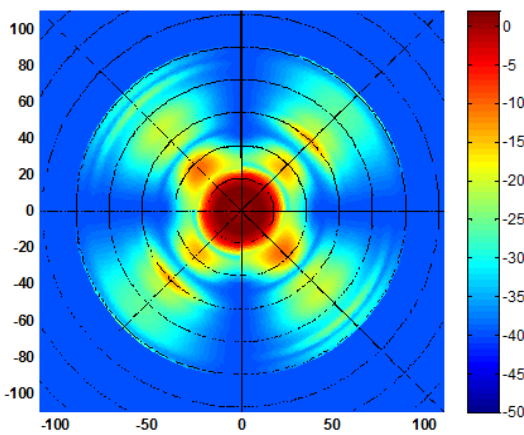


Figure 6-7: Block IIF assumed transmit gain pattern based on a 2D pattern

The Galileo pattern was obtained from Montesano et al (2005), which presented the design of the GIOVE B and In-Orbit Validation (IOV) space vehicle antennas. The IOV antennas are hexagonal. Individual azimuth slices of the antenna gain pattern were digitized from a high-resolution copy of the paper. The reconstructed 3D gain pattern, which has been used for all Galileo satellites in this study, is presented in Figure 6-8.

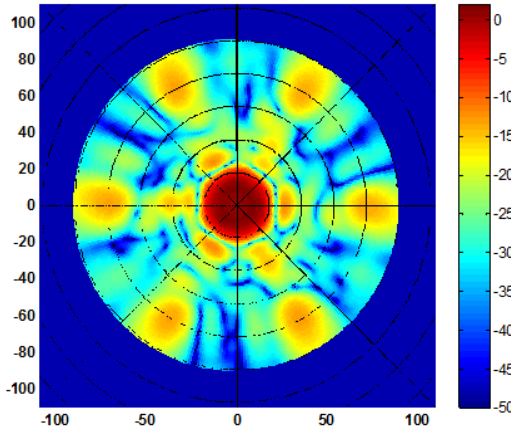


Figure 6-8: Galileo IOV transmit gain pattern

In reality, the final design of the transmit antennas for the fully operational Galileo satellites follows the design of the GIOVE-A spacecraft's square patch antennas rather than the IOV design assumed here, so this study is not fully representative. Some information about the GIOVE-A pattern was published by Valle et al (2006), but they focus on the center of the antenna gain and provide very little information about side lobes, and no information about the azimuthal variation.

BeiDou transmit gain patterns for both the MEO and the GEO/IGSO satellites were published by Zhan et al (2013) with no azimuthal variation information. Although it is not clear from the publication whether these are speculative gain patterns or based on the actual design of the BeiDou III satellites, they have been used for the present study in the absence of other information. Similarly to GPS Blocks IIA and IIF, 3D gain patterns were created based on the assumption that the published profile of the antenna gain refers to the azimuth angle with the highest gain, while at other azimuths there are nulls. Instead of the fourfold symmetry of GPS, online photographs of the BeiDou satellites revealed an inner ring of six antenna elements and an outer ring of twelve elements, so six-fold symmetry has been assumed. The resulting 3D gain patterns used for this study are show in Figure 6-9 for the MEO satellites and Figure 6-10 for the IGSO and GEO satellites.

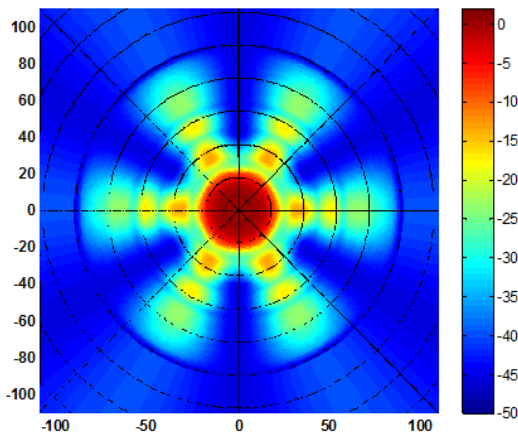


Figure 6-9: BeiDou B1 MEO assumed transmit gain pattern based on a 2D pattern

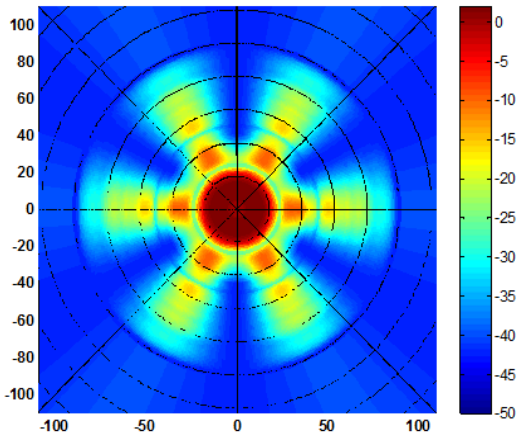


Figure 6-10: BeiDou B1 IGSO/GEO assumed transmit gain pattern based on a 2D pattern

Finally, for the sake of completeness, the patterns assumed for WAAS, GAGAN and QZSS are shown in Figure 6-11, Figure 6-12 and Figure 6-13 respectively, although SBAS and QZSS are neglected for the remainder of this thesis, as the version of the software receiver used here does not support them. The WAAS pattern is derived from the prototype patch antenna in Iriarte et al (2009), and the GAGAN pattern from Jyoti et al (2005). The QZSS pattern is derived from Noda et al (2010), but with the same side lobes added as in the WAAS pattern, given that only the main lobe transmit pattern for the QZSS antenna was published.

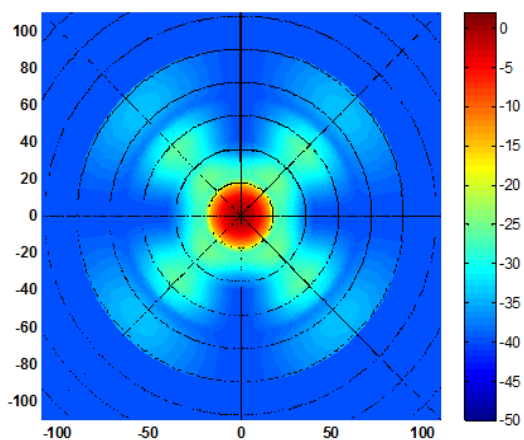


Figure 6-11: WAAS assumed transmit gain pattern based on a 2D pattern

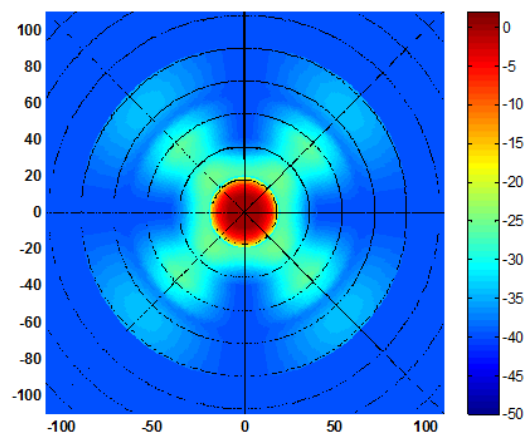


Figure 6-12: QZSS assumed transmit gain pattern based on a 2D pattern for the antenna center and WAAS side lobes

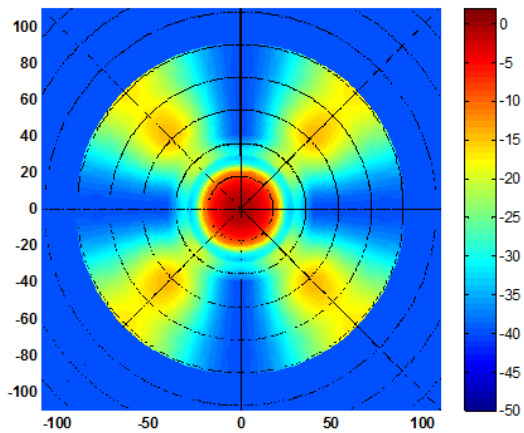


Figure 6-13: GAGAN L1 assumed transmit gain pattern based on a 2D pattern

The Spirent simulator unfortunately does not allow for a realistic modelling of the yaw steering attitude profile employed for GNSS satellites. Consequently, the simulation assumes a GNSS attitude profile in which the same axis is always aligned towards North for all GNSS satellites.

In addition to using appropriate gain patterns, the simulator's signal power was set such that all three signals under investigation were at roughly equal strength, and realistic for a scenario with a user on the Earth's surface. This corresponded to values of -122 dBm for GPS L1 C/A, -123 dBm for BeiDou B1 and -121.88 dBm for Galileo E1b before the above gain patterns (normalized to a peak gain of 0 dB) were applied. Note the simulated signal powers must be intentionally set high in order to compensate for the additional thermal noise in the laboratory setup, mainly from the simulator, and produce realistic values in the receiver.

6.1.2.3 GNSS Errors

Three error sources were considered in the simulation, but only two were modelled in the hardware simulator: ionospheric errors and inter-system timing offsets. The third desired error source, orbit errors for the GNSS satellites, could only be modelled on GPS and Galileo, but the option had not yet been made available on BeiDou or QZSS in the Spirent simulation environment. It was therefore decided not to model orbit errors on any of the constellations, as they have a negligible effect on tracking and can be considered for the navigation solution later by using biased ephemerides in the post processing. Likewise, individual satellite clock errors were not modelled in the simulation.

In order to simulate realistic inter-system timing biases, each satellite's field for setting clock divergence terms was used, and all satellites from the same constellation were given a common value. In all cases only a constant bias was applied (Af_0 term), with an offset of 3 ns for GPS, of -400 ns for Galileo, 7 ns for BeiDou and 35 ns for QZSS. These are the rounded values of the system-UTC offsets obtained in the IGS broadcast ephemeris file from the simulated date (GPUT, GAUT, BDUT and QZUT respectively). The offsets from UTC were used rather than the actual inter-system biases because they were available in a consistent format for all systems,

and offered a realistic order of magnitude. Likewise, the satellite clock divergence field was used to input the parameter because it was consistently handled for all constellations in the Spirent software.

In order to simulate the atmospheric effects, the same height-dependent vertical total electron content (VTEC) profile was used as described in section 5.2.6. Spirent's built-in atmospheric model was then checked by writing an independent program to conduct the same calculation, and comparing with the output simulated delay values from Spirent. A simulation for a LEO satellite (PROBA-V) and a constant TEC atmospheric model ($VTEC = 5 \times 10^{16} \text{ e-}/\text{m}^2$) was initially used, in order to eliminate the dependence of the atmospheric delay on the satellite height.

Based on the user manual (Spirent 2014), for satellites at positive elevations the Lear model is used as shown in Eq. 6-1, where F_c is the centre frequency of the signal, $VTEC$ is the vertical total electron content, and E is the elevation of the GNSS satellite in the receiver's local geodetic frame. A diagram is shown in Figure 6-14a.

$$d_{ionosphere} = \frac{82.1 \cdot VTEC}{F_c^2 \left(\sqrt{\sin^2 E + 0.076} + \sin E \right)}$$

Eq. 6-1

When the receiver is above the atmosphere and the GNSS satellite is visible over the Earth's limb, the Lear function is evaluated for an elevation of zero at the point of closest approach, and multiplied by two for a ray completely crossing the atmosphere (Figure 6-14b). When the receiver is in the atmosphere and the GNSS satellite is at negative elevation, the full delay for a ray crossing the atmosphere is calculated (as in Figure 6-14b), then the "extra" delay on the line of sight beyond the receiver is calculated using a positive elevation and subtracted (Figure 6-14c). All of the elevation and height calculations for finding the point of closest approach are done on the ellipsoid. There are no assumptions of a spherical Earth.

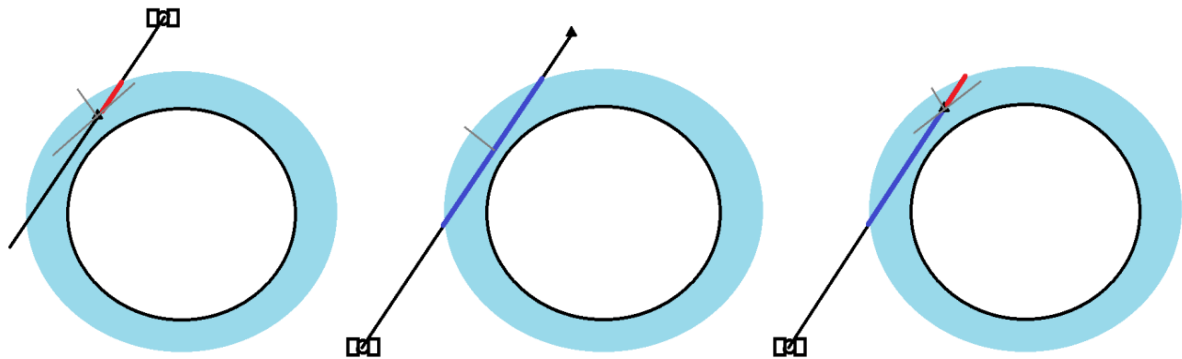


Figure 6-14: a) Positive elevation ionospheric delay (left) b) Negative elevation ionospheric delay when the receiver is outside the ionosphere based on the point of closest approach (centre), and c) Negative elevation ionospheric delay when the receiver is in the ionosphere calculated as figure b – figure a (right)

The result of the comparison with Spirent was that the range delay calculations matched for GNSS satellites at positive elevations, but were slightly different for GNSS satellites at negative elevations (differences of up to 40 cm differences were observed). For the constant VTEC case, a constant offset from Spirent was observed, which indicates that the delay on a signal completely passing through the atmosphere uses some algorithm other than twice the Lear function at zero elevation. A slight discontinuity in the range delay when the GNSS satellite passes from positive to negative elevation also supports this. For the height-dependent VTEC case used in the HEO scenario the mismatch at negative elevations still occurred but was no longer a constant value. Ultimately, it was not possible to completely understand the math behind the simulator, but it was confirmed that the algorithm was allowing for reasonable levels of ionospheric delay to be simulated.

The broadcast orbit errors were modelled based on the study in Montenbruck et al 2015, which assessed the accuracy of a year of broadcast ephemerides for GPS, GLONASS, Galileo, BeiDou and QZSS based on their respective precise ephemerides. For the present study, new sp3 format ephemeris files were generated for use in navigation post-processing, in which constant errors in the radial, along track and cross track directions were added to each GNSS satellite based on normally distributed random numbers, with the standard deviations tabulated in Table 6-3. In this

way the navigation filter of the next chapter can be run either with or without broadcast orbit errors included. Note this is different from the previous chapter, in which only radial errors were applied.

Table 6-3: Simulated Broadcast Ephemeris Standard Deviations

Constellation	Radial (m)	Along Track (m)	Cross Track (m)
GPS	0.18	1.05	0.44
Galileo	0.63	2.65	2.29
BeiDou MEO/IGSO	0.50	2.42	1.31
BeiDou GEO	0.60	9.16	1.38

The impact of these errors on tracking is discussed in further detail in section 6.2.3, and on navigation is discussed in Chapter 7.

6.2 Receiver Algorithms

As mentioned in the previous chapter, the two weaknesses in GSNRTM from the point of view of the HEO research were that it had never been used for any sort of space application, and that it had previously never been used for such a long data set, in particular under weak signal conditions. These new conditions triggered problems in the acquisition and tracking, due, for example, to signals slowly fading out of view, to rapidly changing ionospheric errors as satellites occulted behind the Earth, and to attempting acquisition under high dynamics and when no position fix and consequently no receiver clock update had been obtained for hours.

Furthermore, there is a basic tradeoff involved in detecting and tracking GNSS signals. On the one hand, to detect weak signals the length of the replica and incoming signals which are correlated must be extended, in order for sufficient power to be accumulated to detect the signal above the noise floor. On the other hand, to detect signals under high dynamics shorter coherent integration times are required, because the signal parameters are changing rapidly over time and short coherent integrations are less sensitive to errors in the signal parameters. A receiver in

highly elliptical orbit is faced with both of these situations. Weak signals are prevalent at apogee, while high dynamics are prevalent at perigee. Finding suitable receiver algorithms for highly elliptical orbits is therefore a matter of finding a suitable trade-off between the requirements at different points in the orbit.

While the previous chapter focused on setting up the receiver's higher level logic for space applications, the following sections address the signal processing aspects of the receiver redesign.

6.2.1 Signals

The specifics of the receiver algorithms and achieved performance described in the following sections are driven by the GNSS signal structures. Before discussing the receiver design in depth, this section therefore introduces the specifics of each of the four signals studied: GPS L1 C/A, Galileo E1b, BeiDou B1D1 and BeiDou B1D2. The four signals are depicted in Figure 6-15.

The GPS L1 C/A signal is depicted first. It has a 50 bps data rate, which translates into a data bit, outlined in black, every 20 ms (IS-GPS-200H). This data bit rate is one of the most significant factors in determining signal performance under weak signal conditions, because it limits coherent integration time. Every 1 ms, shown in grey, contains a complete repetition of the PRN ranging code of 1023 chips. The GPS ranging code uses BPSK modulation.

Next is the Galileo E1b signal, which has a 4 ms ranging code of 4092 chips, and a bit rate of 250 bps (European Union 2010). (Note the actual data transmission rate is reduced to 125 bps by the forward error correction. In the context of this study any possible switch in modulation is referred to as a “bit”.) The higher bit rate translates into a possible data bit transition at the end of every 4 ms ranging code, which means acquisition and bit synchronization occur simultaneously, but which presents a disadvantage for acquisition and for tracking with long coherent integration times. To compensate for the limited coherent integration time on E1b, there is also a pilot E1c signal, which similarly has a 4 ms, 4092 chip ranging code and a secondary code with the same 250 bps chipping rate as the navigation data on E1b. For the present study, E1c has not been

considered because no navigation data is transmitted, and because combined data-pilot tracking is outside the scope of the current research. Galileo E1 uses a MBOC(6,1,1/11) modulation, which has a narrower correlation peak than GPS L1 C/A and also side correlation peaks.

Similar to GPS L1 C/A, the BeiDou B1 ranging code is 1 ms in duration. The B1 ranging code, however, has double the chipping rate, with a length of 2046 chips and a QPSK modulation (China Satellite Navigation Office 2016). This again allows for a narrower correlation peak at the cost of requiring a higher bandwidth. Two different data formats are transmitted from the BeiDou system. The BeiDou B1 signal with data message D2 is transmitted by the five geostationary BeiDou satellites, PRNs 1-5, and has a high bit rate of 500 bps which translates to a possible bit transition every 2 ms (again, the actual data bit rate is half due to forward error correction, and “bit” is being used interchangeably with symbol). The high bit rate is necessary because the geostationary satellites function simultaneously as regional navigation satellites and as a satellite based augmentation system. The B1 signal with data message D1 is transmitted from the MEO and IGSO satellites, PRNs 6-35, and has a rate of 50 bps, or one data bit every 20 ms, again similar to the GPS L1 C/A signal. Unlike GPS, it is further modulated by a 20 chip secondary code with a period of 20 ms, aligned with the data bits, leading to a possible chip transition every ms. The purpose of the secondary code is to allow for faster bit synchronization.

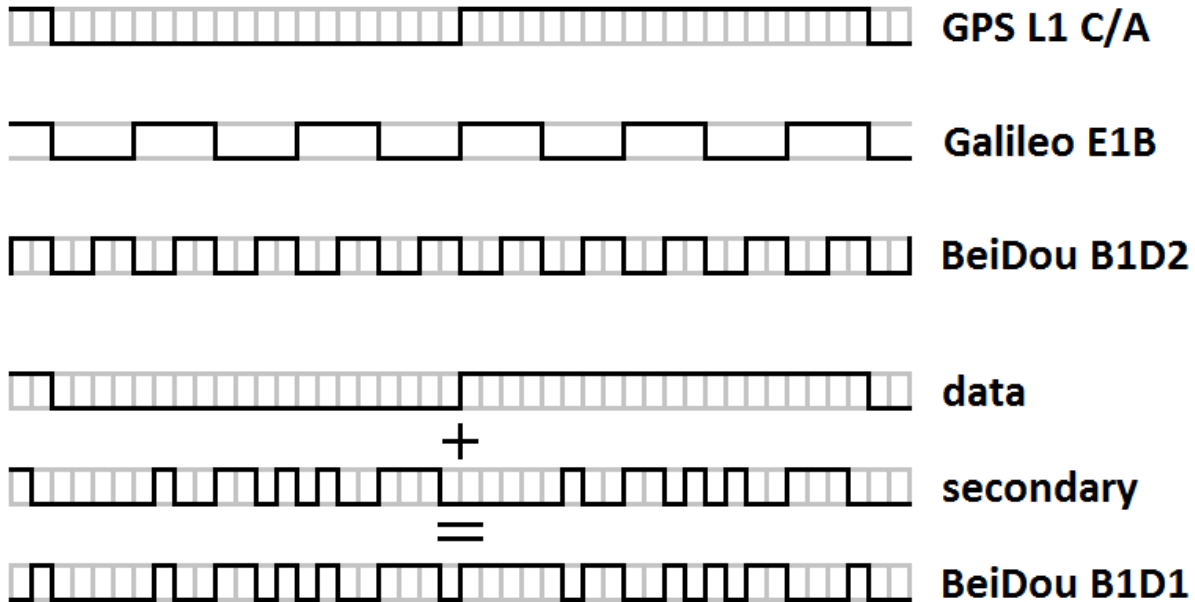


Figure 6-15: GNSS Signal Structures

Two requirements were considered when choosing the signals and tracking algorithms for this study. First, the signals must contain a navigation message and it must be possible to decode and use it – the main advantage of GNSS receivers for spacecraft navigation is that they operate autonomously and therefore avoid the complications and expense of ground infrastructure. A system requiring that data bits or navigation data be constantly uploaded to the spacecraft is impractical. Second, because the larger goal is to use the data for relative positioning, ideally with carrier phase ambiguity resolution, the receiver algorithms presented in the following section must be capable of producing carrier phase measurements of sufficient quality for relative positioning, ideally with integer ambiguity resolution.

6.2.2 Acquisition

In a sky search, the receiver must test all combinations of code delay, Doppler frequency, and ranging code (PRN) to find the signals. As previously explained in section 5.2.3, to decrease the search space a simple orbit propagator was implemented in the receiver, which is used in

conjunction with stored almanacs to predict both the satellites in view and the estimated Doppler shift for its search.

The Keplerian orbit used for the HEO formation flying data set is based on initial osculating orbital elements for the non-maneuvering spacecraft. It is accurate to roughly 100 km and 10 m/s except during perigee passages, when the errors can grow as large as 1000 km and 600 m/s. Because the receiver maintains a position fix through perigee, it is insensitive to these larger errors. To expand the warm start capability for the multi-constellation data set, almanac decoding and storage functionality had to be added for BeiDou B1 and Galileo E1b. The receiver had previously operated using only ephemerides for these systems, which worked well for the typically short research data sets but didn't realistically replicate operations in orbit.

In addition to the relative velocity between the receiver and GNSS satellite, the Doppler shift on acquisition is also a function of the receiver clock drift. For the data sets considered here, the nearly constant clock drift of 2 m/s or 10 Hz is sufficiently small to make very little difference in the identification of the correct Doppler bin. The assumption of a highly stable clock would however have to be carefully revisited for an actual mission, depending on the quality of the onboard clock and its behaviour under the harsher orbital conditions as compared to the benign test conditions in a lab. As a result of the combined Doppler prediction errors, a Doppler search range of +/- 4 kHz around the predicted Doppler bin has been used for the acquisition.

On a signal processing level, the basic version of GSNRxTM acquisition made use of a 1 ms coherent accumulation time for the acquisition of all signals. FFT methods are used to simultaneously search code delays, while the receiver alternately searches positive and negative Doppler shifts. The default algorithm had very low detection thresholds, resulting in a significant number of false positives. These were compensated by two stages of verification, which tested a smaller search grid around the detected signal to confirm that a correlation peak was in fact consistently present before handing it over to the tracking loops. Further, in the absence of an acquisition the receiver was set up to repeat the full search 50 times before giving up on a particular PRN.

In addition to the basic acquisition algorithm, the receiver library also offered a sophisticated “slice-based” weak signal acquisition scheme, which would sweep the search grid at increasing coherent integration times to search for progressively weaker signals, with the goal of quickly acquiring strong signals before beginning a time consuming search for weaker ones. The longer integration time comes at the price of narrower Doppler search bins and a larger acquisition search space, because the replica signal must more closely match the incoming signal for a successful correlation. Neither of these pre-existing acquisition libraries produced the desired acquisition performance, with the simpler acquisition declaring too many false positives to effectively sweep the full search space, and the weak signal strategy being far too time consuming for each PRN given the new “search channel” logic described in section 5.2.5. Customized weak signal acquisition algorithms have therefore been implemented for each of the systems.

6.2.2.1 GPS L1 C/A

The acquisition algorithm implemented for GPS L1 C/A is the half-bits method developed by Psiaki (2001) and implemented into the MMS Navigator receiver (Winternitz et al 2009) as well as the SGR-GEO receiver on Giove-A (Ebinuma and Unwin 2007). This method was chosen based on its proven performance on the Magnetosphere Multiscale Mission, which had been in orbit for nearly a year by the time this work was undertaken. The half-bits method coherently integrates over 10 ms, or half of a data bit. Alternating sets of half-bits are then non-coherently accumulated. As a result of the 20 ms data bits on GPS, one set of half bits will contain all the data bit transitions, while the other set is guaranteed not to include any bit transitions. The greater of the two sets is assumed to be transition free, and is compared to the acquisition threshold. In both the Navigator and GSNRxTM implementations, ten half bits are non-coherently accumulated before detection is attempted, so the testing of a single Doppler bin takes a total of 200 ms. All code delays are searched simultaneously using FFT methods and circular correlation of the GPS ranging code. The Doppler bin width is set to $1/(4 \times \text{CIT})$, where CIT is the coherent integration time. In this case the Doppler bin width is 25 Hz, as per the design of the Navigator receiver.

6.2.2.2 BeiDou and Galileo

The Galileo and BeiDou acquisition schemes are limited by the presence of data or secondary code bit transitions at the end of every ranging code period. In this case FFT methods are still used, but linear rather than circular correlation is used. According to the GSNRx™ documentation (Petovello and O'Driscoll 2007), the underlying algorithm is the overlap-save method from Press et al (1992). The acquisition algorithms do linear FFT correlation by correlating a 1 ms block of incoming signal with a 0.5 ms replica signal, padded with 0.5 ms of zeros. To achieve 1 ms of coherent integration, which is the basic processing block for the receiver, both are then advanced in time by 0.5 ms and a second FFT correlation is carried out and coherently combined with the first. Effectively 0.5 ms worth of code delays are tested with 1.5 ms of incoming data. The choice of a 0.5 ms replica code segment is done based on the current estimate for the range delay. For Galileo each of the eight possible 0.5 ms segments of the 4 ms ranging code must be tested sequentially to guarantee that a signal is detected, and for BeiDou both 0.5 ms segments of the 1 ms ranging code must be tested sequentially. For the 1 ms BeiDou ranging code this doubles the search time, while for the 4 ms Galileo ranging code the search time increases by a factor of 8.

A significant difficulty encountered at this point was recognizing that the FFT code search for Galileo was initially only testing 1 ms of the 4 ms possible code delays. Because the receiver had always previously acquired Galileo satellites based on a hot start using ephemerides and a GPS position solution, which were good enough to predict the initial code delay to within 1 ms, the shortcoming was not apparent. Because of the uncertainty in the HEO scenario's almanacs, approximate orbit and unknown receiver clock, on first testing the multi-constellation functionality Galileo satellites had only a 25% chance of a successful acquisition except during perigee passages. This shortcoming severely degraded the system's usefulness, as Galileo signals were never acquired during the apogee arc when measurements from the other systems were already sparse.

For Galileo, an acquisition scheme is used with 4 ms coherent integration, based on the 4 ms ranging code. These 4 ms coherent integration correlation outputs are further non-coherently accumulated four times. For BeiDou (both B1D1 and B1D2), the presence of either a 1 ms secondary code chip or a 2 ms data bit limited the acquisition to 1 ms of coherent integration. It was calculated that 64 non-coherent accumulations should provide the same power accumulation as the 4 x 4 scheme for Galileo. Upon testing the receiver, the BeiDou acquisition was however increased to use 100 non-coherent integrations in an attempt to acquire signals below 30 dB-Hz.

For both BeiDou and Galileo signals, alternating positive and negative Doppler bins are searched on either side of the predicted bin, and Doppler bin widths of $1/(2 \cdot \text{CIT})$ are used, where CIT is the coherent integration time, as per the original GSNRxTM design.

Finally, while the original GSNRxTM acquisition module was set up to make 50 sweeps through the search space for each PRN in the current receiver implementation this has been reduced to 10 sweeps for Galileo and BeiDou, and to a single sweep for GPS, in order to allow the limited number of search channels to more quickly advance through the full range of PRNs.

6.2.2.3 Dwell Time

Table 6-4 contains a summary of the acquisition parameters for each of the three systems, and dwell time required to search a single PRN of that system based on testing the +/- 4kHz Doppler search space. The total dwell time per PRN is calculated as shown in Eq. 6-2.

$$Dwell = ((coherent + wait) \cdot N_{noncoherent} + realign) \cdot codesegments \cdot Dopplerbins \cdot sweeps$$

Eq. 6-2

Table 6-4: Acquisition Parameters

	Coherent integ. time (ms)	Wait time per coherent integ. (ms)	Number of non-coherent integ.	Average realign time per code segment (ms)	Number of code segments	Dopp bin width (Hz)	Num of Dopp bins	Num of sweeps	Total dwell time per PRN (s)
GPS	10	10	10		1	25	320	1	64
Galileo	4	0.5	4	1.5	8	125	64	10	99.84
BeiDou	1	0.5	100		2	500	16	10	48

From the table, it can be seen that the longer coherent integration time for GPS dramatically increases the search time by increasing the number of Doppler bins, while the longer Galileo code with frequent data bits adds significant inefficiencies into the acquisition search, because time is lost realigning the incoming and replica signals. BeiDou in contrast is limited by a very short coherent acquisition time, which degrades the ability to acquire very weak signals.

6.2.2.4 Threshold Setting

A final important aspect of the acquisition algorithm design is threshold setting. The basic approach to setting an acquisition threshold is to choose a design probability of detection for a single cell, and set the threshold based on the single cell probability distribution function. The probability distribution for a single cell is a Chi-squared distribution with $2K$ degrees of freedom, where K is the number of non-coherent integrations. For purely coherent integration, the threshold can be obtained using the simple relationship in Eq. 6-3, where PFA_{cell_target} is the design probability of false alarm and σ is the standard deviation of the noise floor (Borio 2012).

$$Threshold = -2\sigma^2 \ln(PFA_{cell_target})$$

Eq. 6-3

The system probability of false alarm can then be calculated based on the cell probability of false alarm and the number of cells considered simultaneously, N , using Eq. 6-4 (Borio 2012).

$$PFA_{\text{system}} = 1 - (1 - PFA_{\text{cell}})^N$$

Eq. 6-4

When non-coherent integration is considered, the theoretical cell probability of false alarm can be computed with any of Eq. 6-5, Eq. 6-6, or Eq. 6-7, which are equivalent. Borio (2012) provides the first two alternatives, shown in Eq. 6-5 and Eq. 6-6 (which should be an equivalent function to Eq. 6-5 for use in Matlab), while the GSNRx™ algorithm design document (Petovello and O'Driscoll 2007) provides Eq. 6-7. In all of the equations, Th is the threshold, K is the number of non-coherent integrations, and σ is the standard deviation of a single cell. In Eq. 6-7 Γ is the gamma function and Γ_K the upper incomplete gamma function. The Matlab function *gammaintc* is the lower incomplete gamma function normalized by the gamma function.

$$PFA_{\text{cell}}(Th) = e^{-\frac{Th}{2\sigma^2}} \sum_{k=0}^{K-1} \frac{1}{k!} \left(\frac{Th}{2\sigma^2} \right)^k$$

Eq. 6-5

$$PFA_{\text{cell}}(Th) = 1 - \text{gammaintc}\left(\frac{Th}{2\sigma^2}, K\right)$$

Eq. 6-6

$$PFA_{\text{cell}}(Th) = \frac{\Gamma_K\left(\frac{Th}{2\sigma^2}\right)}{\Gamma(K)}$$

Eq. 6-7

Implementing these equations met with the difficulty that far too many false positives were occurring, causing the acquisition channels to attempt tracking and loose lock before the full acquisition grid could be searched. A potential source of the difficulty is that the distribution is a function of the noise floor standard deviation. In the case of a flexible software receiver such as

GSNRxTM, which may be used with a number of different front ends, the noise floor is estimated based on the incoming samples at run time. The threshold is however a fixed value which must be chosen in advance, and which may not fit with the reality of the data set being processed.

For all of the signal specific acquisition algorithms the acquisition threshold has therefore been determined in two steps. First, Eq. 6-7 was used in order to determine the expected order of magnitude of an acquisition threshold corresponding to a system probability of false alarm of 0.01. Next, using the approximate order of magnitude as a starting point, the static ground data set was repeatedly run through the receiver and the threshold was raised or lowered empirically until the signals were reliably detected with a minimum of false alarms.

One final note about the HEO acquisition is that even at points in the orbit where the signals are expected to be strong, the weak signal acquisition algorithms are used. While this is expected to slightly slow down the acquisition, the visible constellation changes sufficiently slowly compared to the time required for a full sweep through all PRNs to produce good results, and the higher dynamics at perigee do not appear to negatively impact any of the implemented algorithms.

6.2.3 Tracking

Similar to the acquisition, GSNRxTM offered two tracking algorithms of relevance to this research: a standard tracking strategy and a weak signal tracking strategy. In the receiver's architecture, a tracking strategy is essentially a sorted list of available tracking loops, and the logic to seamlessly switch between tracking loops based on the current status of the signal tracking. The switching logic is based on three numbers: the estimated carrier to noise density ratio (C/N_0), the phase lock indicator (PLI), and the frequency lock indicator (FLI), which are further discussed in section 6.2.5. Unlike the acquisition strategies, both pre-existing tracking strategies provided reasonable performance under HEO operating conditions from the beginning. Nevertheless, with some slight tuning the performance was better tailored to the space application. This section first describes the default standard and weak signal tracking strategies, second discusses the creation of a HEO tracking strategy based closely on the weak signal

strategy, and third briefly discusses the receiver's vector tracking algorithm and an attempt to use it for HEO tracking.

6.2.3.1 Pre-existing Tracking Strategies

Although there are a nearly unlimited number of tracking loop permutations and combinations that can be set up and tested in GSNRxTM, two existing tracking strategies have been the basis for the current research. The first is the standard tracking strategy, consisting of six trackers as outlined in Table 6-5, which linearly progresses through all six levels to pull in the signal, and drops to lower levels in case of tracking difficulties. The second is a weak signal tracking strategy, outlined in Table 6-6, which has two possible pull-in paths, either using a fine search grid open-loop tracking to refine the estimates of the signal parameters if the signal is judged to be weak, or a more traditional set of pull-in tracking loops for strong signals. Both paths ultimately lead to the Kalman filter tracking loop.

The Kalman filter tracker simultaneously estimates five states for the signal being tracked: Doppler, Doppler Rate, code delay, carrier phase and signal amplitude. It takes post-coherent accumulation I and Q values as input measurements directly, rather than relying on discriminators. The algorithm is described in detail in Petovello et al (2008b) and He and Petovello (2015).

Table 6-5: Standard Tracking Strategy

Tracker	PLL/FLL loop order	PLL/FLL bandwidth	DLL loop order	DLL bandwidth	max CIT (ms)
FLL DLL Pull-In	2	8.0	2	1.5	1
FLL DLL	2	8.0	2	1.5	1
FLL Assisted DLL	2	6.0	1	1.0	1
PFLL Assisted DLL	3	15.0	1	1.0	5
PLL Assisted DLL	3	15.0	1	2.5	5
PLL Assisted DLL	3	15.0	1	0.5	10

Table 6-6: Weak Signal Tracking Strategy

Tracker	PLL/FLL loop order	DLL loop order	max CIT (ms)	Obs Time (ms)
Fine Search 1			1	200
Fine Search 2			5	200
FLL DLL Pull-In	2	2	1	
FLL DLL	2	2	1	
FLL Assisted DLL	2	1	1	
Kalman Filter	3	1	10	

Note that for any tracker, the maximum coherent integration time is in fact a maximum value, but a shorter coherent integration time may be used if it is limited by the bit rate of the signal being tracked.

6.2.3.2 HEO Tracking Strategy

Over the course of this project, a modified version of the weak signal tracking strategy has evolved specifically for the HEO case, which is the strategy used to produce the majority of the results. The HEO tracking strategy is based on the original weak signal tracking strategy, with the following three differences. First, when tracking difficulties are encountered in the Kalman filter tracker, rather than reverting to the fine search 2 tracker, the receiver has been set up to loose lock. Second, the fine search 2 strategy has been eliminated altogether for the BeiDou signals. Third, the more traditional set of pull-in tracking loops were ultimately eliminated.

The more strict loss of lock conditions are necessary on the one hand because the signals slowly fade out, and on the other hand because it is difficult to reliably estimate C/N_0 for weak signals. The absence of meaningful feedback in the fine search trackers means that they will continue to track the peak bin in the fine search grid indefinitely, provided no C/N_0 below a predefined loss of lock threshold is calculated, with occasional attempts to hand the tracking back to the Kalman

filter loop. The result is that extremely weak signals will continue to be tracked and the fine search grid will eventually drift away from the actual signal based on false peaks higher than the actual signal. In some cases, the receiver was observed to continue attempting to track for hours after the signal was no longer simulated at all. These false locks have the significant disadvantage that when the PRNs actually come back into view later they are not sought or acquired. The other disadvantage is that the fine search trackers are extremely computationally intensive and these incorrectly locked channels slow down the entire processing run, in some cases doubling the run time from less than four days to eight days.

Removing the fine search 2 tracker for the BeiDou signals again relates to the signal structures of the BeiDou signals. Because B1D1 has a secondary code with a rate of 1 ms/chip, and B1D2 has a data rate of 2 ms/bit, the 5 ms coherent integration time of the fine search 2 tracker offers no advantage and frequently loses lock because of bit or chip transitions. To compensate for eliminating the second pull-in tracker, logic was added preventing loss-of-lock within the first 1 second of Kalman filter tracking, giving the loop time to converge and the lock indicators time to stabilize.

Finally, it would occasionally happen that all channels taking the “high power” route to the Kalman filter tracker, based on traditional tracking loops, would get stuck in one of the pull-in tracking loop, failing to advance to the Kalman filter tracker or to bit sync. Due to this suspected bug, it was ultimately possible that for an entire perigee passage no measurements would be formed on any system. While the root cause of this problem was never investigated, the immediate solution of removing the FLL-DLL tracking loops altogether, leaving only the fine search and Kalman filter trackers, was implemented. This solution has the disadvantage that it relies on the more computationally intensive fine search algorithms for all signals, but ultimately there is no change in the number of signals acquired and tracked. Also, because only the Kalman filter tracker produces measurements in the updated receiver version, more consistent tracking performance and consequently measurement quality is achieved. The consistent measurement quality is a significant benefit for tuning the positioning filter presented in the next chapter.

6.2.3.3 Vector Tracking

A final note on the receiver's tracking algorithm concerns vector tracking. Vector tracking makes use of the navigation solution to provide feedback to the tracking loops, rather than more standard discriminators and tracking loop filters (Petovello et al 2008a). The basic principle is that a navigation solution based on some strong signals can enable tracking of much weaker signals than would normally be possible. This works because the code delay and Doppler can, at least in theory, be more accurately computed directly from the navigation solution, which optimally combines all the available information on all channels, rather than filtering only the discriminator output of a single channel which is subject to more noise. The GSNRxTM vector tracking implementation was tested, but it was found to provide poor performance. Some investigation into the reasons behind the performance revealed the following challenges:

1. There is a significant risk factor because all channels diverge together or track together. If the navigation solution diverges under the weak geometry of HEO, not only is there a bad navigation solution but all channels will simultaneously loose lock.
2. All the errors on the individual signals have to be modelled as accurately as possible when calculating the replica's code delay and Doppler. Individual channels biased for example by strong, rapidly changing ionospheric errors will fail unless the receiver is able to accurately anticipate and model these errors. While this could be done for the simulated data set given the algorithm in sections 5.3.6 and 6.1.2.3, under real spacecraft operating conditions it would present a major challenge.
3. The vector tracking for a rapidly moving orbiting object would require a much higher rate navigation solution update than the 1 second currently implemented. Further, to get good tracking performance the existing velocity random walk Kalman filter implemented in GSNRxTM would most likely have to be replaced with a proper orbit filter with at least the level of sophistication as the one presented in the next chapter. While neither of these are infeasible, they are also not trivial and would add a substantial computational burden to the receiver operations.

Given these challenges, the decision was made not to further pursue vector based tracking for the HEO application.

6.2.4 Bit Synchronization

When testing the receiver with the HEO data sets, it was found that bit synchronization has an immediate impact on the number of available measurements, because it plays an important role in the receiver's ability to pull in signals from acquisition to tracking and in maintaining lock. The tracking loops can only take advantage of a maximum coherent integration time of 20 ms on GPS and BeiDou B1D1, or 2 ms on BeiDou B1D2, once the alignment of the bit boundaries are known. When the coherent integration time is maximized more signal power is accumulated, resulting in better measurement quality and more reliable tracking. Incorrect bit synchronization on the other hand means that signals are accumulated over bit boundaries and some of the power is cancelled, often causing tracking difficulties or loss of lock. This section discusses the choice of bit synchronization algorithms for each signal, and some of the specific challenges which had to be overcome to achieve good performance.

6.2.4.1 GPS L1 C/A

While the standard version of GSNRxTM uses a histogram bit synchronization algorithm, a weak signal specific algorithm was also available which was found to provide a substantial improvement in performance. GPS bit synchronization therefore makes use of the Maximum Likelihood algorithm developed by Ren and Petovello (2014). The algorithm coherently accumulates the power for 20 ms assuming each of the 20 possible bit boundaries, and uses the accumulated power as a decision statistic. When an assumed bit alignment consistently has the highest accumulated power over 50 consecutive attempts (corresponding to a full second), it is declared to be the correct alignment and the signal is declared bit synched.

After bit synchronization is successful, bit decoding begins in order to decode the navigation messages. In its original version, the bit decoding operated based on the detection of bit transitions rather than the detection of bits, a strategy which is suited to weak signal tracking using frequency lock loops rather than phase locked tracking loops. The disadvantage of

detecting bit transitions is that a single bit error causes the entire bit stream to reverse polarity into the future. In the GSNRxTM implementation this was causing half cycle slips and ambiguities, a major drawback for the intended goal of phase based relative positioning. To simplify the bit decoding and avoid half cycle slip problems, a simpler bit decoding algorithm based on the sign of the in-phase accumulator was implemented. The correct polarity can however still only be identified after the first preamble is detected.

6.2.4.2 Galileo E1b

The Galileo signal E1b signal has a potential data bit transition at the end of every 4 ms ranging code. Bit synchronization is consequently trivially easy, because as soon as the acquisition algorithm determines the code delay, the location of the bit boundaries is known. The absence of a bit synchronization phase and ability to immediately pull in to a tracking loop using 4 ms coherent integration is the most significant advantage of the Galileo signal for the HEO positioning application.

6.2.4.3 BeiDou B1D1

The BeiDou B1D1 signal, as previously mentioned, has a secondary code with a 20 ms duration, which is used to assist in bit synchronization. The B1D1 bit synchronization algorithm works by circularly correlating the 20 chip secondary code with 20 consecutive 1 ms correlator outputs. The correlation peak occurs when the secondary code is aligned, although this method is susceptible to bit transitions. The secondary code is then wiped off of the next 20 incoming 1 ms correlator outputs, beginning with the detected start of the data bit. If all 20 ms are found to have the same sign after secondary code wipe off, the signal is declared bit synchronized. If the wipe off fails to produce 20 ms with the same sign, the bit synch process is restarted. This bit synchronization method is extremely fast, requiring only 40-60 ms of incoming data depending on the initial bit alignment, and a potential further 40-60 ms if the initial bit boundary estimate is incorrect.

6.2.4.4 BeiDou B1D2

The BeiDou B1D2 signal has a data bit transition every 2 ms. The original bit synchronization algorithm was based on the detection of consecutive identical bits with no transitions, rather than detecting the bit transitions themselves. Unfortunately, significant portions of the simulated navigation message for the BeiDou geostationary satellites are not populated. The simulation only populates subframe 1, containing almanac and ephemeris data, and the preamble and time at the beginning of the remaining four subframes, but not the full augmentation system data. A sample of the data bit stream decoded from BeiDou PRN 5, illustrating this, is shown in Figure 6-16.

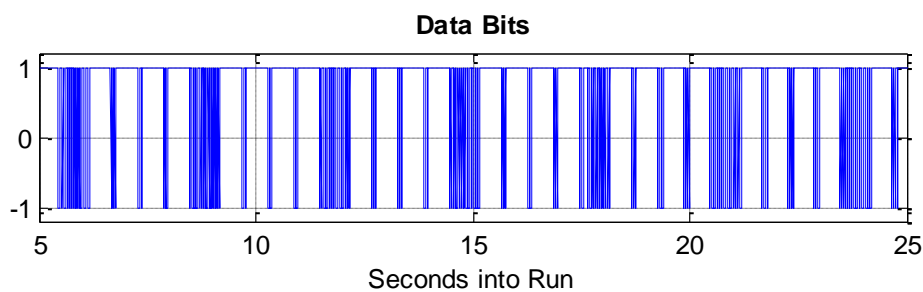


Figure 6-16: BeiDou PRN 5 data bits

Although this is not representative of live data from the actual BeiDou constellation, to achieve reasonable results from the present simulation study it was still necessary to have a functional bit synchronization algorithm. The B1D2 bit synchronization algorithm was therefore rewritten to detect bit transitions rather than continuous bits. It requires that over 2 seconds of data, at least 10 percent of the 2 ms epochs have bit transitions detected before the bit boundary is declared. The low requirement for only 10 percent stems from the simulated data, which is only populated to approximately the 20% level. Note that bit sync will never be declared before the full 2 seconds are elapsed, in order to avoid long periods of simulated data with no bit transitions. This makes the B1D2 bit sync by far the slowest of the algorithms, and along with the high bit rate contributes to the relatively strong signal power required to acquire and pull-in the B1D2 signals, discussed in the results section. The live signal would have improved bit sync performance.

6.2.5 Lock Indicators and C/N₀ Calculations

According to GSNRx™ documentation (Petovello and O'Driscoll 2007), the receiver is using frequency lock indicators as described in Mongrédiens et al 2006, while the phase lock indicator and narrowband to wideband power ratio algorithm used for C/N₀ estimation are described by Van Dierendonck (1996).

6.2.6 Run Time

As a final note of interest on the software receiver, it takes typically 3-4 days to process the 22 hour IF data sets collected for this study, with both data sets running in parallel on an Intel Core i7, 2.2 GHz laptop computer and the raw data stored on an external hard drive.

6.3 Results

The receiver performance results have been sorted based on tracking strategy, with the results from the “standard tracking” version of the receiver, which highlight the constellation dependencies, presented first. The results from the Kalman filter based “HEO tracking” version of the receiver follow, which highlight the advantages and limitations of weak signal tracking. For each receiver version, the C/N₀ at acquisition and loss of lock, the time series of the number of tracked GNSS satellites, and the measurement quality is assessed.

In order to have access to the full array of assessment tools from both the DLR and University of Calgary’s research groups, a converter from GSNRx™ specific data formats to the receiver independent exchange (RINEX) file format was written. In the following sections references to “RINEX” in the text and the figures is therefore referring to receiver output, whereas references to “Spirent” are referring to simulator truth files.

6.3.1 Results for the standard tracking strategy

The standard tracking strategy very nicely highlights the differences among the GPS L1 C/A, Galileo E1b, BeiDou B1D1 and B1D2 signals. For each of the four signals, the C/N₀ at acquisition and at loss of lock throughout both the Occulter (OSC) and Coronagraph (CSC) data

sets have been compiled into a histograms. These histograms are formed based on the receiver's reported C/N₀ values at the first epoch a particular PRN's pseudorange measurement appears in the output RINEX file, and at the last epoch the PRN is present. As such, only signals which have not only been acquired, but have also been stably tracking for long enough to decode the transmission time and form a pseudorange are considered.

Figure 6-17 shows that in spite of the superior acquisition algorithm, the acquisition threshold for GPS L1/CA remains at roughly 37 dB-Hz as first presented in the previous chapter. The loss of lock threshold is likewise similar to the earlier results, and again bi-modal as a result of some signals fading while other GNSS satellites abruptly set behind the Earth. This result is interesting, as it reveals that the acquisition algorithm itself is not the limiting factor in receiver performance. The weakness is instead the pull-in, because while acquisition makes use of longer coherent integration times, the first three levels of pull-in tracking loops are limited to 1 ms coherent integration.

Using GPS as the benchmark, it can be seen that a similar level of acquisition performance is achieved for Galileo E1b, shown in Figure 6-18. In contrast, majority of Galileo signals lose lock at 31 or 32 dB-Hz, higher than the 29 dB-Hz threshold for GPS, in keeping with the shorter maximum coherent integration time.

For the two BeiDou signals, shown in Figure 6-19 and Figure 6-20, B1D1 appears to present a greater challenge to the acquisition, with signals typically being acquired at 40 dB-Hz, while the B1D2 signal has a similar 37 dB-Hz acquisition threshold to the GPS and Galileo signals. In contrast, the loss of lock C/N₀ on B1D1 is the lowest of all the signals, due most likely to the combination of the 20 ms data bits allowing for longer coherent integration. For the BeiDou geostationary satellites transmitting B1D2, the 2 ms data bits limit the coherent integration even more severely than the 4 ms bits on Galileo, and consequently the lock is typically lost at a C/N₀ of 34 dB-Hz or above, which is higher than any of the other signals.

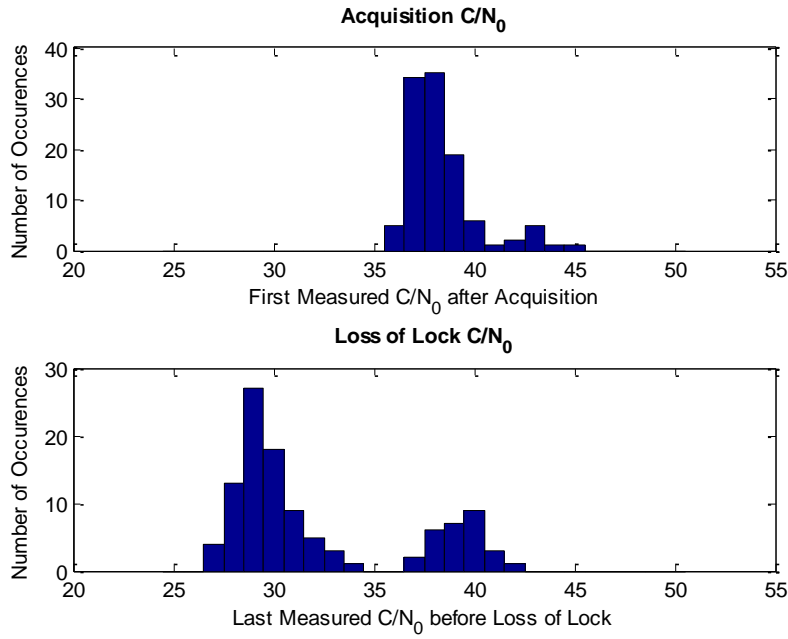


Figure 6-17: GPS C/N₀ at acquisition and loss of lock using standard tracking

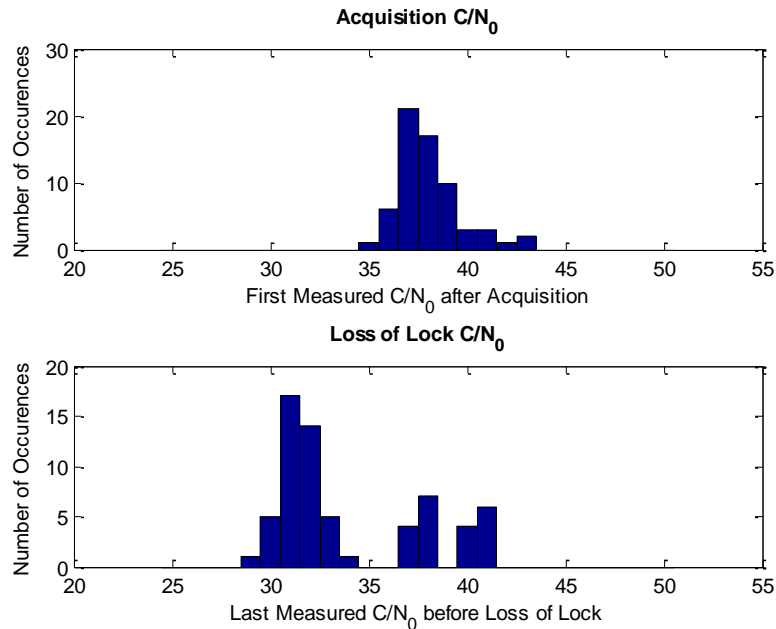


Figure 6-18: Galileo C/N₀ at acquisition and loss of lock using standard tracking

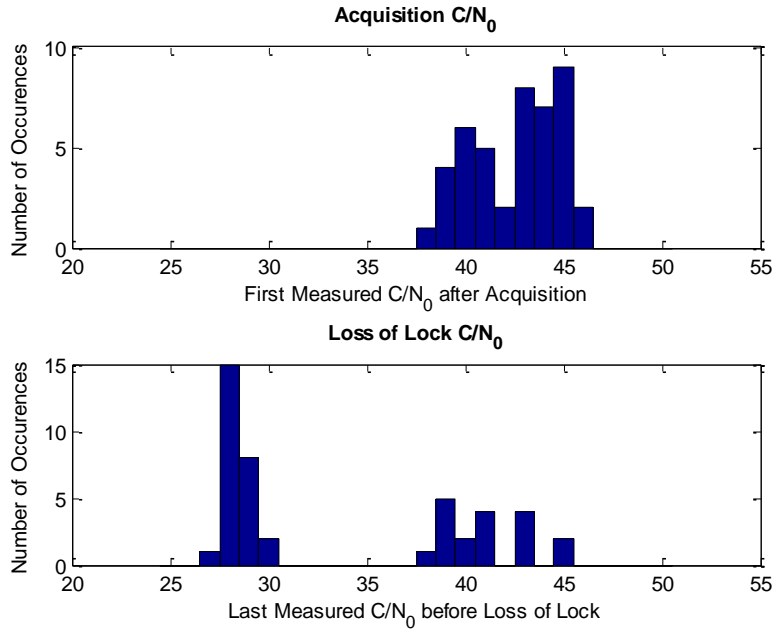


Figure 6-19: B1D1 C/N_0 at acquisition and loss of lock using standard tracking

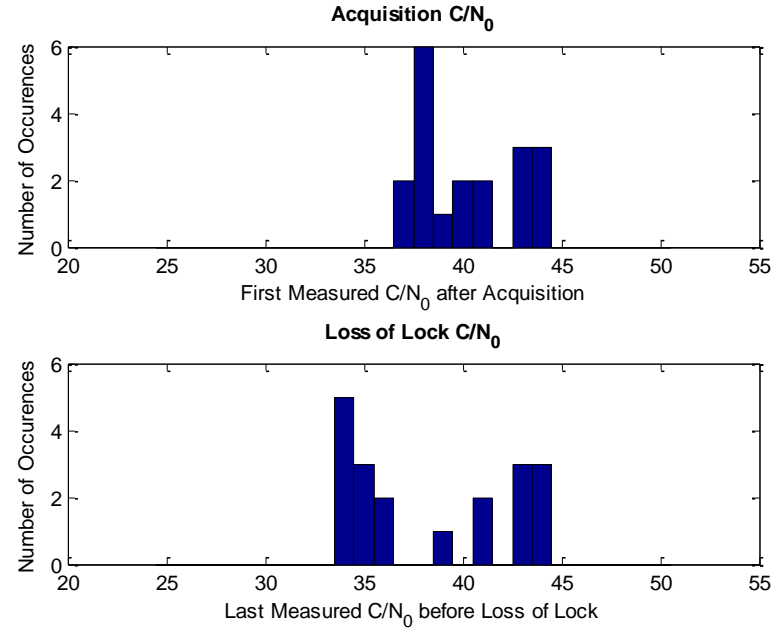


Figure 6-20: B1D2 C/N_0 at acquisition and loss of lock using standard tracking

The contribution of each of the systems to the overall positioning problem is shown in time series in Figure 6-21 for the occulter space craft. The contributions of the constellations are

stacked. The most striking result is that while they have the poorest weak signal acquisition (B1D1) and tracking (B1D2) performance, the geosynchronous IGSO and GEO satellites making up the regional part of the BeiDou system still offer the greatest advantage through the apogee arc. In keeping with the visibility simulation results of Chapter 3, they offer extremely long tracking arcs while they are visible on the far side of the Earth over the Earth's limb. In fact, the only times when sufficient satellites are tracked for a position fix outside of perigee is when two GEO and two IGSO satellites are simultaneously visible at 15:00 and again from approximately 17:00 to 18:00. When the user spacecraft is itself over China these signals are not visible, and the BeiDou system offers no advantage for a standard receiver.

It can be seen that the MEO BeiDou satellites and Galileo satellites are only tracked at or near perigee, leaving a 12 hour gap during which neither of these global systems offers any contribution to a standard receiver. In keeping with the preliminary results from the previous chapter, even with a powerful acquisition algorithm the standard receiver is only able to provide sparse GPS measurements through the apogee arc.

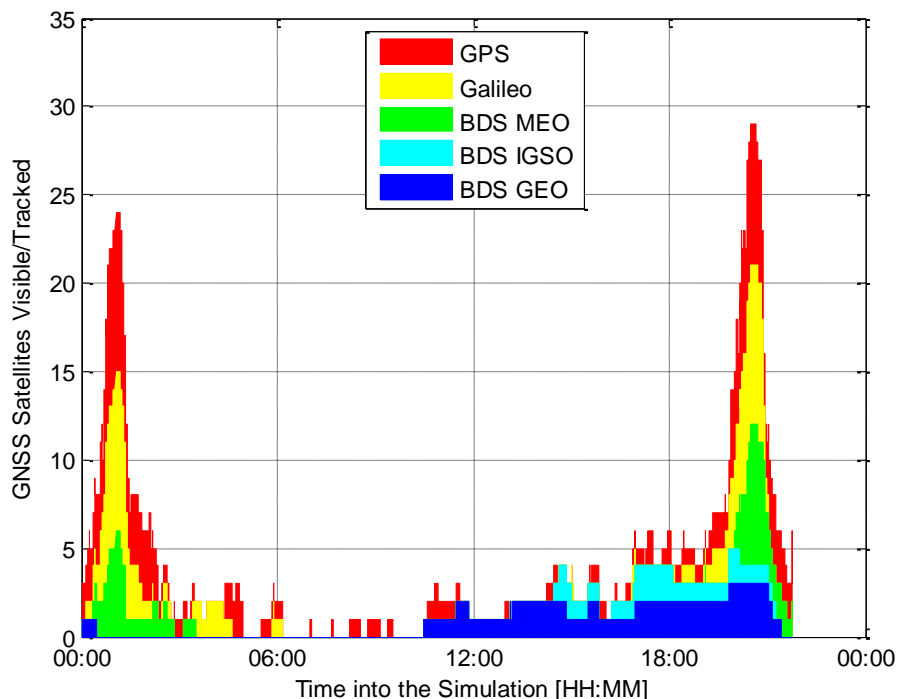


Figure 6-21: Number of tracked satellites on the OSC using the standard tracking strategy

6.3.1.1 Measurement Quality

The measurement quality from the standard receiver was also similar to that presented in the previous chapter. Unbiased phases, pseudoranges and Doppler were produced, and there is a strong dependence between the measurement tracking jitter and the signal power. Representative figures showing the differential measurement noise for a pair of B1D1 signals and E1b signals are shown in Figure 6-22 and Figure 6-23 respectively. The plots show the residual measurement error on a pair of single differenced GNSS satellites from the same system, as compared to the simulator's truth data. Single differencing removes the receiver clock contribution, and the phase measurement single difference has further had a constant ambiguity offset removed.

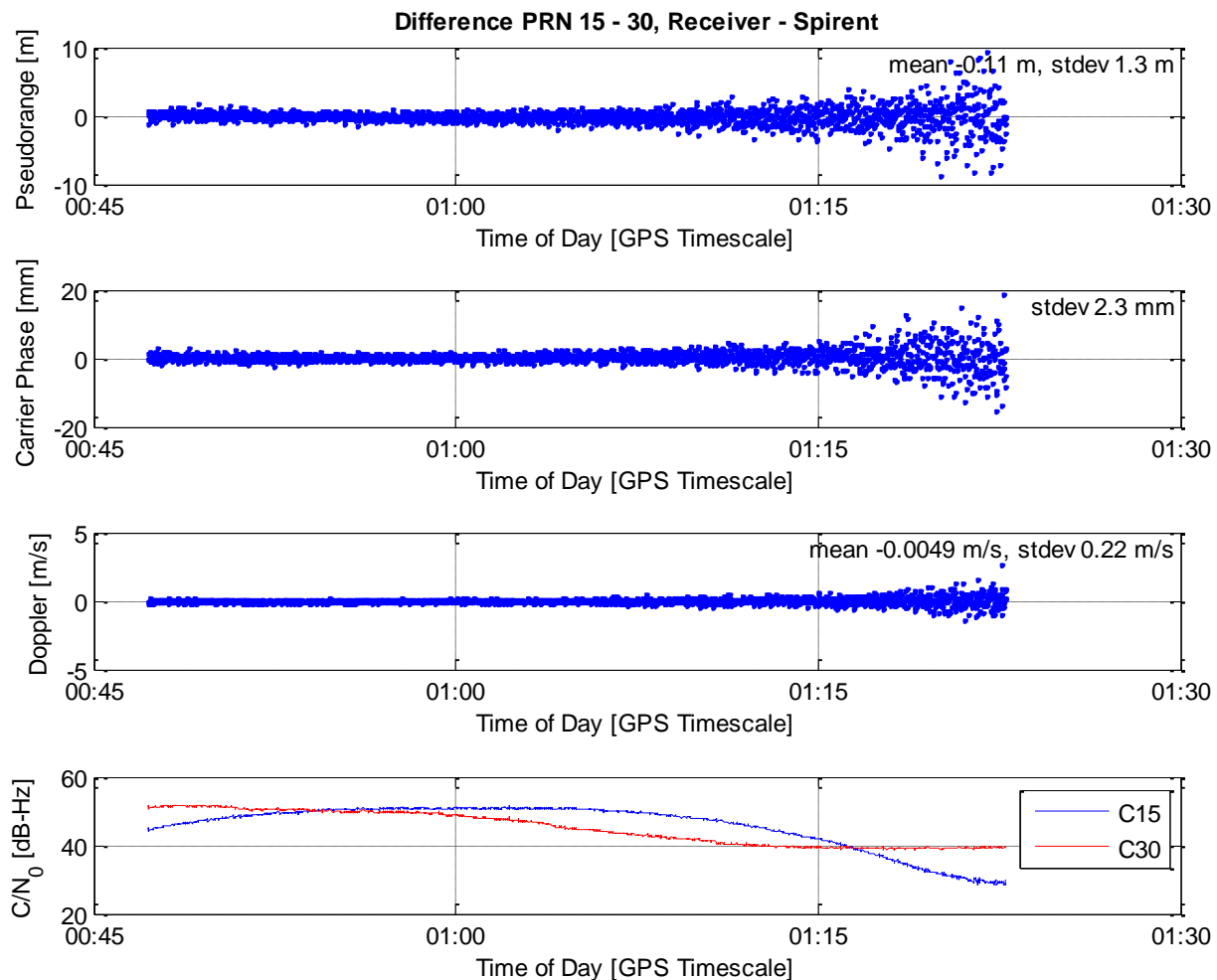


Figure 6-22: Differential measurement errors on a pair of B1D1 signals

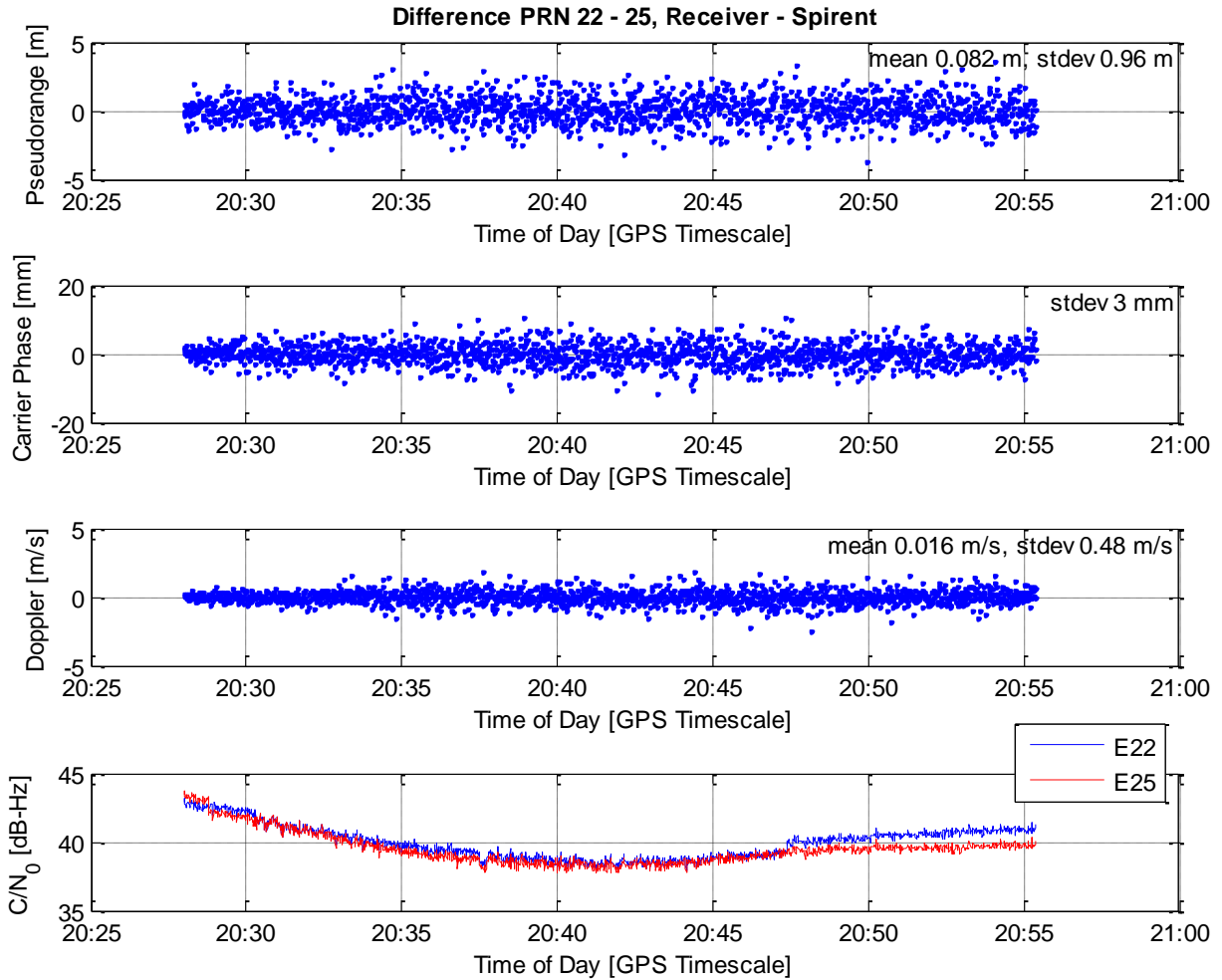


Figure 6-23: Differential measurement errors on a pair of E1b signals

Given the sparseness of the HEO measurements, and how dramatically the conditions change from apogee to perigee, a second specialized tool for assessing the measurement quality when no differences could be formed was also created. A Kalman filter was written which takes as input the simulator truth trajectory for a given data set, as well as the measurements. Only four states are estimated, the clock, clock drift, and inter-system biases for BeiDou and Galileo system time. The clock is modelled as a velocity random walk with a high degree of confidence (low process noise) in keeping with the quality of the oscillator used for the data collections, and pseudoranges as well as time-difference carrier phases are used as input measurements. In this way, the data outages can be bridged and even with sparse measurements residuals can be

calculated between the truth trajectory and filtered clock estimate, and the receiver's output measurements.

Histograms of the pseudorange residuals at C/N_0 values of 45 dB-Hz and 35 dB-Hz are shown in Figure 6-24. Similar to the acquisition and loss of lock results, there is a clearly visible correlation between the signal structures and the tracking jitter, with wider bandwidth signals having less measurement noise.

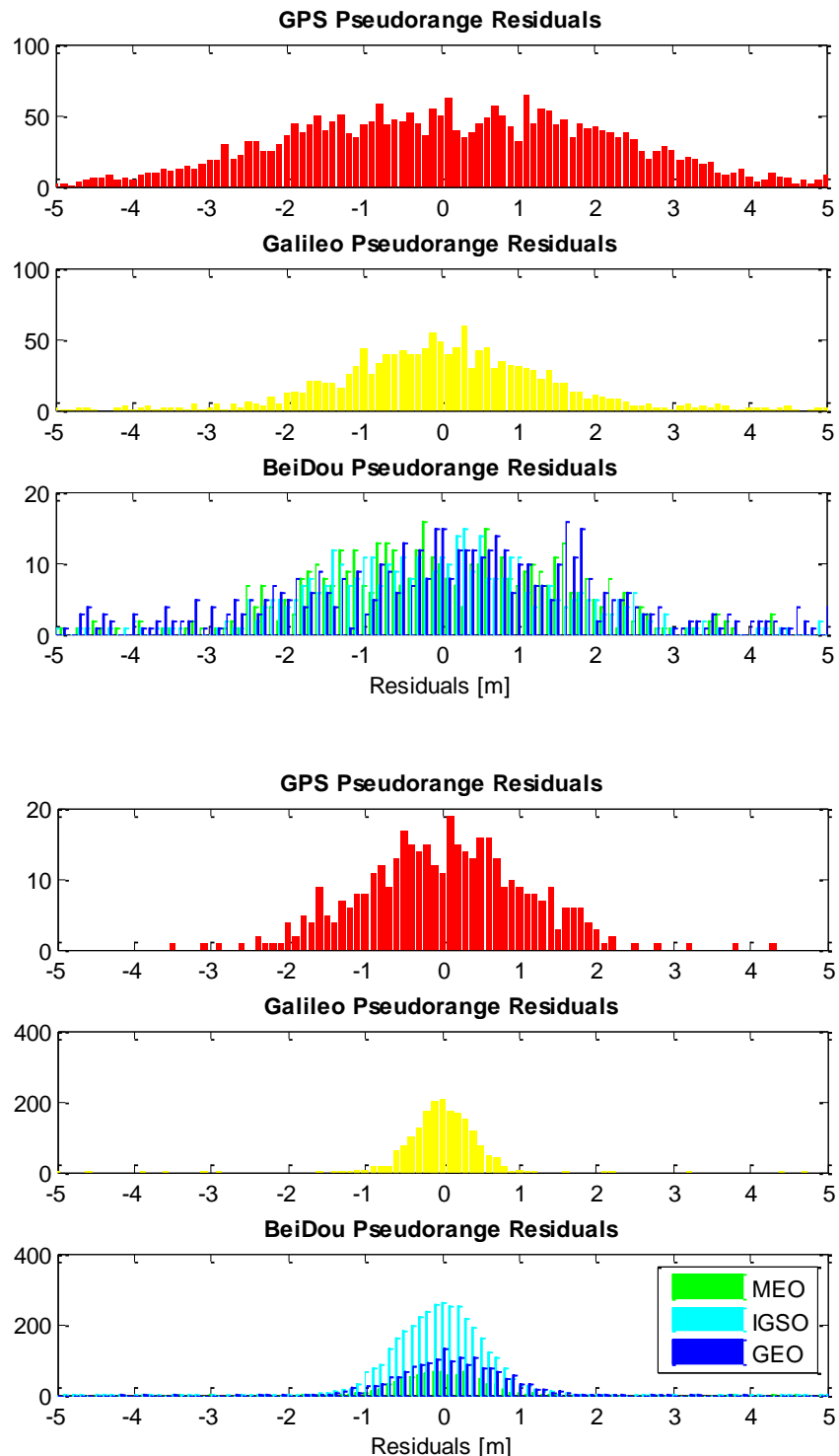


Figure 6-24: Pseudorange residuals at a C/N0 of 35 dB-Hz (above) and of 45 dB-Hz (below) from the standard tracking receiver

While the extremely sparse data from the standard tracking version of the receiver makes for an imperfect assessment, it is still clear from the histograms that, in keeping with expectations, the GPS L1 C/A signal is subject to more tracking jitter than either the Galileo or BeiDou signals. Galileo E1b with its MBOC(6,1,1/11) modulation is subject to the least tracking jitter, closely followed by the B1 signals with their higher chipping rate ranging code.

6.3.2 Results for the HEO tracking strategy

While the standard receiver produced a measurement quality in keeping with expectations, it did not provide sufficient measurements, even with multi-constellation GNSS, for good positioning at apogee. Superior results in terms of the number of tracked satellites were obtained using the HEO tracking version of the receiver, as shown in Figure 6-25. Comparing the figure to Figure 6-21 from the previous section, it can be concluded that under the simulated HEO environment the fine search grid offers superior pull-in performance, because in spite of using the same acquisition algorithms far more measurements are available through the apogee arc. Looking at the two hours following the first perigee passage, it can also be concluded that the Kalman filter tracker has a superior ability to maintain lock on signals fading out of view.

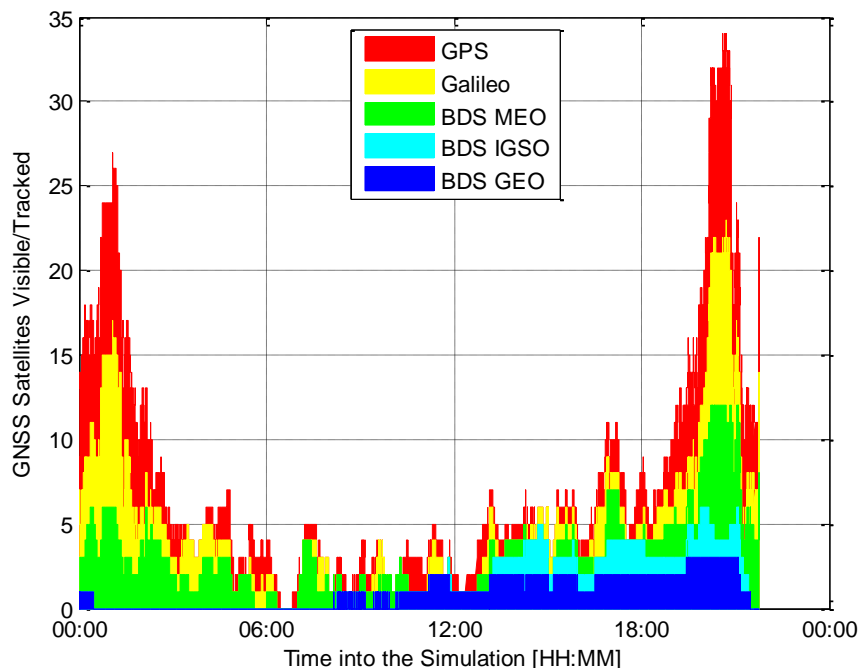


Figure 6-25: Number of tracked satellites on the OSC using the HEO tracking strategy

In the figure, it can be seen that the receiver tracks the single measurement required for clock steering throughout almost the entire data set, with the exception of a brief period at 6:30. In spite of this, it is still a rarity that enough signals are tracked in the apogee arc to produce a position fix, even with all three constellations. Considering the constellations individually, it can also be seen that all constellations now contribute to the increased number of tracked GNSS satellites throughout the orbit and during the apogee arc, although the contribution of the geosynchronous BeiDou satellites remains the most significant. These results highlight the fundamental truth that no matter how good the receiver design, the design of the constellation and transmit gain patterns is still a fundamental limitation, and no amount of receiver design work will make satellites with no line of sight visibility appear.

To get more insight into the improved performance, the acquisition and loss of lock C/N_0 values have also been investigated for the HEO tracking receiver. They are shown in Figure 6-26 for GPS L1 C/A, Figure 6-27 for Galileo E1b, Figure 6-28 for BeiDou B1D1, and Figure 6-29 for BeiDou B1D1.

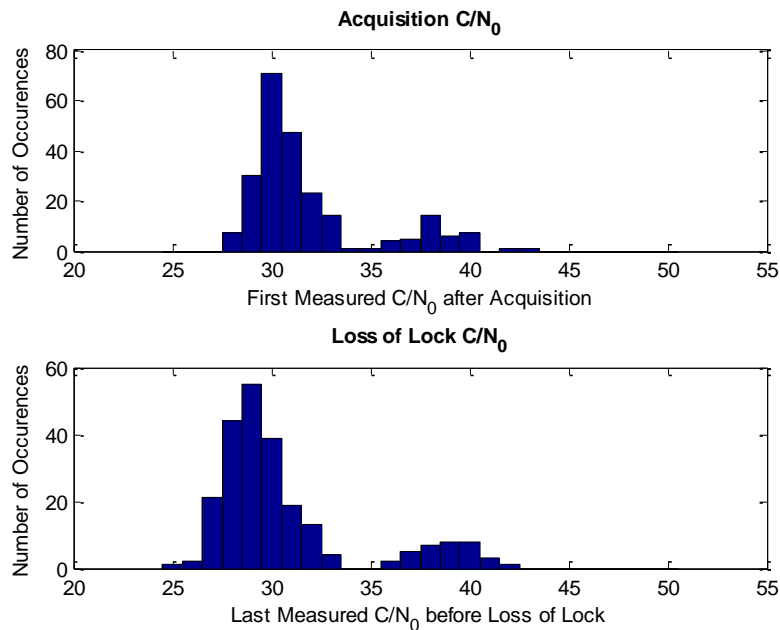


Figure 6-26: GPS C/N_0 at acquisition and loss of lock using HEO tracking

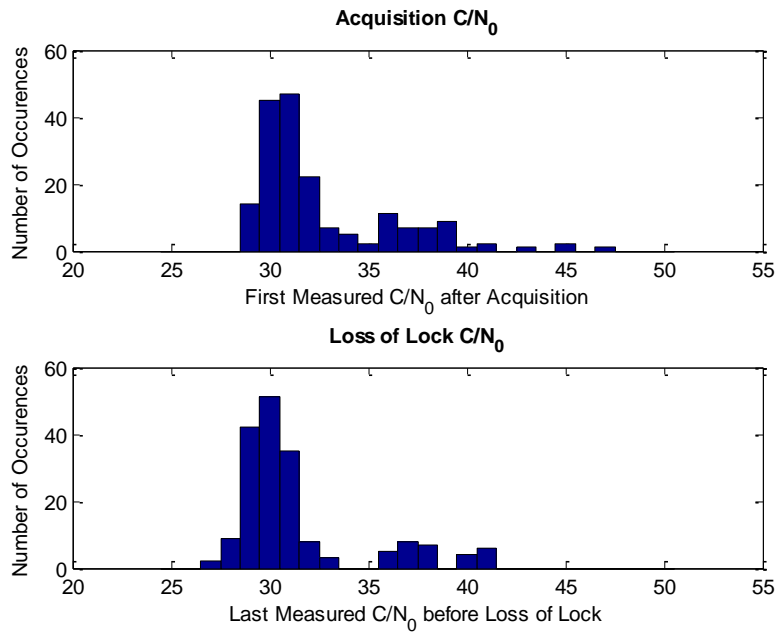


Figure 6-27: Galileo C/N₀ at acquisition and loss of lock using HEO tracking

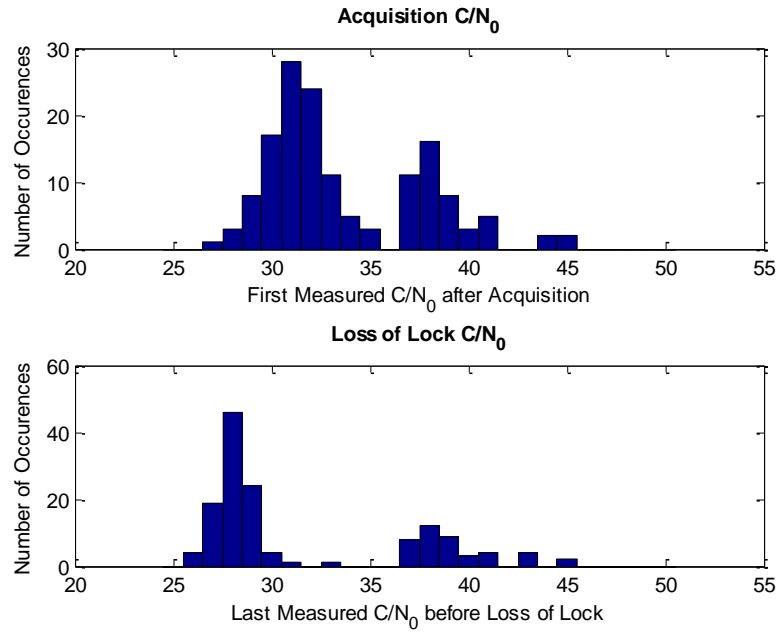


Figure 6-28: B1D1 C/N₀ at acquisition and loss of lock using HEO tracking

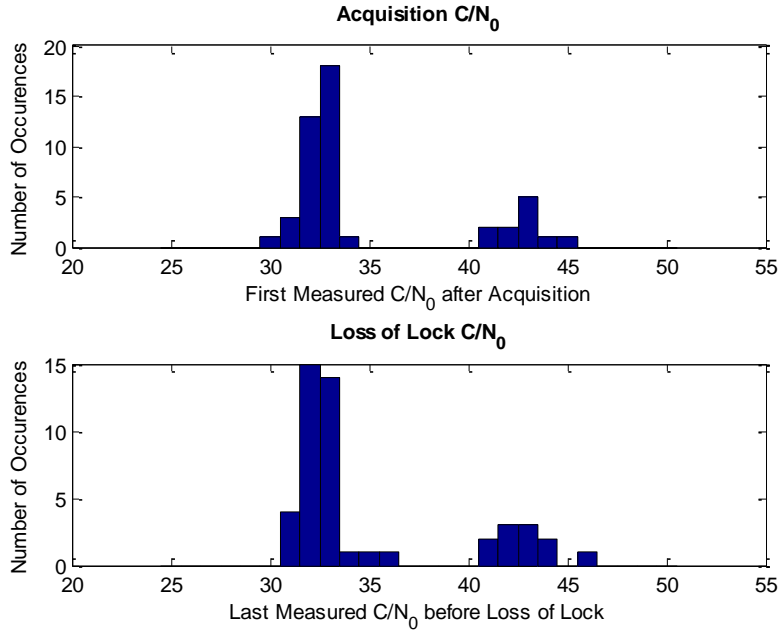


Figure 6-29: B1D2 C/N₀ at acquisition and loss of lock using HEO tracking

First, comparing the figures to those for the standard receiver, it is immediately apparent that the acquisition threshold has been lowered on all four signals. It has dropped by 7 dB from 37 dB-Hz on GPS and Galileo to 30 dB-Hz, by 9 dB-Hz on B1D1 from 40 dB-Hz down to 31 dB-Hz, and by 4 dB-Hz on B1D2, from 37 dB-Hz to 33 dB-Hz. Acquisition at or below 30 dB-Hz has been demonstrated on all signals.

On the contrary, the loss of lock threshold for the fading signals has not changed as much as expected, in particular on the GPS and B1D1 signals, which made use of 10 ms coherent integration both in the standard tracking receiver and here. The signals are lost typically at 28 dB-Hz for B1D1, at 29 dB-Hz for GPS L1 C/A, at 30 dB-Hz for E1b and at 32 for B1D2. These values are not in fact much lower than they were for the standard tracking loops, and are quite far above the 25 dB-Hz threshold achieved by NASA's Navigator receiver (Winternitz et al 2017) or the 26 dB-Hz reported for the MosaicGNSS (Airbus 2014) among others. It can also be interpreted from the histograms that there is a large region of overlap between the acquisition C/N₀ and the loss of lock C/N₀ on all four signals, and comparing the histogram

counts to the actual number of acquisitions visible in the time series of Figure 6-25, in particular for the B1D2 signals which are only on rare occasions acquired, it can be interpreted that the signals are repeatedly being lost and reacquired rather than steadily tracked.

Given the correlation between bit rate and loss of lock threshold it initially appears that the data bit rate and corresponding maximum coherent integration time is playing a role in determining the loss of lock threshold. However, this is not the case. One interesting feature of the Kalman filter tracking loop is that it is insensitive to the coherent integration time. Tests were conducted with maximum coherent integration times of 2 ms, 4 ms, the default value of 10 ms, and 20 ms, and it was found that while enough minor changes occurred to be confident that a different version of the receiver code had in fact been run, the histograms comparing the C/N_0 distributions of the acquired and lost signals remained in essence identical. Expected results, such as all signals exhibiting the same 32 dB-Hz loss of lock C/N_0 as B1D2, did not occur. The same phenomenon was earlier observed by Petovello et al (2008b) and is attributed to the filter receiving additional, noisier measurements at shorter coherent integration times, and fewer, better quality measurements at long coherent integration times, but ultimately getting the same information content regardless.

An alternative explanation is that the fundamental limitation in the receiver performance is not the tracking loops at all, but in fact the C/N_0 estimation and the phase and frequency lock indicators, which are the basis of the receiver's decision to declare loss of lock and stop tracking a signal. It has been observed while watching GSNRxTM run that the C/N_0 estimates can be quite unreliable for signals below 30 dB-Hz. It has also been observed that the lock indicators can be quite susceptible to epochs in which the quadrature correlator output is larger than the in-phase output, an event which starts to occur regularly for weak signals as the noise distributions of the two components begin to overlap. Although all signals use the same lock indicator calculations, it is also plausible that the algorithms are less suited to the signals with higher bit rates which would explain the slightly worse performance on E1b and B1D2. Many of the GSNRxTM utilities were designed for GPS L1 C/A and only revisited for new signals if they obviously failed. Although the algorithms have not been investigated in depth, a test was conducted in

which the lock indicator and C/N_0 thresholds for declaring loss of lock were lowered. While it did produce significantly more measurements, the problem of some receiver channels failing to loose lock on signals which are no longer being simulated also reoccurred. Fine tuning of the decision statistics and decision logic remains an area of future work.

6.3.2.1 Measurement Quality

Overall, the Kalman filter tracking loop produces measurements with far less noise than the standard tracking receiver, in particular on the pseudorange and Doppler measurements. The low noise is a result of its much narrower bandwidth, rather than the Kalman filter specifically. For comparison with the standard receiver results, the same two histograms of the pseudorange measurement residuals at 35 dB-Hz and 45 dB-Hz are shown in Figure 6-30.

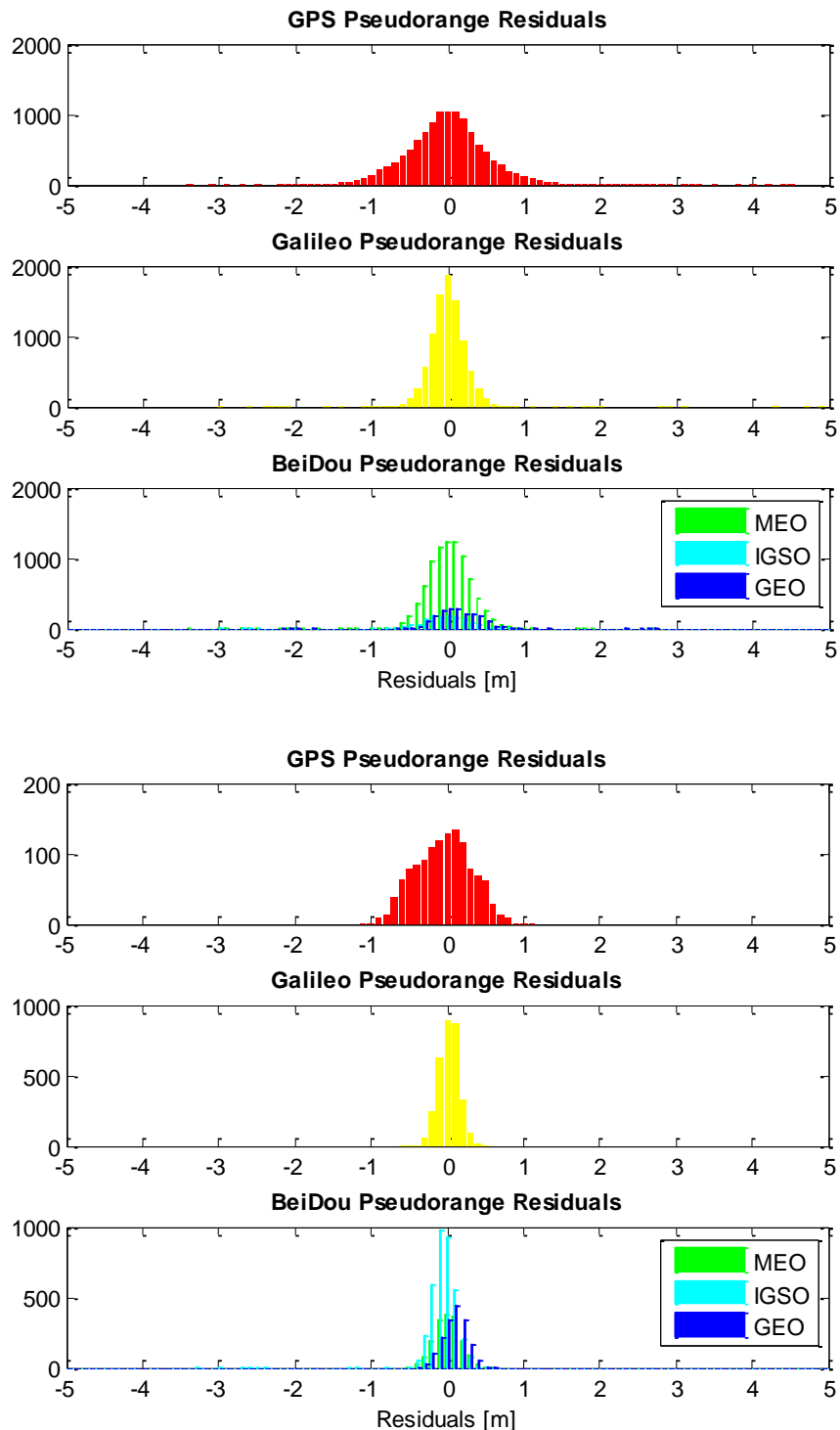


Figure 6-30: Pseudorange residuals at a C/N0 of 35 dB-Hz (above) and of 45 dB-Hz (below) from the HEO tracking receiver

Unlike the standard tracking case, the measurements produced using the HEO tracking strategy are not completely unbiased. There are a few easily visible systematic effects. First, even after tuning it for the HEO case, the Kalman filter tracker is quite susceptible to ionospheric error induced code-carrier divergence. This is because it uses the implicit assumption that the signal parameters undergo the same dynamics and therefore change in proportion to each other. Contrary to this assumption, a receiver on an orbiting spacecraft is subject to rapidly changing ionospheric delay and consequently rapid code-carrier divergence when GNSS satellites rise or set behind the Earth. An example of this is shown in Figure 6-31 and Figure 6-32 from 20:45 to 20:50, when both the pseudorange and Doppler are obviously biased in opposite directions. The time series of the differenced ionospheric error simulated on the PRN pair is shown in Figure 6-33 for comparison. The figure corresponds to the same Galileo PRN pair shown for the standard tracking receiver in Figure 6-23.

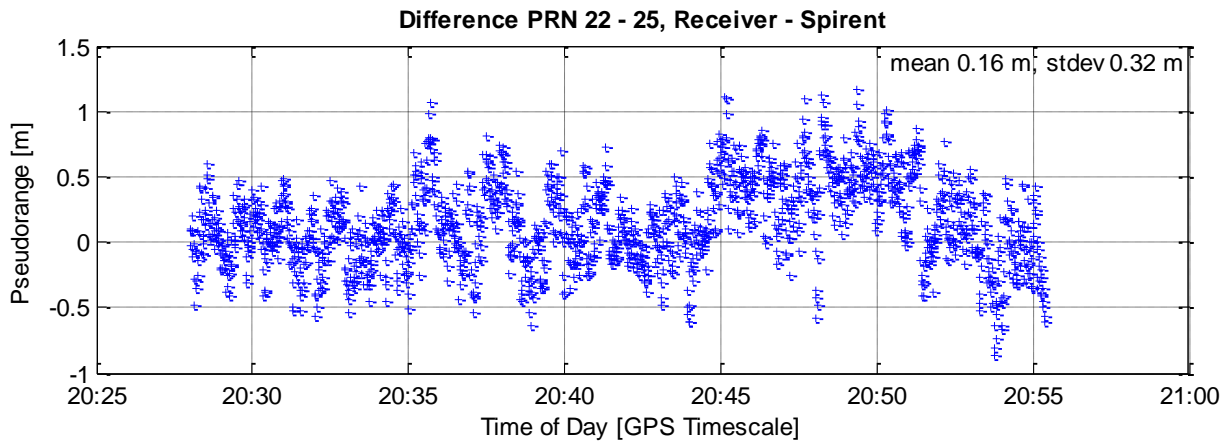


Figure 6-31: Pseudorange error on PRNs E22-E25 showing an ionosphere bias

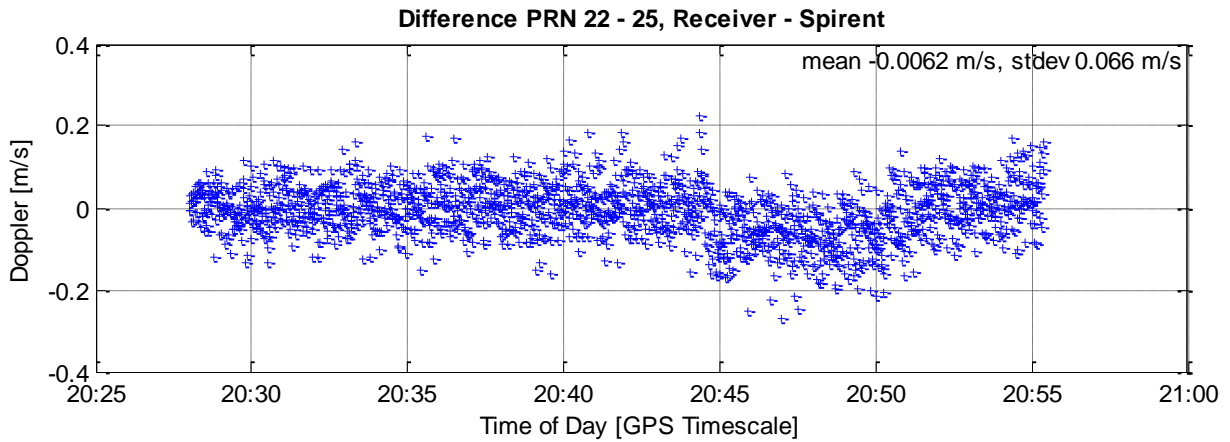


Figure 6-32: Doppler error on PRNs E22 - E25 showing an ionosphere bias

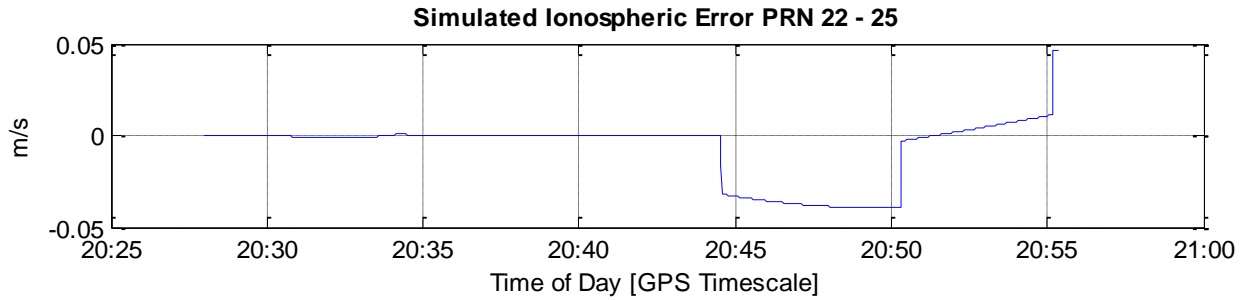


Figure 6-33: Differenced ionospheric error simulated on PRNs E22 - E25

Next, there are biases in the Doppler measurements due to latency in the receiver's Doppler measurement generation. The biases are proportional to the tracking loop's coherent integration time, as shown in Figure 6-34, and to the receiver dynamics. The problem has been traced back to receiver's Doppler output, which simply takes the Doppler at the beginning of the current coherent integration interval, regardless of how the coherent integration interval is aligned with the measurement output epoch and regardless of the current rate of change of the Doppler. In ground applications, the line of sight accelerations are not typically large enough for a clear bias to appear, but the rapidly changing signal parameters as the HEO satellite swings through the perigee arc highlight the problem.

This issue has ultimately been ignored, as the Doppler measurements are not used in the relative positioning filter. Two plots showing the Doppler when the receiver was run with a maximum 10

ms coherent integration time and a maximum 20 ms coherent integration time are shown in Figure 6-34. Signals such as Galileo and B1D2 with shorter coherent integration times are less susceptible to the bias. In the figures it can be seen that the bias occurs to a lesser degree on GPS PRNs 21 and to a greater degree on PRN 25, corresponding to the dynamics. Note the discontinuity at 1:02 hours in the G25 curve on the right occurs because the coherent integration time boundary and the measurement epoch briefly coincide, at which point the bias is briefly zero before it jumps back up to 0.1 m/s when the full 10 ms latency takes effect. The corresponding dynamics are shown later in Figure 6-36. Note that, theoretically, the same bias occurs in the standard tracking version of the receiver, but is invisible below the measurement noise.

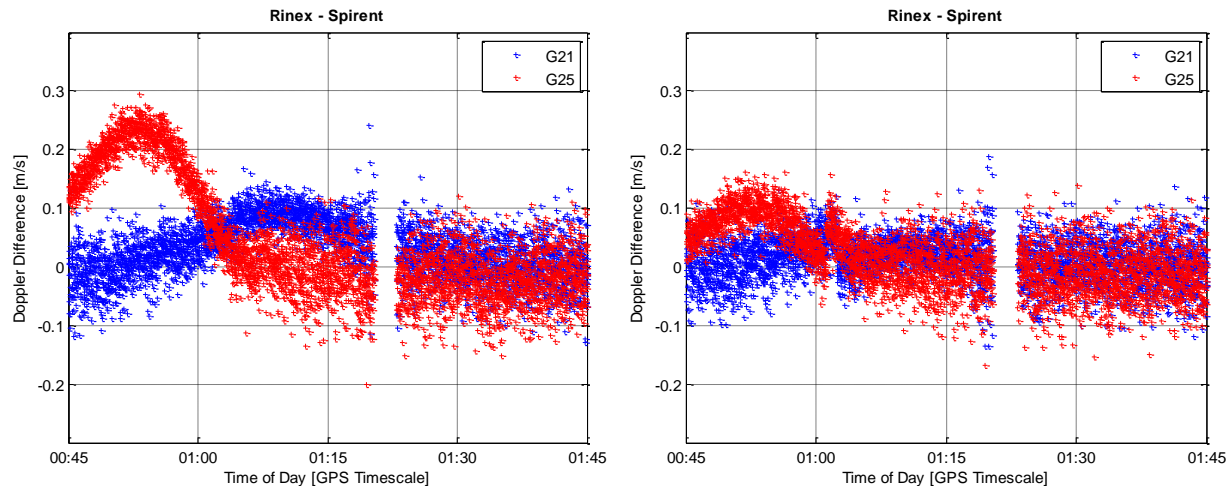


Figure 6-34: Doppler latency effects with 20 ms (left) vs 10 ms (right) coherent integration time

A third source of measurement error is due to the extremely tight bandwidth of the Kalman filter tracker. Dynamics dependent biases occasionally appear in the pseudorange measurements, but were found to be typically no greater than a few metres. Similar effects would be expected to occur for any tracking loop with a very tight bandwidth. An example of this type of pseudorange error, on the same G21 G25 measurement pair as in the previous example, is shown in Figure 6-35, along with a corresponding plot of the dynamics over the same time span in Figure 6-36.

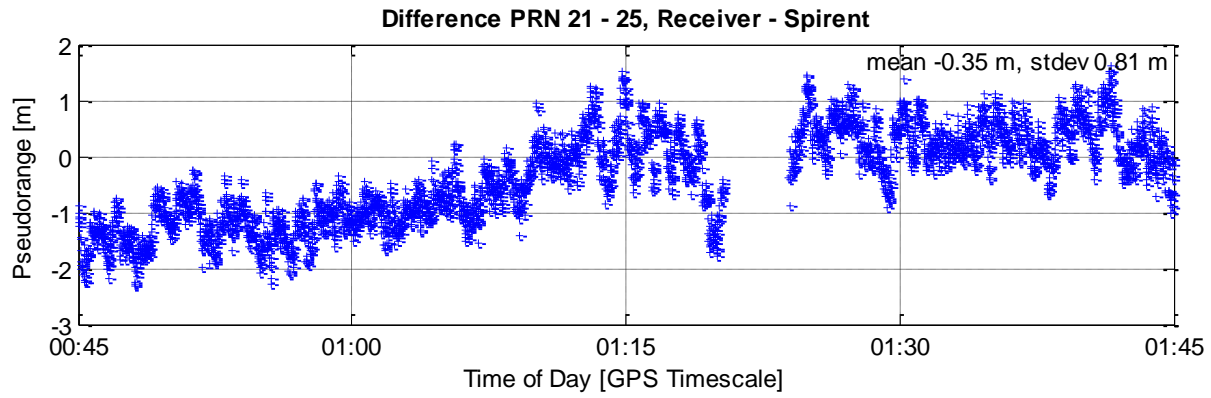


Figure 6-35: Steady state pseudorange tracking error under high dynamics

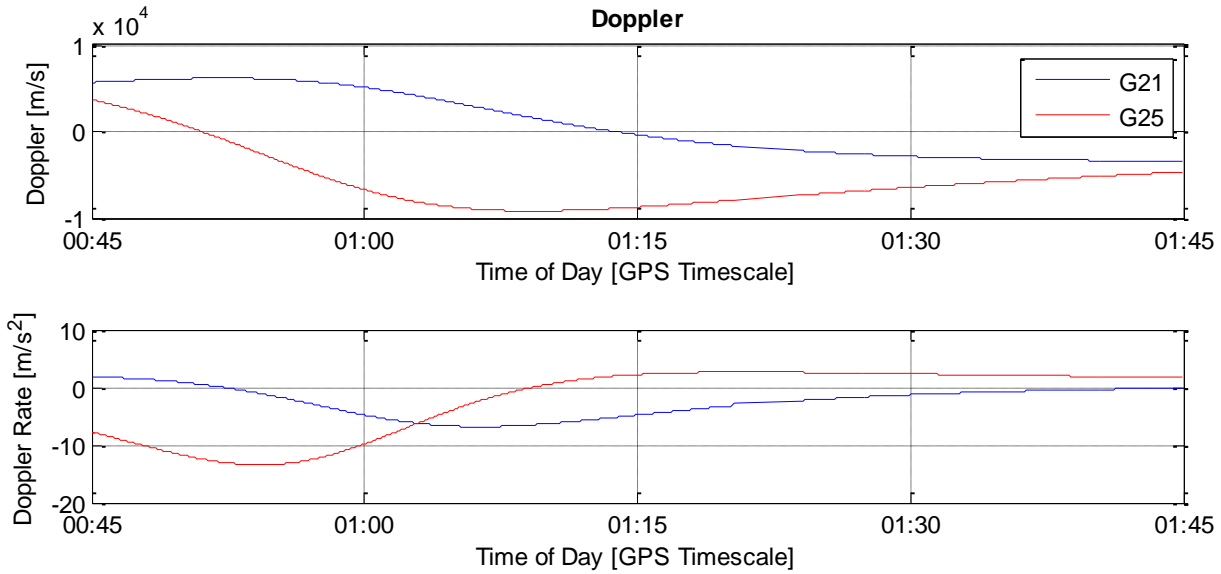


Figure 6-36: Dynamics on the G21 G25 PRN pair

In spite of the many imperfections in the measurements, the Kalman filter based tracking strategy offers advantages that outweigh the problems for the HEO relative positioning application. The biases on the measurements are small, and even at a few metres these errors are ultimately at or below the level of the tracking jitter on the standard tracking strategy. The errors are systematic in most cases and consequently can be differenced out in the relative positioning application, while the benefit in terms of the number of available measurements is substantial. While the Doppler latency would not completely cancel out, the Doppler measurements are not actually necessary for the orbital relative positioning filter developed in the next chapter or any

orbital application, because the same velocity information with less noise can be extracted from the phase measurements. As a result, the decision was made to proceed with the HEO/Kalman filter tracking results for the relative positioning research.

Finally, the number of commonly tracked satellites from the occulter spacecraft (OSC) and coronagraph space craft (CSC) data sets have also been assessed. It can be seen from Figure 6-37 that there is good agreement, which is both an indication of the repeatability of the receiver performance and important for relative positioning.

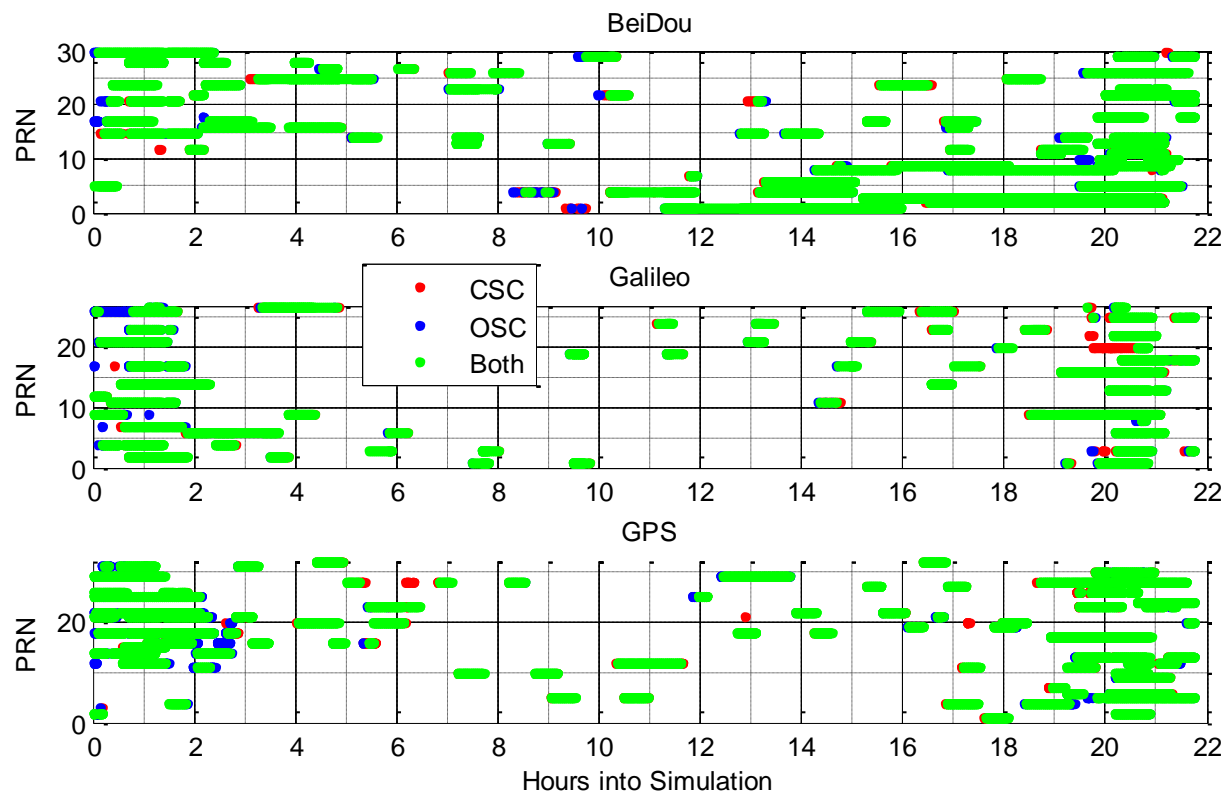


Figure 6-37: Commonly Tracked GNSS Satellites on the Occulter (OSC) and Coronagraph (CSC) spacecraft

6.4 Conclusions

A version of GNSRx™ tailored to the highly elliptical orbit environment has been created. Through the receiver development it was found that the signal structures play a deciding factor in the achievable performance. Signal structure dramatically impacts the pull-in from acquisition to tracking, because it influences the time required for bit synchronization and the point at which the tracking can expand to the maximum coherent integration time. Signal structure is also the limiting factor for choosing an appropriate coherent integration time, both for acquisition and for tracking. Finally, the modulations of the signals determine the level of code noise because they determine the sharpness of the correlation peaks. In spite of this, the underlying constellation geometry and transmit patterns remain the guiding force in how many signals are visible. No level of weak signal tracking will improve the geometry or turn the GNSS satellites around to transmit into deeper space.

Thoroughly understanding and potentially updating the lock indicators and C/N₀ estimator remains an area of future work, as the current performance of the receiver is heavily dependent on them. They are the metrics used by the receiver to decide when to switch tracking loops, and when to declare loss of lock. Occasional problems in receiver performance suggest that the lock indicator algorithms may be poorly suited to the limited coherent integration times of signals other than GPS L1 C/A. Also, a C/N₀ algorithm targeted at weak signals stands to substantially improve the performance of GSNRx™ for HEO tracking, in particular during the pull-in of weak signals, and when declaring loss of lock for PRNs which slowly fade out of view as the orbit of the user spacecraft carries the receiver through nulls in the GNSS transmit gain patterns.

In comparison with the existing Magnetospheric Multiscale Mission and ChangE'5T lunar probe flight results, GSNRx™ is still a step behind, unable to deliver sufficient GPS measurements for a position fix throughout highly elliptical orbit, even using the weak signal tracking algorithms. While this is due in part to the aforementioned weaknesses in GSNRx™, it is also due to the choice of simulation parameters. A conservative link budget has been chosen, along with conservative assumptions about the transmit gain patters wherever no information or no information about the azimuthal variation in the side lobes could be uncovered. Re-calibrating

the simulation using flight results from one of the exiting missions would allow for a globally higher signal power. Similarly, the simulation presented here assumes a hemispheric receive antenna gain pattern, while the existing missions use higher gain antennas, which would also allow for a stronger signal power to be simulated. Together with the proposed improvements to the receiver, similar results to the existing missions carrying high sensitivity receivers would be achieved.

In contrast to MMS and the ChangE lunar program, not every above the constellation mission carries, or plans to carry, a high sensitivity receiver. The receiver performance achieved here is certainly within the realm of achievable results for future above the constellation missions.

Finally, in the context of the current study, the goal has been achieved: an adequate number and quality of measurements have been produced to allow for the development and testing of the multi-constellation relative positioning filter under realistic operating conditions.

Chapter Seven: Design and Performance of the Relative Positioning Filter

Limited work has been done to investigate relative GNSS based positioning for formation flying satellites in highly elliptical orbits. Only Psiaki and Mohiuddin (2007, Mohiuddin and Psiaki (2008) have made use of carrier phase measurements, but in order to track sufficient satellites for ambiguity resolution they assumed a receiver acquisition threshold down to 12 dB-Hz on GPS L1 and 9 dB-Hz on GPS L2C for users in a 17 Earth radii highly elliptical orbit. Using integer ambiguity resolution together with an orbit filter which explicitly estimates ionosphere and broadcast orbit errors, they demonstrate < 5 cm level accuracy for GEO orbits and 20 cm level accuracy for HEO in periods with no occulting satellites, and spikes in error during occultations which were best mitigated with dual frequency data.

Also in simulation, Lane (2007) demonstrates roughly metre level relative positioning accuracy using pseudorange measurements in a filter with a stable osculating orbit state representation. Lane also presents a fascinating discussion on the potential use of reflected, essentially multipath, GPS signals from another spacecraft in the formation for relative positioning.

The Magnetospheric multiscale mission does relative positioning in post processing by simply differencing the pseudorange based absolute trajectories. Winternitz et al (2016) presents a detailed analysis of the MMS flight data, and conclude that potentially < 10 m level absolute positioning is achieved using the GEONS filter onboard the MMS spacecraft, but with no better source of information for comparison they are limited in their analysis.

PROBA-3 will make use of coarse and fine optical sensors for formation control and real time relative positioning though the apogee measurement arc, and consequently above the constellation relative GNSS positioning is not being studied as part of the mission design.

Other positioning filters and studies exist for absolute positioning of HEO satellites using GNSS, such as the onboard extended Kalman filter using GPS and GLONASS pseudorange measurements on ChangE-5T (Wang et al 2015), and the simulation study by Vigneron et al

(2016) which investigated four different filter concepts for the proposed Polar Communication and Weather mission.

Several real time autonomous relative positioning filters have also been designed for actual missions in low Earth orbit using phase measurements. D'Amico (2010) solves for float ambiguities in a more robust filter design for the PRISMA mission while Roth (2010) uses integer ambiguity resolution for the CanX-4/5 formation flying nanosatellites. Millimetre level carrier phase based GPS relative positioning has also been demonstrated for example in post processing for the TerraSAR-X/TanDEM-X missions (Montenbruck et al 2011).

The question this thesis set out to answer was “How accurately can multi-constellation GNSS measure the relative position between formation flying spacecraft in highly elliptical orbits?” This chapter at last presents the design of a relative positioning filter together with positioning results. The filter is capable of handling the inconsistent conditions and sparse measurements faced by a user in highly elliptical orbit for simultaneous estimation of the absolute and relative positions of a pair of formation flying satellites. It has been set up to emulate real time operations, as the most critical use of relative positioning information for formation flying spacecraft is to maintain the safety of the formation (prevent situations where the spacecraft are in danger of colliding with each other), and ideally also to be able to autonomously control the formation. An analysis of the obtained relative positioning accuracy under different receiver assumptions answers the overarching research question.

The remainder of the chapter is organised as follows. Section 7.1 presents the basic design of the relative positioning filter, while section 7.2 presents the state propagation models, and section 7.3 presents measurement considerations. The resulting filter performance is analysed in section 7.4. Performance is demonstrated based on two data sets, the multi-constellation data set discussed in depth in Chapter 6, and data from a slightly modified version of the simulation consisting of higher power GPS only measurements which replicates the MMS operating conditions. The chapter concludes in section 7.5.

7.1 Filter Design

The choice of the filter design was guided by the requirement to handle the sparse GNSS data, the requirement to handle multiple constellations, and the requirement for a robust solution. The most significant criterion for the relative positioning filter design was, however, that it must be capable of handling asynchronous measurements. High end GNSS receivers intended for use in relative positioning in a terrestrial or near Earth environment generally either steer the receiver clock continuously, or apply 1 ms jumps as required to maintain a close alignment with GPS time. The clock alignment allows for measurement synchronization with other receivers. In contrast, receivers in HEO may track insufficient measurements to compute kinematic position solutions and are consequently incapable of steering their own clocks. A possible design feature for a HEO receiver would be a coarse on-board orbital filter, which at 300 m accuracy would allow for a 1 μ s clock steering. In the absence of such a receiver design, there exists a very real possibility that the measurements from formation flying spacecraft in HEO will be asynchronous between receivers.

An extended Kalman filter was chosen as the basis for the relative positioning filter design. While other studies have investigated different filter concepts, such as the unscented Kalman filter, Cubature Kalman Filter, and the Huber filter, they ultimately proved to be more computationally intensive without offering any significant increase in position accuracy (Vigneron et al 2016), or unstable (Wang et al 2011)

In order to handle the asynchronous measurements, a filter design was chosen in which the states of the two receivers are estimated at slightly different epochs. Absolute states for either spacecraft A or B are referred to the measurement epochs on receiver A or B, while relative states describe the four dimensional offset between the states of A at measurement epoch A and the states of B as measurement epoch B. The basic concept for a single filter step from t_0 to t_1 is illustrated in Figure 7-1. When the measurements are applied, the states of the two spacecraft are not synchronized in time, but both have measurements available. With this implementation it is still possible to apply differential GNSS measurements in spite of the asynchronous receivers.

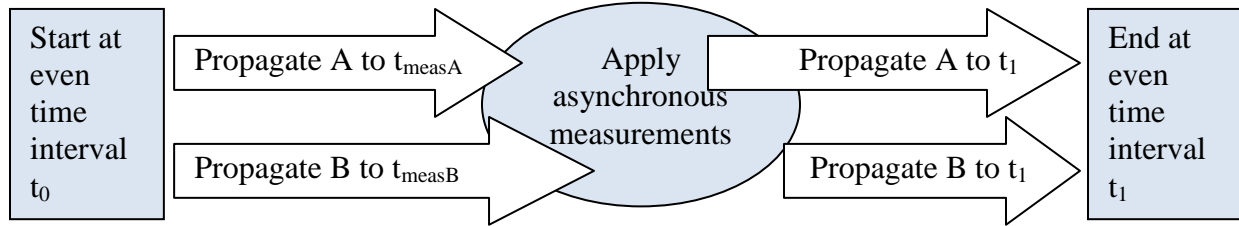


Figure 7-1: Flow chart of a single filter step with the asynchronous filter concept

The disadvantage of using the asynchronous state filter concept is in the orbit propagation. While orbit propagation is subject to some errors, having two orbit propagators which share the same numerical integration steps and orbit models will in large part cancel them out. Here, the orbit is propagated to slightly different epochs, negating this advantage. After the measurement update, a (typically very small) second prediction step is therefore carried out to propagate each spacecraft's states back to the same even time interval. The filter's current estimates of the receiver clock offsets are used to determine the timing and synchronization at each step. While this has the benefit of generating equidistant ephemerides for the user, the technical reason is to synchronize the numerical integrators in the event that a long data outage is beginning. During periods of GNSS tracking, the constant interruption of the pure propagation with measurement updates in any case disturbs the synchronicity of the orbit propagation. In the case where no measurements are available, the filter directly propagates the states to the even time interval.

The estimated states consist of the absolute 3D Cartesian position and velocity in the International Celestial Reference Frame (ICRF) for each of the two formation flying spacecraft, r^A , v^A , r^B , and v^B , force model parameters, and measurement model parameters. Superscripts A and B designate the two formation flying spacecraft. Absolute position states rather than relative states were chosen, because they allow for each receiver's absolute position to be independently updated whenever any measurement is available, regardless of whether the same GNSS satellite is commonly visible to both receivers.

The force model parameters consist of constant coefficients and accelerations. Solar radiation pressure and drag coefficients are estimated for each spacecraft, C_{SRP}^A , C_D^A , C_{SRP}^B , and C_D^B , in

order to better model satellite-specific behaviour under the influence of surface forces, which is particularly important given the difference in size and shape of the two spacecraft in a mission like PROBA-3. Absolute empirical accelerations for spacecraft A in the radial, tangential and normal directions, a_R^A , a_T^A , and a_N^A , are also estimated, as well as relative empirical accelerations describing the difference in accelerations between spacecraft A at measurement time A and spacecraft B at measurement time B. These are also in the radial, tangential, and orbit normal directions, and are designated a_R^{B-A} , a_T^{B-A} , and a_N^{B-A} . The inclusion of relative rather than absolute accelerations on the second spacecraft allows for different tuning of the absolute and relative dynamics, making it possible to more closely tie together the two trajectories even when the absolute position states are poorly known. Additional thrust accelerations during maneuvers are input to the filter and are not estimated.

The measurement model parameters consist of timing parameters and ambiguities. The timing parameters are, for each receiver, a receiver clock offset and clock drift, cdt^A , \dot{cdt}^A , cdt^B , and \dot{cdt}^B , as well as inter-system biases for each additional GNSS system on each receiver, cdt_{ISB}^A and cdt_{ISB}^B . The linear clock model is justified by the observed behaviour of the Morion OCXO used during the data collection. A figure showing an initial assessment of the clock drift based on the receiver's kinematic navigation solution over a 22 hour data take is shown in Figure 7-2. For the data set in question the clock clearly exhibits a stable, nearly constant drift of -10 m/s over the full 22 hour data take, which results in a linear change in clock offset (not shown). The noise on the clock drift estimate is from the receiver's navigation solution, which is still subject to the same shortcomings first noted in Chapter 5. The large spikes around 17:00 and 18:00 occur at a period of worsening geometry, and the outage between them occurs because the receiver does not calculate a position when the geometry is weak, determined by testing if the determinant of the normal matrix is less than 1e-6.

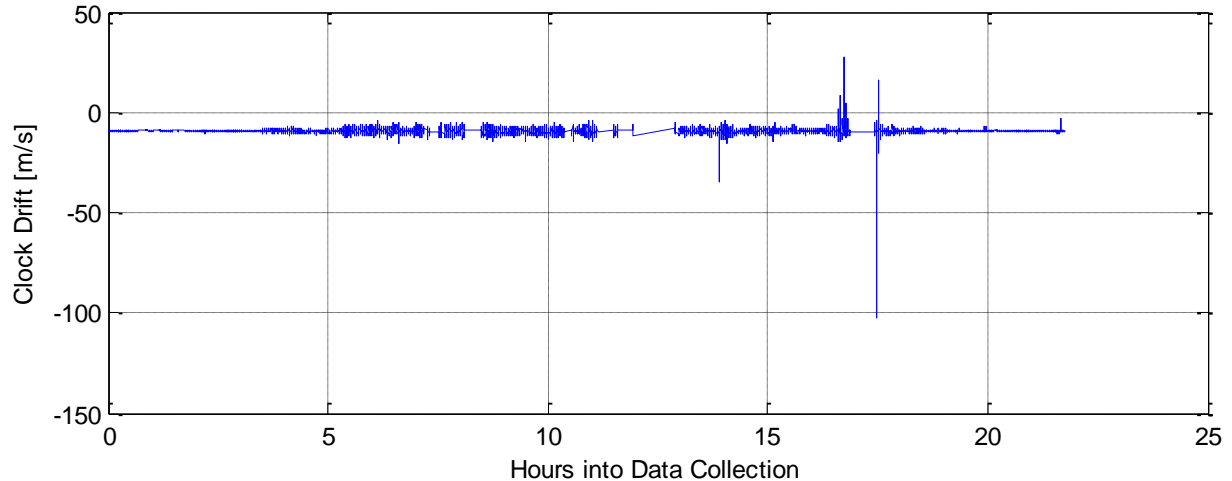


Figure 7-2: Clock drift output from the GNSRx™ kinematic navigation solution

Finally, the ambiguities are un-differenced float ambiguities for each GNSS satellite and receiver, N^A and N^B . Un-differenced ambiguities were chosen because they allow for the flexibility of using the phase measurements in different measurement combinations, and avoid complicated data handling in the filter software when the two receivers fail to track exactly the same set of GNSS satellites. Note that no integer ambiguity resolution has been attempted because there are insufficient measurements from the same system throughout most of the orbit to form the necessary double differences.

The state vector is given in Eq. 7-1.

$$x = [r^{A^T} \quad v^{A^T} \quad C_{SRP}^A \quad C_D^A \quad a_R^A \quad a_T^A \quad a_N^A \quad cdt^A \quad \dot{cdt}^A \quad cdt_{ISB}^{A^T} \quad N^{A^T} \dots \\ \dots r^{B^T} \quad v^{B^T} \quad C_{SRP}^B \quad C_D^B \quad a_R^{B-A} \quad a_T^{B-A} \quad a_N^{B-A} \quad cdt^B \quad \dot{cdt}^B \quad cdt_{ISB}^{B^T} \quad N^{B^T}]^T$$

Eq. 7-1

In Eq. 7-1 r , v , cdt_{ISB} and N are all vectors. r and v each have length 3, cdt_{ISB} has length 2 and consists of a Galileo and a BeiDou time offset, or length zero in the case that only GPS measurements are used, and the length of the sets of ambiguities N^A and N^B would typically be set to the number of receiver channels. Given the flexibility of the software receiver, it is set to

the maximum number of satellites tracked at a single epoch on either of the receivers, in the case of the multi-constellation data set 36, and in the case of the GPS only data set 12.

7.2 State Propagation

This section describes the models used to propagate the state and its associated covariance information between measurement epochs. For an extended Kalman filter, the equations used for the propagation steps are given in Eq. 7-2 and Eq. 7-3.

$$x_{i+1}^- = F(t_{i+1}, x_i^+, u_i)$$

Eq. 7-2

$$P_{i+1}^- = \Phi_{i,i+1} P_i^+ \Phi_{i,i+1}^T + Q_{i+1}$$

Eq. 7-3

These are the same as Eq. 2-11 and Eq. 2-12 from Chapter 2, with the exception that in Eq. 7-2 the linear state transition matrix $\Phi_{i,i+1}$ has been replaced by the non-linear function F to convert the state from the previous filter epoch to the predicted state at the current epoch. F is a function of the current epoch, t_{i+1} , the past state estimates, x_i^+ , and additional parameters u_i which may for example be information about orbital maneuvers. The state transition matrix in Eq. 7-3 is still the simpler linearization which is sufficiently accurate to transform the state covariance matrix P between epochs, in particular given the additional process noise, Q . The details of F , $\Phi_{i,i+1}$ and Q for each state are explained in the following sections. A filter step size of 30 seconds has been used throughout.

7.2.1 Trajectory Model

The position and velocity states are initialized using a single epoch least squares solution at the first epoch with sufficient measurements to calculate one. Both the position and velocity state updates, and the variational equations are calculated by numerical integration (Montenbruck and Gill, 2000). The variational equations consist of the 6x6 trajectory state transition matrix

describing the partial derivatives of the current position and velocity states with respect to the previous epoch's position and velocity states, as well as the 6x5 sensitivity matrix describing the partial derivatives of the current position and velocity with respect to the force model parameters.

A fourth order Runge-Kutta numerical integrator is used, together with a dynamics model of the orbital forces. A comparison between the algorithms used to generate the simulated trajectories of section 6.1.2.1, and the orbit integration used in the relative positioning filter is shown in Table 7-1. The variational equations are integrated with an even simpler force model consisting of only the gravity field, solar radiation pressure, and drag. Note that the relative positioning filter has been built on the foundation of a filter set up to emulate real time navigation for absolute positioning of a single LEO satellite by the GNSS Technology group at DLR. A substantial number of design decisions, in particular where the orbit modelling is concerned, have consequently been inherited directly from the algorithms described in Montenbruck and Ramos-Bosch (2008).

As explained in 6.1.2.1, in the simulated data set there are three maneuvers on the coronagraph spacecraft: 20 minutes after the first perigee passage to set up for the tight formation flying arc, and at the beginning and end of the six hour window around perigee when the spacecraft are held in a rigid formation 150 m apart. To handle these events the force model in the filter's numerical integration is supplemented with information about the maneuvers and tight formation flying control accelerations. The maneuvers are handled by specifying the epochs, thrust forces and desired additional process noise as input to the filter software. The modelling of the control accelerations for the tight formation flying phase initially presented a challenge. To make the filter software as general as possible, it was decided it should take, as optional input, a look up table of control accelerations which are also fed into the numerical integration. The filter's process noise is not increased during a phase of tightly controlled flight. The look up table of control accelerations was calculated as the difference in orbital accelerations at the occulter's position versus at the coronagraph's position.

Table 7-1: Force modelling for the truth trajectory and relative positioning filter

	<i>Truth Trajectory</i>	<i>Positioning Filter</i>
Numerical Integrator	Variable order variable step size Shampine-Gordon	4th order Runge-Kutta
Luni Solar Perturbations	modelled	modelled
Drag	Jacchia 1971 density model	Harris Priester density model
Solar Radiation Pressure	conical shadow model	conical shadow model
Solid Earth Tides	modelled	simplified k_2 model
Pole tides	modelled	
Ocean tides	modelled	
Gravity field	70 x 70	40 x 40
Relativity	modelled	
Tight formation flying	Constant offset, identical velocity	thrust acceleration look up table
Maneuvers	calculated	modelled*

*The maneuvers to acquire the formation shortly after perigee, and to break up the formation at the end of the tight formation flying arc were perfectly known from the truth trajectory generation, and the “true” values could be used as input to the filter. In contrast, the maneuver at the beginning of the tight formation flying arc is the result of the discontinuity between free propagation and a fixed offset between the spacecraft, and had to be estimated. It is modelled with two maneuvers, the magnitudes of which were estimated in a reduced dynamic orbit determination rather than perfectly known.

The filter tuning for the dynamics and force model parameters was done using an alternate form of the relative positioning filter, which was modified to take truth trajectory positions and velocities as the measurement steps. Given the perfect measurements, it was possible to explore the impact of the choice of the orbit model, of the maneuver and tight formation flying phase modelling, and of the tuning of the force model states on the filter behaviour.

It was found that the original force model, using a 10×10 gravity field model, was inadequate to get a good fit between the measurements and orbit model during the perigee passages without estimating very large empirical accelerations. Reducing the weight on the orbit model to allow adequate flexibility at perigee would in turn allow the filter to trust the sparse measurements too much at apogee. (Note that between perigee passages the orbital forces are far less significant, which is the reason missions such as PROBA-3, requiring a very stable baseline, make use of the apogee arc of highly elliptical orbits in the first place.) By upgrading to a 40×40 gravity model the absolute empirical accelerations were reduced to the order of 100 nm/s^2 at perigee, in keeping with typical values for orbit determination of objects in low Earth orbit, and the relative accelerations were on the order of 1 nm/s^2 at perigee. A result showing the ideal case estimated absolute empirical accelerations is shown in Figure 7-3. The absence of any significant empirical accelerations during the apogee tight formation flying arc confirms that the control forces and maneuvers are being accurately modelled.

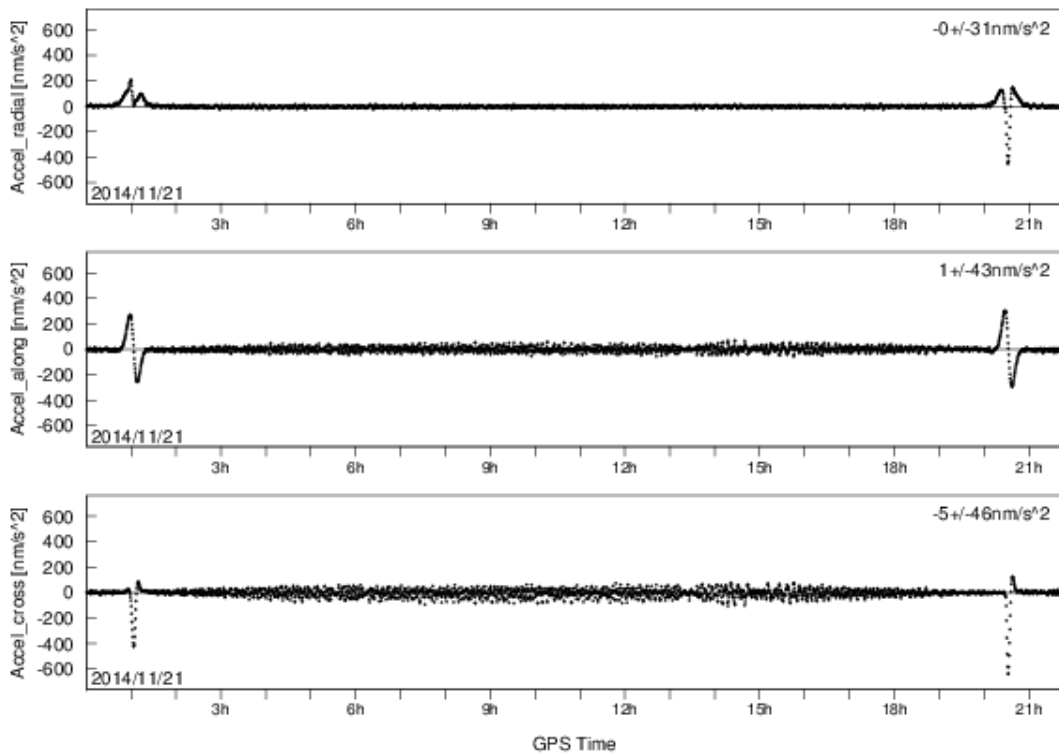


Figure 7-3: Estimated absolute empirical accelerations using perfect measurements and a 40×40 gravity field model

Finally, no process noise is added directly to the position or velocity states in the filter, except in the event of one of the three modelled maneuvers. At the maneuver epochs the velocity states' variances are increased by $(0.001 \text{ m/s})^2$ on the maneuvering spacecraft to account for maneuver modelling uncertainty.

7.2.2 Drag and Solar Radiation Pressure Coefficient Model

The drag and solar radiation pressure coefficients are modelled as random constants. They are initialized to 1.29 for both coefficients for the OSC, and 1.5 for both coefficients for the CSC, which were the values used to generate the truth trajectory, and given an initial uncertainty of 0.1 (coefficients are unitless).

7.2.3 Empirical Acceleration Model

The absolute and relative empirical accelerations are modelled with a first order Gauss-Markov process (Tapley et al 2004). The time update step is given in Eq. 7-4, where dt is the time step and τ is the time constant. For both absolute and relative empirical accelerations a time constant of 600 seconds has been retained from the successful filter implementation in Montenbruck and Ramos-Bosch (2008).

$$a_{i+1} = a_i e^{-dt/\tau}$$

Eq. 7-4

The equation to calculate the empirical acceleration elements in the process noise matrix, Q_a is given in Eq. 7-5, where S_a is the steady state standard deviation of the process noise. The absolute accelerations are tuned to have a process noise standard deviation of 100 nm/s^2 based on the order of magnitude of the expected empirical accelerations from Figure 7-3, while the relative accelerations are given a value of 1 nm/s^2 to constrain the relative orbital dynamics.

$$Q_a = S_a^2 (1 - e^{-2dt/\tau})$$

Eq. 7-5

As explained in the previous section, the blocks of the state transition matrix pertaining to the force model parameters are calculated by numerical integration. They are calculated for each spacecraft independently, and the state transition matrix is block diagonal. The single exception is that the position and velocity states of spacecraft B depend on both the relative empirical accelerations, a^{B-A} , and the absolute empirical accelerations a^A , which must be accounted for with an off-diagonal block.

7.2.4 Clock State Model

As previously explained, the timing parameters consist of a receiver clock bias and drift, as well as inter-system biases on each receiver. The clock offsets and drifts were initialized from the same least squares solutions used to initialize the positions and velocities, while the inter-system biases were initialized based on user input a-priori values.

The clock offsets and drifts are modelled with a clock drift random walk process, while the inter-system biases are modelled as random walk processes (Brown and Hwang 1996). The state prediction equations are given in Eq. 7-6, and the process noise is given in Eq. 7-7.

$$\begin{bmatrix} cdt \\ \dot{cdt} \\ cdt_{ISB} \end{bmatrix}_{i+1} = \Phi_{i+1,i} \cdot \begin{bmatrix} cdt \\ \dot{cdt} \\ cdt_{ISB} \end{bmatrix}_i = \begin{bmatrix} 1 & dt & 0 \\ 0 & 1 & 0 \\ 0 & 0 & 1 \end{bmatrix} \cdot \begin{bmatrix} cdt \\ \dot{cdt} \\ cdt_{ISB} \end{bmatrix}_i$$

Eq. 7-6

$$Q_{clock} = \begin{bmatrix} S_{cdt}^2 dt + S_{\dot{cdt}}^2 dt^3 / 3 & S_{\dot{cdt}}^2 dt^2 / 2 & 0 \\ S_{\dot{cdt}}^2 dt^2 / 2 & S_{cdt}^2 dt & 0 \\ 0 & 0 & S_{cdt_{ISB}}^2 dt \end{bmatrix}$$

Eq. 7-7

Numerically, the clock offset was given process noise density of $S_{cdt} = 0.6 \text{ m}/\sqrt{s}$, the clock drift was given process noise density of $S_{\dot{cdt}} = 0.1 \text{ m/s}/\sqrt{s}$ and the inter-system biases were given

process noise density of $S_{cdt_{ISB}} = 0.01 \text{ m}/\sqrt{s}$. These tuning values were adopted from the clock only filter described in Chapter 6 section 6.3.1.1 and used to assess the measurement quality.

To test the clock parameter tuning, the filter's innovations were normalized using their theoretical standard deviations. A comparison of the normalized innovations of the pseudorange and differential carrier phase measurements (shown in Figure 7-4) with a standard normal distribution demonstrates good agreement. This indicates that there is a good balance between the filter's process noise, the assumed measurement accuracies, and the actual agreement of the measurements with the filtered states and truth trajectory.

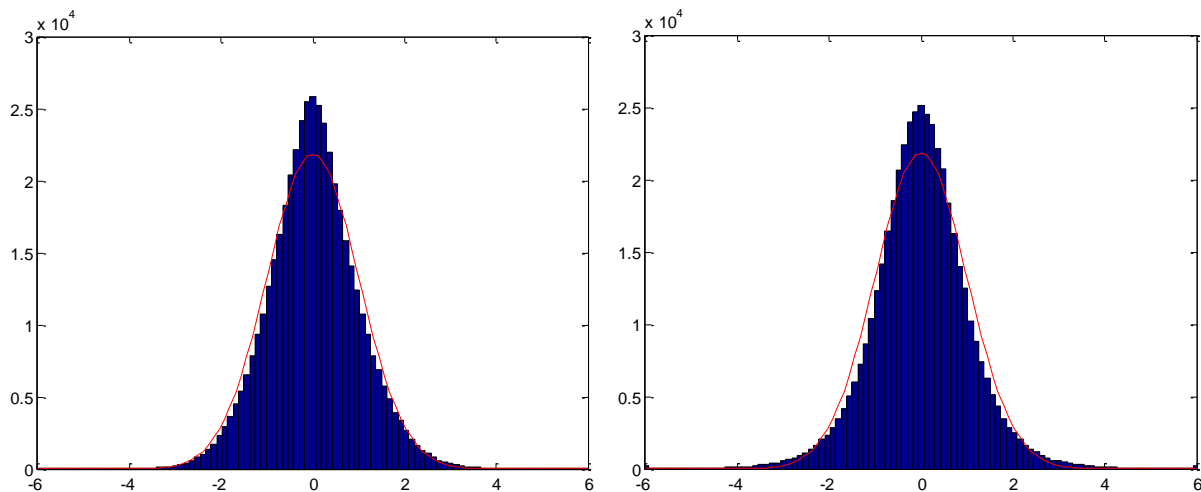


Figure 7-4: Agreement of the pseudorange (left) and differential carrier phase (right) normalized innovations from the clock state filter with the standard normal distribution

If either the process noise or the measurement noise were too large, the histograms would be narrower than the normal distribution, while if the process noise or measurement noise was set too optimistically the histograms would be wider than the theoretical curves. Because the analyses of Chapter 6 has already provided a high degree of confidence in the measurement weighting, the normalized innovations can be used to tune the process noise for the clock states.

7.2.5 Ambiguity Model

The un-differenced ambiguities are theoretically modelled as random walk processes to provide the option for filter tuning flexibility, but they are essentially held constant in that they are tuned

to have extremely low process noise standard deviation of $S_N = 1 \times 10^{-8}$ m. The propagation and process noise equations used in the filter are given in Eq. 7-8 and Eq. 7-9 respectively. The time constant in Eq. 7-9 was set to 30 s in keeping with the filter step size.

$$N_{i+1} = N_i$$

Eq. 7-8

$$Q_N = S_N^2 dt / \tau_N$$

Eq. 7-9

They are initialized based on the difference between the GRAPHIC measurement and the modelled measurement at the same epoch. Their uncertainty at initialization is calculated based on the current uncertainty of the state estimates, according to Eq. 7-10, where P is the current state covariance matrix and H is the row matrix of partial derivatives of the phase measurement model with respect to the states. While code-carrier would be a more typical method of ambiguity initialization, in the HEO scenario the newly acquired signals with the strongest signal power are newly risen from behind the Earth and subject to the greatest ionospheric path delay, on the order of 20 m. Rather than use a pseudorange measurement which is known to have a large bias, the current best estimate of the state, which should theoretically be more accurate than a single measurement, is used.

$$\sigma_N^2 = HPH^T$$

Eq. 7-10

7.2.6 Filter State Transition Matrix

In summary, the structure of the full state transition matrix is shown in Eq. 7-11, corresponding to the state vector in Eq. 7-1. Note the coefficients for each satellite have been grouped as “C” while the accelerations have been grouped as “a” for a cleaner representation. The elements expressed as derivatives are solved by numerical integration.

$$\Phi = \begin{bmatrix} \left[\begin{array}{cccc} \frac{dr^A}{dr_0^A} & \frac{dr^A}{dv_0^A} & \frac{dr^A}{dC_0^A} & \frac{dr^A}{da_0^A} \\ \frac{dv^A}{dr_0^A} & \frac{dv^A}{dv_0^A} & \frac{dv^A}{dC_0^A} & \frac{dv^A}{da_0^A} \\ \frac{dC^A}{dr_0^A} & \frac{dC^A}{dv_0^A} & \frac{dC^A}{dC_0^A} & \frac{dC^A}{da_0^A} \\ 0 & 0 & 1 & 0 \\ 0 & 0 & 0 & e^{-dt/\tau} \end{array} \right] & 0 & 0 & 0 & 0 & 0 \\ 0 & \left[\begin{array}{ccc} 1 & dt & 0 \\ 0 & 1 & 0 \\ 0 & 0 & 1 \end{array} \right] & 0 & 0 & 0 & 0 \\ 0 & 0 & [1] & \left[\begin{array}{cccc} dr^B & dr^B & dr^B & dr^B \\ \frac{dr^B}{dr_0^B} & \frac{dr^B}{dv_0^B} & \frac{dr^B}{dC_0^B} & \frac{dr^B}{da_0^{B-A}} \\ \frac{dv^B}{dr_0^B} & \frac{dv^B}{dv_0^B} & \frac{dv^B}{dC_0^B} & \frac{dv^A}{da_0^{B-A}} \\ \frac{dC^B}{dr_0^B} & \frac{dC^B}{dv_0^B} & \frac{dC^B}{dC_0^B} & \frac{dC^B}{da_0^{B-A}} \\ 0 & 0 & 1 & 0 \\ 0 & 0 & 0 & e^{-dt/\tau} \end{array} \right] & 0 & 0 \\ 0 & 0 & 0 & 0 & \left[\begin{array}{ccc} 1 & dt & 0 \\ 0 & 1 & 0 \\ 0 & 0 & 1 \end{array} \right] & 0 \\ 0 & 0 & 0 & 0 & 0 & [1] \end{bmatrix}$$

Eq. 7-11

7.3 Measurement Updates

Three types of measurements were used in the filter: undifferenced pseudoranges measurements, undifferenced GRAPHIC measurements (Group and Phase Ionospheric Correction, Yunck 1996), and between receiver single difference phase measurements. The measurement model equations are given below.

Eq. 7-12 is the equation for a pseudorange, where $x_{GNSS}, y_{GNSS}, z_{GNSS}$ are the GNSS satellite position from the broadcast ephemeris in an Earth centered Earth fixed coordinate frame (ECEF), x_{rx}, y_{rx}, z_{rx} are the position of the receiver in ECEF from the state vector, cdt_{rx} is the receiver clock offset from GPS system time, and cdt_{ISB} is the inter-system timing bias from GPS time to

the time of the measurement's system and is dropped for GPS measurements. In addition, three error sources are included, cdt_{sat} is the error in the GNSS satellite's clock, $d\rho_{orbit}$ is the broadcast ephemeris error, and n_p is the noise or tracking jitter on a pseudorange measurement. Because they were not simulated, multipath and tropospheric error are not considered. Tropospheric error was not simulated because signals passing close enough to the Earth to experience the error should in any case be excluded, while multipath was not simulated because its behaviour is too situation specific to properly model without a significant increase in the rigorousness of the simulation.

$$P = \sqrt{(x_{GNSS} - x_{rx})^2 + (y_{GNSS} - y_{rx})^2 + (z_{GNSS} - z_{rx})^2} + cdt_{rx} + cdt_{ISB} + cdt_{sat} + d\rho_{orbit} + d_{iono} + n_p$$

Eq. 7-12

Eq. 7-13 is the equation for a GRAPHIC measurement. It is nearly the same as the pseudorange measurement, with the notable exception that there is no longer an ionospheric delay error term. The ionosphere induced phase advance and group delay are equal and opposite, and therefore cancelled in the GRAPHIC measurement combination. The disadvantage is that an ambiguity term $N/2$ with half the magnitude of the phase ambiguity appears. The measurement is subject to 50% of the pseudorange noise and 50% of the carrier phase measurement noise.

$$GR = \sqrt{(x_{GNSS} - x_{rx})^2 + (y_{GNSS} - y_{rx})^2 + (z_{GNSS} - z_{rx})^2} + cdt_{rx} + cdt_{sat} + cdt_{ISB} + N/2 + d\rho_{orbit} + n_p/2 + n_\Phi/2$$

Eq. 7-13

The single difference phase measurement equation is shown in Eq. 7-14. Subscripts A and B differentiate between the two user spacecraft, and Δ designates a between-receiver single differenced quantity. The strength of the single differenced phase measurement is the reduced measurement noise, n_Φ , as compared to any pseudorange based measurements, the cancellation of the GNSS satellite clock error, and the near cancellation of the broadcast ephemeris and ionospheric errors due to the close proximity of the two formation flying spacecraft. The impact of asynchronous measurements is discussed in more detail in the following section.

$$\begin{aligned}\Delta\Phi = & \sqrt{(x_{GNSS} - x_{rxA})^2 + (y_{GNSS} - y_{rxA})^2 + (z_{GNSS} - z_{rxA})^2} + cdt_{rxA} + cdt_{ISBA} + N_A \\ & - \sqrt{(x_{GNSS} - x_{rxB})^2 + (y_{GNSS} - y_{rxB})^2 + (z_{GNSS} - z_{rxB})^2} - cdt_{rxB} - cdt_{ISBB} - N_B \\ & + \Delta d\rho_{orbit} + \Delta d_{iono} + \sqrt{2}n_\Phi\end{aligned}$$

Eq. 7-14

The measurement updates are done using equations 2-13, 2-14 and 2-15 from Chapter 2. The measurement update is done sequentially, with one measurement added at a time. First all available pseudorange measurements and GRAPHIC measurements are applied on each spacecraft, followed by the between receiver single differenced phase measurements for any commonly tracked GNSS satellites.

7.3.1 Measurement Errors and Weighting

In the previous chapter a second filter, used to estimate only clock states and assess the quality of the receiver data with respect to the simulator truth trajectory was introduced in section 6.3.1.1. The measurement screening output from the same filter was used here to determine appropriate weights for the GNSS measurements, based on their tracking jitter standard deviations as a function of C/N₀. It was found that while an exponential relationship was expected, as a result of the Kalman filter tracking loop there was in fact a linear relationship which indicates a varying tracking loop bandwidth. Figure 7-5 and Figure 7-6 show the relationships of the pseudorange error and phase error to C/N₀ for each of the three constellations. These linear relationships formed the basis of the measurement weighting in both the clock only and the relative positioning filters. The theoretical GPS curves in the plots, included purely for interest, are the

expected output from a standard tracking loop based on the same assumptions and equations as the theoretical tracking jitter curves in Chapter 5 section 5.5.2.

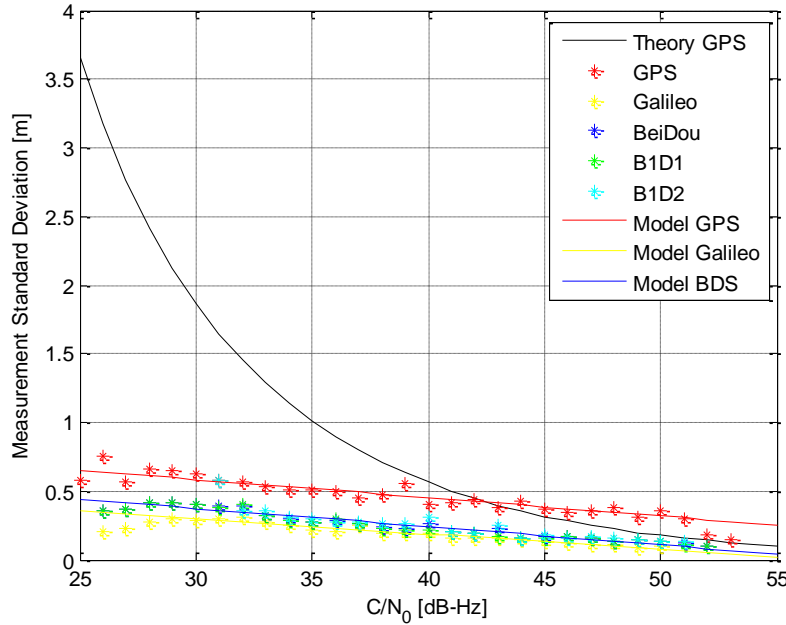


Figure 7-5: Code tracking jitter as a function of C/N_0

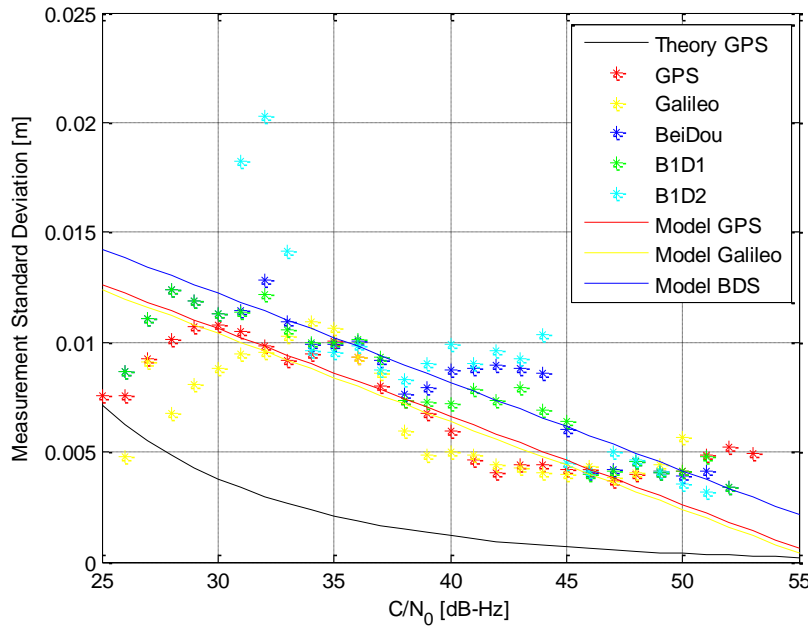


Figure 7-6: Phase tracking jitter as a function of C/N_0

The measurement standard deviations shown in Figure 7-5 and Figure 7-6 were calculated based on the measurement residuals of the clock only filter. The residuals for each system were sorted into 1 dB-Hz bins for the full 22 hour occulter spacecraft data set, and the standard deviation of each C/N₀ bin was calculated. At the end of each clock filter update step residuals from all measurements, even those excluded from the solution, were calculated to get the full error distribution rather than one truncated by blunder detection. Table 7-2 summarizes the actual relationships between the C/N₀ and phase and code noise for GPS, BeiDou and Galileo, calculated using linear regression of the measurement standard deviations, and corresponding to the colored lines in the figures.

Table 7-2: Tracking jitter vs C/N₀ in dB-Hz

<i>Measurement</i>	<i>System</i>	<i>Standard Deviation</i>	
		<i>slope</i>	<i>y-intercept</i>
code	GPS	-0.0133	0.98
	Galileo	-0.0110	0.63
	BeiDou	-0.0133	0.77
phase	GPS	-0.0004	0.023
	Galileo	-0.0004	0.022
	BeiDou	-0.0004	0.024

Although the figures and linear relationships only account for tracking jitter, the actual measurements were subject to more significant errors. The pseudorange measurements were weighted based on the linear relationships in Figure 7-5 plus an additional 1 m of error (added to the y-intercepts of Table 7-2) to account for the broadcast ephemeris errors. Pseudoranges from signals with a line of sight passing closer than 850 km to the Earth were excluded (from both the clock only and the relative navigation filters), as they are known to be biased by systematic ionospheric errors which do not fit with the assumption of normally distributed errors implicit in both the filters and in blunder detection. Consequently, for 10 minutes surrounding the perigee passage when the spacecraft itself is below 850 km, no pseudorange measurements are used.

GRAPHIC measurements are free of ionospheric errors, and are therefore included into the relative positioning filter at any elevation. They are weighted in the filter by propagating the code and phase measurement errors through the GRAPHIC linear combination equation, which should result in Eq. 7-15. σ_p^2 is the pseudorange variance and σ_ϕ^2 is the phase variance. In the actual filter software the factor of 2 was neglected, initially by accident and later because it better represents the reality under broadcast ephemeris errors.

$$\sigma_{GR} = \frac{1}{2} \sqrt{\sigma_p^2 + \sigma_\phi^2}$$

Eq. 7-15

Between receiver differential phase measurements are likewise included for signals at all elevations, as the nearly identical paths they follow through the ionosphere to the two HEO receivers should yield very good error cancellation. Because the phase measurements are differential, the impact of ionospheric errors and broadcast ephemeris errors are both neglected, and the weighting is based on the propagation of the tracking jitter alone through the phase measurement combination. The phase weights are calculated as shown in Eq. 7-16. Note that because the tracking jitter is C/N₀ dependent the phase standard deviations from the two satellites may not be identical.

$$\sigma_{\Delta\phi} = \sqrt{\sigma_{A\phi}^2 + \sigma_{B\phi}^2}$$

Eq. 7-16

7.3.2 Impact of Asynchronous Measurements

As a final point of discussion on the cancellation of errors and the impact of asynchronous measurements, some rough calculations were conducted based on relevant literature to determine how fast the typical GNSS error sources are changing in time from the perspective of a receiver on a HEO spacecraft.

First, because broadcast orbit errors are changing very slowly in time, typically remaining the same over hours, the impact of asynchronous measurements is negligible except at the transition to a new ephemeris data set. The motion of the HEO spacecraft and proximity of the formation flying receivers is more significant.

Next, the impact of GNSS satellite clock errors on asynchronous measurements were considered. Various studies of GNSS short-term clock stability have been conducted, using carrier phase data to get more frequent clock information than the 30 second data available from the IGS and other data processing centers. Based on Allan Deviation curves, at 1 second the deviation is on the order of 10^{-10} (GLONASS) or 10^{-11} (GPS) seconds (Hesselbarth and Wanninger 2008, Hauschild et al 2013, Griggs et al. 2012). By multiplying by the approximate speed of light, a back of the envelope range for clock error rate of change is 3 mm/s to 3 cm/s.

Finally, the rate of change of the ionospheric errors was considered. Based on the figure of excess path delay as a function of ray height in Figure 3 of Hoque and Jakowski (2011), the maximum slope is 2.4 m over 50 km from 200 km above the ground to 250 km above the ground. This corresponds to 0.04 m / km. Next, assuming the rule of thumb from Griggs et al (2012) that the line of sight has a vertical speed of 2.5 km/s during an occultation, this amounts to roughly 10 cm/s of change in ionospheric delay for an occulting signal, which could be significant. A look at the smoother simulated ionospheric error simulated here reveals a slope of 23.5 m / 2 minutes for the entire duration of an occultation, which equates to 4 cm/s of ionospheric error, also potentially significant.

In the case of the ionospheric error the impact of the asynchronous measurements could either be improved or exacerbated by the shape of the formation. For example, if one satellite is following the other with a given delay, and the clock is making measurements with the same delay, the differential measurements would be taken at virtually the same location and would experience excellent error cancellation. If the follower spacecraft's clock had an advance the measurements would be taken further apart and the error cancellation would be worse.

7.3.3 Outlier Detection

Both blunder detection and cycle slip detection have been implemented into the relative positioning filter.

Blunder detection was carried out by rejecting measurements with an innovation exceeding 3 times the innovation standard deviation. The innovation is calculated as the difference between the measurement and the modelled measurement following the equations in section 7.4, while the innovation standard deviations are calculated using the filter covariance information, P , the design matrix, H and the measurement standard deviation, $\sigma_{\text{measurement}}^2$, as shown in Eq. 7-17.

$$\sigma_{\text{innovation}} = \sqrt{H P H^T + \sigma_{\text{measurement}}^2}$$

Eq. 7-17

Cycle slip detection presented a significant challenge. On the one hand, the measurements are only being taken every 30 seconds, which given the dynamics dramatically reduces the effectiveness of the single frequency phase rate cycle slip detection method. A second method was therefore considered, in which the phase difference from one epoch to the next was compared to the modelled phase difference over the same time span. This method is highly sensitive to changes in other states such as the receiver clock or clock drift, and errors in the estimated filter states, for example velocity.

Both methods were implemented, and ultimately the second method, of predicting the phase change based on the filter, was adopted. It marginally outperformed the phase rate method, which is based on Doppler measurements. Good cycle slip detection performance however remains an area of potential future work, as neither method is particularly effective and the detection threshold generally has to be set very high to avoid excluding a substantial portion of the GNSS data. Ideally, the receiver itself would perform cycle slip detection and either repair the detected cycle slips, or flag bad measurements for the filter.

In general, outlier detection for the HEO scenario is challenging. The major difficulty is that there are insufficient measurements to do statistical data screening/blunder detection, but at the same time the geometry is weak enough for the filter to be incredibly sensitive to an outlier. In particular, there are phases of the orbit where a period with no measurements at all is followed by a period in which only one satellite is tracked. In this case, the filter's estimated covariances of the states may grow sufficiently that the filter is extremely sensitive to the first new measurements, and very susceptible to divergence in the case of a blunder. Realistic statistical modelling of the measurement errors and the error growth during orbit propagation in the absence of measurements are therefore both important.

7.4 Results

Results from five different scenarios have ultimately been considered. The first three are the results from the multi-constellation data set detailed in the previous chapter. The fourth is a new data set described in section 7.4.4, which was collected to replicate the performance of the high sensitivity GPS only receivers onboard ChangE-5T and the Magnetospheric Multi Scale Mission, and to continuously track enough GPS satellites for a position fix. The fifth is a zero baseline test between two occulter spacecraft data sets, which removes the impact of the maneuvers and the tight formation flying phase from the problem. Throughout the analysis the two spacecraft are referred to by their abbreviations, where the OSC is the non-maneuvering occulter spacecraft, and the CSC is the maneuvering coronagraph spacecraft.

7.4.1 Multi-Constellation HEO Tracking Strategy

The absolute positioning results are shown in Figure 7-7 and the relative positioning results in Figure 7-8, as compared to the simulated truth trajectory. From the figures, it can be seen that the relative positioning accuracy is at least an order of magnitude better than the absolute positioning, in keeping with expectations and with the superior quality of the differenced phase measurements compared to either the pseudorange or GRAPHIC measurements. The relative positioning accuracy remains below 5 m in any one axis throughout the simulated orbit, while

the absolute positioning accuracy remains below 50 m. To put the results in context, the number of tracked satellites is available in Figure 6-25.

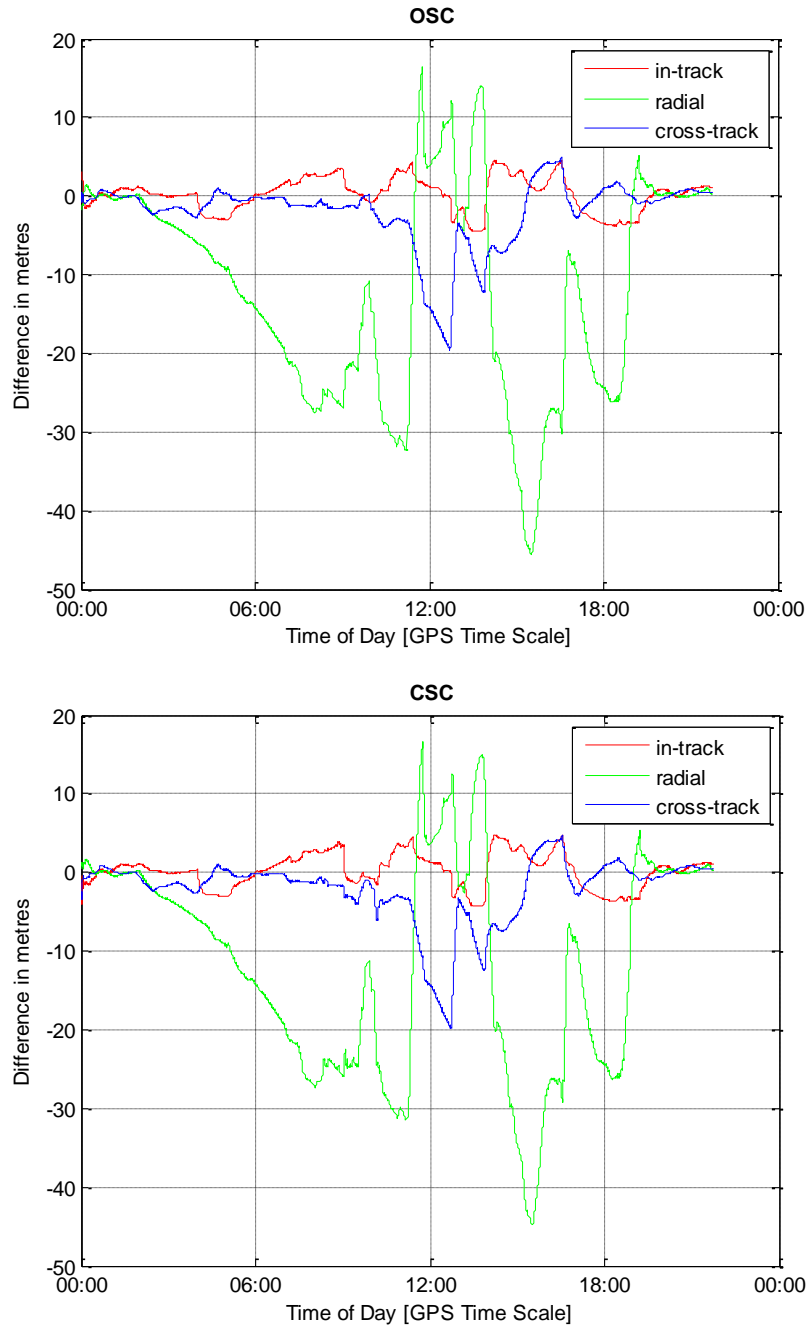


Figure 7-7: Absolute position accuracy on the OSC (upper) and CSC (lower) as compared to the simulated trajectory

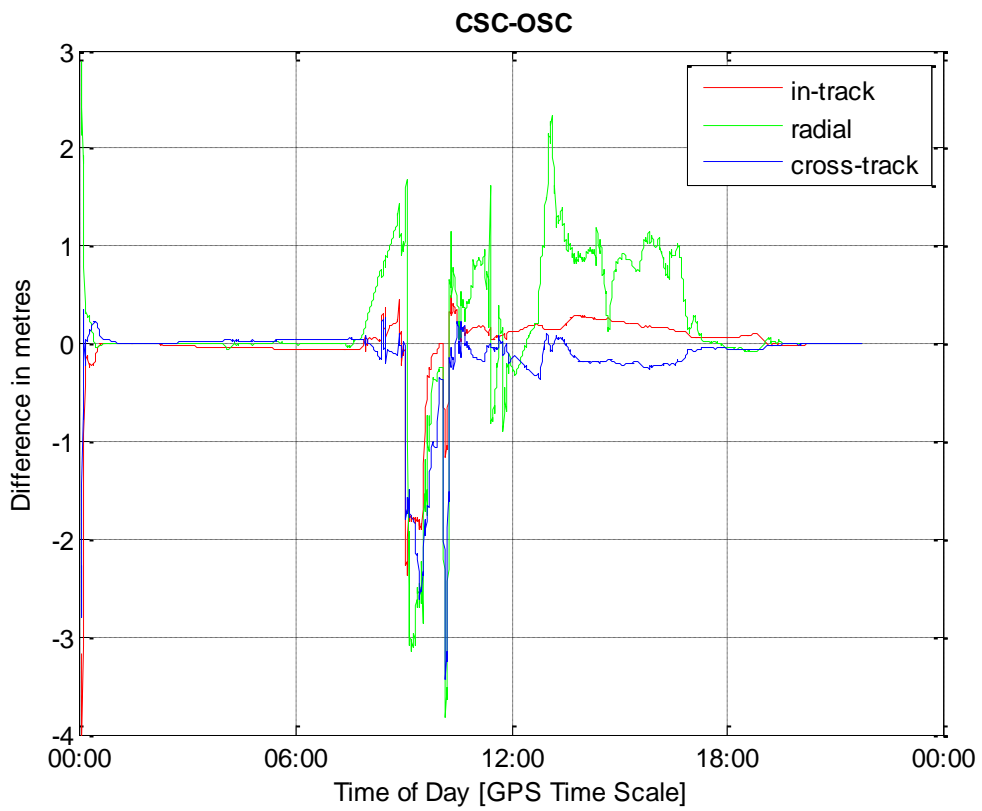


Figure 7-8: Relative position accuracy on the CSC-OSC as compared to the simulated trajectory

To get a better idea of the performance during the perigee arc, zoomed in versions of previous figures are shown in Figure 7-9 and Figure 7-10. Perigee passage occurs at exactly 1:00. It can be seen that while the absolute positioning accuracy is at best roughly at the metre level, in keeping with the simulated ionospheric and broadcast ephemeris errors, the relative positioning accuracy reaches sub-cm level. The exception is at 1:20 when a maneuver is applied to the CSC to begin setting up for the controlled apogee arc.

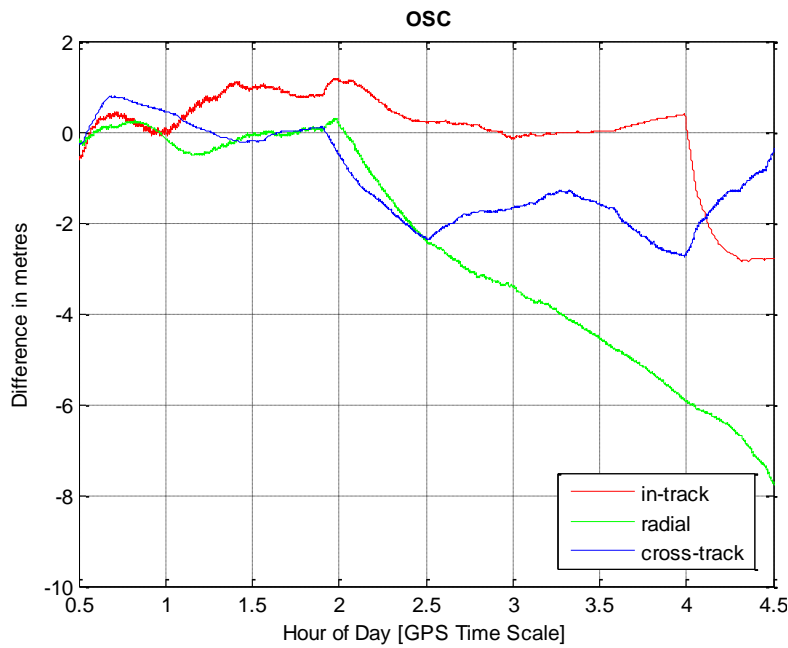


Figure 7-9: Absolute orbital filter accuracy at and following perigee

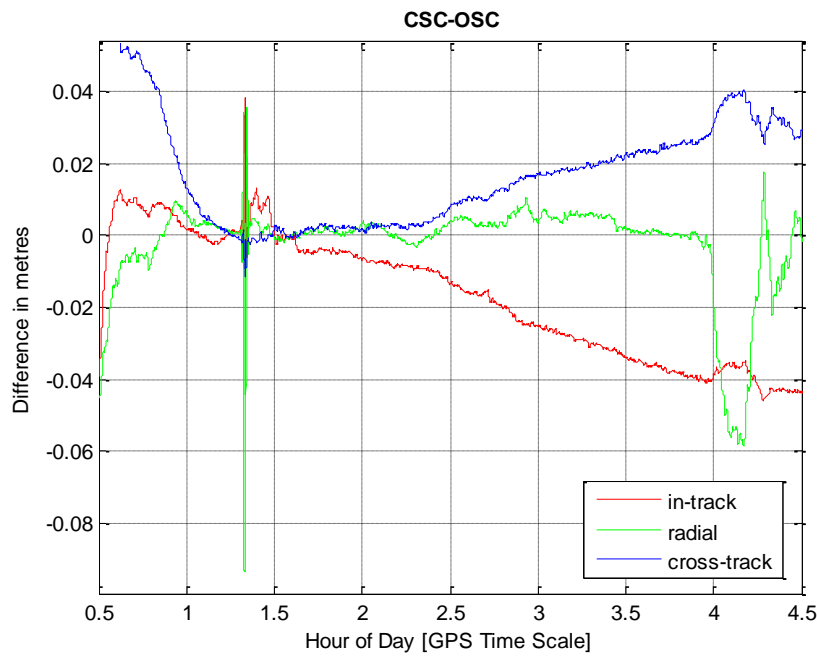


Figure 7-10: Relative orbital filter accuracy at and following perigee

Both absolute and relative positioning are subject to windows of poor geometry or sparse measurements which bias the solution. The trend of worse positioning accuracy at apogee when geometry is poor and measurements sparse is also clearly visible in the full orbit plots. Interestingly, the absolute position begins to diverge almost immediately after the perigee passage, while the relative positioning accuracy stays bounded at the < 10 cm level on each of the three axes until the beginning of the tight formation flying arc. At this point a drift stop maneuver on the coronagraph spacecraft, at 7:48, disturbs the velocity estimate, destroys some of the error cancellation advantages, the covariances grow, and the filter is unable to recover to its former level of accuracy.

Figure 7-11 and Figure 7-12 show the corresponding filter standard deviations on the three components of the absolute and relative positions respectively. For the absolute positioning, only the result from the OSC has been included, as it is representative for both data sets. The covariance information for the relative positions is calculated by applying a Jacobian describing the subtraction of the coronagraph - occulter coordinates, J , to the variance covariance matrix,

followed by the rotation matrix from the ICRF to the radial, in-track, cross track frame, R_{ICRF}^{RTN} , as shown in Eq. 7-18.

$$P_{relpos}^{RTN} = R_{ICRF}^{RTN} J P J^T {R_{ICRF}^{RTN}}^T$$

Eq. 7-18

From the figures it can be seen that the absolute positioning covariance propagation dramatically underestimates the actual error in the states, in particular in the radial and the cross-track directions. On the contrary, there is very good agreement between the theoretical accuracy of the relative position solution and its error compared to the truth trajectory. The true error is bounded by the 1 sigma standard deviation envelope throughout. This would suggest that the absolute positioning is subject to non-Gaussian errors which are poorly modelled by the measurement covariance information, in this case most likely the broadcast orbit errors. The relative positioning is mostly influenced by the high quality single differenced phase measurements which have little to no residual systematic errors.

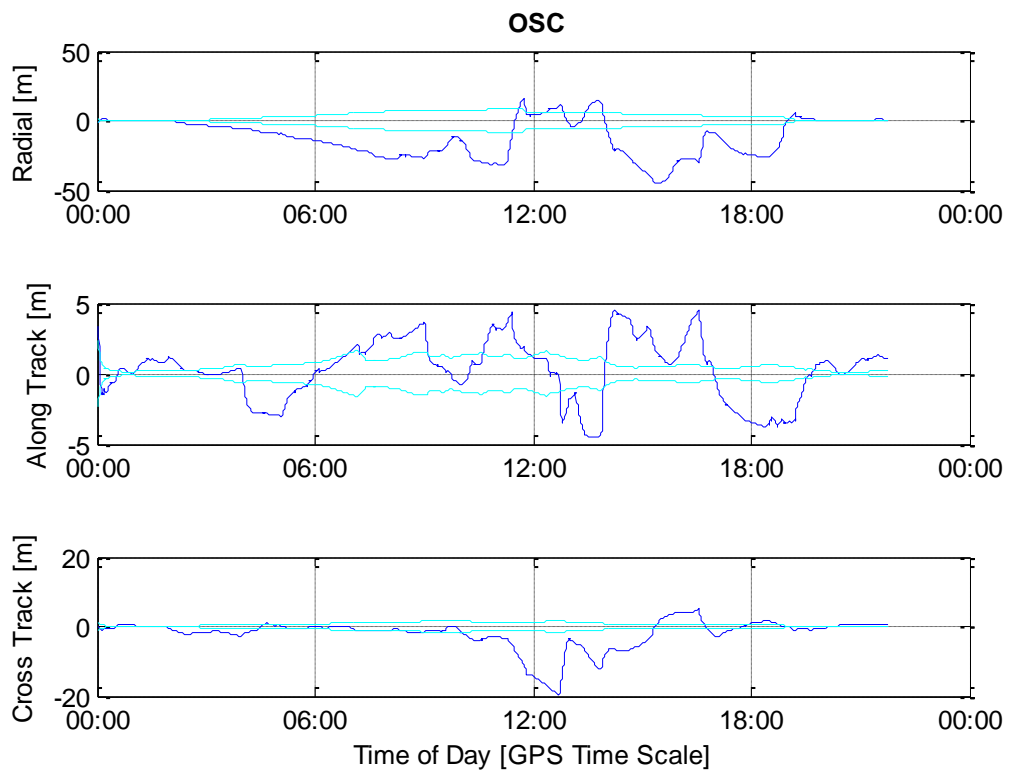


Figure 7-11: Absolute position 1 sigma standard deviation (cyan) versus actual error (blue) on the OSC

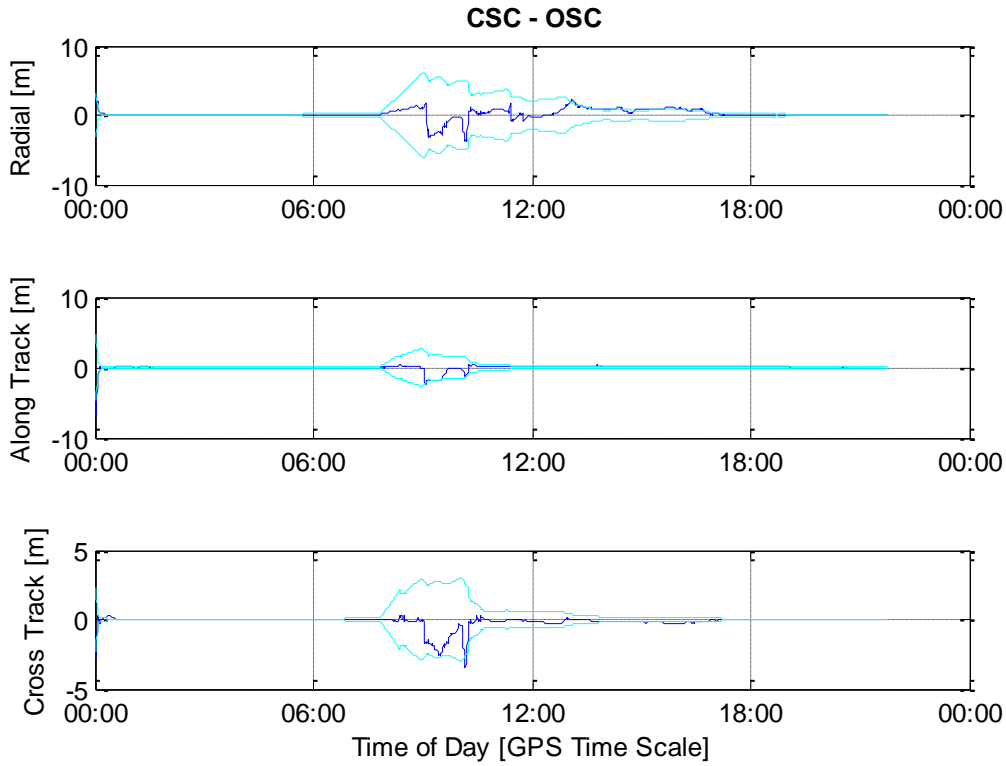


Figure 7-12: Relative position 1 sigma standard deviation (cyan) versus actual error (blue)

Finally, the residuals and other estimated states are investigated. The residuals on the OSC pseudorange and GRAPHIC measurements are shown in Figure 7-13 and single difference phase measurements are shown in Figure 7-14. It is clear that neither the pseudorange nor GRAPHIC residuals are unbiased, in particular around 15:00 when the positioning errors are the greatest. From the density of the residuals it is also possible to make the observation that the poor positioning in the first half of the apogee arc stems from sparse data, while in the second half of the arc it is due to a poor estimate. From the phase residuals it can be seen that while the data is for the most part in good agreement with the filtered solution, both the cycle slip detection and the blunder detection occasionally fail to catch a cycle slip, in this case most notably at 9:00 when the filtered relative position in Figure 7-8 also begins to exhibit problems.

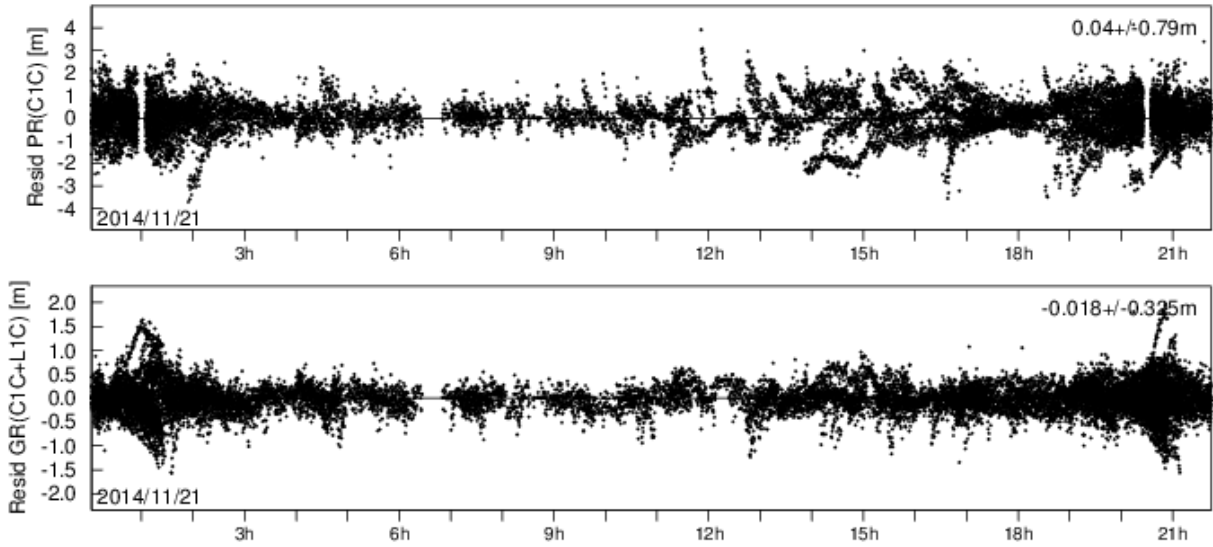


Figure 7-13: Pseudorange (above) and GRAPHIC (below) residuals from the OSC

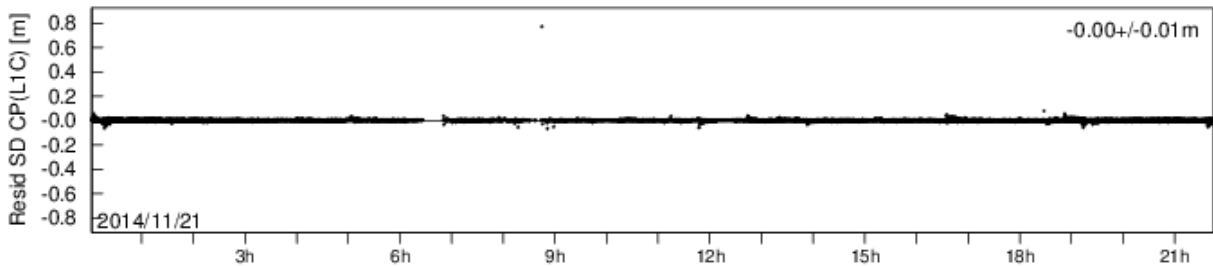


Figure 7-14: Between receiver single difference phase residuals

Some observations can also be made by looking at the estimated receiver clock biases, shown in Figure 7-15 and Figure 7-16, estimated absolute empirical accelerations, shown in Figure 7-17, and estimated relative accelerations, shown in Figure 7-18. First, the clock behaviour clearly fits very well with the assumed bias and drift model, as indicated by the very stable linear increase in clock bias. Note the clock errors are a combination of the error on the receiver and the simulator clocks. Because the simulations were done in two runs, the non-common simulator clock effects are lumped into the estimated receiver clock offset. As a result of the receiver clock quality and ambient conditions in the lab, the measurements are in fact well synchronized with an offset on the order of only 80 μ s.

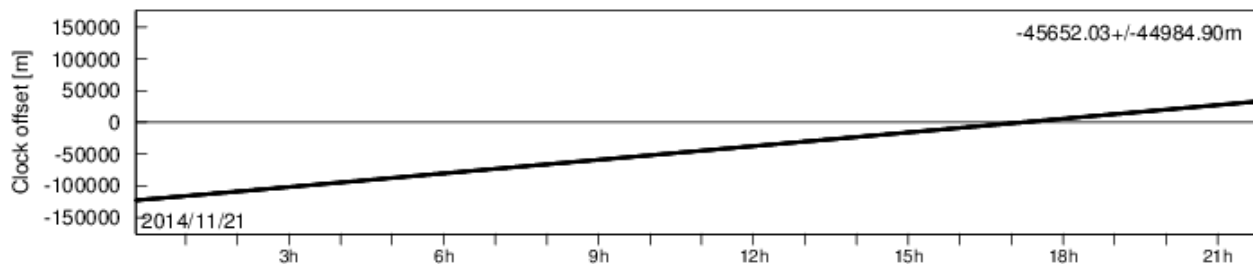


Figure 7-15: OSC estimated receiver clock offset

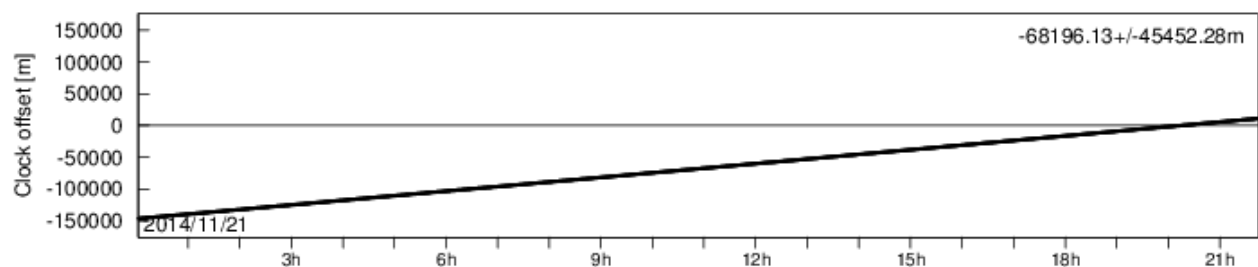


Figure 7-16: CSC estimated receiver clock offset

The absolute empirical acceleration estimates appear to be quite poor. Contrary to expectations they do not manage to capture the actual differences in acceleration between the truth trajectory and the filter trajectory, shown in Figure 7-3. By changing the filter tuning to give more weight to the measurements they can be improved, but at the cost of a reduced positioning accuracy. Likewise, rather than capturing the slight differences in accelerations between the spacecraft, the estimated relative accelerations serve mainly to provide some flexibility during the initial convergence phase of the filter, but only poorly model the expected relative accelerations. The difficulty estimating absolute and relative empirical accelerations could indicate either that the geometry and data rate are insufficient for a good estimate, or that there is still some problem in the filter design. Given the most significant discrepancies occur approaching and leaving perigee, it's also possible that the receiver's biased tracking under high dynamics produces systematic errors on all measurements which impact the estimation, but this explanation fits poorly with the observation that more confidence in the measurements yields a better result.

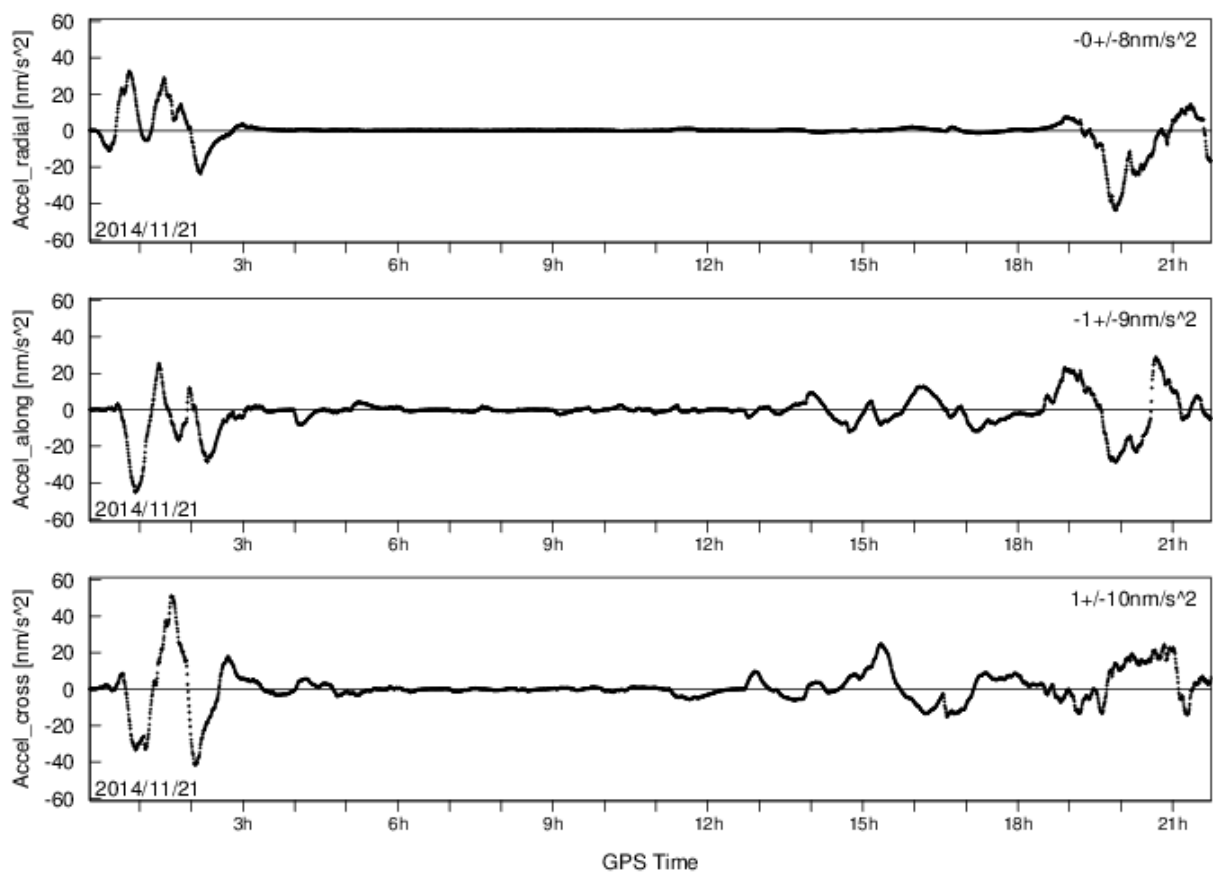


Figure 7-17: OSC estimated absolute empirical accelerations

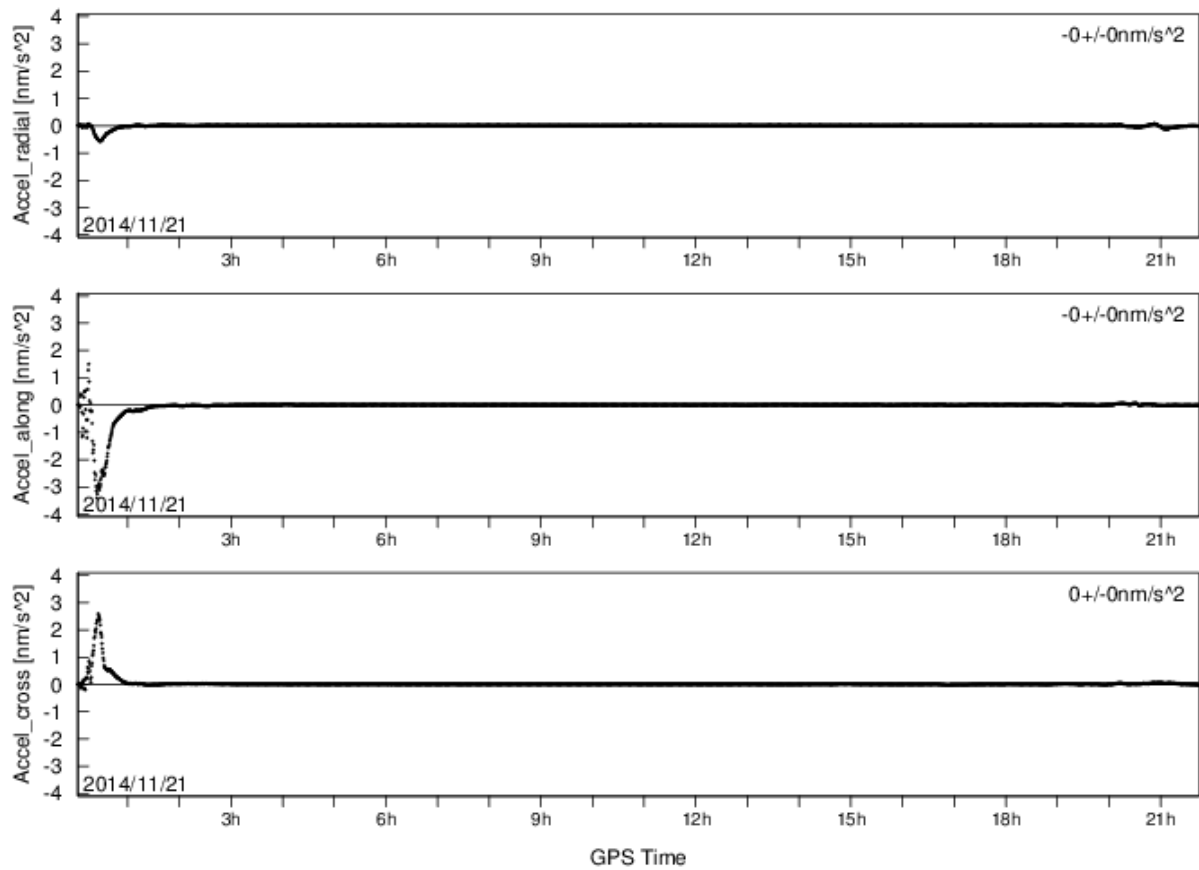


Figure 7-18: Estimated relative empirical accelerations

7.4.2 Multi-Constellation Data with Imperfect Thrust Modelling

Up until this point, a perfect knowledge of the maneuvers and of the control acceleration during the six hour tight formation flying phase has been assumed. This assumption is however unrealistic, and so the filter's modelling of the maneuvers and control accelerations allows the flexibility to input erroneous data. Using exactly the same setup as in the previous section, the filter was re-run but with only 95% of the thrust forces considered. The relative positioning results are shown in Figure 7-19.

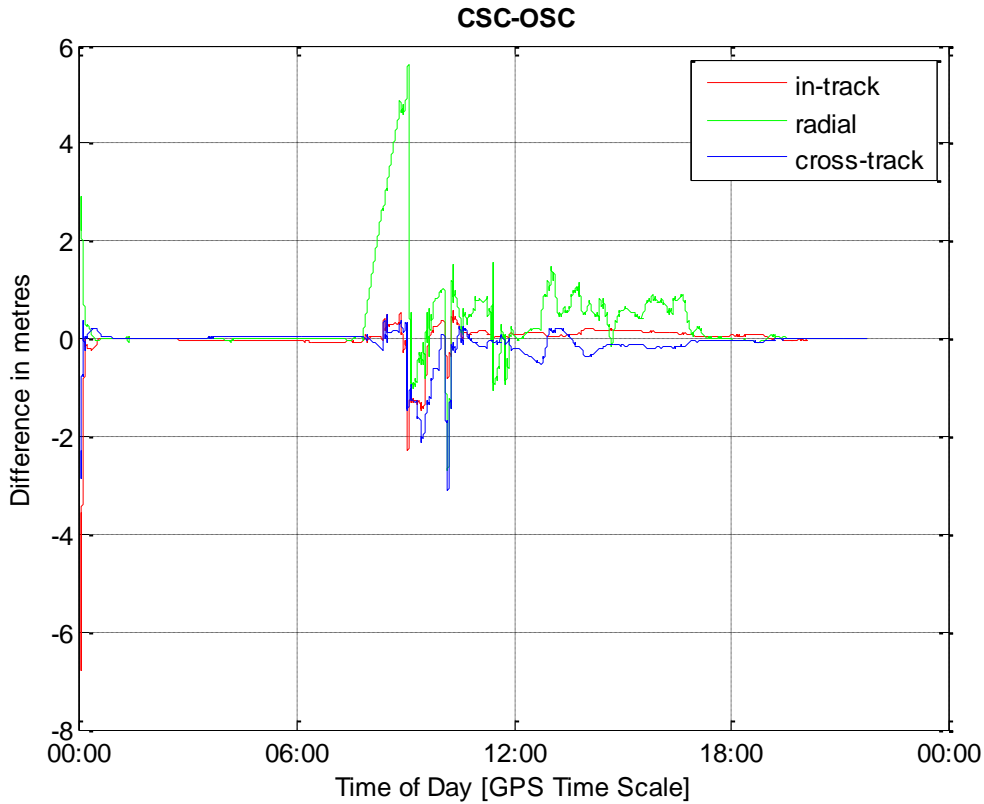


Figure 7-19: Relative positioning results with a 5% error on all control thrusts

As compared to the original relative positioning result in Figure 7-8, there is an obvious increase in error following the 7:48 maneuver, which the filter is unable to recover from quickly. The maneuver immediately following the perigee passage at 1:20 is also now recognizable by a minimal increase in radial error, but given the fantastic geometry and abundant measurements from three constellations at perigee the recovery is very fast. As shown in Figure 7-20, the error is still bounded by the standard deviation envelope, although this would not be the case for a bigger thrust error.

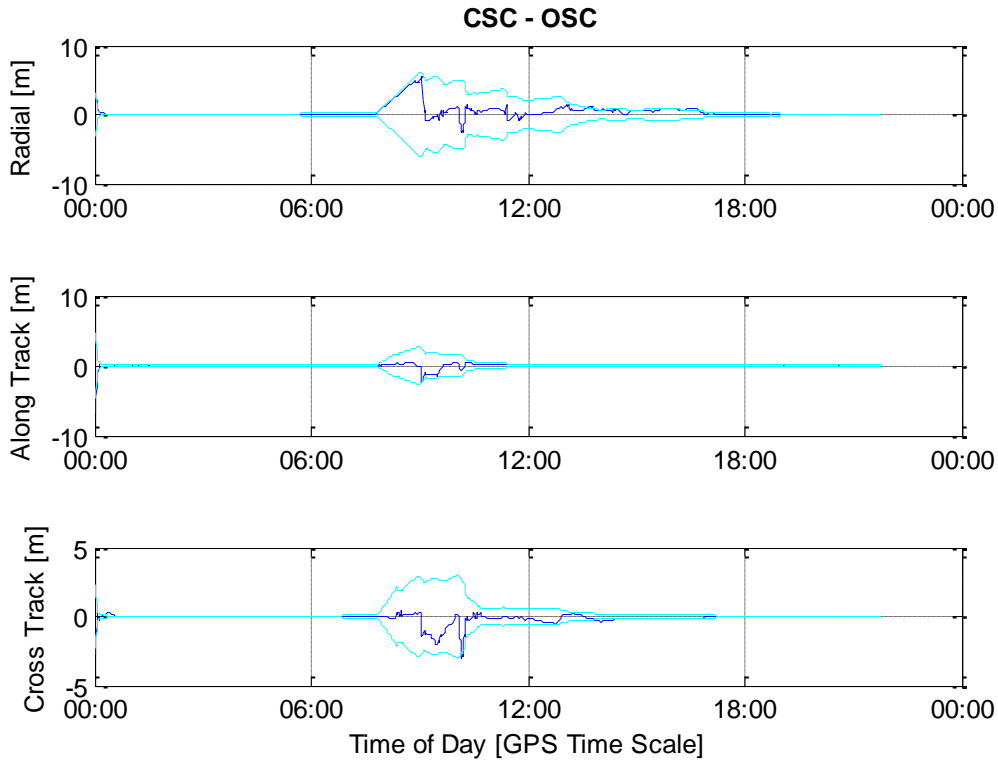


Figure 7-20: Relative positioning 1 sigma standard deviation (cyan) versus actual error (blue) results with a 5% error on all control thrusts

Note that the intentional degradation of the maneuver thrust information and of the tight formation flight control accelerations has been removed again for the remainder of the analysis.

7.4.3 Multi-Constellation Standard Tracking Strategy

Next, the data from the standard tracking version of GSNRTM described in the previous chapter was run through the relative positioning filter. The results for the absolute position on the OSC and for the relative position are shown in Figure 7-21 and Figure 7-22 respectively. It can be seen that the absolute position begins to diverge after a period of bad measurements from approximately 4:00 to 5:00, and the relative position begins to diverge at 7:48 with the maneuver on the CSC and the beginning of the tight formation flying arc.

Note that in this case the assumed standard deviations of the measurement errors were increased in keeping with the different tracking loop design. The same assessment using the clock only

filter was conducted as described in section 7.3.1, and the measurement noise was increased accordingly.

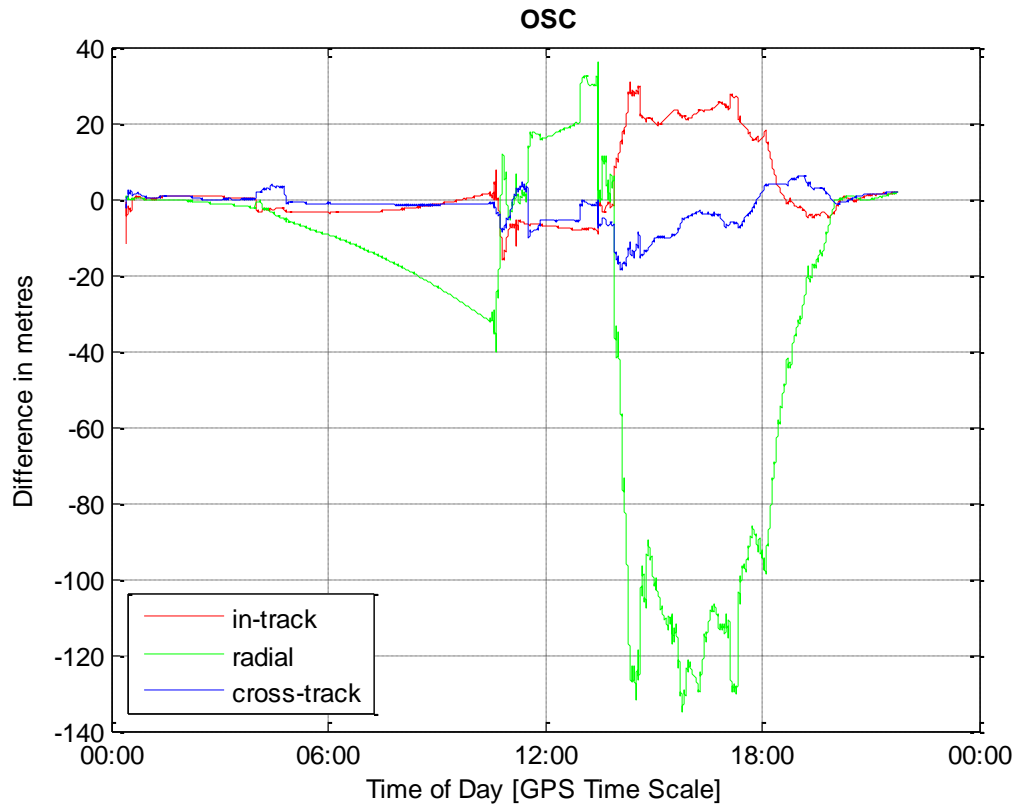


Figure 7-21: Absolute positioning error on the OSC using the standard tracking version of GSNRxTM

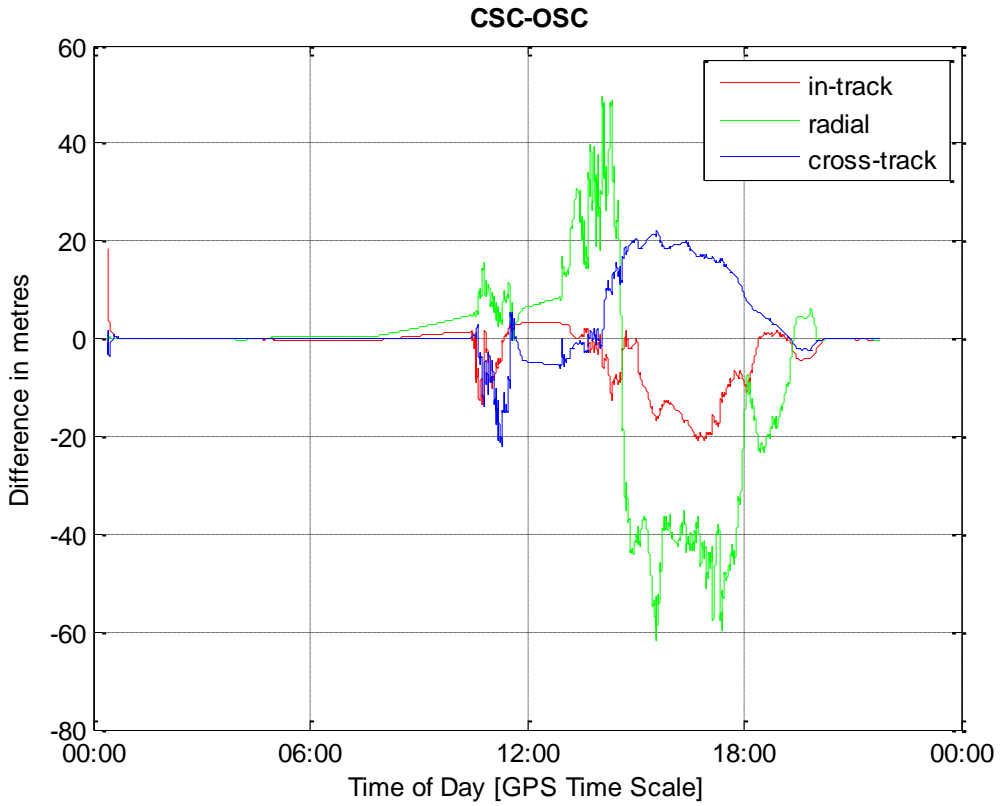


Figure 7-22: Relative positioning error using the standard tracking version of GSNRx™

The sparse and noisier data has a dramatic impact on the performance. The error in the absolute positions has increased by a factor of 2, while the relative positioning errors have grown by at least an order of magnitude, and no benefit appears to come from the phase measurements. These results clearly show the benefit of using a more specialized receiver design, with less measurement noise together with more measurements. While the results may be improved somewhat by tuning the filter to the data set at hand, it will still not compensate for the increased number of complete data outages.

7.4.4 High Sensitivity GPS

Having tested the filter with input data from a “standard” GNSS receiver, it was also desirable to test it with a data set representative of the current state of the art in above the constellation receiver design. To this end, the simulation was re-run with increased signal power, but using GPS alone. Only GPS was simulated as a result of simulator availability. The goal was to

simulate, as closely as possible, the operating conditions on-board the MMS mission using Navigator GPS L1 C/A high sensitivity space receivers. Using figure 6 from Winternitz et al (2017) as a guide, (shown here as Figure 7-23) it can be interpreted that the side lobe signals, as seen from apogee are received at C/No values of approximately 31 dB-Hz, 6 dB higher than the Navigator receiver's acquisition threshold of 25 dB-Hz.

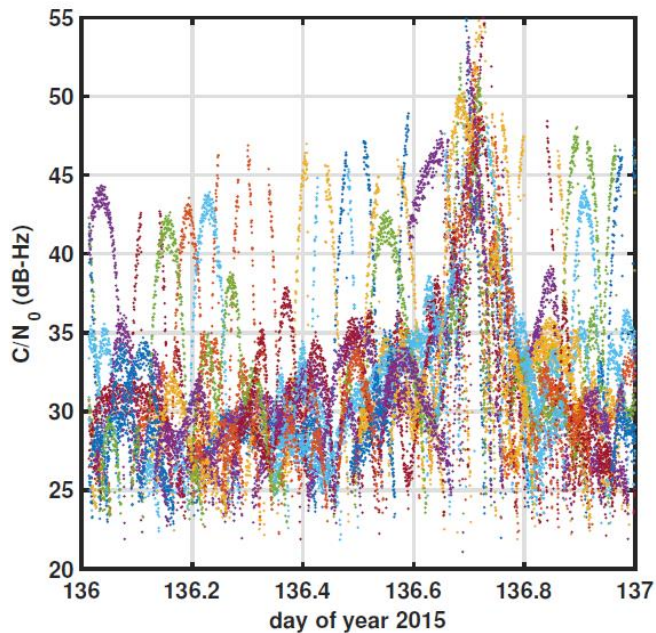


Figure 7-23: Received C/N0 for MMS1 on day 136 of 2015 showing sidelobe tracking (Winternitz et al 2017, used with permission)

In contrast, the multi-constellation simulation created in Chapter 6 has peak side lobe signal power closer to 24 dB-Hz at apogee, as shown in Figure 7-24. This is a full 6 dB below the GSNRxTM acquisition threshold of roughly 30 dB-Hz. In order to replicate the MMS operating conditions with GSNRxTM, the simulator power for the GPS only simulation was therefore increased by 12 dB compared to the original multi-constellation simulation. This yielded peak side lobe power of roughly 36 dB-Hz, 6 dB above the GSNRxTM acquisition threshold. The new simulated signal power is shown in Figure 7-25.

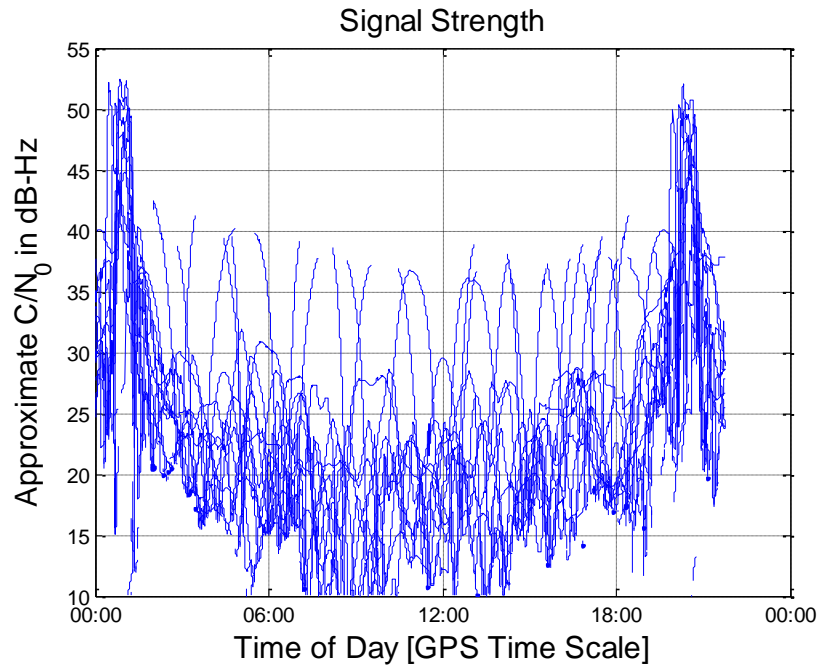


Figure 7-24: Simulated signal strength for GPS in the multi-constellation simulation

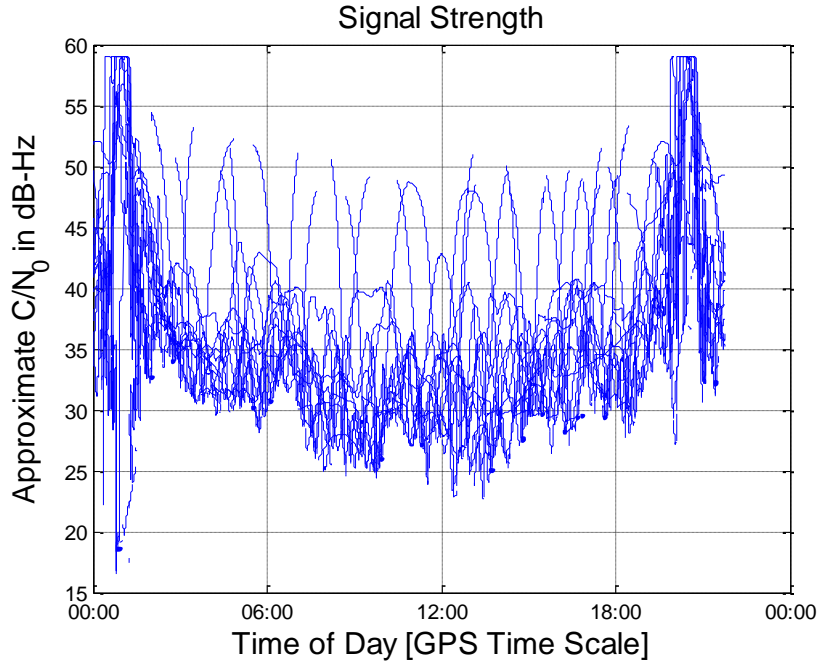


Figure 7-25: Simulated signal strength for GPS in the GPS only simulation

In addition, the gain patterns were for Block IIA and block IIF were updated to more closely reflect the results of the Antenna Characterization Experiment (Martzen et al 2015). The new patterns are the same as the Lockheed Martin block IIR pattern shown in Figure 6-5, with the

exception that it has been decreased by 3 dB overall, and that the IIF pattern has been rotated 45 degrees with respect to the IIR and IIA patterns, in keeping with the Antenna Characterization Experiment results. Due to time constraints and the similarities of the patterns, and the fact that Spirent's simulation environment does not model the azimuthal rotations of the GPS satellites which already prevents a perfect representation of the signal strengths at HEO, no effort was made to digitize the actual patterns of the Boeing satellites from the Martzen et al (2015) paper. The assumed patterns are shown in Figure 7-26, and simulate far more side lobe power than the originally assumed patterns for Blocks IIA and IIF presented in Figure 6-4 and Figure 6-7.

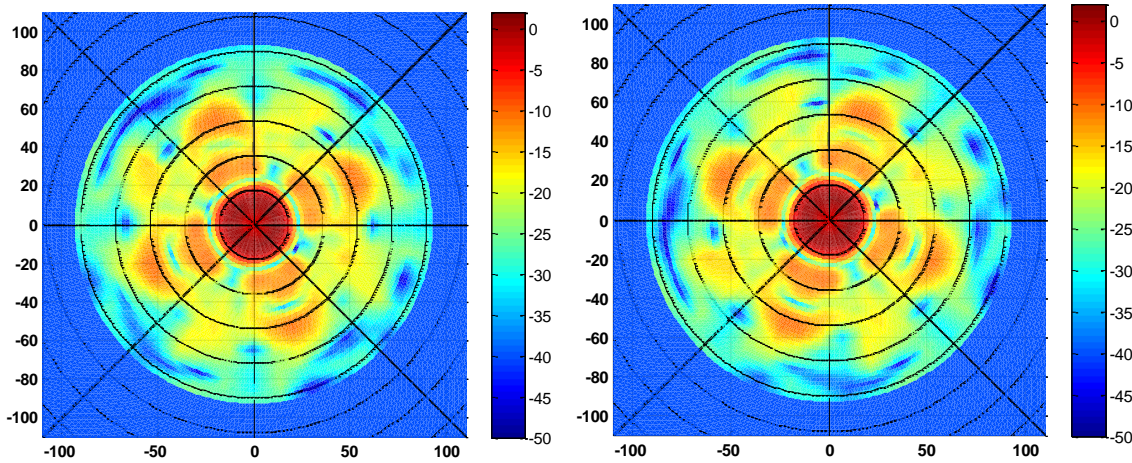


Figure 7-26: Assumed transmit gain pattern for Block IIA (left) and Block IIF (right)

The resulting data set was processed through the HEO tracking strategy version of GSNRTM, and had similar measurement quality to the multi-constellation data set processed through the same receiver version. The new data sets tracks typically between 5 and 10 satellites simultaneously, as shown in Figure 7-27. Significantly less satellites are tracked on the CSC as a result of the hardware setup during the IF data take, which used a splitter to collect data simultaneously on two front ends, while the OSC data was collected on a single front end and therefore benefits from somewhat higher power. The commonly tracked satellites are shown in Figure 7-28.

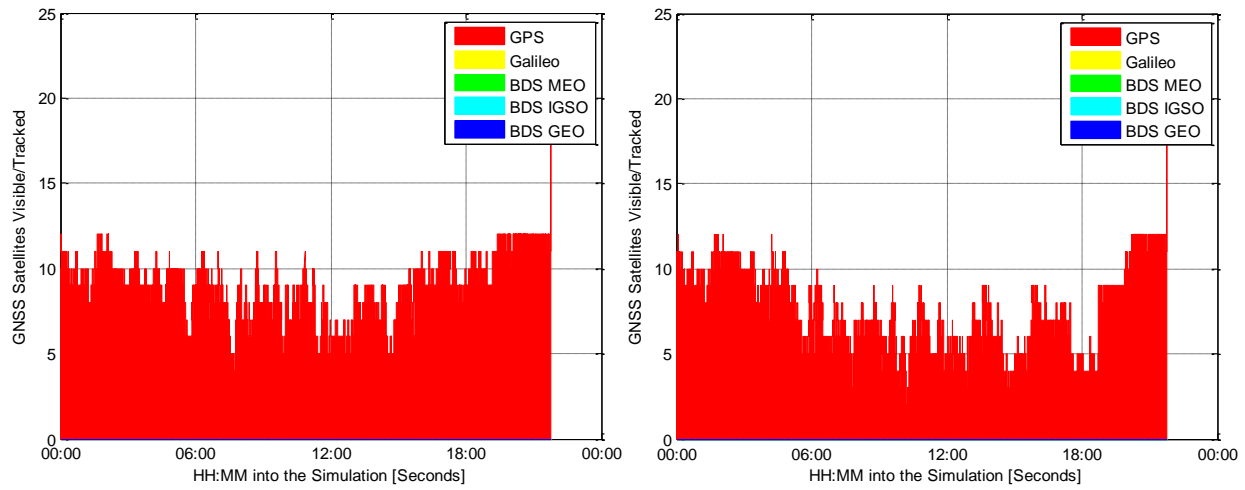


Figure 7-27: Number of tracked satellites on the OSC (left) and CSC (right)

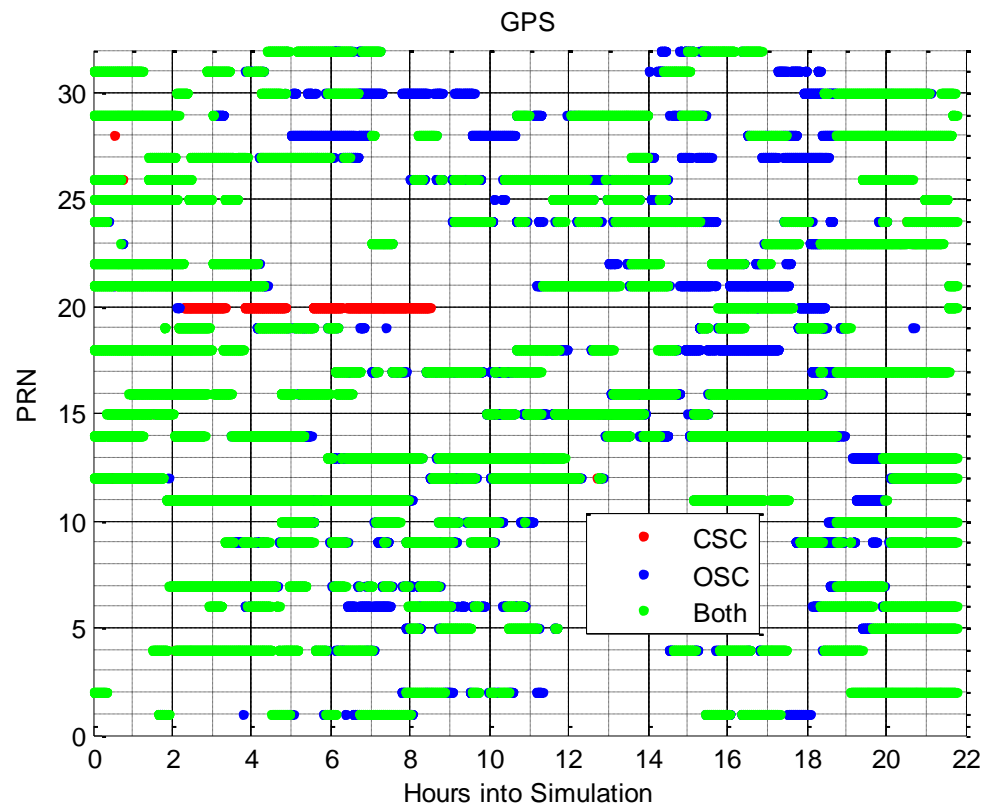


Figure 7-28: Commonly tracked satellites for the GPS only data take

Finally, the new data sets were run through the relative positioning filter. The absolute positioning results are shown in Figure 7-30 and Figure 7-30 while the relative positioning results are shown in Figure 7-31.

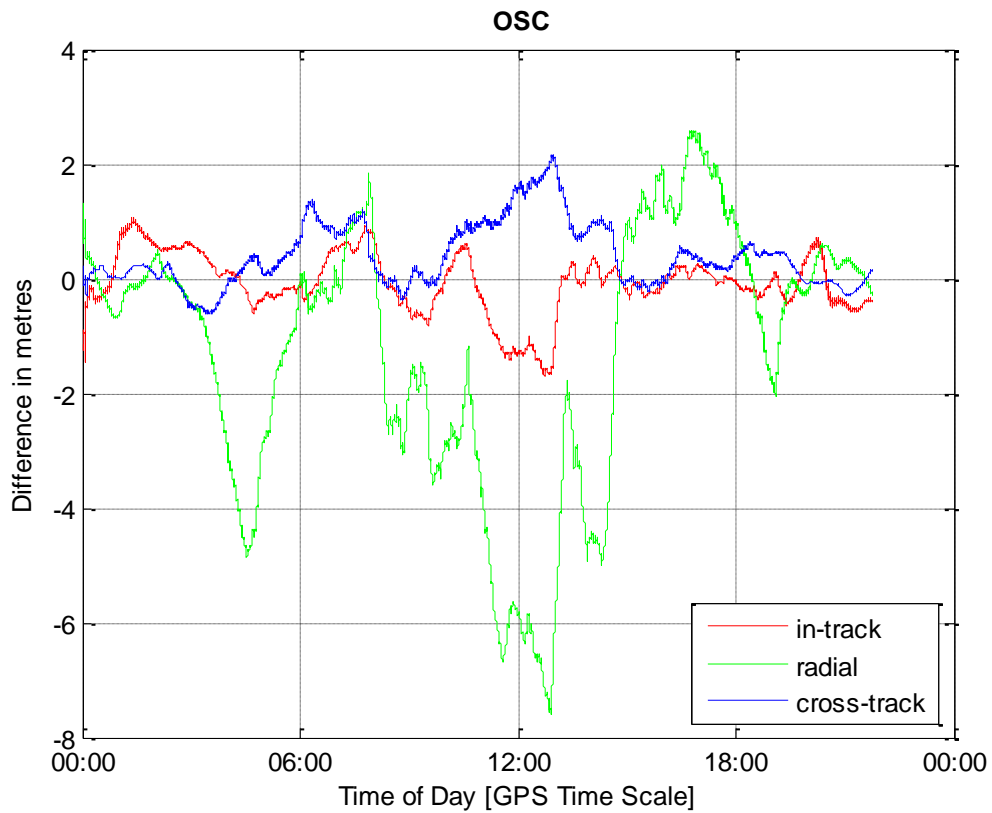


Figure 7-29: Absolute positioning accuracy using the high power GPS only data set on the OSC

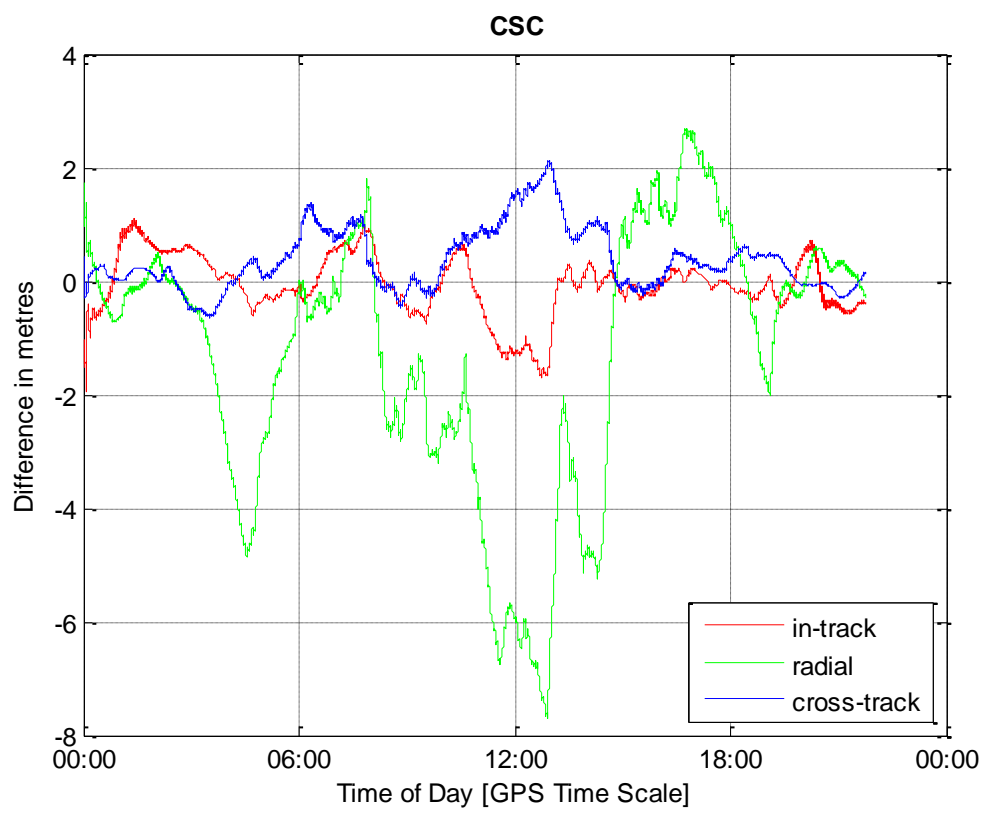


Figure 7-30: Absolute positioning accuracy using the high power GPS only data set on the CSC

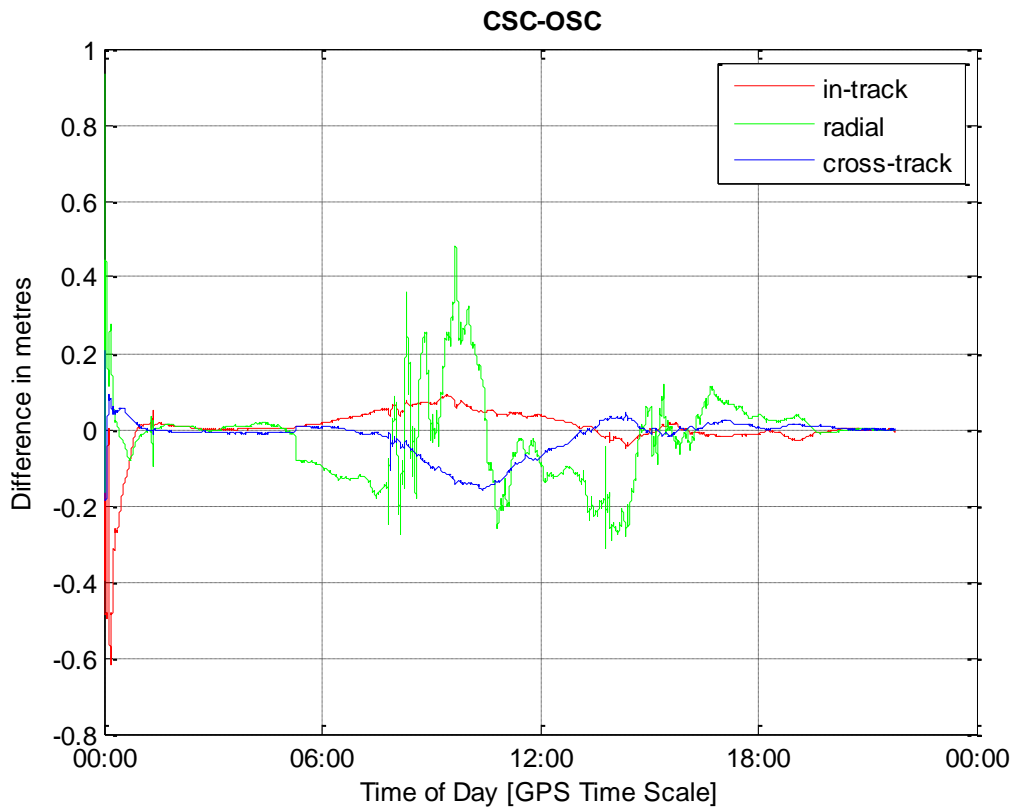


Figure 7-31: Relative positioning accuracy using the high power GPS only data set

The use of the high power GPS only data set makes a dramatic improvement in both the absolute and relative positioning accuracies. The absolute positions are determined throughout the orbit to better than 8 m in any one component, while the relative positioning accuracies remain below 50 cm. There is also sufficient data to overcome the maneuver at the beginning of the tight formation flying arc, which is now marked only by oscillations in the radial component's error rather than a dramatic increase in error on all three components. This certainly justifies the design effort required to develop a suitable receiver for above the constellation use if high accuracy relative positioning is required.

7.4.5 Maneuver Free Zero Baseline Test

As a final test, relative positions were computed between two OSC data sets, both collected with the new high power GPS only simulation, in what is essentially a zero baseline test. The two data sets were collected with independent simulator runs. While these results are somewhat optimistic

given the perfect error cancellation on the simulated GNSS errors such as ionospheric range delay and broadcast orbit error, they are still subject to independent noise and receiver clock imperfections, and provide a first glimpse into the level of performance that might be achievable in a maneuver free scenario with a high sensitivity receiver. The absolute positioning results are shown in Figure 7-32 while the relative positioning results are shown in Figure 7-33.

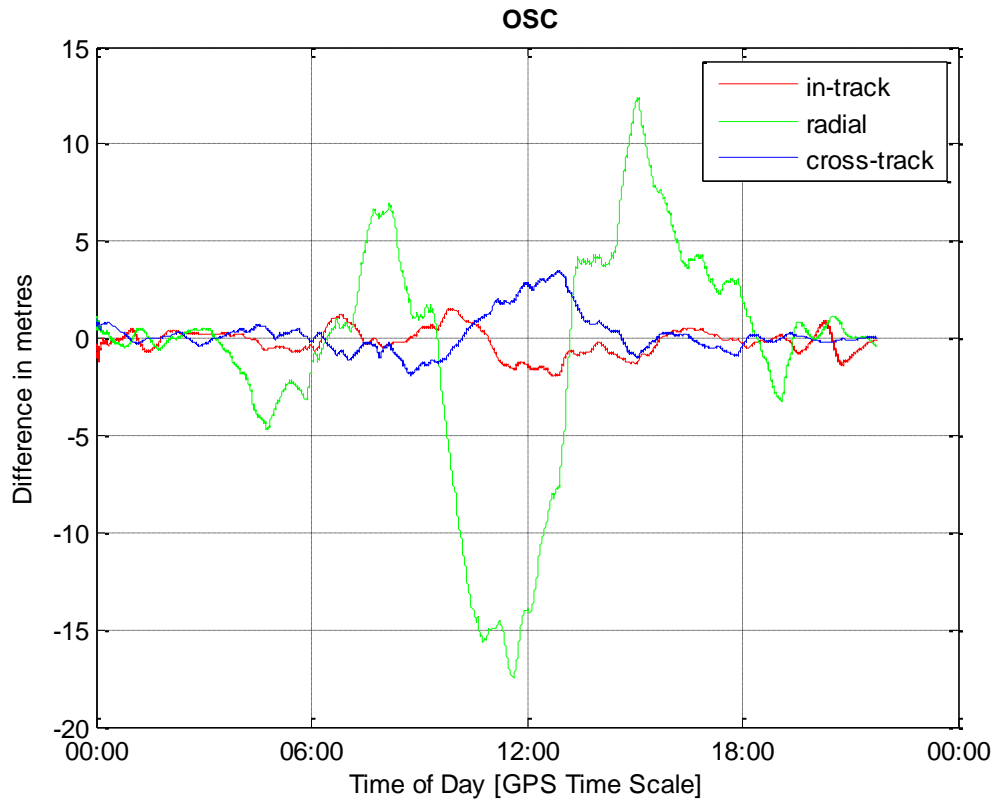


Figure 7-32: Absolute positioning error for a high sensitivity GPS zero baseline test

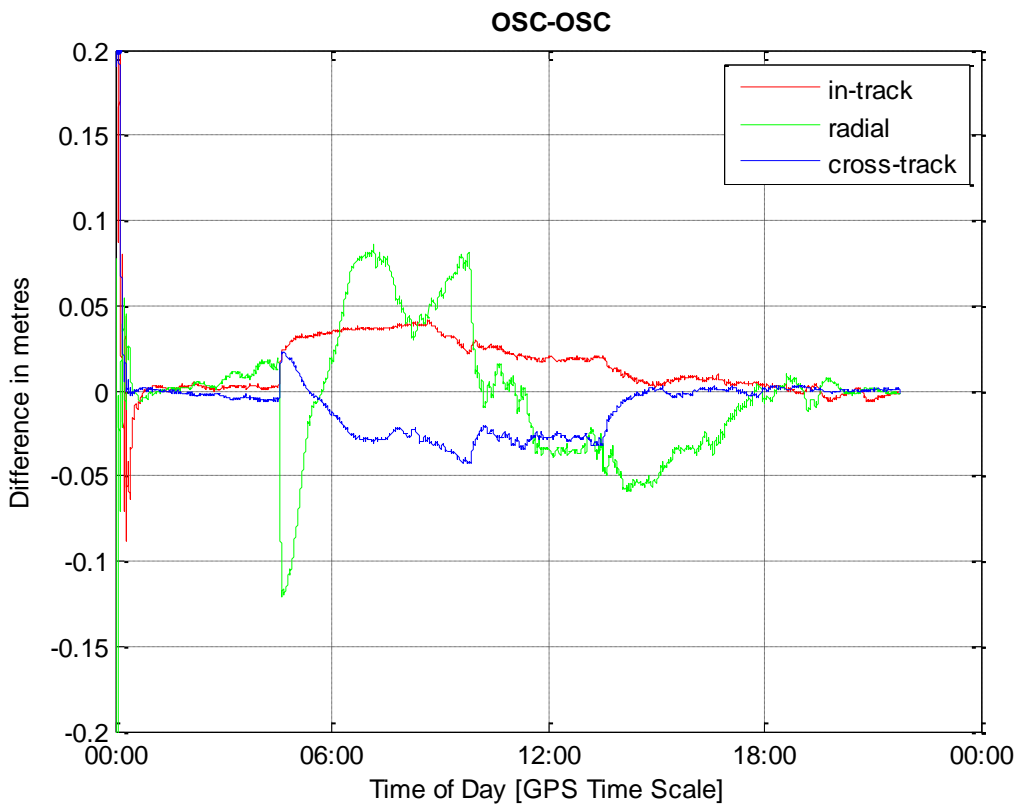


Figure 7-33: Relative positioning error for a high sensitivity GPS zero baseline test

While the absolute positioning error of up to 15 metres in the radial component is comparable with the other tests, an outstanding relative positioning accuracy has been achieved. The peak radial error is 12 cm, while the in-track and cross-track components are bounded by 5 cm throughout the data set. As with the other data sets tested, there is good agreement between the relative positioning errors and associated covariance information, but poor agreement for the absolute positioning.

7.5 Conclusions

A relative positioning filter has been developed and built to handle sparse, asynchronous, multi-constellation GNSS measurements from a pair of formation flying spacecraft in highly elliptical orbits. Data from both the standard tracking version and HEO tracking version of the software

receiver was used to test the filter, and it was found that the receiver design plays a substantial role in determining both the absolute and relative positioning accuracy.

A standard receiver in HEO offers only sparse measurements heavily impacted by noise due to the low signal power. Even in a well-tuned filter these operating conditions translate into an absolute positioning accuracy on the order of tens if not hundreds of metres at apogee, and a relative positioning solution also at the level of tens of metres. There is insufficient information to properly estimate the orbit, and the filter is highly sensitive to outliers, which it is unable to properly detect. The filter in this case is also very sensitive to disruptions such as maneuvers, which, even when properly modelled, cause an increase in velocity error from which the filter is very slow to recover.

As the receiver quality increased, it was found that the relative positioning accuracy improved substantially. Even with maneuvers, the weak signal multi-constellation data set and the high-sensitivity GPS only data set allowed for relative positioning on the level of a few metres, or sub metre, respectively. In both cases it could still be observed that a maneuver at apogee substantially de-stabilized the relative positioning while a maneuver at perigee was quickly recovered from and made no lasting impact. While outlier detection became more reliable with these better quality data sets, it is still an important consideration, and effective cycle slip detection remains a problem.

Finally, as expected, the best relative positioning results by far were achieved using two independent high sensitivity GPS data sets with no maneuvers in a zero baseline test configuration. In spite of the weak HEO geometry at apogee, relative positioning accuracies at the 10 cm or better level were achieved throughout the orbit. These results are in good agreement with those of Mohiuddin and Psiaki (2008) using integer ambiguity resolution in GEO and HEO.

Several areas of further investigation are possible, among them further investigations into the empirical acceleration estimation difficulty, adding stronger constraints on the clock parameters

in keeping with their observed stability, better cycle slip detection, investigation into the impact of including non-commonly tracked satellites, and in general further tuning the filter.

Chapter Eight: Conclusions

Over the course of this project, research contributions were made in four areas. The first were visibility simulations which investigated, in-depth, the contributions of the various GNSS constellations, and considered for the first time the impact of geosynchronous positioning satellites on above-the constellation positioning. It was found that the design of the GNSS receiver would play a significant role in the achievable results, because while the main lobes of the GNSS transmit gain patterns are of limited availability, the side lobes were sufficiently strong to be acquired and tracked by specialized space receivers with weak acquisition and tracking capability. It was found that investing in multi-constellation GNSS would be an asset to mission designers in the face of the uncertainty in modelling the above-the constellation GNSS environment. Finally, an important conclusion was that the geostationary and geosynchronous positioning satellites used for regional systems such as BeiDou, and for Satellite Based Augmentation Systems, could offer above the constellation users a valuable addition to the MEO constellations.

The second area of contribution was an in-depth study of the potential that SBAS ranging held for above the constellation space users. Using the CanX-2 nanosatellite it could be demonstrated for the first time that SBAS signal power on all the active systems does spill over the Earth's limb. It was also possible for the first time to map the transmitted signal power from the SBAS systems on a global scale, and to compare the shapes of the transmit gain pattern main beams from the various SBAS systems and satellites. A study of SBAS pseudoranges from six globally distributed IGS stations revealed sufficient ranging measurement accuracy to provide information to above the constellation users, provided steps were taken to mitigate timing errors. It was found that WAAS in particular would be a good candidate for above the constellation use, given its stronger signal power, relatively wide transmit beam and more accurate ranging service as compared to the other SBAS systems.

The third area of contribution was in the study and testing of receiver algorithms for four different GNSS signals, with the goal of tracking through the weak signal and high dynamics environments faced by a receiver in highly elliptical orbit. The GSNRx™ research software

receiver was expanded to operate under simulated HEO conditions and to reliably acquire and track signals from GPS, Galileo and BeiDou in that environment, a capability that no commercially available receiver currently has. While it was not ultimately possible to replicate the performance of existing high sensitivity GPS only or GPS/GLONASS space receivers, a tool was created capable of providing the necessary data to study relative positioning in HEO under realistic receiver operating conditions and error sources. Further, valuable insight into the advantages and disadvantages of the Galileo E1b and BeiDou B1 signals in comparison with the benchmark GPS L1 C/A from the perspective of above the constellation users was gained. The earlier conclusions that multi-constellation GNSS adds value in terms of more measurements, compensating in part for the weak signals visible to a user in HEO, was confirmed. It was also confirmed that the geosynchronous satellites from the regional part of the BeiDou constellation added significant value when they were in view. The general conclusion can be drawn that future above the constellation receiver designs should support the geosynchronous BeiDou, QZSS, IRNSS or SBAS satellites.

The fourth and final area of contribution was the relative positioning study. For the first time, a real-time relative positioning filter was developed capable of handling the potentially asynchronous measurements coming from a pair of formation flying satellites in highly elliptical orbits. It is also the first time that carrier phase based multi-constellation GNSS relative positioning for above the constellation users was studied at all. It was found that in the challenging HEO positioning environment, the accuracy of the achieved relative positioning was heavily dependent on the number of tracked satellites, on the quality of the outlier detection algorithms, on the ability to mitigate error sources, and on the accuracy of modelled manoeuvres and other thrust activities. Cycle slip and outlier detection is particularly critical for HEO's sparse measurements and weak geometry, because outliers will dramatically degrade the filter performance. Further, the use of a high quality clock proved valuable both to time-tag the GNSS measurements and avoid synchronization problems, and to help constrain the filter.

While the absolute positioning accuracy for the chosen filter design was limited to tens of metres through the HEO apogee arc, significantly better relative positioning could be achieved. Using a

multi-constellation receiver with a standard set of tracking loops a relative positioning accuracy of tens of metres could be achieved. Using a multi-constellation receiver with a tight bandwidth, weak signal, Kalman tracking loop, relative positioning accuracy of a few metres could be achieved. Using a high sensitivity, single constellation receiver, which tracked sufficient satellites for a nearly continuous position fix, a relative positioning accuracy of tens of cm could be achieved. Finally, using the high-sensitivity receiver in the absence of manoeuvres over a zero baseline, roughly 10 cm level relative positioning was achieved. It can be concluded that for a receiver with limited sensitivity multi-constellation GNSS significantly contributes to the availability of measurements, but that a high sensitivity single constellation receiver can achieve similar results, and potentially experiences improved geometry by tracking side lobes. While the relative positioning results using GNSS alone was not found to be sufficiently accurate to meet the stringent science requirements for a mission like PROBA-3, it would be of value for monitoring formation safety, acquiring a tight formation, or could serve as a redundant system in case of other sensor failures.

There are countless areas of future research work that could be undertaken to extend the research presented here. Any of the simulations could, and possibly should, be made more sophisticated, in particular as more information about the GNSS constellation designs becomes available in future.

The SBAS results would greatly benefit from an opportunity to map not only the centers of the gain patterns, but also the side lobes, should they exist. While SBAS and QZSS were simulated in Chapter 6, they could not be used in the current “space capable” version of GSNRxTM, and given the weaker side lobe signal strengths simulated as compared to the other GNSS satellites, it is unlikely that they would have contributed to the relative navigation solution meaningfully even if they had been tracked. More work is also required to more thoroughly understand the nature and frequency of the ranging errors on the SBAS measurements, as there were occasions when the ranging error appeared to have entirely different characteristics on different days. Further, it would be essential for a space user capable of simultaneously tracking more than one SBAS system to understand the implications of applying corrections from different systems.

The receiver development work in particular presents an open door for further research. Most significant would be an effort to adapt the tracking loop lock indicators to the weaker, fading signals seen from an above the constellation spacecraft. The initial set of loss of lock criteria would often result in receiver channels failing to lose lock, even when the GNSS satellite being tracked was no longer simulated. Setting more stringent loss of lock criteria has ultimately resulted in the receiver having similar performance on all signals in spite of the differences in coherent integration time, and likely also prevents the acquisition and pull-in of weaker signals, which should be possible based on results presented in relevant literature.

Furthermore, the receiver is capable of tracking several signals, and even systems, which have not been tested at all for the HEO scenario. Most notable among them is GLONASS, although given the advantages of the higher geostationary satellites IRNSS would also be worth exploring. Dual frequency tracking, although it seems to be disabled in the version of the receiver used at present, also offers advantages. Using dual frequency data to mitigate ionospheric effects and form widelane combinations for ambiguity resolution would be beneficial for relative positioning, but have yet to be tested due to the absence of any dual frequency data set.

Finally, the latest advancements in tracking loop design research could be implemented and applied to the HEO problem. The receiver's existing data pilot signal tracking capability would be worth exploring, as it would unlock the potential of the new GNSS signal designs. Finally, the potential benefits of vector based tracking, while they did not materialize in the initial tests, could be further pursued by incorporating an orbital filter and more suitable error models for the space application into the receiver.

Another area of future investigation is the impact of the phase patterns on the GNSS transmit antennas. MMS found data from the side lobes to be unbiased, but given that only pseudorange measurements were used, and that their positioning and truth trajectories were at similar levels of accuracy, both 10's of metres, a fairly substantial bias could be present but undetectable. The data from the SBIRS GEO satellite showed evidence of substantial differences in the L1 and L2

phase centres which were magnified the further off-boresight the receiver travelled (Barker and Frey 2012). This would bear further investigation for a mission planning to use phase based positioning outside of the service volume.

Finally, it would be interesting to understand how some of the filter design choices might improve the absolute or relative positioning accuracy. For example, given the high sensitivity data set, implementing integer ambiguity resolution would be interesting. It would also be of value to explore the use of dual frequency measurements either for wide lane ambiguity resolution techniques or for mitigating atmospheric effects. A different choice of parameters or better filter tuning might help to mitigate the impact of broadcast orbit errors on the absolute positioning.

Beyond the direct research contributions, the outcome of this research is that a test bed has been set up taking advantage of the tools and expertise of two research institutions, making it possible to study the impact of simulation settings, different GNSS constellations and signals, different receiver algorithms for acquisition and tracking, and different orbital positioning filter concepts on the above the constellation positioning problem. The possibilities for future research work on any of the frontiers breached by this research project are vast.

References

Airbus Defense and Space (2014) *GEO MosaicGNSS Receiver Stand-alone GPS receiver for GEO applications*, data sheet, http://www.space-airbusds.com/media/document/pdh_6_geo-2014-bd.pdf, last accessed Nov 4, 2016.

Ardaens, J.-S., D'Amico, S. and Cropp, A. (2012) "GPS-Based Relative Navigation for the PROBA-3 Formation Flying Mission," *63rd International Astronautical Congress*, October 1-5, Naples, Italy, paper IAC-12.B4.7B.4.

Arinc Research Corporation (2003) *Navstar GPS Space Segment / Navigation User Interfaces*, ICD-GPS-200C IRNs 12345, January 14, 2003.

Asaki, Y., Takeuchi, H., and Yoshikawa, M. (2008) "Next Space-VLBI Mission, VSOP-2, and the Precise Orbit Determination with GNSS Navigation and SLR," *Proceedings of the 21st International Technical Meeting of the Satellite Division of The Institute of Navigation (ION GNSS 2008)*, Savannah, GA, pp. 710-718.

Axelrad, P., Bradley, B. K., Donna, J., Mitchell, M., and Mohiuddin, S. (2011) "Collective Detection and Direct Positioning Using Multiple GNSS Satellites", *NAVIGATION*, Vol. 58, No. 4, Winter 2011-2012, pp. 305-321.

Balbach O., and Eissfeller B. (1999) "Analyses of the Equator-S GPS Mission Data at Altitudes above the GPS-Constellation" *4th ESA International Conference on Spacecraft Guidance, Navigation and Control Systems*, Oct. 18-21, ESTEC, Noordwijk, The Netherlands.

Bamford, W., Mitchell, J., Southward, M., Baldwin, P., Winternitz, L., Heckler, G., Kurichh, R., and Sirotzky, S. (2009) "GPS Navigation for the Magnetospheric Multi-Scale Mission," *Proceedings of the 22nd International Technical Meeting of The Satellite Division of the Institute of Navigation (ION GNSS 2009)*, Savannah, GA, pp. 1447-1457.

Bamford, W., Naasz, B. and Moreau, M. (2006) "Navigation Performance in Higher Earth Orbits using Navigator GPS Receiver," *Proceedings of the 29th Annual Guidance and Control Conference*, Breckenridge, CO.

Bamford, W., L. Winternitz and M. Moreau, (2005) "Real-Time Geostationary Orbit Determination Using the Navigator GPS Receiver," *2005 Flight Mechanics Symposium*, NASA Goddard Space Flight Center, October 18-20, Greenbelt, MD.

Bandecchi, M., and Ockels, W. J. (1998) "The TEAMSAT Experience," *ESA Bulletin 95*, pp. 132-143.

Barker, L. and Frey, C. (2012), "GPS at GEO: A First Look at GPS from SBIRS GEO1," *35th Annual AAS Guidance and Control Conference*, Breckenridge, Colorado.

Barrios-Montalvo, A. R. (2010) *In-Orbit Autonomous Position Determination of Satellites Using Sparsely Distributed GNSS Measurements For Geostationary Transfer Orbits, Geostationary Earth Orbits and Higher Altitudes*, Master's thesis, Cranfield University.

Bauer, F. (2015a) 'GPS Space Service Volume (SSV) Ensuring Consistent Utility Across GPS Design Builds for Space Users,' *Proceedings of the 15th PNT Advisory Board Meeting*, Annapolis, MD.

Bauer, F. (2015b) 'GNSS Space Service Volume & Space User Data Update,' *10th Meeting of the International Committee on GNSS*, Boulder, Colorado, USA, November 3, 2015.

Bauer, F.H., M.C. Moreau, M.E. Dahle-Melsaether, W.P. Petrofski, B.J. Stanton, S. Thomason, G.A Harris, R.P. Sena, L. Parker Temple III, (2006) "The GPS Space Service Volume," *ION GNSS*, September 26-29, Fort Worth, TX.

Birmingham, W. P., B. L. Miller and W. L. Stein (1983) "Experimental Results of Using the GPS for Landsat 4 Onboard Navigation," *Navigation: Journal of the Institute of Navigation*, vol. 30, no. 3, Fall, pp. 244-251.

Borio, D. (2012) *GNSS Receiver Design*, ENGO 638 Course Notes, Geomatics Engineering, University of Calgary, Canada.

Bradley, B.K., Axelrad, P., Donna, J., Mohiuddin, S., (2010) "Performance Analysis of Collective Detection of Weak GPS Signals," *Proceedings of the 23rd International Technical Meeting of The Satellite Division of the Institute of Navigation (ION GNSS 2010)*, Portland, OR, pp. 3041-3053.

Brown, R.G. and P.Y.C. Hwang (1996) *Introduction to Random Signals and Applied Kalman Filtering*, 3rd Edition, John Wiley & Sons, Inc.

Carpenter J. R., D. C. Folta, and M. C. Moreau, (2004) "Libration point navigation concepts supporting the vision for space exploration," *AIAA/AAS Astrodynamics Specialist Conference and Exhibit*, 16 - 19 August, Providence, Rhode Island.

Casotto, S., Zin, A., Padovan, B., (2002) "SAC-C orbit reconstruction using the experimental GPS/GLONASS receiver LAGRANGE," *Proceedings of the 15th International Technical Meeting of the Satellite Division of The Institute of Navigation (ION GPS 2002)*, Portland, OR, pp. 85-93.

Centre National D'Études Spatiales (CNES) Server to Retrieve and Export Navigation Data (SERENAD) <http://sis-perfandata.cnes.fr/index.html>, last accessed June 11, 2015.

Chapel, J., Stancliffe, D., Bevacqua, T., Winkler, S., Clapp, B., Rood, T., Gaylor, D., Freesland, D. and Krimchansky, A. (2015) "Guidance, Navigation and Control Performance for the GOES-R Spacecraft," *CEAS Space Journal*, Vol. 7, No. 2, pp. 87-104.

China Satellite Navigation Office (2011) *BeiDou Navigation Satellite System Signal in Space Interface Control Document* (Test Version), BeiDou-SIS-ICD-Test, December 2011.

China Satellite Navigation Office (2012) *BeiDou Navigation Satellite System Signal in Space Interface Control Document Open Service Signal (Version 1.0)*, BeiDou-SIS-ICD-1.0, China.

China Satellite Navigation Office (2013) *BeiDou Navigation Satellite System Signal in Space Interface Control Document Open Service Signal (Version 2.0)*, BeiDou-SIS-ICD-2.0, China.

China Satellite Navigation Office (2016) *BeiDou Navigation Satellite System Signal in Space Interface Control Document Open Service Signal (Version 2.1)*, BDS-SIS-ICD-2.1, China.

Computer Sciences Corporation (2002) *Autonomous Navigation of Geosynchronous Satellites Using GPS: Maneuver Recovery Study*, Technical Report No. CSC-5547-05 Prepared for the National Aeronautics and Space Administration CONTRACT GS 35F-4381-G, Task Order No. S-15614-Y.

Curtis, S. (1999) *The Magnetospheric Multiscale Mission...Resolving Fundamental Processes in Space Plasmas*, Technical Report NASA/TM-2000-209883, Greenbelt, Maryland, December 1999.

Czopek, F. and S. Schollenberger (1993) "Description and Performance of the GPS Block I and II L-Band Antenna and Link Budget," *Proceedings of the Institute of Navigation GPS 93 Conference*, pp. 37-43.

D'Amico S. (2010) *Autonomous formation flying in low earth orbit*, PhD thesis, Technical University of Delft.

Davis, G., Moreau, M., Bauer, F., Carpenter, J.R. (2002) "GPS Based Navigation and Orbit Determination for the AMSAT AO-40 Satellite," *AIAA Guidance and Control Conference*, August, Monterey, CA.

Dion, A., Calmettes, V. and Boutillon, E. (2007) 'Reconfigurable GPS-Galileo Receiver for Satellite Based Applications,' *Proceedings of ION GNSS 2007*, Fort Worth, TX, pp. 2448-2458.

DLR/GSOC (2012) *GPS Navigation Analysis for PROBA-3*, Report ID PROBA-3-DLR-TN-003, Space Flight Dynamics, German Space Operations Centre, Deutsches Zentrum fuer Luft- und Raumfahrt, Munich, Germany, January 13th.

Dvorak-Wennersten, M., A. V. Banes, G. J. Boegner, L. Dougherty, B. L. Edwards, and J. Roman. (2001) "PiVoT GPS Receiver," *Proceedings of the ION GPS Conference 2001*, Salt Lake City, UT, pp. 855-861.

Ebinuma, T. and Unwin, M. (2007) "GPS Receiver Demonstration on a Galileo Test Bed Satellite," *Journal of Navigation*, vol. 60, No. 3, pp 349-362. doi:10.1017/S0373463307004365

Enderle, W., (1999) "Attitude Determination of an User Satellite in a GEO Transfer Orbit (GTO) using GPS Measurements," *Proceedings 4th ESA International Conference on Spacecraft Guidance, Navigation and Control Systems*, ESTEC, Noordwijk, The Netherlands, 18-21 October 1999, (ESA SP-425, February 2000)

Ericson, S. D., Shallberg, K. W. and Edgar, C. E. (2010) 'Characterization and Simulation of SVN49 (PRN01) Elevation Dependent Measurement Biases,' *Proceedings of the 2010 ION International Technical Meeting*, San Diego, CA, pp. 963-974.

European Commission (2011) "EGNOS Safety of Life Service Definition Document," EGN-SDD SoL, V1.0.

European Commission Directorate-General for Enterprise and Industry (2013) *EGNOS Open Service Definition Document*, Version 2.0.

European GNSS Service Centre (2017) *Constellation Information* <https://www.gsc-europa.eu/system-status/Constellation-Information>, last accessed May 13, 2017.

European Space Agency (2016) *Space Images* http://www.esa.int/spaceinimages/Images/2016/05/Models_of_Proba-3_designs, last accessed Nov 4, 2016.

European Space Agency (2017) *SmallGEO (Small Geostationary Satellite Platform) Initiative / Hispasat AG1 Mission*, <https://directory.eoportal.org/web/eoportal/satellite-missions/s/smallgeo>, last accessed May 1, 2017.

ESA Space Debris Office (2017) *Classification of geosynchronous Objects*, GEN-DB-LOG-00211-OPS-GR, issue 19, April 6.

European Union (2010) *European GNSS (Galileo) Open Service Signal in Space Interface Control Document*, OD-SIS-ICD Issue 1.1, September 2010.

Fan, M., Hu, XG., Dong, G., Huang, Y., Cao, J., Tang, CP., Li, P., Chang, S., and Yu, Y. (2015) “Orbit Improvement for Chang’E-5T Lunar Returning Probe with GNSS Technique,” *Advances in Space Research*, vol. 56, no. 11, pp. 2455-2472.

Farahmand, M., Long, A., and Carpenter, R. (2015) ‘Magnetospheric MultiScale Mission Navigation Performance Using the Goddard Enhanced Onboard Navigation System,’ *Proceedings of the 25th International Symposium on Space Flight Dynamics*, Munich, Germany.

Federal Aviation Administration/Department of Transportation (2008) *Global Positioning System Wide Area Augmentation System (WAAS) Performance Standard*, 1st Edition, 31 October, USA.

Fedora, N. and O. Tyler (2007) "Hardware in the Loop Blended and GPS Navigation, Acquisition and Tracking Performance for Lunar Transfer and Return Missions," *30th Annual AAS Guidance and Control Conference*, February 3-7, Breckenridge, Colorado.

Fernández Ibarz, J.M., L. Tarabini Castellani, M. Ruiz, J.S. Llorente, A. Mestreau-Garreau, K. Gantois and A. Cropp (2011) 'PROBA-3: Demonstrating Formation Flying,' *Proceedings of the Spacecraft Formation Flying Missions and Technologies Conference*, May 18-20, Montreal, Canada, 2011.

Filippi, H., Gottzein, E., Kuehl, C., Mueller, C., Barrios-Montalvo, A. and Dauphin, H. (2010) 'Feasibility of GNSS receivers for satellite navigation in GEO and higher altitudes,' *5th ESA Workshop on Satellite Navigation Technologies and European Workshop on GNSS Signals and Signal Processing (NAVITEC)*, Noordwijk, The Netherlands.

Fisher, S. C. and Ghassemi, K. (1999) 'GPS IIF—The Next Generation,' *Proceedings of the IEEE*, Vol. 87, No. 1, pp 24-47.

Fortin, M.-A., Guay, J.-C. and Landry, R. Jr. (2014) "Single Frequency WAAS Augmentation Observations (L1 & L5) on a Ground Based GPS L1 C/A Solution" *Positioning*, vol. 5, pp 70-83. <http://dx.doi.org/10.4236/pos.2014.53010>

Ganeshan, Dr. A. S., Director of Space Navigation Group and Project Director, GAGAN (2013) email communication.

Garrison, J. L., Moreau, M. C., Axelrad, P., (2001) "Tracking Loop Optimization for On-Board GPS Navigation in High Earth Orbit (HEO) Missions," *Proceedings of the 57th Annual Meeting of The Institute of Navigation*, Albuquerque, NM, pp. 168-175.

Gerner, J. L., J. L. Issler, D. Laurichesse, C. Mehlen, N. Wilhelm (2000) "TOPSTAR 3000 – An Enhanced GPS Receiver for Space Applications," *ESA bulletin 104*, November 2000.

Global Positioning System Directorate (2011) *Navstar GPS Space Segment/User Segment L5 Interfaces*, IS-GPS-705B, 21 September 2011.

Global Positioning System Directorate (2011) *Navstar GPS Space Segment/User Segment L1C Interface*, IS-GPS-800B, 21 September 2011.

Global Positioning System Directorate (2013) *Navstar GPS Space Segment/User Segment L5 Interfaces*, IS-GPS-705D, 24 September 2013.

Global Positioning System Directorate (2013) *Navstar GPS Space Segment/User Segment L1C Interface*, IS-GPS-800D, 24 September 2013.

Global Positioning System Directorate (2013) *Navstar GPS Space Segment/Navigation User Interfaces*, IS-GPS-200H, 24 September 2013.

Global Positioning System Wing (2010) *Navstar GPS Space Segment / Navigation User Interfaces*, IS-GPS-200E, 8 June, 2010.

GOES-R Series Program Office (2017) *Launch and Orbit*, <http://www.goes-r.gov/> last accessed May 1, 2017.

GPS World (2016) *The Almanac* <http://gpsworld.com/the-almanac>, last accessed December 12, 2016.

Gowdayyanadoddi, S. N., A. Broumandan, J. T. Curran and G. Lachapelle (2015) "Indoor GPS Positioning Using A Slowly Moving Antenna and Long Coherent Integration," *International Conference on Localization and GNSS*, 22-24 June, Gothenburg, Sweden, 6 pages.

Gramling, C., Carpenter, J. R., Long, A., Kelbel, D., and Lee, T. (2000) "Autonomous Relative Navigation for Formation-Flying Satellites Using GPS," *Proceedings of the International Symposium on Space Dynamics*, CNES, Biarritz , France, June 26-30, Paper MS00/18,.

Gramling, C. (2009) "Overview of the Magnetospheric MultiScale Formation Flying Mission," *Advances in the Astronautical Sciences*, Vol. 135, suppl. 1, pp. 407-417.

Griggs, E., R. Kursinski, D. Akos (2012) "An Analysis of the Short-Term Stability of GNSS Satellite Clocks" *Sixth FORMOSAT-3/COSMIC Data Users' Workshop*, Oct 30-Nov 1, Boulder, CO.

Hartrampf, M., Filippi, H., Krauss, P. A., Montenbruck, O., and Gottzein, E. (2015) "LION Navigator for Transfer to GEO using Electric Propulsion," *Proceedings of the 28th International Technical Meeting of The Satellite Division of the Institute of Navigation (ION GNSS+ 2015)*, Tampa, Florida, pp. 3910-3927.

Hauschild, A., Montenbruck, O., Sleewaegen, J. M., Huisman L. and Teunissen, P. J. G. (2012) 'Characterization of Compass M1 Signals,' *GPS Solutions*, Vol. 16, pp. 117-126. DOI 10.1007/s10291-011-0210-3

Hauschild, A., O. Montenbruck and P. Steigenberger (2013) "Short Term Analysis of GNSS Clocks," *GPS Solutions*, vol. 17, no. 3, pp. 295–307. DOI 10.1007/s10291-012-0278-4

He, Z. and Petovello, M. (2015) "Performance Comparison of a Kalman Filter and Maximum Likelihood Carrier Phase Tracking for Weak GNSS Signals," *2015 International Conference on Indoor Positioning and Indoor Navigation (IPIN)*, 13-16 Oct, Banff, Canada, 8 pages.

Hesselbarth, A., and Wanninger, L., (2008) "Short-term Stability of GNSS Satellite Clocks and its Effects on Precise Point Positioning," *Proceedings of the 21st International Technical Meeting of the Satellite Division of The Institute of Navigation (ION GNSS 2008)*, Savannah, GA, pp. 1855-1863.

Holt G., Lightsey E. G., and Montenbruck O. (2003) "Benchmark Testing for Spaceborne Global Positioning System Receivers," *AIAA Guidance, Navigation and Control Conference*, Aug 11-14, Austin, Texas, AIAA-2003-5666.

Hoque, M. M., and N. Jakowski (2011), Ionospheric bending correction for GNSS radio occultation signals, *Radio Sci.*, 46, RS0D06, doi:10.1029/2010RS004583

Inside GNSS News, (2014a) "U.S. Eases Export Regulations for GPS Receivers," May, <http://www.insidegnss.com/node/4051>, last accessed July 4, 2017.

Inside GNSS News, (2014b) "AFRL ANGELS Take Flight with GPS On Board," July, <http://www.insidegnss.com/node/4129>, last accessed Nov 7, 2016.

ISRO Satellite Center (2014) *Indian Regional Navigation Satellite System Signal in Space ICD for Standard Positioning Service Version 1.0*, ISRO-IRNSS-ICD-SPS-1.0, Bangalore, India.

Indian Space Research Organization (2016) *Satellite Navigation*, <http://www.isro.gov.in/spacecraft/list-of-navigation-satellites>, last accessed Oct 28, 2016.

Iriarte, J. C., Ederra I., Gonzalo, R., Brand, Y., Fourmault, A., Demers, Y., Salgetti-Drioli, L., and de Maagt, P., (2009) "EBG Superstrate Array Configuration for the WAAS Space Segment," *IEEE Transactions on Antennas and Propagation*, Vol. 57, No. 1, pp. 81-93.

Issler, J.L., Fourcade, J., Lestarquit, L., Mehlen, C., and Gamier, G. (1998) "High Reduction of Acquisition and Tracking Thresholds of GPS Spaceborne Receivers," *Proceedings of the 1998 National Technical Meeting of The Institute of Navigation*, Long Beach, CA, pp. 123-131.

Japan Aerospace Exploration Agency (2012) *Interface Specification for QZSS*, IS-QZSS V1.4, Feb 28, 2012.

Japanese Cabinet Office (2017) *Quazi-Zenith Satellite System Interface Specification, Satellite Positioning, Navigation and Timing Services*, IS-QZSS-PNT-001, March 28.

Japan Civil Aviation Bureau (2008) "Overview of MSAS MTSAT Satellite-based Augmentation System for ICG-3" *3rd Meeting of the International Committee on GNSS*, December 23, 2008.

Johnson-Freese, J. (2007) *Space as a Strategic Asset*, Columbia University Press.

Julien, O. (2005) 'Carrier-Phase Tracking of Future Data/Pilot Signals,' *Proceedings of ION GNSS 2005*, Long Beach, CA, pp. 113-124.

Jyoti, R., Sanandiya, H. C., Kumar, S. S., Kumar, A. and Sharma, S. B. (2005) 'Wideband Printed Helix Array Antenna at L1 & L5 for Navigation Satellite,' *Proceedings of the International Conference on Antenna Technologies*, ICAT 2005, pp. 23-27.

Kahr, E. (2011) *In Orbit Performance of the Can X-2 Nanosatellite's GPS Receiver*, MSc. thesis, Department of Geomatics Engineering, University of Calgary, Canada, UCGE Report 20329.

Kahr, E., Montenbruck, O., O'Keefe, K., Skone, S., Urbanek, J., Bradbury, L., and Fenton, P., 2011) "GPS Tracking of a Nanosatellite - the CanX-2 Flight Experience," *Proceedings of the 8th International ESA Conference on Guidance, Navigation and Control Systems*, June 5–11, Karlovy Vary, Czech Republic.

Kaplan E.D., and Hegarty C.J. (2006) *Understanding GPS Principles and Applications, Second Edition*", Artech house Inc., Second Edition.

Karutin, S. (2014) "GLONASS Status and Modernization Plans," *9th Meeting of the International Committee on GNSS*, November 10, GSA, Prague, Czech Republic.

Kelbel, D., Lee, T., Long, A., Carpenter, J. R., & Gramling, C. (2001) "Evaluation of Relative Navigation Algorithms for Formation-Flying Satellites," *Proceedings of the 2001 Flight Mechanics Symposium*, NASA Goddard Space Flight Center, Greenbelt, Maryland, June 19-21.

Kelso, T. S. (2000) Celestrak, <https://celestrak.com/>, last accessed May 15, 2017.

Kidder, S.Q., Kankiewicz, J.A., Vonder Haar, T.H. (2007) "The A-Train: How Formation Flying is Transforming Remote Sensing," *In Proceedings of The Joint 2007 EUMETSAT Meteorological Satellite Conference and the 15th American Meteorological Society Satellite Meteorology and Oceanography Conference*, 24–28 September, Amsterdam, The Netherlands.

Kim, J. and Kim M., (2015) "ARMA Prediction of SBAS Ephemeris and Clock Corrections for Low Earth Orbiting Satellites," *International Journal of Aerospace Engineering*, Volume 2015, Article ID 165178, 8 pages. doi:10.1155/2015/165178

Kim, J. and Lee Y. J., (2015) "Using Ionospheric Corrections from the Space-Based Augmentation Systems for Low Earth Orbiting Satellites," *GPS Solutions*, Vol. 19, pp 423-431. DOI 10.1007/s10291-014-0402-8

Kramer H. J. (2015) “MTSAT (Multifunction Transport Satellite” in the *eoPortal Directory*, <https://directory.eoportal.org/web/eoportal/satellite-missions/m/mtsat#spacecraft>, last accessed May 19, 2015.

Krieger, G., Moreira, A., Fiedler, H., Hajnsek, I., Werner, M., Younis, M. and Zink, M., (2007) “TanDEM-X: A Satellite Formation for High Resolution SAR Interferometry,” *IEEE Transactions on Geoscience and Remote Sensing*, Vol. 45, No. 11, pp. 3317-3341.

Kronman, J.D., (2000) “Experience Using GPS for Orbit Determination of a Geosynchronous Satellite,” *Proceedings of the Institute of Navigation GPS 2000 Conference*, Salt Lake City, UT.

Kuehl, C.T.F. , H. Filippi, A. Barrios-Montalvo, P.A. Krauss, J. Heim, C. Mueller, E. Gottzein, H. Dauphin (2011) “Potential of Multi Frequency, Multi Constellation Receivers for Spacecraft Navigation in GEO and Higher Altitudes,” *ESA GNC 2011*, June 5-10, Karlovy Vary, Czech Republic.

Kelbel, D., Lee, T., Long, A., Carpenter, R. and Gramling, C. (2003) ‘Relative Navigation Algorithms for Phase 1 of the MMS Formation,’
http://lampp03.gsfc.nasa.gov/downloads/featured_technologies/aerospace_aeronautics/14687_fms03_relnav.pdf last accessed July 8, 2013.

Lachapelle, G. (2009) *Advanced GNSS Theory and Applications*, ENGO 625 Course Notes, Geomatics Engineering, University of Calgary, Canada.

Lane, C. M. (2007) *Formation design and relative navigation in high earth orbits*. PhD Thesis, Department of Aerospace Engineering Sciences, University of Colorado, Colorado, USA.

Landgraf, M., and Mestreau-Garreau, A. (2013) “Formation flying and mission design for PROBA-3”, *Acta Astronautica*, Vol. 82, No.1, pp. 137-145.
<http://dx.doi.org/10.1016/j.actaastro.2012.03.028>

Li, J., Zhang, J., Zhang, B. and Shen, B. (2015) "Operation and Development of BeiDou Navigation Satellite System," *2015 International Association of Institutes of Navigation World Congress*, 20-23 October, Prague, Czech Republic.

Liu, H., Tang, G., Cheng, X., Ni S., and Cui, H. (2015) 'The Signal Characteristic Analysis for the use of GNSS in the CHANG'E 5T1 Mission,' *Proceedings of the 25th International Symposium on Space Flight Dynamics*, Munich, Germany.

Liu, H., Cao, J., Cheng, X., Peng, J., Tang, G. (2017) "The data processing and analysis for the CE-5T1 GNSS experiment," *Advances in Space Research*, Vol. 59, pp. 895-906.

Llorente, J.S., Agenjo, A., Carrascosa, C., de Negueruela, C., Mestreau-Garreau, A., Cropp, A. and Santovincenzo, A. (2013) 'PROBA-3: Precise Formation Flying Demonstration Mission,' *Acta Astronautica*, Vol. 82, No. 1, pp. 38–46.

Long, A., Farahmand, M., and Carpenter, R. (2015) 'Navigation Operations for the Magnetospheric Multiscale Mission,' *Proceedings of the 25th International Symposium on Space Flight Dynamics*, Munich, Germany.

Long, A., Kelbel, D., Lee, T., Garrison, J., and Carpenter, J.R., (2000) "Autonomous Navigation Improvements for High-Earth Orbiters Using GPS," *Proceedings of the 15th International Symposium on Spaceflight Dynamics*, CNES, June 26-30, Biarritz, France, Paper no. MS00/13.

Long, A., Kelbel, D., Lee, T., Leung, D., Carpenter, J. R., & Gramling, C. (2002) "Relative navigation of formation-flying satellites," In *Proceedings of the 1st International Symposium on Formation Flying Missions and Technologies*, ISFF, October 29-31, Toulouse, France.

Lorga J.M., P.F. Silva, F. Dovis, A. Di Cintio, R. Jansson (2010a) “Autonomous Orbit Determination for Future GEO and HEO Missions,” *Proceedings on ION GNSS 2012*, Portland, Oregon.

Lorga J.M., P.F. Silva, F. Dovis, A. Di Cintio, S. Kowaltschek, D. Jimenez and R. Jansson (2010b) ‘Autonomous Orbit Determination for Future GEO and HEO Missions’ *Proceedings of NAVITEC*, Noordwijk, the Netherlands, 8-10 December.

Lulich, T., W. A. Bamford, L. M. B. Winternitz, and S. R. Price (2012) “Results from Navigator GPS Flight Testing for the Magnetosphere Multi scale (MMS) Mission,” *Proceedings of ION GNSS 2012*, September 17-21, Nashville, Tennessee.

Lutz, S., Beutler, G., Schaer, S., Dach, R. and Jäggi, A. (2016) “CODE’s new ultra-rapid orbit and ERP products for the IGS,” *GPS Solutions*, Vol. 20, No. 2, pp 239-250. DOI: 10.1007/s10291-014-0432-2

Ma, M., C. O’Driscoll and G. Lachapelle (2011) “Automatic Parameter Determination for Real-Time Acquisition Using Frequency Domain Methods in a High Sensitivity Software Receiver,” *Proceedings of International Technical Meeting, Institute of Navigation*, San Diego, 24-26 January, pp. 1257-1269.

Marquis, W. (2013) *The GPS block IIR/IIR-M antenna panel pattern rev.3*, Lockheed Martin Corporation. (Publically releasable data)

Marquis, W. A., and Reigh, D. L., (2015) "The GPS Block IIR and IIR-M Broadcast L-band Antenna Panel: Its Pattern and Performance", *NAVIGATION, Journal of The Institute of Navigation*, Vol. 62, No. 4, pp. 329-347.

Martzen, P., Highsmith, D. E., Valdez, J. E., Parker, J. J., and Moreau, M. C., (2015) “GPS Antenna Characterization Experiment (ACE): Receiver Design and Initial Results,” *Institute of*

Navigation Joint Navigation Conference, 22-25 June 2015, Orlando, FL, GSFC-E-DAA-TN24090.

Mehlen, C., and D. Laurichesse (1999) "Improving GPS Navigation with Orbital Filter," *Proceedings of the 4th ESA International Conference on Spacecraft Guidance, Navigation and Control Systems*, 18-21 October, ESTEC, Noordwijk, The Netherlands.

Mestreau-Garreau, A., K. Gantois, A. Santovincenzo, A. Cropp, D. Evans, M. François, P. Kerhousse and F. Teston (2011) "PROBA 3 High Precision Formation Flying Mission" *Proceedings of the Spacecraft Formation Flying Missions and Technologies Conference*, May 18-20, Montreal, Canada.

Misra, P. and Enge, P. (2006) *Global Positioning System: Signals, Measurements and Performance*, Ganga-Jamuna Press, Lincoln, MA.

Mohiuddin, S., and Psiaki, M. (2008) "Carrier-Phase Differential Global Positioning System Navigation Filter for High-Altitude Spacecraft," *Journal of Guidance, Control, And Dynamics*, vol. 31, no. 4, pp. 801-814. DOI: 10.2514/1.33948

Mongrédiens, C., G. Lachapelle and M.E. Cannon (2006) "Testing GPS L5 Acquisition and Tracking Algorithms Using a Hardware Simulator," *ION GNSS 2006*, Fort Worth, TX, Institute of Navigation, 2901-2913.

Montenbruck, O. (2017) Personal Communication.

Montenbruck O., Garcia-Fernandez M., Williams J. (2006) "Performance Comparison of Semi-Codeless GPS Receivers for LEO Satellites," *GPS Solutions*, vol. 10, pp. 249-261. DOI 10.1007/s10291-006-0025-9

Montenbruck, O. and Gill, E. (2000) *Satellite Orbits, Models, Methods and Applications*, Springer Berlin Heidelberg, New York.

Montenbruck O., Hauschild A., Steigenberger P., Hugentobler U., Teunissen P., and Nakamura S. (2013) 'Initial Assessment of the COMPASS/BeiDou-2 Regional Navigation Satellite System,' *GPS Solutions*, Vol. 17, No. 2, pp. 211-222. DOI 10.1007/s10291-012-0272-x

Montenbruck, O., Markgraf, M., Issler, J-L., Mercier, F., Santandrea, S., A. Garcia, A., Naudet, J. and Serre, S. (2010) "GPS-Based Precise Orbit Determination and Real-Time Navigation of the PROBA-2 Spacecraft," *Proceedings of NAVITEC 2010 (5th ESA Workshop on Satellite Navigation Technologies and Euopen Workshop on GNSS Singnals and Signal Processing)*, Noordwijk, The Netherlands.

Montenbruck O., and Ramos-Bosch P.(2008) "Precision Real-Time Navigation of LEO Satellites using Global Positioning System Measurements," *GPS Solutions*, vol. 12, no. 3, pp. 187-198. DOI 10.1007/s10291-007-0080-x

Montenbruck, O., Steigenberger, P. and Hauschild, A. (2015) "Broadcast versus Precise Ephemerides: a Multi-GNSS Perspective," *GPS Solutions*, vol. 19, pp. 321-333. DOI 10.1007/s10291-014-0390-8

Montenbruck, O., Steigenberger P., Khachikyan R., Weber G., Langley R. B., Mervart L., Hugentobler U. (2014) "IGS-MGEX: Preparing the Ground for Multi-Constellation GNSS Science," *InsideGNSS*, vol. 9 no. 1, pp. 42-49.

Montenbruck O., van Helleputte T., Kroes R. and Gill E. (2005) "Reduced Dynamic Orbit Determination using GPS Code and Carrier Measurements," *Aerospace Science and Technology*, vol. 9, no.3, pp. 261-271. DOI 10.1016/j.ast.2005.01.003

Montenbruck, O., Wermuth, M., and Kahle, R. (2011) ‘GPS Based Relative Navigation for the TanDEM-X Mission - First Flight Results,’ *Navigation, Journal of The Institute of Navigation*, Vol. 58, No. 4, pp. 293-304.

Montesano, A., Monjas, F., Cuesta, L. and Olea, A., (2005) “Galileo System Navigation Antenna for Global Positioning”, *28th ESA Antenna Workshop on Space Antenna Systems and Technologies*, May 31-June 3, ESTEC, Noordwijk, Netherlands, pp. 247-252.

MOOG (2016) *TriG RO and TriG POD*, data sheet, form 500-1033 0316.

Moreau, M. (2001) *GPS Receiver Architecture for Autonomous Navigation in High Earth Orbits*, Ph.D. Dissertation, Department of Aerospace Engineering Sciences, University of Colorado at Boulder.

Moreau, M., Axelrad, P. Garrison, J. and Long, A. (2000) “GPS Receiver Architecture and Expected Performance for Autonomous Navigation in High Earth Orbits,” *NAVIGATION: Journal of the Institute of Navigation*, Vol. 47, No. 3, pp. 191-204.

Moreau, M., P.Axelrad, J.Garrison, M.Wennersten, A.Long, (2001) "Test Results of the PiVoT Receiver in High Earth Orbits using a GSS GPS Simulator," *Proceedings of the Institute of Navigation GPS 2001 Conference*, Salt Lake City, UT.

Moreau, M., Davis, E.P., Carpenter, J.R., Kelbel, D., Davis, G.W., and Axelrad, P. (2002) ‘Results from the GPS Flight Experiment on the High Earth Orbit AMSAT OSCAR-40 Spacecraft,’ *Proceedings of ION GPS-2002*, Portland, OR, pp. 122-133.

Moreau, M., Naasz, B., Leitner, J., Carpenter, R., Gaylor, D. (2005) "Hardware in-the-Loop Demonstration of Real-Time Orbit Determination in High Earth Orbits," *Proceedings of the 2005 National Technical Meeting of The Institute of Navigation*, San Diego, CA, pp. 523-536.

Morion (2012) *Double Oven Ultra Precision OCXO MV89*, Datasheet, Morion Inc.,
http://www.morion.com.ru/catalog_pdf/MV89-OCXO.pdf, last accessed 2 July, 2017.

Morrison, A. (2010) *GNSS Signal Tracking Methods under Ionospheric Scintillation*, PhD Thesis, published as Report No. 20312, Department of Geomatics Engineering, University of Calgary, Canada.

NASA Goddard Space Flight Center (2006) *GPS-Enhanced Onboard Navigation System (GEONS)*, data sheet,
http://itpo.gsfc.nasa.gov/downloads/featured_technologies/aerospace_aeronautics/gsc_14687_1_geons.pdf, last accessed May 15, 2017.

Noda, H., Kogure, S., Kishimoto, M., Soga, H., Moriguchi, T. and Furubayashi, T. (2010) ‘Development of the Quasi-Zenith Satellite System and High-Accuracy Positioning Experiment System Flight Model,’ *NEC Technical Journal*, Vol. 5, No. 4, pp. 93-97.

Olson, C., Wright, C., and Long, A. (2012) “Expected Navigation Flight Performance for the Magnetospheric Multiscale (MMS) Mission,” *Proceedings of the 22nd AAS/AIAA Conference*, Charleston, SC.

Parker, J., Valdez, J., Bauer, F., and Moreau, M. (2016) “Use and Protection of GPS Sidelobe Signals for Enhanced Navigation Performance in High Earth Orbit,” *39th Annual AAS Guidance and Control Conference*, Breckenridge, CO, AAS 16-72.

Parkinson B.W., Spilker J.J. (eds.) (1996) *Global Positioning System: Theory and Applications*. AIAA Publications, Washington DC.

Perea L., D'Amico S., Ardaens J.S., Elosegui P. (2010) “Relative Control of a Virtual Telescope in a High Elliptical Orbit using GNSS and Optical Metrology”, *Journal of Guidance, Control and Dynamics*, 33/4, 1281-1287 (2010). DOI 10.2514/1.48287

Persson, S., Jakobsson, B., and Gill, E. (2005) "PRISMA—Demonstration Mission for Advanced Rendezvous and Formation Flying Technologies and Sensors," *56th International Astronautical Congress*, Fukuoka, Japan, International Astronautical Congress Paper 05-B56B07.

Petovello, M. (2014) *Satellite Positioning*, ENGO 465 Course Notes, Geomatics Engineering, University of Calgary, Canada.

Petovello, M. and O'Driscoll, C. (2007) *GSNRxTM Algorithm Design Document*, Position Location and Navigation Group, Department of Geomatics Engineering, Schulich School of Engineering, University of Calgary.

Petovello, M.G., C. O'Driscoll and G. Lachapelle (2008a) "Carrier Phase Tracking of Weak Signals Using Different Receiver Architectures," *Proceedings of ION NTM08*, San Diego, 28-30 Jan, pp. 781-791.

Petovello, M.G., C. O'Driscoll and G. Lachapelle (2008b) "Weak Signal Carrier Tracking Using Extended Coherent Integration with an Ultra-Tight GNSS/IMU Receiver," *Proceedings of European Navigation Conference*, Toulouse, 23-25 April, 11 pages.

Petovello, M.G., C. O'Driscoll, G. Lachapelle, D. Borio and H. Murtaza (2009) Architecture and Benefits of an Advanced GNSS Software Receiver. *Journal of Global Positioning Systems*, Vol. 7, No. 2, pp. 156-168.

Pogorelc, S., Cashin, T., and Lage, M., (1997) "Analysis and Test Results of GPS and Geostationary Satellite Orbit Determination for WAAS," *Proceedings of the 1997 National Technical Meeting of The Institute of Navigation*, Santa Monica, CA, January, pp. 429-439.

Powell, T.D., Martzen, P. D., Sedlacek, S.B., Chao, C., Silva, R., Brown, A. and Belle, G. (1999) ‘GPS Signals in a Geosynchronous Transfer Orbit: Falcon Gold Data Processing,’ *ION National Technical Meeting*, San Diego, CA, pp. 575-585.

Press, W.H., S.A. Teukolsky, W.T. Vetterling and B.P. Flannery (1992) *Numerical Recipes in C: The Art of Numerical Computing*, Cambridge University Press.

The PROBA-3 Phase A Team (2007) *Proba-3 Phase A Study Executive Summary Report*, Technical Report PROBA3-ASU-RPT-14, Issue 1.0, Astrium Limited.

Psiaki, M. L. (2001) “Block Acquisition of Weak GPS Signals in a Software Receiver,” *Proceedings of the Institute of Navigation GPS 2001 Conference*, Salt Lake City, Utah, pp.2838-2850.

Psiaki, M. L., (2002) “Extended Kalman filter methods for tracking weak GPS signals,” *Proceedings of the Institute of Navigation GPS 2001 Conference*, Portland, OR, pp. 2838–2850.

Psiaki, M. L., and Mohiuddin, S. (2005) “Relative Navigation of High-Altitude Spacecraft Using Dual-Frequency Civilian CDGPS,” *Proceedings of the ION GNSS 2005*, Long Beach, CA, pp. 1191–1207.

Psiaki, M. L., and Mohiuddin, S. (2007) “Modeling, Analysis, and Simulation of GPS Carrier-Phase for Spacecraft Relative Navigation,” *Journal of Guidance, Control, and Dynamics*, Vol. 30, No. 6, pp. 1628–1639.

Qiao, L., L. Samsung, C. Rizos and J. Liu, (2009a) “Autonomous GEO Satellite Navigation with Multiple GNSS Measurements,” *22nd International Meeting of the Satellite Division of The Institute of Navigation*, Savannah, GA, September 22-25, pp. 2169-2177.

Qiao, L., L. Samsung, C. Rizos and J. Liu, (2009b). GNSS-based orbit determination for highly elliptical orbit satellites. *2009 Int. Symp. On GPS/GNSS*, Jeju, Korea, 4-6 November, session TC4 POD (Precise Orbit Determination), CD-ROM procs.

Rathinam, A., and Dempster, A. (2016) "Multi-GNSS for Space Service Volume," *Proceedings of the IGNSS Conference 2016*, 6-8 December, Sydney, Australia.

Ramakrishnan, S., Reid, T., Enge, P., (2013) "Leveraging the L1Composite Signal to Enable Autonomous Navigation at GEO and Beyond," *Proceedings of the 26th International Technical Meeting of The Satellite Division of the Institute of Navigation (ION GNSS+ 2013)*, Nashville, TN, pp. 3336-3346.

Rebhan H., Aguirre, M., Johannessen, J. A. (2000)' The Gravity Field and Steady-State Ocean Circulation Explorer Mission — GOCE', *Earth Observation Quarterly*, Vol. 66, July, pp. 6-11.

Ren, T. and M. Petovello (2014) "An analysis of maximum likelihood estimation method for bit synchronization and decoding of GPS L1 C/A signals," *EURASIP Journal on Advances in Signal Processing*, 2014:3. doi:10.1186/1687-6180-2014-3

Revnivykh, S. (2011) "Glonass Status and Modernization," *6th Meeting of the International Committee on GNSS*, Tokyo, Japan.

Rho H. and R. B. Langley, (2008) "Evaluation of the New WAAS L5 Signal," *Proceedings of the 21st International Technical Meeting of the Satellite Division of the Institute of Navigation (ION GNSS 2008)*, Savannah, GA, September 2008, pp. 1667-1678.

Roth, N. (2010) *Navigation and control design for the CanX-4/-5 satellite formation flying mission*, Master's thesis, University of Toronto.

RTCA, "Minimum Operation Performance Standards for Global Positioning System/Wide Area Augmentation System Airborne Equipment," RTCA DO-229D, December 13, 2006.

RUAG Space (2016) *Multi-Constellation Precise Orbit Determination GNSS Receiver*
<http://www.ruag.com/de/space/produkte/digital-electronics-for-satellites-launchers/satellite-navigation-receivers-signal-processing/multi-constellation-pod-gnss-receiver/>, last accessed Nov 4, 2016.

Ruiz, J. L., Frey, C. H., (2005) "Geosynchronous Satellite Use of GPS," *Proceedings of the 18th International Technical Meeting of the Satellite Division of The Institute of Navigation (ION GNSS 2005)*, Long Beach, CA, pp. 1227-1232.

Russian Institute of Space Device Engineering (2008) *Global Navigation Satellite System Glonass Interface Control Document*, Edition 5.1, Moscow.

Russian Space Systems (2012) *System of Differential Corrections and Monitoring Interface Control Document*, Edition 1.

Sarda, K., C. Grant, S. Eagleson and D. Kekez A. Shah and R. Zee, (2009) "Canadian Advanced Nanospace Experiment 2 Orbit Operations: One Year of Pushing the Nanosatellite Performance Envelope" *Proceedings of the 23rd Annual AIAA/USU Conference on Small Satellites*, SSC09-IV-6.

Schempp, T., Burke, J. and Rubin, A. (2008) "WAAS Benefits of GEO Ranging," ION GNSS 2008, 21st International Technical Meeting of the Satellite Division, 16-19 September, Savannah, GA, pp. 1903-1910.

Serre, S., Mehlen, C., Boyer, C., Holsters, P., Seco-Granados, G., Garcia-Rodriguez, A., Issler, J-L., and Grondin, M. (2006) "A Dual Frequency GPS Receiver (L1/L2c or L1/Lp) for Space Applications in LEO and GEO Orbit," *Proceedings of the 19th International Technical Meeting*

of the Satellite Division of The Institute of Navigation (ION GNSS 2006), Fort Worth, TX, pp. 2563-2570.

Smith, C., Bandecchi, M., Habinc, S., Hardy, D. and Sinander, P., (1998) "Low-cost, ASIC-based Telemetry and Telecommand Systems - The TEAMSAT Experience," *Proceedings of the 4th International Symposium on Small Satellites Systems and Services*, Sept. 14-18, Antibes Juan les Pins, France.

Spirent (2014) *SimGen Software User Manual Software for the Spirent Range of Satellite Navigation Simulator Products*, DGP00686AAA, Issue 5-02, 1 August.

Stupak, G (2010) "Glonass Status and Development Plans," *5th Meeting of the International Committee on GNSS*, Turin, Italy.

Stupak, G., (2015) "Status of SDCM and strategy of development," *Munich Satellite Navigation Summit*, March 24-26, Munich, Germany.

Surrey Satellite Technology Ltd. (2014) *SGR-Axio, Data Sheet*,
<https://www.sstl.co.uk/Products/Subsystems/Navigation/SGR-Axio>, last accessed Nov 6, 2016.

Tapley, B.D., S. Bettadpur, M. Watkins, C. Reigber, (2004) "The gravity recovery and climate experiment: Mission overview and early results," *Geophysical Research Letters*, vol. 31, no. 9, L09607.

Tapley, B.D., Schutz, B.E., and Born, G.H. (2004) *Statistical Orbit Determination*, Elsevier Academic Press, Burlington, MA.

Unwin, M., Van Steenwijk, R. De Vos, Blunt, P., Hashida, Y., Kowaltschek, S., and Nowak, L., (2013) "Navigating Above the GPS Constellation – Preliminary Results from the SGR-GEO on

GIOVE-A," *Proceedings of the 26th International Technical Meeting of The Satellite Division of the Institute of Navigation (ION GNSS+ 2013)*, Nashville, TN, pp. 3305-3315.

Urlichich, Y., Subbotin, V., Stupak, G. Dvorking, V., Povalyaev, A., Karutin, S. and Bakitko, R. (2011) "GLONASS Modernization," *GPS World Magazine*, <http://gpsworld.com/glonass-modernization-12232/>, last accessed February 16, 2016.

US State Department (2017) "The International Traffic in Arms Regulations (ITAR)," https://www.pmddtc.state.gov/regulations_laws/itar.html, last accessed August 11, 2017.

Valle, P., Netti, A., Zolesi, M., Mizzoni, R. Bandinelli, M. and Guidi, R. (2006) "Efficient Dual-Band Planar Array Suitable to Galileo," *Proceedings of EUCAP 2006*, 6-10 November, Nice, France.

Van Dierendonck, A.J. (1996) "GPS Receivers," [Chapter 8] in *Global Positioning System: Theory and Applications*, B. W. Parkinson and J. J. Spilker, Jr., eds., Vol. 1, Progress in Astronautics and Aeronautics, American Institute of Aeronautics and Astronautics, Inc., pp. 329-407.

Van Graas, F. (2009) "Use of GNSS for Future Space Operations and Science Missions," *Sixth Meeting of the National Space-Based Positioning, Navigation and Timing (PNT) Advisory Board*, November 5-6, Alexandria, Virginia.

Vigneron, A., de Ruiter, A. Burlton, B., and Soh, W. (2016) 'Nonlinear Filtering for Autonomous Navigation of Spacecraft in Highly Elliptical Orbit", *Acta Astronautica*, vol. 126, pp 138-149.

Voboril, C., Winkler, S., Larson, K. and Freesland, D. (2016) "Solar Flare Degradation of GPS Navigation at GEO," *AAS GN&C Conference*, AAS-16-073, Breckenridge, CO.

Walker, J.G. (1984) “Satellite constellations,” *Journal of the British Interplanetary Society*, vol. 37, pp. 559–572.

Walter, T., Blanch, J. and Enge, P., (2013) “Implementation of the L5 SBAS MOPS,” *Proceedings of the 26th International Technical Meeting of the Satellite Division of the Institute of Navigation (ION GNSS+ 2013)*, Nashville, TN, pp. 814-824.

Wang, D., Dong, Q., Wang, M., Li, Y., Li, L. and Li, R. (2015) “Results from the GNSS flight experiment on the circumlunar free return trajectory of China CE-5T1 spacecraft,” *Proceedings of the 66th International Astronautical Congress*, Jerusalem, Israel.

Wang, X., Han, X., Li, L., Qu, B., Wang, Y., Han, L., Meng, Y., Hu, X., Fan, M., Li, P., Huang, Y., Gong, D. (2017) “HiSGR: A Novel High Sensitive Spaceborne GNSS Receiver for Lunar Missions,” *Proceedings of ION ITM 2017*, Monterey, CA.

Wang, X., Shao, X., Gong, D. and Duan, D. (2011) “Improved adaptive Huber filter for relative navigation using global position system,” *Proceedings of the Institution of Mechanical Engineers, Part G: Journal of Aerospace Engineering*, Vol. 225, pp. 769-777. DOI: 10.1177/0954410011399226

Wang, X., Sun, Y., Du, Q., Bai, W., Wang, D., Cai, Y., Wu, D. and Yu, Q. (2014) “GNOS – radio occultation sounder on board of Chinese FY3 satellite,” *IEEE International Geoscience and Remote Sensing Symposium*, Quebec City, Canada, pp. 4982-4985.

Wanninger, L., (2008) “The future is now: GPS + GLONASS + SBAS = GNSS,” *GPS World*, July, Vol. 19, No. 7, pp. 42-48.

Ward, P., Betz, J. and Hegarty, C. (2006) “Satellite Signal Acquisition, Tracking, and Data Demodulation,” [Chapter 5] in Understanding GPS Principles and Applications, 2nd Ed, E. D. Kaplan and C. Hegarty, Ed., Artech House Publishers, Boston, London, pp 153-242.

Welch, G. and Bishop, G. (2006) *An Introduction to the Kalman Filter*, University of North Carolina, Department of Computer Science, TR 95-041.

William J. Hughs FAA Technical Center website (2015) [<http://www.nstb.tc.faa.gov/index.htm>]
Last accessed June 11, 2015

Winternitz, L. Bamford, B., and Heckler, G, (2009) "A GPS receiver for High-Altitude Navigation", *IEEE Journal of Selected Topics in Signal Processing*, vol. 3 no. 4, pp. 541-556.

Winternitz, L., Bamford, W., Price, S., Carpenter, R., Long, A. and Farahmand, M. (2016) "Global Positioning System Navigation Above 76,000 km for NASA's Magnetospheric Multiscale Mission," *2016 AAS GN&C Conference*, Breckenridge, CO, United States.

Winternitz, L., Bamford, W., Price, S., Carpenter, R., Long, A. and Farahmand, M. (2017) "Global Positioning System Navigation Above 76,000 km for NASA's Magnetospheric Multiscale Mission," *Navigation, Journal of the Institute of Navigation*, in press.

Winternitz, L., Moreau, M., Boegner, G. J., and Sirotzky, S., (2004) "Navigator GPS Receiver for Fast Acquisition and Weak Signal Space Applications," *Proceedings of the 17th International Technical Meeting of the Satellite Division of The Institute of Navigation (ION GNSS 2004)*, Long Beach, CA, pp. 1013-1026.

Xiao, W., Liu, W., and Sun, G. (2016) "Modernization milestone: BeiDou M2-S initial signal analysis," *GPS Solutions*, vol. 20 no. 1, pp. 125–133. DOI 10.1007/s10291-015-0496-7.

Yanovsky, M.I., Eismont, N.A., and Kaurova, I.E. (2002) "Application of Radio-Navigation Methods for Perspective High Elliptical Orbit Space Vehicles of Scientific Assignment," *Proceedings of the XXVIIth URSI General Assembly*, August, Maastricht, the Netherlands.

Yunck T.P. (1996) "Orbit Determination" in: Parkinson B.W., Spilker J.J. (eds.); *Global Positioning System: Theory and Applications*. AIAA Publications, Washington DC.

Zentgraf P., Berge, S., Chasset, C., Filippi, H., Gottzein, E., Gutiérrez-Canas, Hartrampf, M., Krauss, P., Kuehl, C., Lübke-Ossenbeck, B., Mittnacht, M., Montenbruck O., Müller, C., Rueda Boldo, P. and Truffi, A. (2010) "Preparing the GPS Experiment for the Small GEO Mission", *33rd Annual AAS Guidance and Control Conference*, February, Breckenridge, Colorado, AAS 10-038.

Zhan, X., Jing, S. and Wang, X. (2013) "BeiDou Space Service Volume Parameters and its Performance," *ICG -8 Working Group B*, Nov 12, 2013, Dubai, UAE.

Zin, A., Landenna, S., Conti, A., Marradi, L., and Di Raimondo, M. S. (2007) "ENEIDE: an experiment of a spaceborne, L1/L2 integrated GPS/WAAS/EGNOS receiver," *Microgravity Science and Technology*, Vol. 19, no. 5–6, pp 54–59. DOI 10.1007/BF02919453

Zin, A., Scotti, M., Mangolini, E., Cappelluti, I., Fiordiponti, R., Amalric, J., Flament, P., Brouillard, E., and Kowaltschek, S. (2015) "Preparing an autonomous, low-cost GNSS positioning and timing function on board a GEO telecom mission: a study case," *CEAS Space Journal*, Vol. 7, no. 2, pp. 247-262.

APPENDIX A: SUMMARIZED GNSS SIGNALS AND SIGNAL POWERS

Table A-1: GNSS signal definitions considered while designing the visibility simulator

Constellation	Block	Signal	Frequency	Min Strength*	Source	Note
GPS	II,IIA,IIR	L1 C/A	1575.42	-158.1	ICD-GPS-200C IRNs 12345	
GPS	IIR-M	L1 C/A	1575.42	-158.1	IS-GPS-200E	
GPS	IIF	L1 C/A	1575.42	-158.1	IS-GPS-200E	
GPS	III	L1 C/A	1575.42	-158.1	IS-GPS-200E	
					ICD-GPS-200C IRNs	
GPS	II,IIA,IIR	L1 P(Y)	1575.42	-161.1	12345	
GPS	IIR-M	L1 P(Y)	1575.42	-161.1	IS-GPS-200E	
GPS	IIF	L1 P(Y)	1575.42	-161.1	IS-GPS-200E	
GPS	III	L1 P(Y)	1575.42	-161.1	IS-GPS-200E	
					ICD-GPS-200C IRNs	
GPS	II,IIA,IIR	L2 P(Y)	1227.6	-164.1	12345	
GPS	IIR-M	L2 P(Y)	1227.6	-161.1	IS-GPS-200E	
GPS	IIF	L2 P(Y)	1227.6	-161.1	IS-GPS-200E	
					ICD-GPS-200C IRNs	
GPS	II,IIA,IIR	L2C	1227.6	-164.1	12345	1
GPS	IIR-M	L2C	1227.6	-159.6	IS-GPS-200E	
GPS	IIF	L2C	1227.6	-159.6	IS-GPS-200E	
GPS	III	L2C	1227.6	-158.1	IS-GPS-200E	
GPS	IIF	I5	1176.45	-157.5	IS-GPS-705B	
GPS	IIF	Q5	1176.45	-157.5	IS-GPS-705B	
GPS	III	I5	1176.45	-156.6	IS-GPS-705B	
GPS	III	Q5	1176.45	-156.6	IS-GPS-705B	
GALILEO		E5a I	1176.45	-158.25	OD-SIS-ICD Issue 1.1	
GALILEO		E5a Q	1176.45	-158.25	OD-SIS-ICD Issue 1.1	2
GALILEO		E5b I	1207.14	-158.25	OD-SIS-ICD Issue 1.1	
GALILEO		E5b Q	1207.14	-158.25	OD-SIS-ICD Issue 1.1	2
GALILEO		E6 B	1278.75	-158.25	OD-SIS-ICD Issue 1.1	
GALILEO		E6 C	1278.75	-158.25	OD-SIS-ICD Issue 1.1	
GALILEO		E1 B	1575.42	-160.25	OD-SIS-ICD Issue 1.1	2
GALILEO		E1 C	1575.42	-160.25	OD-SIS-ICD Issue 1.1	2
GLONASS	legacy	L1	1602 + nx0.5625	-160.6	Russian Institute of Space Device Eng. 2008	

GLONASS	legacy	L2	1246 + nx0.4375	-166.6	Russian Institute of Space Device Eng. 2008	
GLONASS	M,K1,K2,KM	L1OF	1602 + nx0.5625	-160.6	Russian Institute of Space Device Eng. 2008	3
GLONASS	M,K1,K2,KM	L2OF	1246 + nx0.4375	-166.6	Russian Institute of Space Device Eng. 2008	3
GLONASS	M,K1,K2,KM	L1SF	1602 + nx0.5625		Revnivkh 2011	3
GLONASS	M,K1,K2,KM	L2SF	1246 + nx0.4375		Revnivkh 2011	3
GLONASS	K1	L3OC	1207.14 (1202.025)	-157.6	Stupak, 2010	3,4
GLONASS	K2, KM	L3OC	1207.14		Revnivkh 2011	3
GLONASS	K2, KM	L1OC	1575.42		Revnivkh 2011	3
GLONASS	K2, KM	L1SC	1575.42		Revnivkh 2011	3
GLONASS	K2, KM	L2SC	1242		Revnivkh 2011	3
GLONASS	KM	L1OCM	1575.42		Revnivkh 2011	3
GLONASS	KM	L2OC	1242		Revnivkh 2011	3
GLONASS	KM	L5OC	1176.45		Revnivkh 2011	3
QZSS		L1 C/A	1575.42	-158.75	IS-QZSS V1.4	5
QZSS		L1 CD	1575.42	-163.25	IS-QZSS V1.4	5
QZSS		L1 CP	1575.42	-158.5	IS-QZSS V1.4	5
QZSS		L1-SAIF	1575.42	-161.25	IS-QZSS V1.4	5
QZSS		L2C	1227.6	-160.25	IS-QZSS V1.4	5
QZSS		L5 I	1176.45	-158.15	IS-QZSS V1.4	5
QZSS		L5 Q	1176.45	-158.15	IS-QZSS V1.4	5
QZSS		LEX	1278.75	-155.95	IS-QZSS V1.4	5
COMPASS	MEO	B1 I	1561.098	-163	BeiDou-SIS-ICD-Test	
COMPASS	MEO	E2 I	1561.098	-157.5	Hauschild et al 2012	6
COMPASS	MEO	E6	1268.52		Hauschild et al 2012	
COMPASS	MEO	E5b I	1207.14	-156.6	Hauschild et al 2012	6
COMPASS	IGSO	B1 I	1561.098	-163	BeiDou-SIS-ICD-Test	
COMPASS	GEO	B1 I	1561.098	-163	BeiDou-SIS-ICD-Test	
WAAS		L1	1575.42	-158.1	FAA/DoT 2008	
WAAS		L5	1176.45			
MSAS		L1	1575.42	-160.6	Japan Civil Aviation Bureau 2008	
EGNOS		L1	1575.42	-160.6	egnos-sol-sdd-v1.0	
SDCM		L1	1575.42	-158.7	Urlichich et al 2011	7

GAGAN		L1	1575.42	-160.6	A. Ganeshan, priv com.	
GAGAN		L5	1176.45			

* dbW, as seen by a RHCP isotropic antenna for a satellite at 5° elevation

- 1 Either L2C or P(Y) may be transmitted for block II satellites, but not both.
- 2 According to Hauschild et al (2012) the signal power from the GIOVE satellites is lower.
- 3 In the GLONASS signal definitions O is open, S is high precision not open, F is frequency division multiple access, and C is code division multiple access
- 4 The first two experimental block K1 satellites' L3OC signals will have centre frequencies of 1207.14 MHz, subsequent satellites will have centre frequencies of 1202.025 MHz.
- 5 QZSS minimum received power levels are specified for a RHCP isotropic antenna and a satellite at 10° elevation in the ICD. The Galileo correction factor of -0.25 dB to convert from 10° to 5° elevation has been applied to the QZSS values in this table.
- 6 COMPASS E2 and E5 minimum signal levels are not officially documented. These values have been extrapolated from the GPS minimum signal levels based on the comparison of live signal strength in Hauschild et al 2012.
- 7 This value was extrapolated from a plot, which was created under uncertain assumptions.

For the studies conducted in Chapter three, only the signals in turquoise were included in the visibility simulator due to lacking gain pattern or minimum signal strength information, or because either no satellites were launched or none were still active. Note that this is not a complete list of possible signals.

APPENDIX B: COPYRIGHT PERMISSIONS



PUBLISHERS OF DISTINGUISHED ACADEMIC, SCIENTIFIC AND PROFESSIONAL JOURNALS

Author Agreement

Inderscience Enterprises Ltd, trading as Inderscience Publishers, of World Trade Center Building II, 29 Route de Pre-Bols, Case Postale 856, CH-1215 Genève 15, Switzerland ("Inderscience").

If your article has been accepted for publication, each author must sign a copyright agreement form after reading the Explanatory Notes below and either (for online submissions) follow the online instructions or (for email submissions) send the signed forms, in electronic format, to the Editor (or other recipient as advised by the Editor of the specific journal), together with the final version of the article. If it is not practical to obtain a physical signature from all authors, you must have their agreement in writing to enable you to enter into this Author Agreement on their behalf and must ensure that all their details are provided to Inderscience correctly, including spellings and the sequence of names as they are to be listed on publication.

So that we can ensure both the widest dissemination and protection of material published in Inderscience's journals, we ask authors to assign copyright in their articles, including abstracts, to Inderscience. This enables us to ensure copyright protection against infringement, and to disseminate your article, and our journals, as widely as possible.

1. In consideration of the undertaking set out in paragraph 2, and upon acceptance by Inderscience for publication in the Journal, [insert the full names of all authors, reflecting the name order given in the article]
Erin Kahr

hereafter 'the Author' hereby assigns and transfers to Inderscience, the copyright in and to [insert article title]

PROSPECTS OF MULTIPLE GLOBAL NAVIGATION SATELLITE SYSTEM TRACKING FOR FORMATION FLYING IN HIGHLY ELLIPTICAL EARTH ORBITS

hereafter 'the Article' by the Author to be published in [insert journal title]

[Int. J. of Space Science and Engineering]

hereafter ('the Journal'). This assignment provides Inderscience the sole right and responsibility to publish the Article, including the right to sub-license publishing or distribution rights to the Article as may be appropriate, in both printed and electronic form; the Article may be published in printed, online, CD-ROM, microfiche or in other media formats.

2. In consideration of this assignment, Inderscience hereby undertakes to prepare and publish the Article named in paragraph 1 in the Journal, subject only to its right to refuse publication as provided in paragraph 5 or if there are other reasonable grounds; in such case Inderscience reverts and assigns to the Author any and all copyright and other rights in the Article otherwise assigned to it under this Agreement.
3. The Editor of the Journal and Inderscience are empowered to make such editorial changes as may be necessary to make the Article suitable for publication. Every effort will be made to consult the Author if substantive changes are required.
4. The Author hereby asserts his/her moral rights under the UK Copyright Designs and Patents Act 1988 to be identified as the Author of the Article.
5. The Author warrants that the Article is the Author's original work, it has not been published before either in full or in part and is not currently under consideration for publication elsewhere; and that the Article contains no libellous or unlawful statements and that it in no way infringes the rights of others, nor it is in breach of any English law, and that the Author, as the owner of the copyright, is entitled to make this assignment. The Author warrants that s/he is authorised to act on behalf of any co-authors and has provided full and accurate information relating to them on the understanding that no further changes can be made after signature of this Agreement.

Signed by the Author

September 9, 2013

Date

To: Jeanette Brooks <jrb@inderscience.com>
Subject: Permission to use my article as part of my PhD thesis

Hello,

I am writing to ask permission to reproduce the contents of my paper, cited below, in my PhD thesis.
The original copyright form is attached.

Written permission is an official requirement of the copyright office of my university, and must acknowledge that the thesis will be subject to the University of Calgary Non-Exclusive Distribution License, that all University of Calgary theses are harvested by the Library and Archives Canada, and that the thesis may be submitted to ProQuest.

The paper in question is:

Kahr, E. (2013) 'Prospects of Multi-GNSS Tracking for Formation Flying in Highly Elliptical Earth Orbit', *International Journal of Space Science and Engineering*, Vol. 1, No.4 pp. 432-447.
[10.1504/IJSPACESE.2013.059267](https://doi.org/10.1504/IJSPACESE.2013.059267)

If this is acceptable to the publishers of the journal, permission can be granted either by a letter or by a direct reply to this email. Please let me know by August 4, 2017.

Thank you,

Erin Kahr

FW: Permission to use my article as part of my PhD thesis

Jeanette Brooks <jrb@inderscience.com>

Wed 2017-07-19 1:55 AM

To: erinkahr@hotmail.com <erinkahr@hotmail.com>;

CC: Jeanette Brooks <jrb@inderscience.com>;

1 attachments (51 KB)

authoragree_EK.pdf;

Thank you Erin for your email. Inderscience is happy to give you permission to include your paper in your PhD. Please ensure full acknowledgement of the original source of publication is made clear, and a statement included that Inderscience retains copyright of the article.

Kind regards and good luck with your endeavours.

Jeanette

J R Brooks (Dr)
Publications Director
Email: jrb@inderscience.com

Inderscience Enterprises Limited
World Trade Centre Building II
29 route de Pre-Bois
Case Postale 856
CH-1215 Geneve 15
Switzerland



Sign up to our Newsletter for highlights from our journals and related industry events:
<http://www.inderscience.com/newsletter>

THE INSTITUTE OF NAVIGATION
COPYRIGHT RELEASE FORM
ION PROCEEDINGS

Signing of "Statement A" or "Statement B" is required except that employees of governments other than the U.S. Government may submit equivalent statements. It is essential that The Institute of Navigation (ION) and its agents or assignees have the right of publication and reproduction.

Proceedings to Appear in: **ION GNSS+ 2014**

Session Number & Title: **C5: Remote Sensing; Space Applications; Timing and Scientific Applications 2**

Paper Title (*exactly as it appears on the paper*): **Hardware-in-the-loop Simulation of GNSS Signal**

Tracking in Highly Elliptical Orbits Using the GSNRx Software Receiver

Author(s) & Affiliation(s) (*in the exact order they appear on the paper*): **Erin Kahr, Department of Geomatics Engineering, University of Calgary, Canada;**

Kyle O'Keefe, Department of Geomatics Engineering, University of Calgary, Canada; Oliver Montenbruck, Deutsches Zentrum für Luft- und Raumfahrt (DLR), Germany

Primary Author Address: **3444 Caribou Drive NW, Calgary AB Canada T2L 0S5**

Phone/Fax/E-Mail: **403-210-9798, erinkahr@hotmail.com**

STATEMENT A:

The undersigned "Copyright Owner," desiring to publish a paper (the "Paper") in ION Proceedings and/or through other publications of The Institute of Navigation ("ION"), hereby grants to ION the following rights in exchange for good and valuable consideration:

- 1.) the exclusive, royalty-free right of first publication of the above Paper throughout the world as part of the proceedings named above and;
- 2.) a non-exclusive, perpetual, royalty-free, worldwide license to reprint and/or provide in electronic format the above Paper, either in excerpt, in summary, or in completed form, for free or in exchange for a fee.

Copyright Owner reserves all rights not specifically granted to ION herein and has the right after the Paper has been published, to reprint the Work in any publication, provided that the terms of such republication do not conflict with this license. Copyright Owner agrees to include the proper credit to ION for prior publication of the Paper in any reprint of the Paper in a publication, including date (month and year) and location (city and state) of the meeting at which the paper was presented.

Copyright Owner warrants that the Paper is original with him/her, that its publication will not infringe the rights of others, that the Paper is factually accurate and contains no defamatory or otherwise unlawful material, and that Copyright Owner has full power to make this agreement. Copyright Owner further warrants that the Paper has not been published elsewhere in whole or in part (except as set out in a rider attached thereto if applicable) and that no agreement to publish the Paper or any part or version thereof is outstanding. Should the Paper contain any material which requires permission for inclusion in the Paper, Copyright Owner agrees to obtain such permission in writing and provide a copy of such permission to ION.

1. Erin Kahr

PRIMARY AUTHOR'S SIGNATURE

University of Calgary

EMPLOYER FOR WHOM WORK WAS PERFORMED

2. _____

August 13, 2014

DATE FORM SIGNED

STATEMENT B:

This will certify that all authors of the above Paper are employees of the U.S. Government and that the authors created the Paper as part of their employment and that the Paper is therefore not subject to U.S. Copyright protection.

2. _____
PRIMARY AUTHOR'S SIGNATURE

EMPLOYER FOR WHOM WORK WAS PERFORMED

3. _____
AUTHORIZED SIGNATURE

DATE FORM SIGNED

Crown Copyright Certification (where applicable)

This will certify that all authors of the Work are employees of the British or applicable Commonwealth Government and prepared the Work in connection with their official duties. As such, the Work is subject to Crown Copyright and is not assigned to the ION as set forth above. The Undersigned acknowledges, however, that the ION has the right to publish, distribute and reprint the Work in all forms and media.

3. _____
AUTHORIZED SIGNATURE

DATE FORM SIGNED

(Authors who are British or applicable Commonwealth Government employees should also sign line (1) above to indicate their acceptance of all terms other than the copyright transfer.)

THE INSTITUTE OF NAVIGATION
COPYRIGHT RELEASE FORM
ION PROCEEDINGS

Signing of "Statement A" or "Statement B" is required except that employees of governments other than the U.S. Government may submit equivalent statements. It is essential that The Institute of Navigation (ION) and its agents or assignees have the right of publication and reproduction.

Proceedings to Appear in: **ION GNSS+ 2015**

Session Number & Title: **F6: Remote Sensing; Space Applications; Timing and Scientific Applications 2**

Paper Title (exactly as it appears on the paper): A Comparative Study of SBAS Systems for Navigation in Geostationary Orbit

Author(s) & Affiliation(s) (in the exact order they appear on the paper): Erin Kahr, Department of Geomatics Engineering, University of Calgary, Canada;

Oliver Montenbruck, Deutsches Zentrum für Luft- und Raumfahrt (DLR), Germany; Kyle O'Keefe, Department of Geomatics Engineering, University of Calgary, Canada

Primary Author Address: 3444 Caribou Drive NW, Calgary, Alberta, Canada, T2L 0S5

Phone/Fax/E-Mail: erinkahr@hotmail.com

STATEMENT A:

The undersigned "Copyright Owner," desiring to publish a paper (the "Paper") in ION Proceedings and/or through other publications of The Institute of Navigation ("ION"), hereby grants to ION the following rights in exchange for good and valuable consideration:

- 1.) the exclusive, royalty-free right of first publication of the above Paper throughout the world as part of the proceedings named above and;
- 2.) a non-exclusive, perpetual, royalty-free, worldwide license to reprint and/or provide in electronic format the above Paper, either in excerpt, in summary, or in completed form, for free or in exchange for a fee.

Copyright Owner reserves all rights not specifically granted to ION herein and has the right after the Paper has been published, to reprint the Work in any publication, provided that the terms of such republication do not conflict with this license. Copyright Owner agrees to include the proper credit to ION for prior publication of the Paper in any reprint of the Paper in a publication, including date (month and year) and location (city and state) of the meeting at which the paper was presented.

Copyright Owner warrants that the Paper is original with him/her, that its publication will not infringe the rights of others, that the Paper is factually accurate and contains no defamatory or otherwise unlawful material, and that Copyright Owner has full power to make this agreement. Copyright Owner further warrants that the Paper has not been published elsewhere in whole or in part (except as set out in a rider attached thereto if applicable) and that no agreement to publish the Paper or any part or version thereof is outstanding. Should the Paper contain any material which requires permission for inclusion in the Paper, Copyright Owner agrees to obtain such permission in writing and provide a copy of such permission to ION.

1. _____
PRIMARY AUTHOR'S SIGNATURE

University of Calgary

EMPLOYER FOR WHOM WORK WAS PERFORMED

AUTHORIZED SIGNATURE

June 15, 2015

DATE FORM SIGNED

STATEMENT B:

This will certify that all authors of the above Paper are employees of the U.S. Government and that the authors created the Paper as part of their employment and that the Paper is therefore not subject to U.S. Copyright protection.

2. _____
PRIMARY AUTHOR'S SIGNATURE

EMPLOYER FOR WHOM WORK WAS PERFORMED

AUTHORIZED SIGNATURE

DATE FORM SIGNED

Crown Copyright Certification (where applicable)

This will certify that all authors of the Work are employees of the British or applicable Commonwealth Government and prepared the Work in connection with their official duties. As such, the Work is subject to Crown Copyright and is not assigned to the ION as set forth above. The Undersigned acknowledges, however, that the ION has the right to publish, distribute and reprint the Work in all forms and media.

3. _____
AUTHORIZED SIGNATURE

DATE FORM SIGNED

(Authors who are British or applicable Commonwealth Government employees should also sign line (1) above to indicate their acceptance of all terms other than the copyright transfer.)

**JOHN WILEY AND SONS LICENSE
TERMS AND CONDITIONS**

Jul 18, 2017

This Agreement between Ms. Erin Kahr ("You") and John Wiley and Sons ("John Wiley and Sons") consists of your license details and the terms and conditions provided by John Wiley and Sons and Copyright Clearance Center.

License Number	4152090897452
License date	Jul 18, 2017
Licensed Content Publisher	John Wiley and Sons
Licensed Content Publication	Navigation
Licensed Content Title	An Analysis of SBAS Signal Reception in Space
Licensed Content Author	Erin Kahr,Oliver Montenbruck,Kyle O'Keefe
Licensed Content Date	Sep 27, 2016
Licensed Content Pages	13
Type of use	Dissertation/Thesis
Requestor type	Author of this Wiley article
Format	Print and electronic
Portion	Full article
Will you be translating?	No
Title of your thesis / dissertation	Multi-Constellation GNSS for Absolute and Relative Navigation in Highly Elliptical Orbits
Expected completion date	Aug 2017
Expected size (number of pages)	290
Requestor Location	Ms. Erin Kahr 3444 Caribou Drive NW Calgary, AB T2L 0S5 Canada Attn: Ms. Erin Kahr
Publisher Tax ID	EU826007151
Billing Type	Invoice
Billing Address	Ms. Erin Kahr 3444 Caribou Drive NW Calgary, AB T2L 0S5 Canada Attn: Ms. Erin Kahr
Total	0.00 CAD
Terms and Conditions	

TERMS AND CONDITIONS

This copyrighted material is owned by or exclusively licensed to John Wiley & Sons, Inc. or one of its group companies (each a "Wiley Company") or handled on behalf of a society with which a Wiley Company has exclusive publishing rights in relation to a particular work (collectively "WILEY"). By clicking "accept" in connection with completing this licensing transaction, you agree that the following terms and conditions apply to this transaction (along with the billing and payment terms and conditions established by the Copyright Clearance Center Inc., ("CCC's Billing and Payment terms and conditions"), at the time that you opened your RightsLink account (these are available at any time at <http://myaccount.copyright.com>).

Terms and Conditions

- The materials you have requested permission to reproduce or reuse (the "Wiley Materials") are protected by copyright.
- You are hereby granted a personal, non-exclusive, non-sub licensable (on a stand-alone basis), non-transferable, worldwide, limited license to reproduce the Wiley Materials for the purpose specified in the licensing process. This license, and any CONTENT (PDF or image file) purchased as part of your order, is for a one-time use only and limited to any maximum distribution number specified in the license. The first instance of republication or reuse granted by this license must be completed within two years of the date of the grant of this license (although copies prepared before the end date may be distributed thereafter). The Wiley Materials shall not be used in any other manner or for any other purpose, beyond what is granted in the license. Permission is granted subject to an appropriate acknowledgement given to the author, title of the material/book/journal and the publisher. You shall also duplicate the copyright notice that appears in the Wiley publication in your use of the Wiley Material. Permission is also granted on the understanding that nowhere in the text is a previously published source acknowledged for all or part of this Wiley Material. Any third party content is expressly excluded from this permission.
- With respect to the Wiley Materials, all rights are reserved. Except as expressly granted by the terms of the license, no part of the Wiley Materials may be copied, modified, adapted (except for minor reformatting required by the new Publication), translated, reproduced, transferred or distributed, in any form or by any means, and no derivative works may be made based on the Wiley Materials without the prior permission of the respective copyright owner. For STM Signatory Publishers clearing permission under the terms of the [STM Permissions Guidelines](#) only, the terms of the license are extended to include subsequent editions and for editions in other languages, provided such editions are for the work as a whole in situ and does not involve the separate exploitation of the permitted figures or extracts. You may not alter, remove or suppress in any manner any copyright, trademark or other notices displayed by the Wiley Materials. You may not license, rent, sell, loan, lease, pledge, offer as security, transfer or assign the Wiley Materials on a stand-alone basis, or any of the rights granted to you hereunder to any other person.
- The Wiley Materials and all of the intellectual property rights therein shall at all times remain the exclusive property of John Wiley & Sons Inc, the Wiley Companies, or

their respective licensors, and your interest therein is only that of having possession of and the right to reproduce the Wiley Materials pursuant to Section 2 herein during the continuance of this Agreement. You agree that you own no right, title or interest in or to the Wiley Materials or any of the intellectual property rights therein. You shall have no rights hereunder other than the license as provided for above in Section 2. No right, license or interest to any trademark, trade name, service mark or other branding ("Marks") of WILEY or its licensors is granted hereunder, and you agree that you shall not assert any such right, license or interest with respect thereto.

- NEITHER WILEY NOR ITS LICENSORS MAKES ANY WARRANTY OR REPRESENTATION OF ANY KIND TO YOU OR ANY THIRD PARTY, EXPRESS, IMPLIED OR STATUTORY, WITH RESPECT TO THE MATERIALS OR THE ACCURACY OF ANY INFORMATION CONTAINED IN THE MATERIALS, INCLUDING, WITHOUT LIMITATION, ANY IMPLIED WARRANTY OF MERCHANTABILITY, ACCURACY, SATISFACTORY QUALITY, FITNESS FOR A PARTICULAR PURPOSE, USABILITY, INTEGRATION OR NON-INFRINGEMENT AND ALL SUCH WARRANTIES ARE HEREBY EXCLUDED BY WILEY AND ITS LICENSORS AND WAIVED BY YOU.
- WILEY shall have the right to terminate this Agreement immediately upon breach of this Agreement by you.
- You shall indemnify, defend and hold harmless WILEY, its Licensors and their respective directors, officers, agents and employees, from and against any actual or threatened claims, demands, causes of action or proceedings arising from any breach of this Agreement by you.
- IN NO EVENT SHALL WILEY OR ITS LICENSORS BE LIABLE TO YOU OR ANY OTHER PARTY OR ANY OTHER PERSON OR ENTITY FOR ANY SPECIAL, CONSEQUENTIAL, INCIDENTAL, INDIRECT, EXEMPLARY OR PUNITIVE DAMAGES, HOWEVER CAUSED, ARISING OUT OF OR IN CONNECTION WITH THE DOWNLOADING, PROVISIONING, VIEWING OR USE OF THE MATERIALS REGARDLESS OF THE FORM OF ACTION, WHETHER FOR BREACH OF CONTRACT, BREACH OF WARRANTY, TORT, NEGLIGENCE, INFRINGEMENT OR OTHERWISE (INCLUDING, WITHOUT LIMITATION, DAMAGES BASED ON LOSS OF PROFITS, DATA, FILES, USE, BUSINESS OPPORTUNITY OR CLAIMS OF THIRD PARTIES), AND WHETHER OR NOT THE PARTY HAS BEEN ADVISED OF THE POSSIBILITY OF SUCH DAMAGES. THIS LIMITATION SHALL APPLY NOTWITHSTANDING ANY FAILURE OF ESSENTIAL PURPOSE OF ANY LIMITED REMEDY PROVIDED HEREIN.
- Should any provision of this Agreement be held by a court of competent jurisdiction to be illegal, invalid, or unenforceable, that provision shall be deemed amended to achieve as nearly as possible the same economic effect as the original provision, and the legality, validity and enforceability of the remaining provisions of this Agreement shall not be affected or impaired thereby.

- The failure of either party to enforce any term or condition of this Agreement shall not constitute a waiver of either party's right to enforce each and every term and condition of this Agreement. No breach under this agreement shall be deemed waived or excused by either party unless such waiver or consent is in writing signed by the party granting such waiver or consent. The waiver by or consent of a party to a breach of any provision of this Agreement shall not operate or be construed as a waiver of or consent to any other or subsequent breach by such other party.
- This Agreement may not be assigned (including by operation of law or otherwise) by you without WILEY's prior written consent.
- Any fee required for this permission shall be non-refundable after thirty (30) days from receipt by the CCC.
- These terms and conditions together with CCC's Billing and Payment terms and conditions (which are incorporated herein) form the entire agreement between you and WILEY concerning this licensing transaction and (in the absence of fraud) supersedes all prior agreements and representations of the parties, oral or written. This Agreement may not be amended except in writing signed by both parties. This Agreement shall be binding upon and inure to the benefit of the parties' successors, legal representatives, and authorized assigns.
- In the event of any conflict between your obligations established by these terms and conditions and those established by CCC's Billing and Payment terms and conditions, these terms and conditions shall prevail.
- WILEY expressly reserves all rights not specifically granted in the combination of (i) the license details provided by you and accepted in the course of this licensing transaction, (ii) these terms and conditions and (iii) CCC's Billing and Payment terms and conditions.
- This Agreement will be void if the Type of Use, Format, Circulation, or Requestor Type was misrepresented during the licensing process.
- This Agreement shall be governed by and construed in accordance with the laws of the State of New York, USA, without regards to such state's conflict of law rules. Any legal action, suit or proceeding arising out of or relating to these Terms and Conditions or the breach thereof shall be instituted in a court of competent jurisdiction in New York County in the State of New York in the United States of America and each party hereby consents and submits to the personal jurisdiction of such court, waives any objection to venue in such court and consents to service of process by registered or certified mail, return receipt requested, at the last known address of such party.

WILEY OPEN ACCESS TERMS AND CONDITIONS

Wiley Publishes Open Access Articles in fully Open Access Journals and in Subscription journals offering Online Open. Although most of the fully Open Access journals publish open access articles under the terms of the Creative Commons Attribution (CC BY) License

[https://s100.copyright.com/App/PrintableLicenseFrame.jsp?
publisherID=140&publisher](https://s100.copyright.com/App/PrintableLicenseFrame.jsp?publisherID=140&publisher)

only, the subscription journals and a few of the Open Access Journals offer a choice of Creative Commons Licenses. The license type is clearly identified on the article.

The Creative Commons Attribution License

The [Creative Commons Attribution License \(CC-BY\)](#) allows users to copy, distribute and transmit an article, adapt the article and make commercial use of the article. The CC-BY license permits commercial and non-

Creative Commons Attribution Non-Commercial License

The [Creative Commons Attribution Non-Commercial \(CC-BY-NC\) License](#) permits use, distribution and reproduction in any medium, provided the original work is properly cited and is not used for commercial purposes.(see below)

Creative Commons Attribution-Non-Commercial-NoDerivs License

The [Creative Commons Attribution Non-Commercial-NoDerivs License](#) (CC-BY-NC-ND) permits use, distribution and reproduction in any medium, provided the original work is properly cited, is not used for commercial purposes and no modifications or adaptations are made. (see below)

Use by commercial "for-profit" organizations

Use of Wiley Open Access articles for commercial, promotional, or marketing purposes requires further explicit permission from Wiley and will be subject to a fee.

Further details can be found on Wiley Online Library

<http://olabout.wiley.com/WileyCDA/Section/id-410895.html>

Other Terms and Conditions:

v1.10 Last updated September 2015

Questions? customercare@copyright.com or +1-855-239-3415 (toll free in the US) or +1-978-646-2777.

August 1, 2017

To Whom It May Concern,

I grant Erin Kahr permission to reproduce the research in the following co-authored papers in her PhD thesis. I am aware that the thesis will be subject to the University of Calgary Non-Exclusive Distribution License, that all University of Calgary theses are harvested by the Library and Archives Canada, and that the thesis may be submitted to ProQuest.

Kahr, E., Montenbruck, O., and O'Keefe, K. (2016) 'An Analysis of SBAS Signal Reception in Space,' *Navigation, Journal of the Institute of Navigation*, Vol. 63, No. 3, pp. 321-333.

Kahr, E., Montenbruck, O., O'Keefe, K. (2015) 'A Comparative Study of SBAS Systems for Navigation in Geostationary Orbit,' *Proceedings of ION GNSS+ 2015*, Tampa, FL, pp. 3875-3886.

Kahr, E., O'Keefe, K. and Montenbruck, O. (2014) 'Hardware-in-the-Loop Simulation of GNSS Signal Tracking in Highly Elliptical Orbits using the GSNRx™ Software Receiver,' *Proceedings of ION GNSS+ 2014*, Tampa, FL, pp. 1448-1458.

Sincerely,

31 July 2017

August 1, 2017

To Whom It May Concern,

I grant Erin Kahr permission to reproduce the research in the following co-authored papers in her PhD thesis. I am aware that the thesis will be subject to the University of Calgary Non-Exclusive Distribution License, that all University of Calgary theses are harvested by the Library and Archives Canada, and that the thesis may be submitted to ProQuest.

Kahr, E., Montenbruck, O., and O'Keefe, K. (2016) 'An Analysis of SBAS Signal Reception in Space,' *Navigation, Journal of the Institute of Navigation*, Vol. 63, No. 3, pp. 321-333.

Kahr, E., Montenbruck, O., O'Keefe, K. (2015) 'A Comparative Study of SBAS Systems for Navigation in Geostationary Orbit,' *Proceedings of ION GNSS+ 2015*, Tampa, FL, pp. 3875-3886.

Kahr, E., O'Keefe, K. and Montenbruck, O. (2014) 'Hardware-in-the-Loop Simulation of GNSS Signal Tracking in Highly Elliptical Orbits using the GSNRx™ Software Receiver,' *Proceedings of ION GNSS+ 2014*, Tampa, FL, pp. 1448-1458.

Sincerely,

31 July 2017

RE: MMS reference

Mitra Farahmand <mitra.farahmand@ai-solutions.com>

Mon 2017-07-10 7:49 AM

thesis

To: Erin Kahr <erinkahr@hotmail.com>;

Cc: Winternitz, Luke B. (GSFC-5960) <luke.b.winternitz@nasa.gov>; Bill Bamford (bill.bamford@emergentspace.com) <bill.bamford@emergentspace.com>; Price, Samuel R. (GSFC-5960) <samuel.r.price@nasa.gov>; Carpenter, Russell (GSFC-4440) <russell.carpenter@nasa.gov>; Anne Long <anne.long@ai-solutions.com>;

Hi Erin,

Good to hear back from you.

If not mistaken you are referring to the C/N0 plot for MMS1 with sidelobe tracking.

This was generated by the Navigator folks using the telemetry from the GPS receiver and not GEONS.
I have cc'd the co-authors on the ION paper.

The first author is Luke Winternitz.

I personally think it is cool to have MMS referenced in a Ph.D. thesis and say yes!

But I wanted to keep Luke, Bill, and Sam in the loop who are in charge of the Navigator receiver.

Luke, Bill, Sam, Russell, and Anne,

I had sent Erin who I met at ISSFD in 2015 a draft copy of ION paper.

Please see below her request. Let her know if any problem with using the figure.

Thanks, Mitra

From: Erin Kahr [mailto:erinkahr@hotmail.com]
Sent: Sunday, July 9, 2017 8:49 PM
To: Mitra Farahmand <mitra.farahmand@ai-solutions.com>
Subject: Re: MMS reference

Hi Mitra,

You sent me this a proof of your Navigation paper months ago. I was just wondering I could use one of the figures, Figure 6, in my PhD thesis (obviously with a reference to the source!). Or maybe a reference to the conference paper, they both use the same figure.

Please let me know!

Erin